Observing change in glacier flow by using optical satellites

Optiske satellitter observerer endringer i isbevegelse

Bas Altena

Dissertation submitted for the degree of Philosophiae Doctor (PhD)

Department of Geosciences
Faculty of Mathematics and Natural Sciences
University of Oslo

Oslo, Norway
February 2018

Series of dissertations submitted to the
Faculty of Mathematics and Natural Sciences, University of Oslo
No. 1977

ISSN 1501-7710

Cover: Hanne Baadsgaard Utigard.
Print production: Reprosentralen, University of Oslo.

Abstract

Complex natural systems are measured through indicators. An effective indicator for the climate system are glaciers. A glacier's surface mass balance relates to climate, while its dynamics depend upon local characteristics and the mass distribution of the glacier, responding to climate in a variety of ways. We therefore have to study the dynamics of many glaciers in order to reach a better understanding of the climate and how it changes.

In this study, we use optical satellite systems to observe a large number of glaciers, and construct long and short timescale records of their dynamics. There now exists decades of satellite imagery to extract reliable glacier displacement data, though errors from faulty orthorectification have limited use to same orbit calculations. In this thesis, a method is introduced to estimate displacements from images taken from different orbits, which are normally contaminated by orthorectification offsets. This integrative approach estimates elevation change and corrects glacier displacements simultaneously. To improve robustness of image matching, a novel matching scheme is applied based on triangle closure that automatically removes outliers.

The observation of short-term dynamics occurring on glaciers from satellites has only been possible because of an increase in the number of satellites, their acquisition frequency, and the fact that in recent years their data has become available for the public. Based on applying new techniques, based on "optical flow", timing of small speed-ups related to subglacial water input can be located precisely in time and space. In addition, this methodology makes it possible to quickly assess the dynamic status of glaciers, and to identify any abnormal dynamic behaviour.

Recently, the amount of satellite data has increased exponentially making it difficult to easily interpret spatio-temporal velocity data. A satellite-based understanding of glacier dynamics requires the transformation of displacement data into structured information. Here, we introduce a post-processing scheme based upon voting to effectively filter outliers on a large collection of satellite based velocity fields. This allows the construction of monthly time-series over several mountain ranges in Alaska. Observing both seasonal and annual fluctuations in dynamics where even the influence of small tributaries can be detected.

Sammendrag

Komplekse sytemer er ofte målt med indikatorer. Isbreer endrer seg i takt med klimaet, og er derfor viktige klimaindikatorer. En bres massebalanse er relatert til klima og dens dynamikk er relatert til lokale egenskaper og systemets tilstand. Når vi vil ha en bedre oversikt over klimaet så må dynamikken på mange breer observeres.

I denne doktorgradsavhandlingen brukes optiske satellitt systemer til å observere mange breer og registrere bredynamikk på kort og lang tidsskala. Fokuset i denne avhandlingen er å observere brebevegelse fra forskjellige optiske satellitt systemer for å registrere mest mulig pålitelig informasjon fra fire tiår med data fra satellittarkiver. Det introduseres en ny metode for å estimere brebevegelse fra forskjellige satellittbaner. Innfallsvinkelen er å estimere høydeforandringer og brebevegelse samtidig. I tillegg introduserer vi en bildesammenlikning basert på “triangle closure” som gjør metoden robust, men fortsatt pålitelig.

Det er mulig å observere brebevegelse med korte tidsintervall med en ny metode basert på “optical flow”. Små perioder med økt brehastighet på grunn av økt vannmengde i det subglasiale systemet under en bre, kan bli observert nøyaktig både romlig og i tid. Dette er kun mulig på grunn av den økte tilgangen de siste årene på gratis og fritt tilgjengelige satellittbilder. Metoden gjør det mulig å raskt undersøke og identifisere om en bre er ustabil.

For å bedre forstå bredynamikk kan man transformere data fra brebevegelse til strukturert informasjon. Jo mer brehastighetdata man har tilgjengelig, jo vanskeligere blir det å tolke hastighetssignalet til breen. Men ved å introdusere etterprosessering basert på votering så kan man filtrere ville observasjoner. Dette ble anvendt på et stort datasett av brehastigheter til å konstruere månedlige tidsserier over flere fjellkjeder i Alaska. Både årlige og sesongbaserte observasjoner var mulig å finne, også for mindre brearmer.

Samenvatting

Om inzicht te krijgen in de toestand van complexe systemen gebruiken we veelal indicatoren. Het klimaat is zo'n complex systeem. Een goede indicator voor hoe het met het klimaat is gesteld, is door te kijken naar gletsjers en hoe deze veranderen. De oppervlakte massabalans van een gletsjer is gerelateerd aan het klimaat, terwijl de dynamiek is gekoppeld aan lokale eigenschappen en de staat van het systeem. Om een beter idee te krijgen van het klimaat, moeten we de dynamiek van vele gletsjers observeren.

In dit proefschrift gebruiken we optische satellietsystemen om gletsjers te onderzoeken. We proberen een registratie te maken van gletsjer dynamiek op de lange en korte termijn. De focus ligt op gletsjer snelheden die worden geobserveerd door verschillende satellietsystemen. Uit het vier decennia oude satellietarchief genereren we zoveel mogelijk betrouwbare data middels een nieuwe methode. Deze methode maakt metingen mogelijk tussen verschillende omloop banen van kunstmanen. Tegelijkertijd is er een schatting mogelijk van hoogteverschillen en gletsjerverplaatsing. Daarnaast introduceren we een nieuw koppelschema gebaseerd op een driehoekssluiting. Dit maakt het vergelijken van beelden betrouwbaarder en de implementatie van deze methode efficiënt.

We introduceren een nieuwe methode gebaseerd op optische vloeiing. Daarmee is het mogelijk om gletsjerdynamica op korte termijn waar te nemen. Versnellingen gerelateerd aan een overvloed van subglaciale waterinvoer kunnen we nu precies lokaliseren in plaats en tijd. Dit is nu mogelijk omdat er recentelijk een grote hoeveelheid satellietdata openbaar is gemaakt. Onze methode maakt het mogelijk om snel een schatting te maken van de situatie; is een gletsjer onstabiel, of is deze uit de pas?

Tenslotte is de mogelijkheid gecreëerd om snelheidsdata te transformeren naar gestructureerde informatie. Duiding wordt namelijk lastig als de hoeveelheid data toeneemt. Daarom introduceren we een nabewerkingsstap door de zoekruimte discreet te maken en gebruik te maken van een stemming. Zo zuiveren we data van uitschieters. Deze methode is toegepast op een grote verzameling van snelheidsvelden waardoor er een maandelijkse tijdreeks is gemaakt van meerdere hooggebergtes in Alaska. Seizoensgebonden en jaarlijkse fluctuaties zijn nu te zien en het is zelfs mogelijk om de invloed te zien van kleine zijgletsjers.

Acknowledgment

I am very much aware of the fact that this page will be the most read part of the whole dissertation. But I hope that if you discuss this work around the coffee machine or in the bar, it will also cover subjects which are on another page within this booklet. That said, I fore mostly want to acknowledge my supervisor Andy. His support and guidance have been essential to this work. I very much enjoyed our discussions and very much appreciate the space you gave me to do this research. Furthermore, I want to thank my other supervisor Paul, he was able to better crystallize my thoughts through discussions. While on the other hand Chris has always been supporting me to think outside the box, which has been a great combination.

Another aspect why I have very much enjoyed working on this dissertation, is the good atmosphere present in the section of the department of Geosciences. Colleagues have been very supportive in and outside the office. Many thanks goes to PiM how has been a great friend and seems to be always sending positive energy. Live in the aquarium was better thanks to my office mates Adrien and Luc. But also many others within department, as well as, our weekly soccer team of geo-scientists.

There have been many opportunities during the PhD to meet some amazing people, either at conferences, summer-schools or fieldwork. But from all of those I want to especially thank Ted, for hosting me during a research visit in Boulder. Our discussions about next-level satellites were very inspiring, especially after some glasses of your own bottled wine. Another shout-out goes to Joe, through his efforts the cubesats are now an ideal constellations for cryospheric research. He and the team at Planet clearly demonstrate that industry and research can work in harmony, eventough their pace is different.

I also very much appreciated the work the committee has put into this. They might not have known before they agreed, but my ideas go in all directions, while my writing skills can not always keep up. Hence, they must have put in quite some effort to go through this work. Frankly this is the case for all others who I have asked to corrected and edit previous versions of this work, thanks for that!

I also want to thank my family and friends back home as well, as throughout the years they have been a great support or distraction. Lastly, my writers resort provided by Esther, along the channels of Amsterdam, have done me much good. Finally, there will be a good amount of people I have not mentioned. But at this time of writing, the defense date is approaching soon and this works needs to get printed. Hence for all those how I forgot, please confront me and get your acknowledgments when you meet me at the coffee machine or at the bar.

Contents

Part I

Overview

1 Introduction

1.1 Significance

A change in climate has global implications for a long period of time. Current policies aim to keep the global average temperature increase below two degrees Celsius, in respect to pre-industrial levels, with the ambition to stay below one-and-a-half degrees. However, for most people, these terms are abstract and difficult to grasp and it might not be clear why such seemingly small temperature changes are of such importance. To give context we can look at temperature fluctuations that have happened in the past, from today, back to the rise of civilization. In figure 1.1 two temperature reconstructions, based on the analysis of pollen, are plotted for two parts of Europe spanning the past 10 000 years.

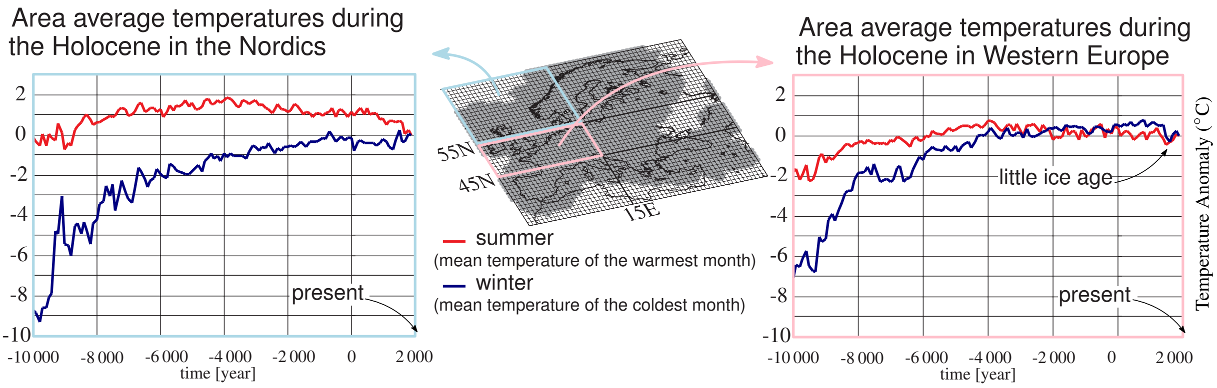

Figure 1.1: Reconstructed European surface temperatures, modified from Davis et al. (2003).

For Western Europe the temperature during the last 6 000 years seems to have been fairly constant. Before this time, at the start of the graph, civilization was sparse and re-population of this part of the world had begun after the last iceage. The growing population was nomadic in nature, with a hunter-gatherer lifestyle. These parts of Europe at that time were mostly boreal or arctic. The Nordic temperature reconstruction shows that mostly the winter temperatures were lower than those of today. At this time, the icesheet over Fennoscandia just disappeared from the peninsula. For Oslo specifically, the retreat of the icesheet margin occurred around 12 000 years before present (Stroeven et al., 2016). From this it is apparent that small fluctuations in temperature can have a large environmental impact. Another demonstration of this in the temperature reconstruction can be seen in Western Europe with the small dip in temperature close to modern day. This small fluctuation is the Little Ice Age, a time when ice-skating on the Dutch channels was common in winter. Hence, there is an important urgency to adjust our anthropogenic impact and innovate in order to reach our climate ambitions. With our emissions, we influence the atmosphere and thus climate. Serious consequences are connected to these pathways of possible climate futures and therefore limiting our impact is essential.

1.1.1 Sea level rise

The size and dynamics of a glacial system is related to climate. A positive contribution of mass is formed by precipitation, avalanches or windblown transportation of snow, while a negative contribution of mass is caused by surface (and basal) melt, evaporation and calving. Especially the precipitation and melting are climate dependent and changes therein influence the glaciers mass budget (i.e.: mass balance). If the budget is not in equilibrium with current climate, the glacier will change its water storage capacity (Cuffey and Paterson, 2010). The volume response of a glacier can be estimated through a ratio between the representative thickness of a glacier and its mass balance rate (Jóhannesson et al., 1989). As temperatures increase, this will cause a retreat in a glaciers volume. If the response time is taken into account, one can see that small alpine glaciers will melt away more quickly than the large icesheets of Greenland and Antarctica. The total water storage of Greenland and Antarctica, equals an approximate sea level equivalent of 64 meters (Lemke et al., 2007). Compared to these icesheets, the contribution of glaciers and ice fields is only a small fraction (i.e.: 0.15 - 0.37 meter). However, these smaller reservoirs are of most importance in the near future, as their response time is shorter.

1.1.2 Water shortage

The effect of climate change on glaciers can have implications on a regional scale. Rivers running out of the Himalaya, like the Indus or Ganges depend on glacial melt water which makes 40% of their discharge (Immerzeel et al., 2010). These rivers are heavily used for agriculture and thus future water availability is at risk depending on the glacier's reaction to climate change. Glaciers can also function as a buffer for droughts, as melting glaciers result in a steady runoff (Pritchard, 2017). As the Himalaya contains heavily variable climatic settings, topography and glaciers of different sizes, the influence and reaction to future run-off volume over time is different for each basin. In general, melting glaciers will produce an extra hydrological surplus in summer, although after some decades this mass will have disappeared and contribution of glaciers in summer will diminish (Lutz et al., 2014). At several down stream basins within the world summer meltwater is already declining (Huss and Hock, 2018). For the Himalayas, 800 million people depend on this water resource, but for many rivers decline is already occurring or will happen in some decades. Such timescales are out of sync with current agricultural operations, hence irrigation infrastructure will be set in place relying on glacial water estimates from present discharge, while these water resources will be vastly declining in some years.

1.1.3 Natural hazards

The impacts of climate change and glaciers may also be very local. Glacier retreat has been directly linked to rock slope response and instability (Kos et al., 2016) in which deglaciation increases landslide activity. In addition, increases in outburst floods (Narama et al., 2010; Stoffel and Huggel, 2012) or ice avalanches can occur due to warming of the ice (Gilbert et al., 2012). To make matters worse, many glaciers are situated in steep and high elevation environments, hence the potential energy of such landslides is considerable. Combined with a narrow run-out, such mass movements can be disastrous for communities living down-valley (Kääb et al., 2018).

1.2 Motivation

Glaciers and glacier change are of strong global significance, and we cannot understand their mechanisms by analyzing one single glacier. Thus, in this thesis repeat satellite imagery is used to estimate a large number of glaciers, covering multiple mountain ranges over the entire globe.

Knowledge of weather conditions can be extracted from meteorological stations. Such stations help us to understand the climate, its behavior and connections to other elements of the Earth system. There are systematic recordings available for certain points which span several hundreds of years. The stations are not evenly distributed around the globe (figure 1.2), with most of the stations situated in the civilized world. The majority of meteorological stations have been collecting data for just some decades, hence are limited when investigating climate which is defined by a period of 30 years or more. Other indicators for climate that can be used are therefore useful so they can complement in order to better understand climate patterns. This is especially true for the polar regions, where polar amplification results in an especially fast high-latitude warming (Serreze et al., 2000).

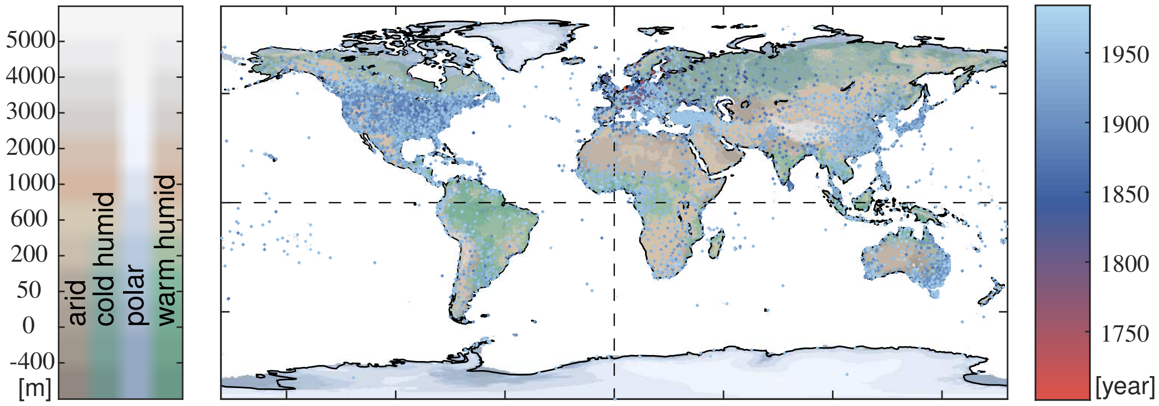

Figure 1.2: Global distribution of weather stations within the global historical climatology network (GHCN) and their color coding is in accordance with its first recording. Base map is constructed from an updated Köppen-Geiger classification (Peel et al., 2007), with cross-blended hypsometric tints (Patterson and Jenny, 2011).

One important climate indicator are therefore terrestrial icebodies, such as glaciers and icesheets (Lemke et al., 2007), as their global distribution complements the meteorological sensor network, as can be seen in (figure 1.3). Glaciers are mostly situated in remote areas where meteorological records are absent. These bodies of ice are reactive with their size and elevation profile to atmospheric conditions and thus understanding of their behavior is essential to derive a meaningful climate signal from them.

Earlier measurements and documentation of glaciers at such remote locations are valuable but fragmented. Data is often limited to expedition logs and journals describing a small area with a minimal amount of (geo)metric information. More systematic acquisitions that stretch over larger areas is sometimes available in the form of aerial photographic reconnaissance campaigns. These campaigns originated because of border disputes or as cadastral baselines, see for example figure 1.4. Using (Tennant et al., 2012) or reprocessing these imagery makes it possible to generate topographic data, and compare against todays maps, such as for Greenland (Bjørk et al., 2012; Korsgaard et al., 2016) or Svalbard (Girod, 2018). However these campaigns were often not repeated, as the need for map updates is of low priority and thus flight are typically

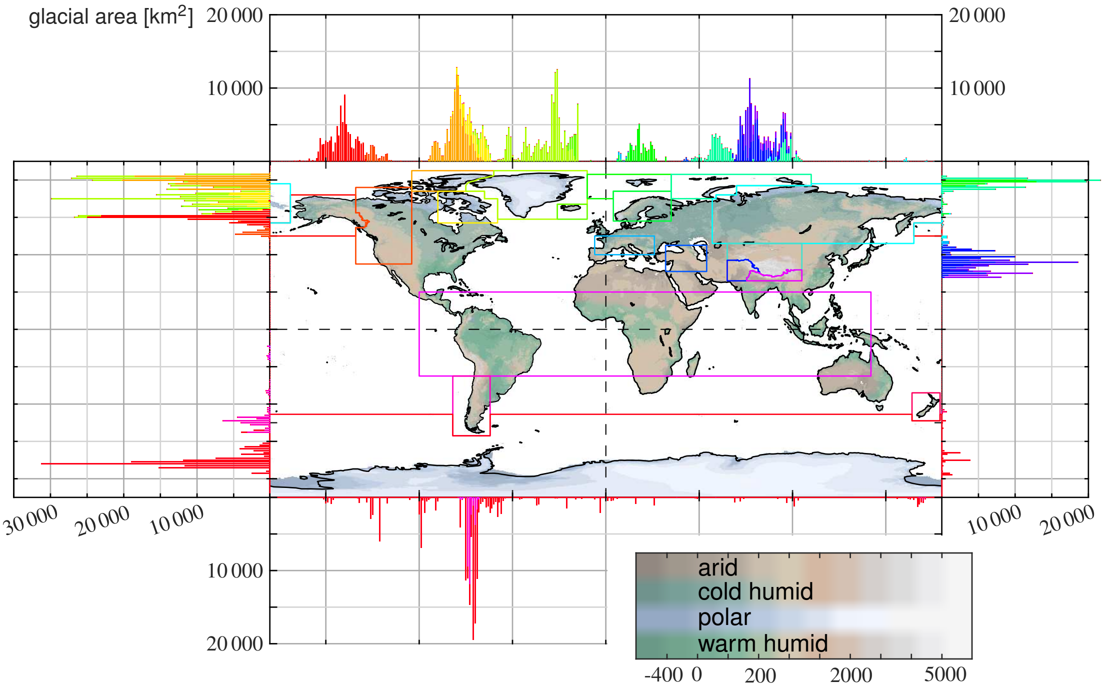

Figure 1.3: Global distribution of glaciers and small ice-caps, based on data from the Randolph glacier inventory (RGI) (Pfeffer et al., 2014)

separated by several decades.

Optical instruments on-board satellites has been collecting data since the 1960's making this temporal record long enough to be of use for climatological assessments (again, 30 year records or more). With this especially rich archive containing most polar and mountainous regions, modern day processing-power with state-of-the-art mathematical algorithms are able to process such data, that means that these archives can be re-analysed. For example by extracting geometric parameters and changes of glaciers (Kargel et al., 2014; Paul et al., 2015) through time.

1.2.1 Improved process understanding

A second motivation to use optical spaceborne remote sensing is to get a better understanding of glacier dynamics. When glaciers are used as climate indicators, the dynamical component, which can be glacier specific, needs to be separated from the surface mass balance component, called the climatic mass balance in Cogley et al. (2011). For example, the geology, bedrock topography and conditions (i.e. at the base, rock-ice mixture), are all site specific elements that influence glacier dynamics. Our understanding of these factors and their influence on ice

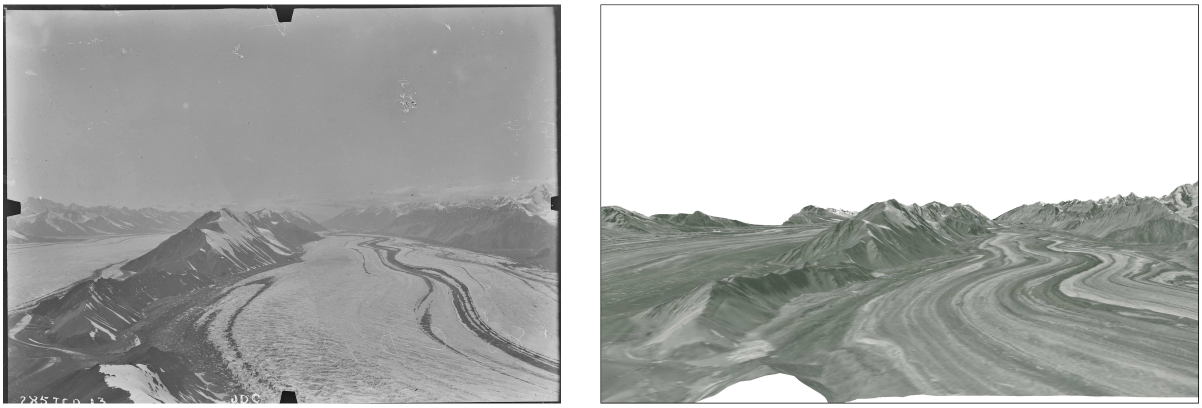

(a) Terrestrial image (1913)

(b) Aerial reconstruction (1951)

Figure 1.4: a) image taken from a marker station over the snout of Walsh and Logan glacier, Alaska/Yukon. The glass plate was part of a series to construct a panorama. Courtesy to the international boundary commission, photo (presumably) by A. Baldwin. b) Photorealisitic reconstruction of the same section based upon aerial imagery from an early systematic flight over the Centinental range by the government of Yukon.

dynamics needs improvement. Generalizations from single glaciers might not be sufficient to extrapolate and therefore glacier dynamics of entire mountain ranges is required. Again optical remote sensing is one of the only efficient options, as the satellites overpass more frequently and the spatial resolutions are at sufficient scale.

Earth observation satellites are able to extract surface features such as topography, displacement, water-content or changes therein. This thesis will focus mainly on ice velocity. Analyzing the glacier's velocity regime and changes through time of it will help understand its adjustment to climate and it's changes. Only with a large collection of remote sensing data spanning back in time for several decades and with an inter-seasonal resolution, is it possible to investigate or unravel different processes and feedbacks occurring through different time scales (figure 1.5).

Relative velocity increase can occur due to a short-term positive feedback, when increases in surface melt promote basal sliding, transporting more ice to lower elevations, melting ice more rapidly. This feedback promotes a glaciers attempt to reach an equilibrium with current climate. Interestingly, a negative feedback is also promoted by surface melt which decreases the thickness of the ice. This reduction of the ice collumn results in less pressure at the base and therefore a reduced deformation, speed in the viscous component of the ice flow. At the same time, a positive feedback involving the temperature of the ice column is also apparent with a warming climate. When ice gets warmer, the bindings between ice crystals become less

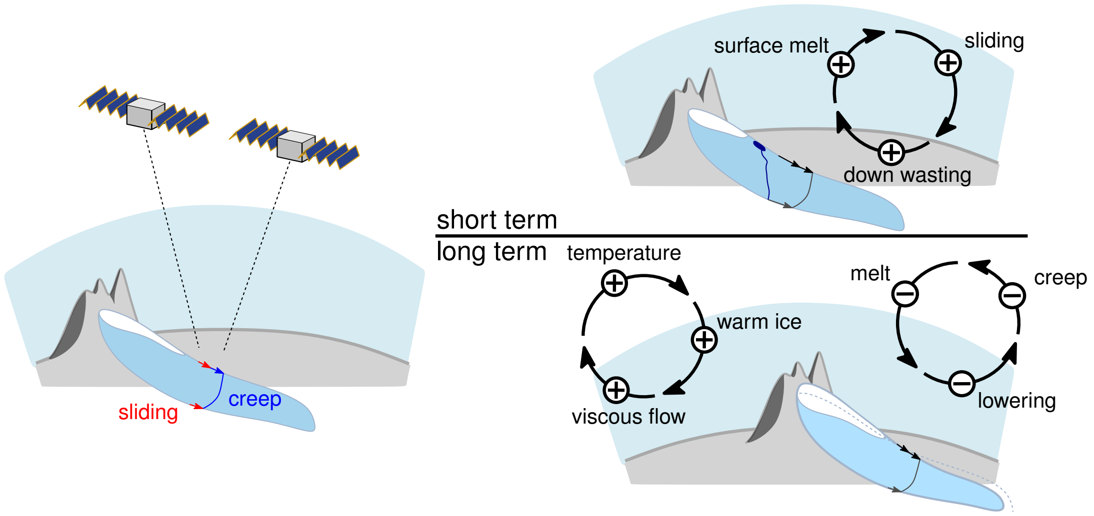

Figure 1.5: Schematic drawing of remote sensing of a glacier. On the right side different feedback loops are shown that occur on a glacier due to atmospheric forcing.

stiff and the ice will flow more easily. The dominant feedback or the net effect depends on site specific geometric conditions. In addition, the time scale at which these feedback loops operate are different. When a sufficient group of glaciers is analyzed within a similar climate setting or mountain range, the different velocity patterns provide the necessary spatio-temporal data from which to separate the contribution of the individual processes. Because of the vast scope, generation of such datasets can only be achieved with spaceborne instruments.

1.3 Opportunity

1.3.1 Opening of the Earth observation archives

Through the open data policy of many space agencies (ESA, NASA, JAXA, INPE, ...), the exploitation of remote sensing archives becomes more and more feasible for both scientists and the public. This has fostered transparency (Sá and Grieco, 2016) and advances into large scale and high temporal resolution data analysis, and enhanced exchange of ideas between different disciplines (Wulder et al., 2012). This goes in conjunction with an increase in present day computing power, bringing the opportunity to process large amounts of imagery.

1.3.2 Current increased Earth observation

Currently an extensive amount of Earth observation data is collected by Earth observation missions and constellations (Berger et al., 2012). Much of these optical- or radar-data are ideal for estimating surface velocity over glaciers and ice-caps. Most of the improvements can be attributed to the continuously enhanced instrumentation on-board the satellites. Optical instruments on satellites have improved their radiometry, and are now able to record the surface in more radiometric detail (both pixel-depth and its spectal range). Spatial resolution of optical satellite imagery has increased as well, providing a higher level of spatial detail. Importantly, the amounts of recording over time is increasing from a growth in number of satellites available. Especially non-systematic overpasses occur when various orbit constellations are combined and orbits are in tandem or as a swarm (Doan et al., 2017). Finally, coverage by these satellites has enabled the entire globe to be observed and with increased on-board storage capacity, improved downlink data transmission, and use of communication relay satellites, unprecedentedly high spatial resolution images with daily to weekly temporal resolutions are available.

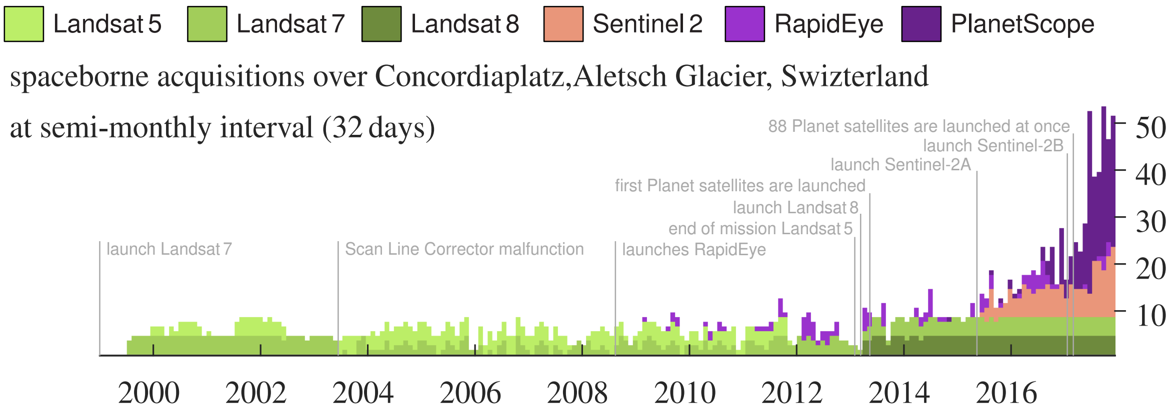

Figure 1.6: An example that illustrates the recent increase in optical satellite observations over glaciers. The data from Landsat 5 is from the USGS, hence more data might be available for this instrument.

This recent evolution in Earth observation capability provides an enormous potential (figure 1.6) to discover and quantify components of this fast changing world. While formerly spaceborne data was difficult to purchase and handle, large volumes of data are now available which in turn need to be transformed into digestible information. Therefore robust and efficient processing practices are required to capitalize on the large data volumes.

1.4 Objectives

The current warming in the cryosphere during recent decades may trigger many types of dynamic reactions in glaciers which fortunately are recorded by our spaceborne instruments. Current methods for analyzing glacier flow from optical satellite imagery have not changed considerably since the first automatic implementation (Scambos et al., 1992; Rolstad et al., 1997). Thus, while technical advances in the space industry have eased extraction of glacier displacements, there are relatively minor advances in the algorithms' abilities to tackle the new highly detailed information available. Specifically for glacier velocity assessments, large scale data processing has occurred, and processing pipelines with minimal manual intervention are implemented. Quality control is still lacking, eventhough this is an essential part when one aims to deliver products for analysis, instead of working with raw imagery and data.

Today, efficient image matching pipelines are available, though quality control is still problematic. The next challenges are therefore post-processing procedures and a potential universal translation allowing automatic analysis. These processing steps are the subject of this thesis which loosely aims for completely automatic image analysis and velocity generation over large spatial scales and many glaciers, allowing more advanced process understanding of glacier dynamics. Thus, the following objectives formulated relate specifically to our current situation with lots of data but inefficient extraction of information. These can be categorized into the following topics:

- **increased imagery** - In recent years several Earth observation satellite systems are deployed in space, and their imagery is available to the public (i.e.: Landsat or Sentinels). This increased coverage (along with increased geometric accuracy) makes it possible to monitor seasonal varition of fast flowing glaciers. Hence this thesis aims to get most out of the available imagery, in terms of seasonal glacier flow variability.

- **better resolution** - Glacier displacements estimated from optical satellites traditionally uses annual images in order to allow for enough displacement to be above the noise in the measurements. Improved instrumentation on satellites allow to acquire imagery with better resolutions. Consequently, better results can be achieved, but the information extraction might be improved further as well, through exploration of other displacement estimation techniques. This thesis aims to explore and exploit improved high resolution imagery to investigate in detail unique short-term processes on glaciers.

- **information extraction** - the satellite image archives now represent a *big data* set. The quality of extracted velocity products strongly depends on characteristics of the image data used, as influences from temporal coherence in conditions and resolution are variable. Often, extracted displacements can be false-positive, meaning a correct geometric displacement but deriving from a different physical phenomena or technical origin. Therefore, this thesis aims to improve the extraction or separation of correct glacier displacement fields from outliers.
- **characterization** - the extraction of multi-temporal region-wide glacier velocity data generates a challenge for information extraction. The discovery of abnormal glacier behavior or lack thereof becomes labor intensive. Therefore, this thesis aims to apply new visualization tools to ease the extraction of important velocity information. Improved characterization of these ever improving multi-temporal datasets is therefore of great importance and simply very exciting!

1.5 Outline

The background leading into this thesis is the recent explosion of Earth observation imagery and further need for exploitation of large volumes of data. In order to do this reliable and efficient, a large amount of technical detail is needed. This dissertation is divided into three parts, the first part will introduce many technical and glacier specific details. The present first chapter, introduces the overall subject and aims of this thesis. After this, chapter 2 introduces Earth observation in relation to glaciology with a focus on glacier flow. Chapter 4 highlights the methods to extract velocity from optical data and further post-processing to improve the reliability of glacier velocity estimates. This is by no means a full review within this application domain which is more provided in general within Kääb et al. (2014a) or focused on icesheets (Quincey and Luckman, 2009) or geomorphology (Watson and Quincey, 2012).

The bulk introduction is followed by chapter 5 which highlights the different publications stemming from this research. Chapter 6 provides general conclusions and future perspectives. The second part of this dissertation is composed of published and submitted journal articles. The appendix lists other research done during this period.

2 Optical remote sensing of glaciers

2.1 Observing glacier flow

In this section, various approaches for measuring glacier surface displacement or ice surface deformation are described. First the different remote sensing platforms will be discussed, from close-range to spaceborne. Then the different instruments and methodologies to measure displacement are highlighted, which is of use for paper I&II. To put this thesis into perspective, a brief historical review of glacier velocity studies is given, which is followed by a time line of satellite observation. The subsequent parts give an overview of processes involved with or causing glacier motion, which is relevant for paper III. Lastly, the scale of the velocity fields and their applications are briefly set apart to put a broader perspective to this work and outlook to future directions.

2.1.1 Platforms

Glacier velocity data can be collected from a variety of vantage points. Due to technical advances, many approaches have evolved into economic and efficient mapping tools. The earliest research was limited to terrestrial work, while today most information is gathered from instrument deployed onto platforms. Recently, the abundance of satellites as platforms has transformed the scale and coverage of potential velocity estimation. Various platforms to measure ice velocity are described hereafter, ordered from close to far range.

In-situ measurements

As satellite navigation became publicly available, the deployment of global navigational satellite systems (GNSS) receivers on glaciers became feasible. The advantage of independent positioning sensors is its ability to measure at a high temporal frequency in all three dimensions of space, and continuously over seasons and years. This allows measurement of short-term processes occurring on glaciers. However, as shown in figure 2.1(a), it is challenging to place GNSS instruments on glaciers, and they only provide measurements at a single point. On this glacier, Kronebreen, a summer speed-up is clearly identifiable, but also an additional second peak towards the end of the summer (figure 2.1(b)). However, glacier velocity variations are not constant over the entire surface as can be seen by the different shapes of the curves of the different stakes located across the glacier. Thus glacier flow is more complicated as measurements from several stakes along a flowline already suggest.

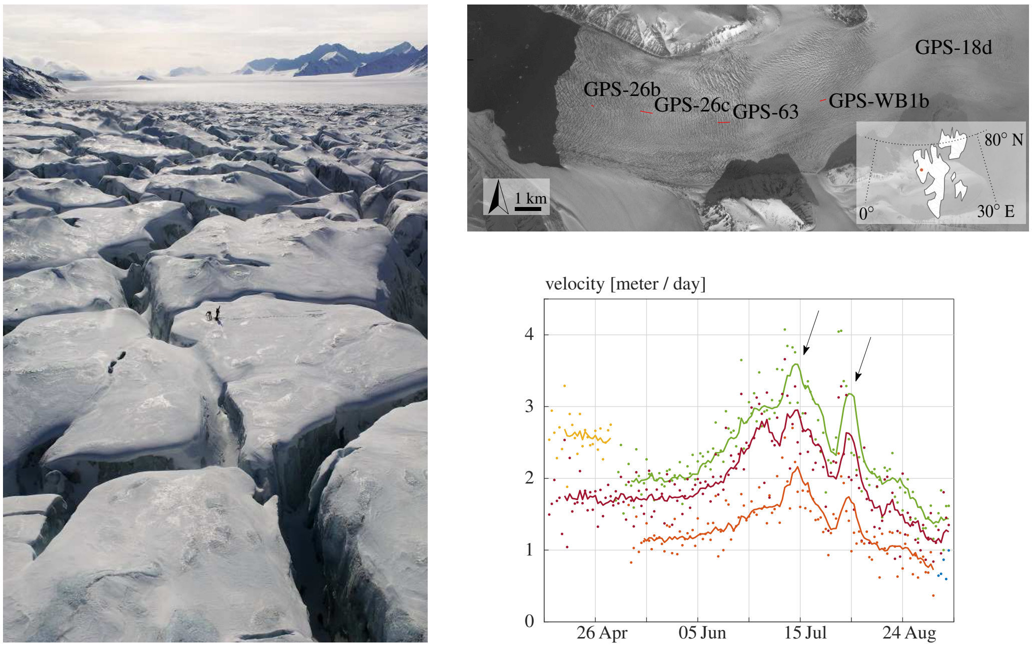

(a) GPS stake deployment (b) Seasonal glacier velocity on Kronebreen

Figure 2.1: a) Kirsty Langley and Jack Kohler deploy a GPS stake on Kronebreen glacier, Svalbard. Photo by Elvar Orn Kjartansson. b) Map of Kronebreen with the location of several GPS stakes. In the lower panel are the velocities of these stakes over a summer season in 2015, with a weekly traveling mean drawn along each stake. Data provided by Jack Kohler, Norwegian Polar Institute.

Terrestrial remote sensing

Another possibility to extract velocity is from a terrestrial vantage point, for example from a time-lapse camera (Ahn and Box, 2010), or terrestrial lidar and radar. In all the above, measurements are acquired in sequence through time and as such are multi-temporal by nature.

Typically, glacier ice moves slow, limiting campaigns to a summer season or annual snapshots. However, in recent years automatic triggering devices have made it possible to deploy camera set-ups all year round. In this way, glacier velocities over larger sections or regions can be measured (Ahn and Box, 2010; Messerli and Grinsted, 2015; Giordan et al., 2016) rather than the single point measurements by GNSS instrumentation.

Airborne remote sensing

From a birds' eye view, it is possible to observe large areas. Airplanes, balloons, kites and other platforms are ideal for monitoring efforts at glacier basin scales or even for small mountain ranges. Aerial photography can be used to extract glacier wide velocity fields when dedicated monthly flights are conducted (Meier et al., 1985). However, this involves a good weather window for the airplane to conduct the flight. Furthermore, the processing used to be done through restitution, which is a labor intensive task. Analogue stereo pairs were used to identify point on the glacier, hence the glaciers surface needed to be heavily crevassed, so unique identification was possible. In addition, the flights were at high elevation, as the photo's field-of-view should include stable terrain in its borders. As such photogrammetric processing advanced, block triangulation of multiple flightlines became possible. Imagery could be orhtorectified, which eased the processing burden and made airborne analysis of glacier velocity more accessible (Debella-Gilo and Kääb, 2012b).

The last decade has seen an increase in the use of fixed-wing or multi-rotor autonomous aerial vehicles, or simply drones. The ease of deployment makes it possible to survey a larger part of the glacier within one or a few days (Kraaijenbrink et al., 2016). These platforms allow data collection at high resolution, acquiring velocity data of terrain that may otherwise be difficult to access, such as debris covered snouts, which is typically, hummocky, loose and steep. The high detail of resulting products are ideal to track changes over time, or measure flow features.

Spaceborne remote sensing

For mountain ranges and global scale monitoring, it is necessary to use instruments deployed in space. To some extent this method is not hampered by political, safety or logistical struggles, which is the case when one is involved in a terrestrial mapping campaign. However it does introduce other challenges, mostly technical, as setting such instruments into space is still an achievement. Nonetheless, such spaceborne instruments have changed the field of glaciology and our understanding of the natural world in general. This subject will therefore be further highlighted in section 2.2.

2.1.2 Electromagnetic instruments to measure movement

In the following section several instruments are highlighted that are able to record glacier flow or ice movement. This section will be limited to instruments that operate in the electromagnetic spectrum.

Optical instruments (passive remote sensing)

Optical instruments (cameras) sense wavelengths in the visible, near infrared (NIR) and shortwave infrared (SWIR) domain of the electromagnetic spectrum. When light is polarized, the stress of a material is able to change the orientation of the light waves as it travels through. This photo-elasticity can be recorded by cameras and ice does experience this material behaviour. However, the sun's polarization emits isotropically, hence, laboratory experiments can only take advantage of this property. Nevertheless, this can give insights into the stress regime and evolution of simple geometries such as ice wedges (Davidson and Nye, 1985).

The majority of optical imaging sensors are used to collect numerous measurements in a rectangular grid (i.e. pixels), from a certain vantage point. Objects in the field-of-view provide an unique spatial arrangement of reflected intensities. When multiple images are acquired, similar spatial arrangements of pixels may be detected across the images. When images are acquired through time, the relative displacement can be used to estimate movement (paperI). When the images are acquired from different positions, the relative position of the objects can be obtained, also known as photogrammetry.

Microwave instruments (active remote sensing)

Microwave sensors record energy in the electomagnetic spectrum with wavelengths between 1 centimeter and 1 meter. A major advantage of microwave sensors is their limited sensitivity to perturbance by clouds and they don't require sunlight. In microwave wavelengths, raindrops and clouds are too small to block transmission of the microwave pulses. However, microwave

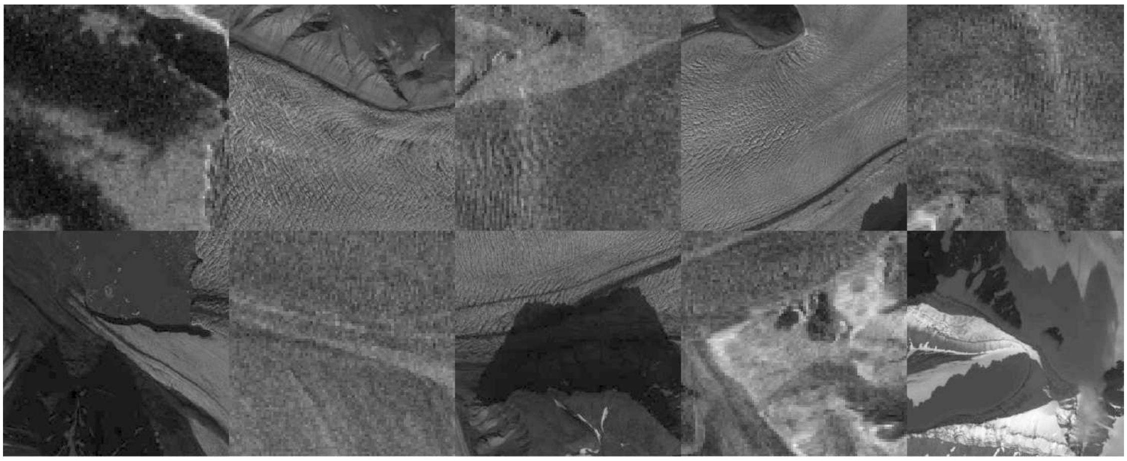

Figure 2.2: Checkerboard composition of an optical and SAR image, (1) is an orthorectified optical acquisition over Kronebreen glacier, Svalbard. The image was taken with the SPOT5 satellite at the 22nd of August 2015, (2) is an orthorectified intensity SAR acquisition by Sentinel-1 on the 26st of August 2015. Both instruments record objects differently, as well as, geometric artifacts have different specifics.

travel time through the atmosphere is effected by humidity, which in many remote places is not known sufficiently as it is highly variable over space and time.

Active microwave sensors transmit pulses and receive their reflections. In this way, the two-way travel time can be used to estimate the distance of travel. Phase differences of the returned signals may also be used, instead of the absolute travel time, leading to the method of radar interferometry useful for the measurement of small displacements in line of sight under the preservation of interferometric phase coherence. If multiple antennas are deployed, a baseline between them can be established and when rotated imaging capabilities become possible. Portable terrestrial installations have been developed (Strozzi et al., 2012) and with such instrumentation it is possible to extract velocity fields on a short interval (Voytenko et al., 2017). In this way glacier fronts, snouts or individual calving blocks can be monitored. This is especially of interest for glacier fronts, as the wall of ice functions as a good reflector. While ice is a surface reflector, for snow volume scattering occurs and the amount of penetration and scattering depends on snowpack properties (density, liquid water content, ...) but also the wavelength of the instrument. For dry snow and X-band radar this can be in the order of several meters (Dehecq et al., 2016).

When such techniques are used in space, the microwave acquisitions over its full orbit can be used to construct a synthetic aperture radar (SAR) scene (figure 2.2). The next acquisition which is somehow in the same orbital track can then be used to construct a baseline, and the resulting interferometric phase difference can be related to the terrain displacement (InSAR), if the atmospheric delay is known sufficiently. This technique has been used considerably, for ice fields (Mouginot and Rignot, 2015), rock slopes (Rott et al., 1999) or rock glaciers (Strozzi et al., 2004). Due to its insensitivity to clouds it is a reliable approach for consistent monitoring of large regions with slow moving land surfaces.

The imaging capabilities of SAR sensors can be used to track ice surface movement (Fahnestock et al., 1993). The technique uses similar methods as based on repeat optical data, however, radar has a complex signal, thus the phase, intensity or both components can be used for image matching (Michel and Rignot, 1999; Gray et al., 2001). In Arctic regions the reflection stays coherent within the snowpack for the accumulation area of the glacier and throughout the winter (Weydahl, 2001). It is this situation that makes this techniques nowadays heavily exploited for the construction of multi-annual velocity mosaics of the icesheets (Joughin et al., 2017).

Laser instruments (active remote sensing)

A light detection and ranging (lidar) systems is able to generate point clouds, which produce three dimensional data. With such data it is possible to observe slow moving rock glaciers (Kenner et al., 2014), or glaciers in general (Schwalbe et al., 2008; Telling et al., 2017). Typically, a high-pass filter over the elevation data, or an artificially generated hillshade (Rees and Arnold, 2007) is used. When the topographic data is irregular, iterative closed point (ICP) algorithms or other co-registring techniques can be used.

The main advantage of laser is the invariance to visual appearance. When the data over the glacier is of high resolution, most of the time crevasses will stand out of a glacier surface. Fortunately these features are very stable against melt, as crevasses can be relatively large, and their relative complex spatial composition will not change considerably. Nevertheless, due to the melt, which is typically highest at the snout, the following of crevasses might not co-align with the movement but with down-wasting. The topographic data can also be used to automatically map crevasses (Kodde et al., 2007), which is a glacial flow feature.

Apart from the geometric information given by a lidar instrument, the intensity of the return signal is sometimes used as well. However, in order to get from intensity to surface reflectance, advanced radiometric processing is needed. Hence, its use might be better for surface classification (Höfle et al., 2007), such as snow line monitoring (Prantl et al., 2017).

2.1.3 Spatial & temporal scales of glacier flow

Velocity products can be of use for applications at different scales in time and space. At millimeter or centimeter scale insight is given on material processes or individual gravelstone interaction. Through the use of a telescopic pole, it is possible to see seasonal frost-heave processes, such as sorted circles (Kääb et al., 2014b). Also by pressurizing ice in a laboratory setting, shear tests can give measures to observe ice deformation, and help to test hypothsis of bedrock interaction (Iverson and Petersen, 2011).

At meter scale, analysis on individual failures of ice blocks or hanging glaciers is feasible. Before release, the velocity seems to follow a log-periodic function (Rothlisberger, 1981; Faillettaz et al., 2016), and therefore early warning might be possible. Moreover, with a terrestrial camera it is possible to see the vertical motion of glacier ice. When a supra-glacial or marginal lakes drain into an englacial hydrologic system, uplift of the glacier surface will occur. Hence, the localization of such a drainage network can be extracted from terrestrial photogrammetry (Schwalbe et al., 2016).

Optical satellites are ideal for analysis that cover single or several glaciers. Dynamic ice flow instabilities on seasonal (paper II), yearly (Mayer et al., 2011; Quincey et al., 2015) or decadal scale (Nolan, 2003) can be extracted. This scale is the main focus of this thesis and more examples will be given later (paper I&III). On kilometer scale, velocity products data can be input for mechanical ice shelf models. In this way it is possible to predict the trajectory of rift failure and model crack propagation (Borstad et al., 2017).

At a continental scale, velocity products can be used to look at total mass balance of ice sheets (Andersen et al., 2015; Gardner et al., 2018) using velocity products to estimate ice flux through a perimeter around an ice sheet or an ice cap. The input is given by the surface mass balance from atmospheric re-analysis data or directly from weather stations data. Surface velocities are used to delineate the basins and form together with bedrock topography an estimate for the mass-output.

2.1.4 Time-line of glacier velocity observations

Since the early days of glaciology glacier flow has been a subject of study. The first systematic surveys have been conducted by James Forbes on Mer de Glace, France. Such surveys were conducted through markers and theodolites. One of the first notable surveys exploiting cameras was the Cambridge expedition to Austerdalsbreen, Norway (Nye, 1958). Over the course of a short summer season the velocity of Odinsbreen icefall was estimated. After that, technology advanced and it became possible to use aerial campaigns and satellites to estimate glacier velocity.

To get a better idea of the history and advances over time, some studies are organized into a timeline in figure 2.3. Different colours in the annotations relate to the different vantage points or platforms used in the study, as described in the above sections. The colors of the timespan represent the temporal sampling interval, which the study conducted. The dashing of the line is an indication when the processing was done: has it been within a campaign, or was the archive used as reprocessing of data becomes more feasible with modern processing tools.

What can be seen from this graph is in general the upscaling of the studies over time, which is logical as the extent of terrestrial field work is limited, similar to aerial campaigns. The grouping in the table is also following milestones. Since the 1990's computers became a powerful working horse to extract velocities (semi)automatically. This made it possible to process aerial and spaceborne data. In the 2000's the emphasis begins to shift to summer speed-ups in relation to annual velocities. While the present decade sees an increase in the computing power, making it possible to look at mutliple mountain ranges or continents in addition to re-processing of older data to get a better historical perspective.

This diagram is by no means inclusive and has a strong bias towards large-scale processes. In the present decade the processing of velocity data over the scale of a full glacier has evolved as well, and many studies exist investigating single glacier dynamics. However, for sake of simplicity and space limitations, these are left out of the diagram. Nonetheless, some of the results of this thesis are set in this diagram as well. These have slanted text and give an indication how this study could be seen in a broader context.

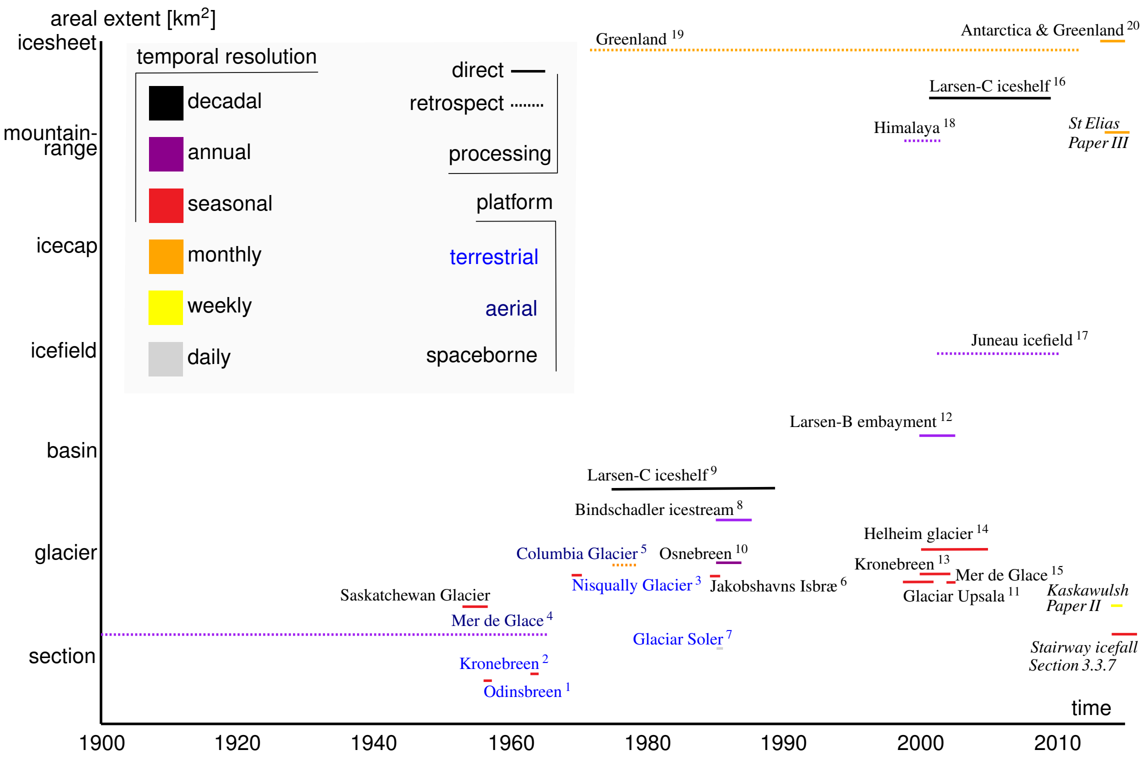

<1990's	1990's	2000's	2010's
1 Nye (1958)	6 Echelmeyer and Harrison (1990)	11 Skvarca et al. (2003)	16 Heid and Kääb (2012b)
2 Pillewizer and Voigt (1968)	7 Naruse et al. (1992)	12 Scambos et al. (2004)	17 Melkonian et al. (2014)
3 Hodge (1974)	8 Scambos et al. (1992)	13 Kääb et al. (2005)	18 Dehecq et al. (2015)
4 Lliboutry and Reynaud (1981)	9 Bindschadler et al. (1994)	14 Howat et al. (2005)	19 Rosenau et al. (2015)
5 Meier and Post (1987)	10 Rolstad et al. (1997)	15 Berthier et al. (2005)	20 Fahnestock et al. (2016)

Figure 2.3: A historical selection of studies extracting glacier velocities from optical data. The slanted text are studies of this thesis. The numbers indicate the studies as given in the table below the figure.

2.2 Spaceborne Earth observation

Earth observation satellites have been launched since the start of the space-race in the early 1960's. The first satellites, like Sputnik, functioned as radio beacons in which signals were pinged back to Earth to be used as travel time measurements for estimating orbits, the Earth's geoid or Earth's curvature. Shortly after, instrumentation was installed on board satellites. These initial satellite instruments defined the pathway for future satellite system developments, which can in many ways be seen as an evolution (figure 2.4).

The first high resolution cameras on board satellites were used for espionage and defense intelligence at the end of the 1960's, named the Corona missions. Film-rolls were send back into the atmosphere and caught in the air by nets attached behind aircrafts (McDonald, 1995). The resulting image rolls have a complicated panoramic acquisition geometry but have been used to extract topographic data (Sohn et al., 2004). Because of its long time span, this data source is of great interest for glaciological studies (Bolch et al., 2011).

With the advancement of digital recording technology, it became possible to filter and isolate a selective part of the electromagnetic spectrum. This resulted in the earth resources technology satellite (ERTS, later named Landsat 1) for environmental monitoring, which also had a mission objective for cryospheric applications (Krimmel and Meier, 1975; Østrem, 1975). The first series of the Landsat satellite legacy had four spectral bands with a resolution (pixel size) of roughly 80 meters. The original targeted users where industries related to geological mapping and governmental agencies dealing with environmental planning, though today the Landsat fleet is heavily used in all fields studying Earth's natural environment.

The optical satellite evolution branches as sensor technology advances. This is due to design constrain on the satellite, as only a limited amount of reflected energy from the earth surface is available for recording as a satellite overpasses. Hence, when one wants to have a better spatial resolution, one needs to decrease the spectral resolution, and vice versa. The satellite evolutionary branching in light brown is the direction with emphasis on the spectral detail. This started with the launch of the advanced very-high-resolution radiometer (AVHRR) legacy in 1978. Its suit of satellites is operated by the national oceanic and atmospheric administration (NOAA) and newer generations are still in use today. Typically these sensors have a high radiometric resolution (10 bit), but a lower spatial resolution of 1100 meters. Dispite a low spatial resolution, this satellite has been used in glaciology for terrain refinement (Scambos and Fahnestock, 1998) or glacier facies classification. In 1999, the Terra and Aqua satellites were launched containing the moderate-resolution imaging spectroradiometer (MODIS) instrument on board and both satellites are still in orbit today. A similar sensor (MERIS) on board the European counterpart, the Envisat satellite, was launched in 2002 by the european space agency (ESA) and was superseded in 2016 by Sentinel-3. The spatial resolution of these instruments is in the order of 300 to 500 meters. Despite their large spatial resolution, it is still possible to extract glacier velocity from these sensors (Haug et al., 2010). However, the method is limited to areas with relatively constant surface reflection characteristics and large displacement rates such as the ice shelves of Antarctica.

The second major evolutionary branch in optical remote sensing includes those satellites with an emphasis on high spatial resolution imagery. This began with the launch of satellite pour

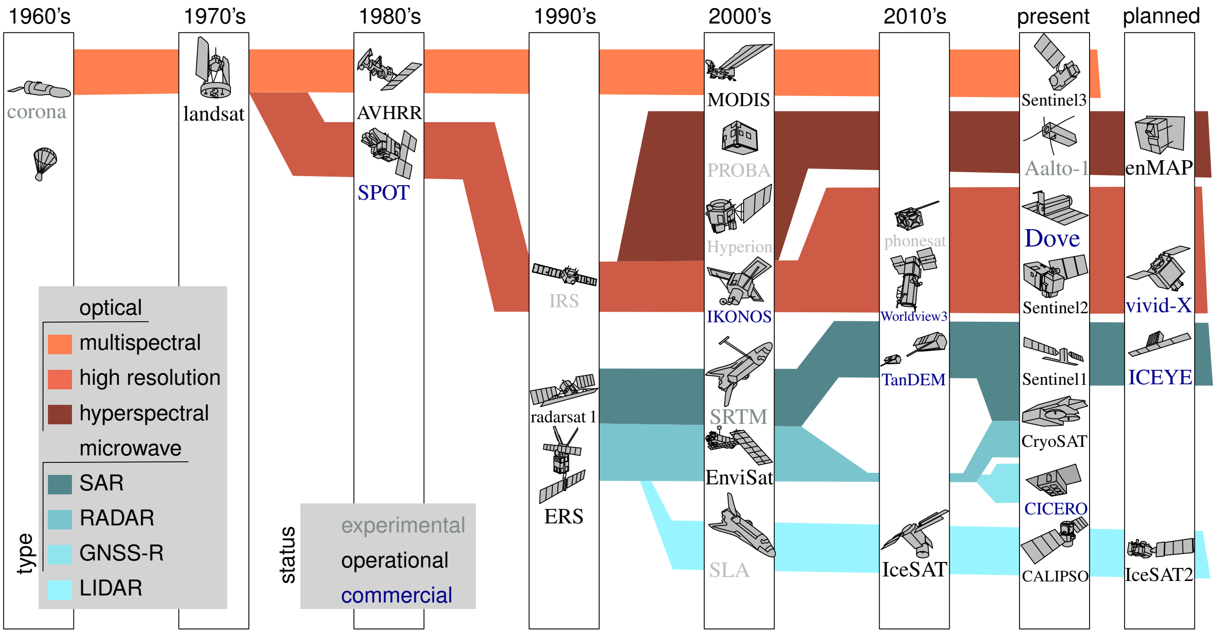

Figure 2.4: Pathways of Earth observation missions, specifically for surface monitoring and structured by their instrumental characteristics.

l'observation de la terre (SPOT) in 1986. Interestingly, this launch was the first public-private endevaour, marking a change in the business model of the industry. In glaciology, the data has mostly been used to classify surface characteristics, discriminating between snow, ice or shadow (Parrot et al., 1993). However, with increased image resolution and advances in computational power, the first glacier velocity fields where extracted in the early 1990's (Lefauconnier et al., 1994). Then in 1999 the branch transforms with the launches of the first commercial private satellites, such as IKONOS. These satellites systems were developed with highly agile pointing abilities, so revisit times could be reduced at specific regions of interest. Amazingly, IKONOS had a resolution of one meter, while at the same time the public optical satellite counterpart, ASTER, was launched in 1999 and had a 15m spatial pixel resolution. Currently, the resolution of private developed optical satellite systems are well below a meter (i.e. Worldview, Pléiades).

As a large branch of the space-based Earth observation development continued to increase the spatial resolution of their systems, another branch emerged to utilize a larger breadth of spectral characteristics. Instead of a spatial refinement, a spectral refinement was envisioned. In glaciology, this is of interest as defined frequencies within the electromagnetic spectrum serve as a fingerprint for material properties such as snow fraction (Dozier and Painter, 2004), or supra-glacial geology (Casey and Kääb, 2012). Such surface properties may be extracted through techniques such as spectral unmixing with end-members or band ratios (Casey et al., 2012). The first space based hyperspectral sensors (that is 200+ bands) include the Hyperion on the EO-1 satellite launched in 2000, a test satellite for than soon to be developed Landsat 8 satellite. In 2001 one of the first generations of small satellites (Proba) were launched, in this case with the compact high resolution imaging spectrometer (CHRIS) instrument on board with 19 spectral bands. Since then several hyperspectral missions have been proposed, but up to now these are still envisioned. Despite several mission proposals over the years, the hyperspectral branch has developed at a slower pace than other developments. Recently, the future in hyperspectral satellite remote sensing may rely on a more experimental mission using cubesats (i.e.: Aalto-1 (Praks et al., 2011)).

In the early 1990's, experiments with microwave sensors were deployed in space. This development lagged in comparison to optical satellite evolution due to the larger energy requirements to send signals back and forth through the atmosphere. At first these instruments were radio detection and ranging (RADAR) distance measurements (altimeters). Such systems are still in space, but a split came in 1995, when the first imaging radar (excluding defense systems) were tested and deployed (RADARSAT 1). In recent years these synthetic aperture radars (SAR) have been constructed with various wavelengths. Notable developments in satellite radar technology is the merge of radar altimetry and interferometry (CryoSAT), or the use of "signals of opportunity", where global navigation satellite systems reflectometry (GNSS-R) is used to estimate topography, or atmorpheric profiles. This technology has matured and after some experiments on the ground (Rius et al., 2012) and in space (UK-DMC), there are now several small satellites constellations in orbit (CICERO). At the forefront of development, plans for cubesat constellation with SAR instruments are at an advanced level with the first launch in 2018 (IceEYE, X-band: 3.2 cm).

The use of SAR in glaciology is important as it is independent of natural illumination, which allows observations in the polar night and through clouds. Furthermore, microwaves sense not only the surface, but receives reflections from the subsurface as well. Which also allows glacier facies identification (König et al., 2001; Winsvold, 2017). For glacier velocity estimation, a disadvantage is the side looking nature of such systems which can result in missing data from shadowing or layover by high mountains. Nonetheless, displacements can be extacted using two different methods. Semi-planar displacement can be estimated through image matching of the radar imagery (Fahnestock et al., 1993) while also small displacements in line-of-sight can be extracted from interferometry (Goldstein et al., 1993; Joughin et al., 2010) (InSAR). These differing methods ultimately complement each other and when combined, are capable to extract a full three dimensional displacement vector.

After the maturization of satellite radar altimetry, another split in technological development occurred in which laser systems were tested in space (SLA). The advantage of laser systems over radar is its ability to have a coherent beam with a small field-of-view, as the signal is in the optical spectrum. Smaller footprints are possible, of several tens to hundreds of meters (ICEsat), in relation to radar altimeters which is on the order of kilometers. Current technology is able to use beam splitters, and send multiple pulses per burst (ICEsat-2). Space laser has mostly been used for glacier elevation change or snow height (Treichler and Kääb, 2017), but has also been used for along track velocity estimation on ice shelves (Marsh and Rack, 2012).

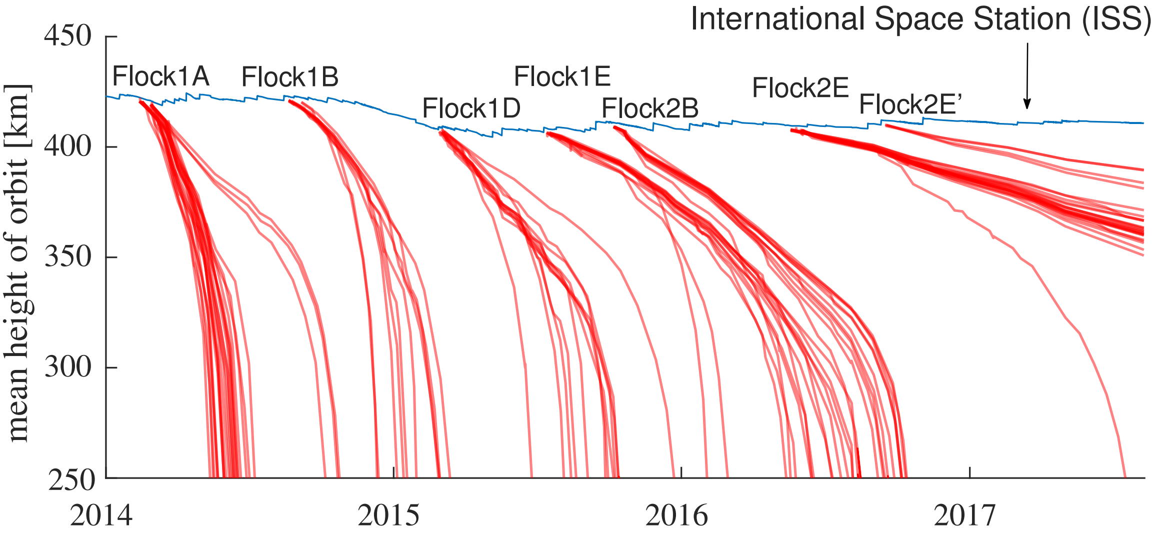

Figure 2.5: Orbital decay of the ISS in blue and different generations of Planet cubesats (called Doves) deployed from it. For every Dove the orbit altitude is plotted.

The timeline in figure 2.4 shows some characteristics of the evolution of the space industry. In general, innovation has been driven through experimental studies initiated by research and coordinated through the space agencies. Once the technology is established, missions are taken over by governmental institutions in order to function as a secure baseline, delivering data in a fixed format. The next step in this evolution is the valorization of satellite missions to the commercial market. As the optical sensor branch of satellite development is the most established, much commercial innovation occurs here. Recently, the miniaturization of satellites has shaken this industry. In conjunction with the reduction in launch prices, which was partly boosted a commercial space-race.

However, such mini satellite systems are a design compromise, as thrusters are mostly absent for many cubesat missions. Drift in orbit can change acquisitioning towards a different time of day. In addition, these satellites will have a shorter life time, as boosting to higher orbit is not possible. This can be seen by the lifetime of several generations of flocks in figure 2.5. Here the international space station (ISS) decays towards the Earth, but every now and then gets boosted further out of the atmosphere. This is not the case for the cubesats, which are destinated to eventually burn in the atmosphere. The atmospheric drag causing this delay is proportional to their elevation. Acceleration increases when closer to the Earth, thus a higher orbit is preferred. Nevertheless, as can be seen in this plot as well, improvements in time of life are significant, as generations of satellites with improved design and orbit maintenance algorithms get developed over time (Foster et al., 2015), see also figure 2.6.

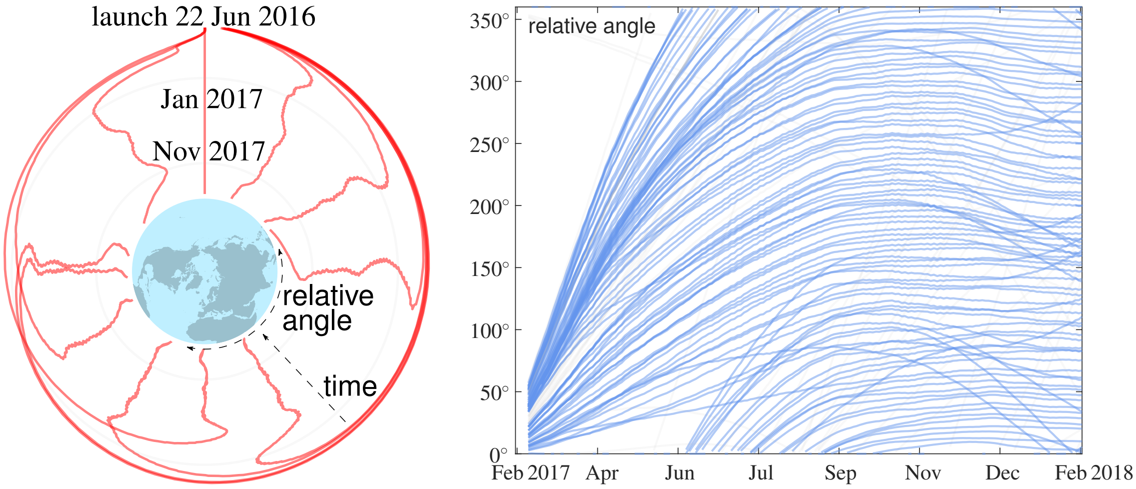

(a) Doves of Flock 2P

(b) Doves of Flock 3P

Figure 2.6: a) Relative angle or equatorial crossing over time for Dove satellites (in red) of the Flock 2P launch. The satellites are deployed from the rocket and spread out though different drag. An equal distribution is reached in early 2017. Later in 2018some Doves adjust, as more Doves are added to the orbital plane. b) Relative angle of the 88 Dove satellites launched on 14th of February as the flock 3P batch. Some satellites seem to have malfunctioned, as their orbit does not follow the group and therefore are given a faint gray colour. In November 2017 all Doves are aligned and evenly spaced. Afterwards adjustments are still made, as these Doves need to orchestrate within the constellation with other Doves, especially after the Flock-2k launch brought an additional 48 Doves in space. Graph is modified from (Foster et al., 2015).

2.3 Optical remote sensing

Acquisitions from spaceborne optical sensors can be analyzed through two approaches. First, one can analyze intensity of a single pixel and deduce information about the surface or the atmosphere at the time and place of acquisition. This approach is quantitative remote sensing, where the objective is to retrieve physical parameters. Second, one can analyze the intensity of neighboring pixels to deduce information about texture or structure. This is qualitative remote sensing, the aim here is to extract geometric parameters. In the latter approach, knowledge about acquisition geometry is essential, while the state of the atmosphere and surface is less of importance. Most of the work presented in this thesis is focused on qualitative remote sensing. However, during photo interpretation, our brain uses multiple clues. Consequently, when optical remote sensing is used, it is of importance to extract information from as much approaches as possible (paper II). In this thesis there is also a considerable amount of text about quantitative remote sensing for the simple fact, that in order to understand glacier velocities, surface characteristics such as crevasses and water can also help to interpret the underlying processes occurring in, on or under a glacier.

2.3.1 Pushbroom & frame cameras

Satellite optical images are recorded through photosensitive cells that can be arranged in several configurations. The first generation of Landsat satellites had only a few multi-spectral photosensitive cells. In order to record aside of the satellite track an oscillating mirror perpendicular to the flightpath was installed. This recording mechanism is called whiskbroom due to its sweeping mirror. Technological advances in electronics allowed more photosensitive cells that could be arranged together in long strips and deployed on a satellite. These instruments, called pushbroom sensors, acquire an image strip over a wide range in across track direction as they fly in orbit, see figure 2.7.

It is also possible to install a full frame sensor behind the telescope enabling acquisition of an entire scene at once, simplifying geometric location and orientation. Nonetheless, the high velocity of the satellite in orbit ($\approx$ 7km/s) requires the sensor to record rapidly to minimize directional blur. To receive enough energy, sensors have multiple readouts, that are stacked together after acquisition. The pixel index in the across track is time-consistent, though an offset at every measurement will occur along track, known as time dependent integration. Hybrid configuration are also possible, where small frame segments are aligned in a pushbroom con-

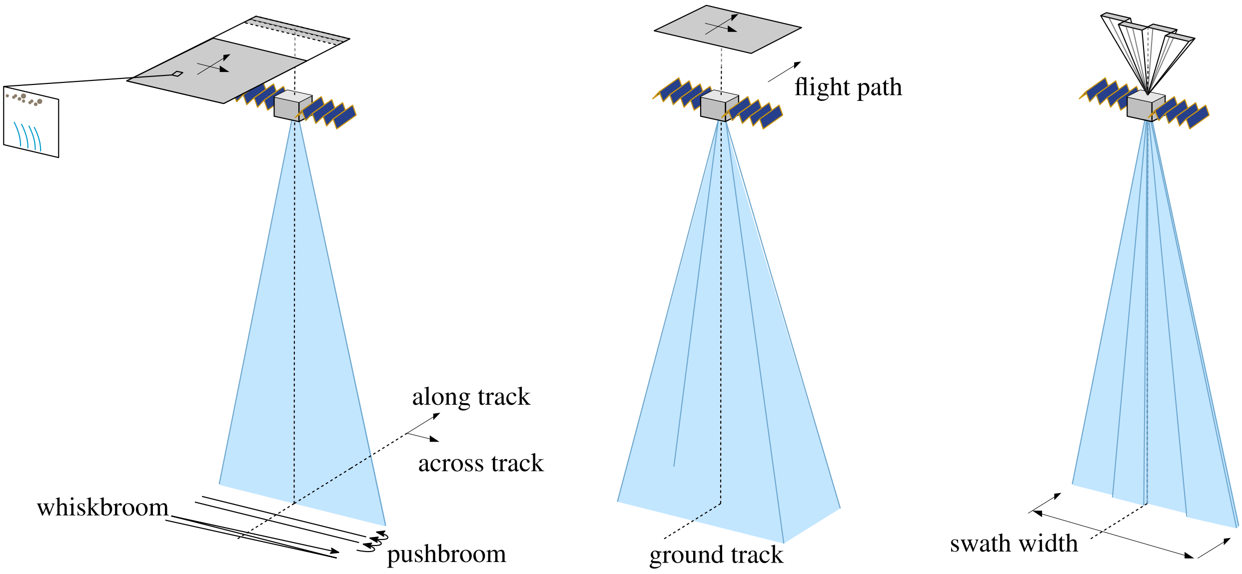

Figure 2.7: Different sensor configurations, from left to right: pushbroom, frame, and push-frame.

figuration. This invites ideas towards video capturing, a concept called pushframe (dAngelo et al., 2016).

It is of interest to describe the different sensor systems, as the imagery of these systems are later used to estimate glacier displacements and elevation (paper I). The acquisition is only the first step in a whole remote sensing chain, where the analysis of the imagery is at the other end of the line. Consequently, the geometry of the sensor needs to be known in order to interpret the results. Displacements within imagery can occur due to acquisition geometry and should not be translated to physical displacements. Hence it is of interest to describe how an image is created and how the terrain projection is changing through perspective.

2.3.2 Acquisition geometry

A camera at a certain time has a projection centre, here denoted by O', where the prime specifies the numbering of the camera. It has a position in world coordinates (X,Y,Z), and an orientation with different angles. These can be specified by a matrix, and for this example, are aligned with the world coordinate axis ($\mathbf{R}$). The camera will have a specified focal length (f, or magnification) and the acquisition pixels will have a defined width (m), that can be combined into a normalized term ($\alpha = f/m$). The origin of an image might not co-align with the principle point of the camera, therefore a shift (τ in pixels) describes this translation, and can be considered the pixel coordinates of the principle point. These components make up the camera matrix, and a transformation can now be defined, expressed in a linear form, between the pixels coordinates (i, j) to the world coordinates (Moons et al., 2009);

$$\zeta \underbrace{\begin{bmatrix} j \\ i \\ 1 \end{bmatrix}}_{x} = \underbrace{\begin{bmatrix} \alpha_x & 0 & \tau_j \\ 0 & \alpha_y & \tau_i \\ 0 & 0 & 1 \end{bmatrix}}_{\mathbf{K}} \underbrace{\begin{bmatrix} 1 & 0 & 0 \\ 0 & 1 & 0 \\ 0 & 0 & 1 \end{bmatrix}}_{\mathbf{R}} \begin{bmatrix} X_p - X_O \\ Y_p - Y_O \\ Z_p - Z_O \end{bmatrix}. \tag{2.1}$$

Here ζ is the projective depth, a positive real number. Apart from a clear representation, this formulation has the advantage that two separate matrices can be retrieved from the multiplied matrices (**KR**) through QR-factorization (Moons et al., 2009).

When a second image (with notation $''$) at a different location is included, one has a photogrammetric setup. For sake of simplicity, the orientation of the second camera is also parallel to the axis of the world frame ($\mathbf{R}'' = \mathbf{I}$). And the translation of the camera is only along the X-axis. Now the parallax is in one direction, and thus the coplanarity constraint can be formulated as a tensor product,

$$x' \cdot (\mathbf{b} \times x'') = 0, \qquad \text{where } \mathbf{b} = O' - O''. \tag{2.2}$$

Here **b** is the baseline vector and is one of the sides of a triangle. A simpler form can be created by defining the baseline vector as a skew-symmetric matrix, denoted as $[\mathbf{b}]_\times$, than the coplanarity constraint can be formulated as,

$$x'^{\top} \underbrace{\mathbf{K}^{-\top} [\mathbf{b}]_\times \mathbf{K}^{-1}}_{\mathbf{F}} x'' = 0. \tag{2.3}$$

The matrix multiplication here is known as the fundamental matrix (**F**) and formulates a direct linear mapping from one image to the other. It is the fundamental building block for many stereo reconstruction problems. For pushbroom sensors one can formulate a similar linear formulation, see Gupta and Hartley (1997). In this case, with a frame camera and the base-vector along one axis, this formulation in equation 2.3 simplifies to (Förstner and Wrobel, 2016),

$$\begin{bmatrix} j' & i' & \alpha \end{bmatrix} \begin{bmatrix} 0 & 0 & 0 \\ 0 & 0 & -\mathbf{b}_x \\ 0 & \mathbf{b}_x & 0 \end{bmatrix} \begin{bmatrix} j'' \\ i'' \\ \alpha \end{bmatrix} = \frac{\mathbf{b}_x(i''-i')}{\alpha} = 0. \tag{2.4}$$

This is a base to height relationship, and with this one can already look at the performance of several spaceborne imaging systems for topographic reconstruction. Given, for example, that the location of a point can be measured with an accuracy of half a pixel, the precision of depth retrieval can be estimated. This is done for several satellite systems in table 2.1, where the base of the triangle is in across-track direction, i.e: between different orbits. If one wants to detect a relative elevation change with, for example, the PlanetScope constellation, than the algorithm needs to be as accurate as .1 pixel to observe a change of 10 meters.

Satellite system characteristics				Retrieval precision	
	Height [km]	Width [km]	Pixel [m]	0.5px [m]	0.1px [m]
Resourcesat-2	817	140	23.5	137	27
Landsat 8	705	185	15	57	11
Sentinel-2	786	290	10	27	5
SPOT-5	832	60	5	69	13
PlanetScope	420	20	3	63	12

Table 2.1: Estimated precision of height retrieval for different satellite systems in different orbits $((0.5 \cdot \text{width})/(\text{height} \cdot \text{pixel} \cdot \sigma))$.

This property also defines the pixel distortions possible in an optical image due to topography. Orthorectification is necessary for every satellite image that does not acquire data at perfect nadir. To visualize the effect of topography in a raw frame image acquired from space, figure 2.8 shows the displacements between a raw image and an orthorectified image over the steep valley of Zermatt, Switzerland. Here, the pixel displacement corresponds well with topography, though systematic effects seem also to be present, indicated with white arrows.

The formulation given in equation 2.1 is a physical model of the acquisition geometry of a satellite. It may also be transformed to a different formulation, known as the direct linear transform (DLT). Here, the local coordinate shift of the image is moved towards the principle

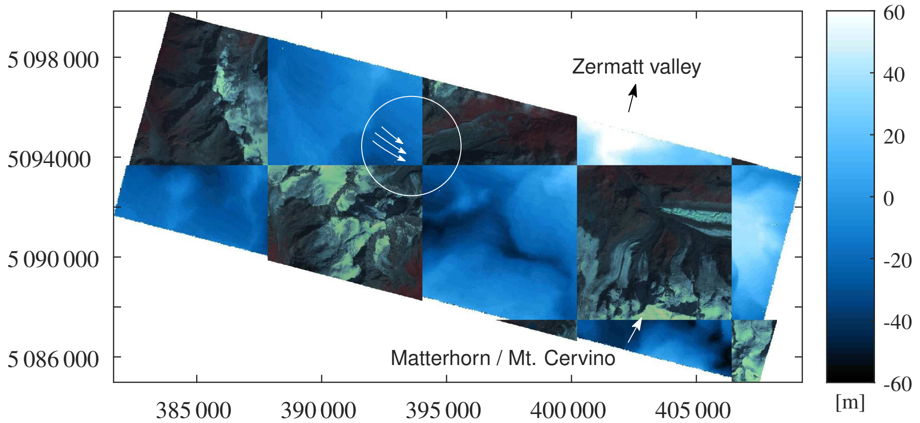

Figure 2.8: Relative displacement between a raw PlanetScope image and a orthorectified PlanetScope image. These displacements correspond to the terrain corrections applied in the orthorectification process. Some systematic effects are highlighted as well.

point ($\tau = 0$) and the normalization ($\alpha = f/m$) is reversed,

$$\underbrace{\begin{bmatrix} j \\ i \\ f \end{bmatrix}}_{x} = \underbrace{\begin{bmatrix} m & 0 & 0 \\ 0 & m & 0 \\ 0 & 0 & f \end{bmatrix}}_{\mathbf{S}} \underbrace{\begin{bmatrix} r_{11} & r_{12} & r_{13} \\ r_{21} & r_{22} & r_{23} \\ r_{31} & r_{32} & r_{33} \end{bmatrix}}_{\mathbf{R}} \begin{bmatrix} X - X_O \\ Y - Y_O \\ Z - Z_O \end{bmatrix}. \tag{2.5}$$

This formulation is provided in projective geometry through homogeneous coordinates. These can be written out fully and by doing so transformed into the co-linearity equations (Abdel-Aziz and Karara, 2015 (&1971));

$$j = f\frac{r_{11}(X - X_O) + r_{12}(Y - Y_O) + r_{13}(Z - Z_O)}{r_{31}(X - X_O) + r_{32}(Y - Y_O) + r_{33}(Z - Z_O)}, \tag{2.6}$$

$$i = f\frac{r_{21}(X - X_O) + r_{22}(Y - Y_O) + r_{23}(Z - Z_O)}{r_{31}(X - X_O) + r_{32}(Y - Y_O) + r_{33}(Z - Z_O)}. \tag{2.7}$$

This is a transformation from a two dimensional Cartesian coordinate system to a three dimensional Cartesian coordinate system. However, lens distortion or sensor miss-alignments are absent in this formulation. Such distortions can be integrated into this polynomial formulation by including parameters for non-linear terms ($X^2, XY, \ldots$). The parameters in such a formulation are called rational polynomial coefficients (RPC), and the formulation has become the standard for the formulation of satellite image acquisition parameters. It is similar to equation 2.6&2.7,

but now extended with more terms,

$$\tilde{j} = \frac{p_{11}(\Delta\psi) + p_{12}(\Delta\lambda) + p_{13}(\Delta h) + p_{14}(\Delta\psi\Delta\lambda) + p_{15}(\Delta\psi\Delta h) + p_{16}(\Delta\lambda\Delta h) + p_{17}(\Delta\lambda^2) + \cdots}{p_{21}(\Delta\psi) + p_{22}(\Delta\lambda) + p_{23}(\Delta h) + p_{24}(\Delta\psi\Delta\lambda) + p_{25}(\Delta\psi\Delta h) + p_{26}(\Delta\lambda\Delta h) + p_{27}(\Delta\lambda^2) + \cdots},$$

$$\tilde{i} = \frac{p_{31}(\Delta\psi) + p_{32}(\Delta\lambda) + p_{33}(\Delta h) + p_{34}(\Delta\psi\Delta\lambda) + p_{35}(\Delta\psi\Delta h) + p_{36}(\Delta\lambda\Delta h) + p_{37}(\Delta\lambda^2) + \cdots}{p_{41}(\Delta\psi) + p_{42}(\Delta\lambda) + p_{43}(\Delta h) + p_{44}(\Delta\psi\Delta\lambda) + p_{45}(\Delta\psi\Delta h) + p_{46}(\Delta\lambda\Delta h) + p_{47}(\Delta\lambda^2) + \cdots}.$$

Typically, this mapping is formulated in a spherical coordinate frame, where the latitude and longitude are shifted to a local system (e.g.: $(X - X_O) \rightarrow (\psi - \psi_O)$, here denoted by $\Delta\psi$), and the image frame is normalized to its pixel extent $(\tilde{i}, \tilde{j})$. The advantage of this formulation is the possibility to include other types of satellite sensors, such as a pushbroom or pushframe. In addition, optimization is possible through block adjustment and readjusting its terms, without requiring a complicated sensor model (Grodecki and Dial, 2003) which may also be seen as a disadvantage, as there will be a lack of physical meaning of the empirical aggregated terms. Back-calculation becomes difficult as decomposition back into physical geometric parameters is ill-conditioned. Especially when RPC's are used in photogrammetry, triangulation is done through iterative procedures, see for example Oh (2011). Another limitation is the reliability of the terms within the design matrix. A situation emerges when over-fitting may occur or a model is used that neglects imperfections of the telescope.

2.3.3 Spectral & radiometrical properties

Optical instruments measure the radiative energy that is received by their photo sensitive area. The instrument is similar to a normal camera, with a lens and a focal plane. Incoming photons enter the detector and cause an electric signal. The amplitude of the signal is related to the amount of photons. Their spectral response can be sections in the visible- or thermal infrared part, i.e.: wavelength of $\approx 0.1\mu$m - 10μm.

Sensors only measure the radiation within a small fraction of this spectrum. Energy received on the sensor is collected and registered onto a digital scale, known as quantization level. Its range depends on bit length, with the most common radiometric range of 2^8 or 2^{12} (8 or 12 bit). The sensitivity of the sensor is adaptable in modern instruments, but pre-set, often providing several operation modes that adjust/adopt to the incoming energy.

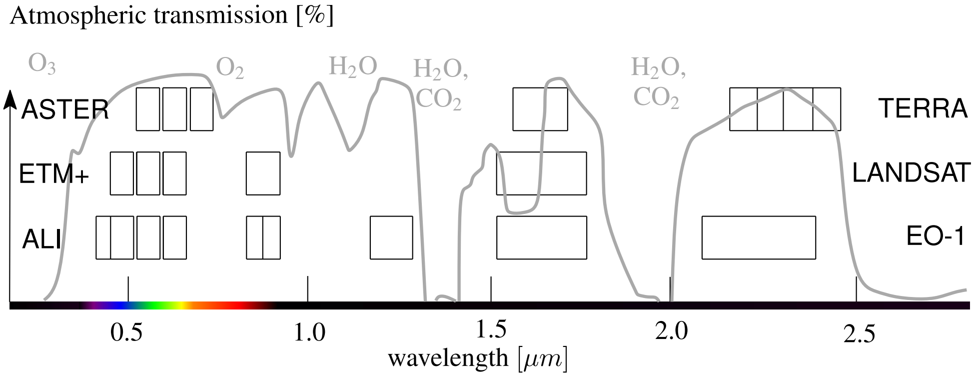

Figure 2.9: Spectral coverage of bands from different optical remote sensing instruments. In the background in gray the atmospheric transmittance is plotted together with the absorption bands that are caused by different gasses (Fraunhofer lines).

Apart from the spatial resolution of an Earth's observation system, the relation between ground coverage and pixel element, there are other camera specifications which are of importance. For example, the spectral resolution is the interval of measured radiation within the electromagnetic spectrum. A specific domain of frequencies is detected by the CCD elements of the instrument, as illustrated in figure 2.9. These bands may not be too narrow, as there is a physical limit on the amount of radiative energy entering the sensor. Instruments with a narrow spectral band, will have a relatively wide spatial resolution in order to collect sufficient amount of energy.

The atmospheric transmission of the Earth atmosphere for the visible wavelengths is also illustrated in gray on figure 2.9. The curve that describes this property has distinct and abrupt transitions. Such attenuation of spectral windows occur because the absorption properties of molecules in the atmosphere are dependent on wavelength. The absorption bands shown are for an atmosphere which is clean and dry. However, when ice crystals or water droplets are present in the atmosphere, absorption and reflection increases over the visible spectral range. However, the microwave frequencies have much larger wavelength and are less affected by clouds. Attenuation only increases when the water content is relatively high, as can be seen in figure 2.10. This effect is even more clear when surface water is sampled, as combination of high density and high absorption of water result in minimal backscatter.

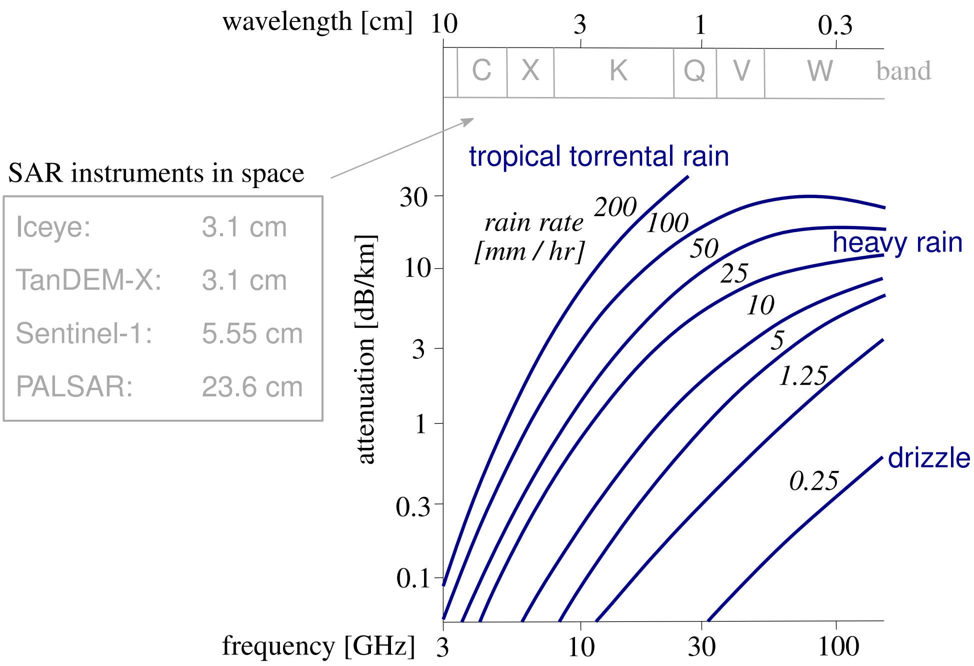

Figure 2.10: The effect of rainfall intensity on the attenuation of microwave signals at different frequencies. On the top of the figure different radar band classifications are shown in gray together with some SAR satellites. Graph modified from de Loor (1993).

A quantitative formulation of the radiometry is now discussed to better understand the collected intensities on a photosensitive cell (I), which is of importance for paper II. First the radiation of the sun (S) arrives at the surface in which some of it reflects. The amount of received energy is dependent on the insolation, which is an interplay between the surface normal ($\mathbf{n}$) and the sun direction ($\mathbf{s}$), both vectors having unit length. When isotropic reflection is assumed, than the reflectance (R) can be seen as a constant, otherwise it can be function dependent on incident angles, orientation, roughness, etc. To simplicity formulation, we exclude in-path absorption, however for a full account on radiative transfer modelling see Mousivand et al. (2015). In this simplistic description, the sensor has a defined transmittance (T), in which energy of certain bandwidth over different wavelengths (λ) is collected and transformed (C) to a digital number. The sensor sensitivity has a lower bound (L_0) and (A) denotes indirect radiance. Sensor noise is excluded for simplicity, than the energy collection can be stated as (Bindschadler and Vornberger, 1994),

$$I = C\int_{\lambda} T(\lambda)\,[S(\lambda)\,R(\lambda)\,\mathbf{n}\cdot\mathbf{s}+A(\lambda)-L_0(\lambda)]\,d\lambda. \tag{2.8}$$

For Earth surface analysis only the surface features ($R,\mathbf{n}$) are of interest. Many of the other terms can be roughly estimated, making it possible to tune the dynamic range of satellite instruments towards an expected interval of energy. This is done to be able to record the signal from the surface with a very high quantization level, or contrast. The objective of the first suits of Earth observation satellites of the Landsat legacy was with an emphasis on environmental monitoring of agriculture and geological prospectus. Due to technological limitations, these instruments recorded in the visible spectrum and had a radiometric range of 7 bits. This often resulted in no data over snow covered terrain (Dowdeswell and McIntyre, 1986), as the high reflection of snow saturated the detectors.

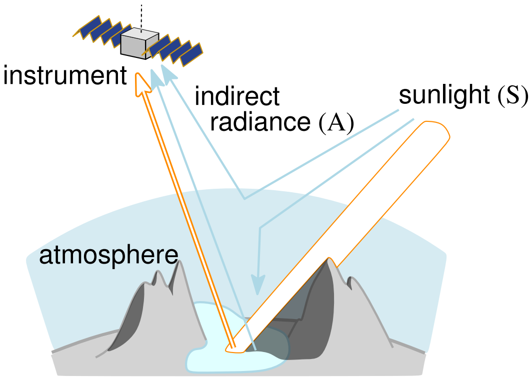

Figure 2.11: Schematic drawing of the remote sensing chain, where the energy from the sun travels through different atmospheric paths towards the sensor.

From the above example one can distil a point of importance; as older snow has lower reflection, it is of benefit to use autumn imagery for glacier displacement measurement. In late summer most of the melt has occurred and melt features can be sensed. An additional benefit is that the snow-free lower part of the glacier has more low reflecting features on its tongue. When more recent satellite systems are used, the quantization level is of such level that features in the upper accumulation area can be seen (Kääb et al., 2016). However, the saturation problem still occurs for some modern satellites, as heavy compression is used in the downlink, or cut-off occurs in the quantization level (Altena, 2009).

2.3.4 Orbital characteristics for Earth observation

A satellite can be in various different orbits, though most high resolution Earth observation satellites fly rather close to Earth at an altitude of 500+ kilometers, as opposed to common weather satellites that fly in geostationary orbits (35 786 km). They follow a near-polar orbit corresponding to a sun-synchronous orbit which means that a satellite overpass of a position somewhere on Earth is always at the same local time of the day, resulting in similar cast shadows. Landsat 8, for example, is in this type of orbit and its daily coverage is illustrated in figure 2.12(a). Here the red polygons represent the ground coverage, which is 185 kilometers in cross-track direction converging with high overlap in the polar regions. The seemingly change in width of the swath with latitude is an illusion due to the map projection. Furthermore, only the descending orbit is shown on this illustration, as the ascending orbit is in local night time.

A part of the sun-synchronous constellation of PlanetScope is illustrated in figure 2.12(b). This system is different in the sense that the field-of-view is only about 20 kilometers in width (table 2.1). In order to get sufficient coverage many small satellites are deployed. When in full operation (170+ micro satellites are in orbit), the system revisits any place on Earth every day, in relation to every 5 (Sentinel-2) or 16 (Landsat 8) days. However, from convergence and overlap in higher latitudes provides an even shorter revisit (figure 5.2). At high latitudes, successive acquisitions from multiple satellites allow viewing the same area with a short delay of roughly 90 seconds.

An additional strategy to improve the revisit time is the ability of the satellite to point or stare at a certain object, while passing over. Some satellites are equipped with reaction wheels or gyros, which can be programmed to change the orientation of the satellite. Consequently, it is possible to look off-nadir and increase the revisit time for specific areas of interest.

Advances in sensor technology have made it possible to sample the Earth more densely both spatially and temporally. However, there is a double-bind in the spatial, temporal, spectral, and radiometric-domain that requires a compromise which results in different system designs and specifications. Here we focus on the high to medium-resolution imagery, as these are sensing glacial systems at the scale of our interest. A comparison of important specifications of todays sensors is illustrated in figure 2.13 which shows the sampling interval against the field of view for several Earth observation systems. Two outliers with operational capacity can be seen in this figure. These systems solve the spatial-temporal balance by using multiple fleets (Dove:200, UrtheDaily:18, SkySat:19) instead of a single platform. For a more complete overview, even extending to aerial platforms, see Toth and Jóźków (2016).

Also GISAT is worth mentioning, as it is planned to be launched in the very near future and set into a geo-stationary orbit, overlooking central Asia. The main mission objective is cloud detection for weather forecasting, and typically these satellites have a coarse pixel resolution. However, this new generation of satellite sensor can have a medium size resolution. Opening

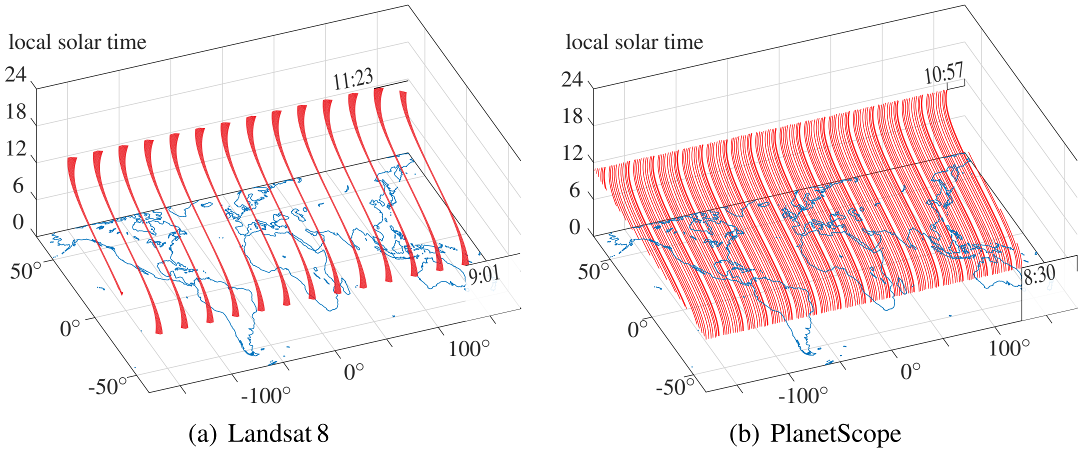

(a) Landsat 8 (b) PlanetScope

Figure 2.12: Coverage of different optical satellite systems in red. Highlighting the achievable world wide coverage within a day. The planar axis are latitude and longitude, while the vertical axis illustrates the local time. Only the descending orbits are shown in this figure, as the ascending tracks are in the (local) night.

new application in time series, as will be highlighted in section 3.4.

These advances in satellite Earth observing systems open a door for exploration of a new dimension. One is today not bounded to only the spatial relations (object based recognition) or its reflection function (spectral mapping) for recognition. The temporal domain can be used, making it possible to decompose signals using the time domain. One could think of short term (clouds), re-occurring (shading and shadowing), state changing (land cover) and continuous (atmospheric absorption) patterns and associated applications. These are future potential applications, though some of these aspects are exploited in paper II.

2.3.5 Measurement configurations

Within this thesis data from Earth observation satellites are used to measure displacements, mostly in lateral sense. Depending on the configuration of these satellites, several techniques can be used to extract shifts between different images, either through optical or SAR data. Therefore it is of interest to highlight these configurations, which have mostly been used to directly translate parallaxes into elevation. However such techniques can also be used to translate to physical movement. In figure 2.14 the different geometric measurement set-ups are illustrated and are described below in more detail.

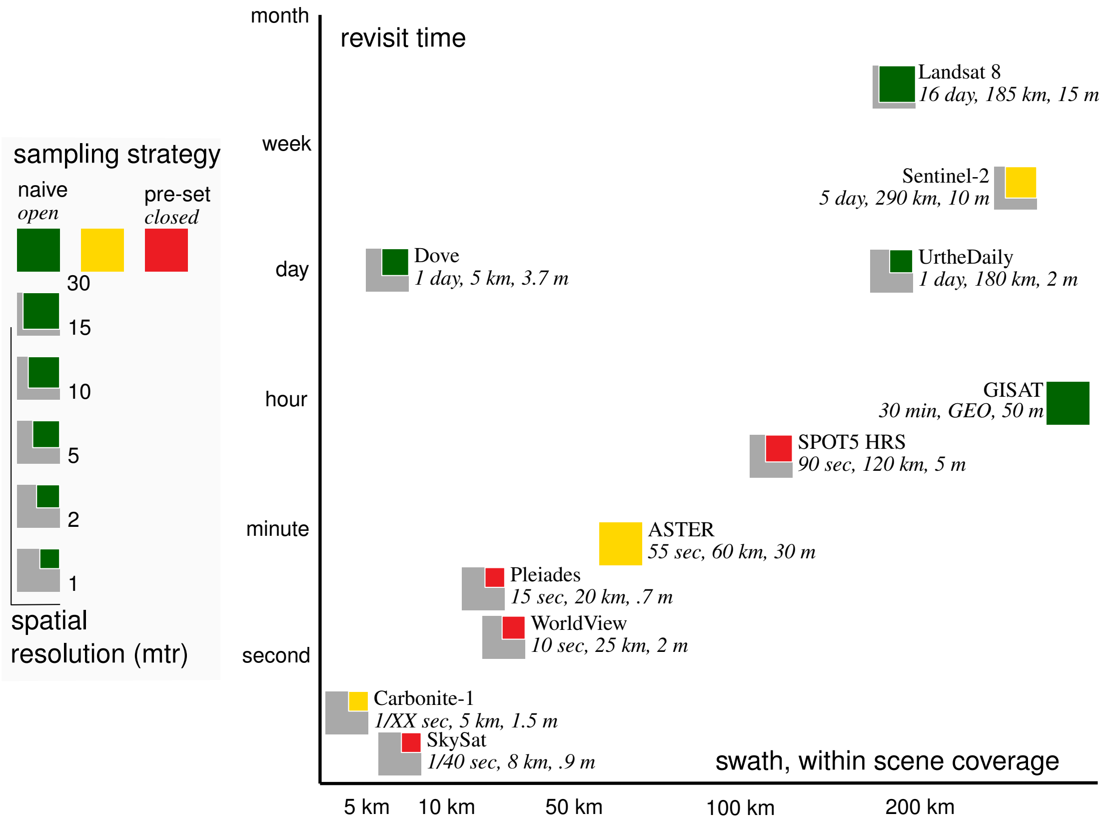

Figure 2.13: Sensing characteristics of a selection of present day optical (very)high-resolution satellite systems.

As can be seen in figure 2.14, there is a distinction between multi-sensor and single sensor configuration. The latter two techniques take advantage of the surface characteristics and their geometric relation between the illumination source and the sensor. Such techniques depend on quantitative measures to deduce topography, and, in addition due to their single sampling instance, have no time component. Consequently, movement cannot be to extracted, but when multiple acquisitions are used, elevation change can be deduced, therefore they are included here.

Stereoscopy The change of perspective and its corresponding parallax, has been formulated in equation 2.3 and the surrounding section for the optical case. For optical satellites, the line of flight co-aligns with the baseline (**b**), and instruments are installed in forward, or backward looking direction to get repeat coverage. In like manner, this can also be accomplished with SAR satellites, called radargrammetry (Toutin et al., 2013). For snow-covered surfaces, the microwave signal penetrates into the snowpack, making the return signal a complicated composition of volume scattering. However, when the snowpack is wet, most response will derive from surface scattering, allowing the possibility of radargrammetry to estimate topography (Papasodoro et al., 2016).

Interferometry When the orbits of two satellites overpasses are close together in space, the intersection angle (ϑ) and baseline ($\mathbf{b}_\perp$) are small and changes in terrain are subtle. For imaging radar (SAR) the interferometric property of the acquired complex signals can be used to extract line-of-sight displacements. Depending on the wavelength of the signal, different movements can be detected at centi- or millimeter level scale (Hanssen, 2001).

Clinometry The shading caused by the incidence angle of the sun can be used to extract terrain slope. For snow-covered surfaces reflection is close to isotropically (Lambertian), making the relation between terrain slope and sun angle fairly direct. The potential of photoclinometry has been shown by the extraction of topographic features, such as the size of dolines (Bindschadler et al., 2002) or streaklines (Raup et al., 2005). Full integration across an image is possible when constrains are given about the terrain, or imagery is used with different sun angles (Altena et al., 2017), called photometry. The same technique may also be exploited by SAR (Guindon, 1990), though it is more complicated as layover conditions can occur. Here again, the slope in across-track direction is best determined. Constraints or different track orientations are needed to extract a full surface model.

Polarimetry A radar instrument can send and receive different polarizations. When co- and cross-polarization is recorded, a slope induced shift of the polarimetric peak can be seen (Schuler et al., 1998). Hence, slope values can be estimated in along-track direction. This technique seems to be complementary to radarclinometry, as both techniques solve in orthogonal directions. In this respect polarimetry for spaceborne applications is only developed for SAR, as the polarization of natural light is isotropic.

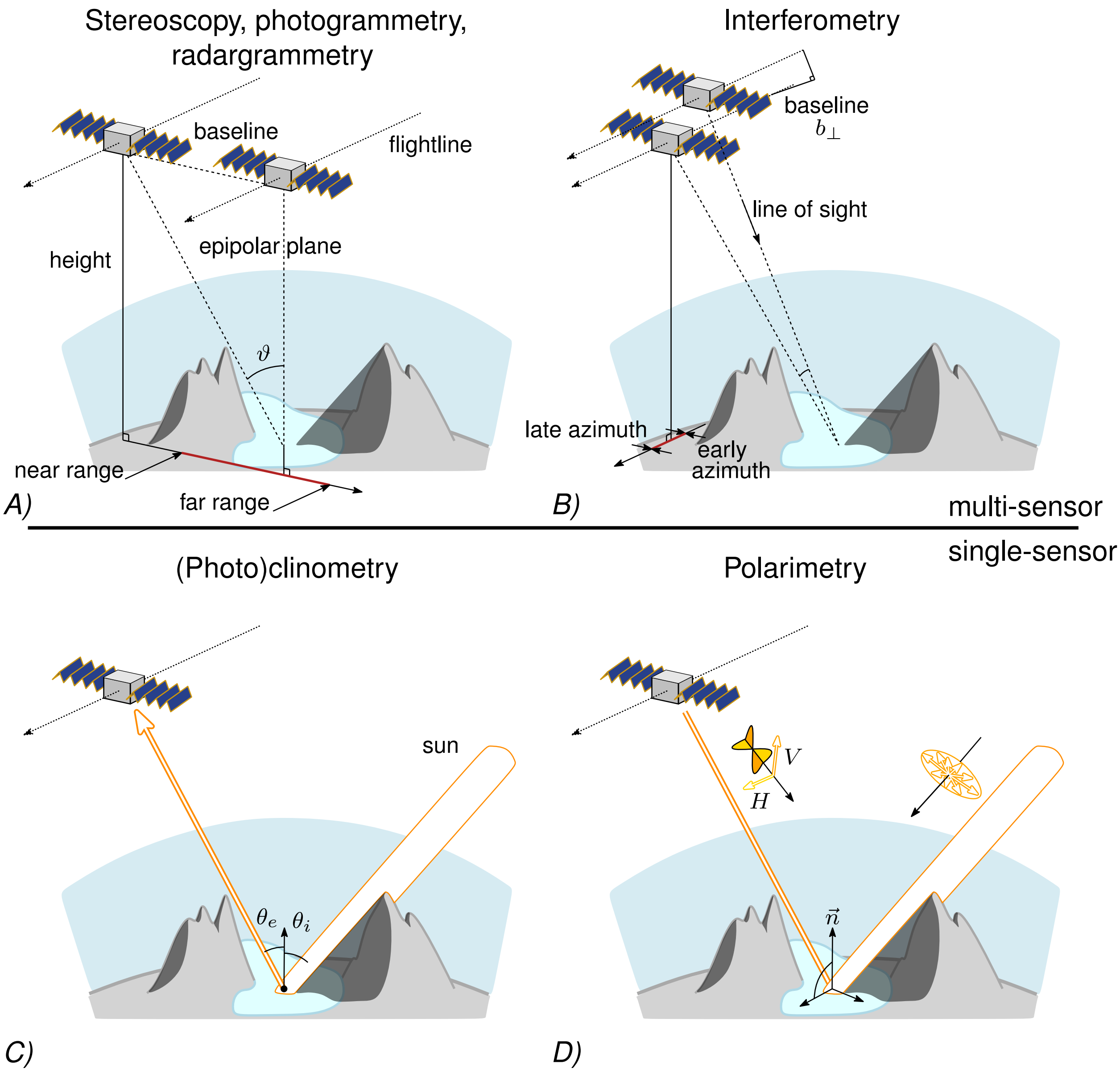

Figure 2.14: *A*) Configuration for stereoscopy. With parallax angle (ϑ). The range notations in the figure are terms for SAR systems, for optical systems this is termed the swath. *B*) Configuration for interferometry, this is only done with SAR systems.*C*) Geometric configuration for clinometry, for optical systems the sun is the illumination source, while for active SAR systems, the sensor sends the energy and illumination(θ_i, ψ_i) and reflection(θ_e, ψ_e) angles are the same. *D*) configuration of polarimetry, a SAR technique which uses the polarization of a signal (horizontal - H and/or vertical - V). It is an active technique as the sun is a random polarized source. Modified illustration, but originally from Toutin and Gray (2000).

3 Glacier dynamics

This chapter provides an overview of processes that cause glacier flow. Such an overview is relevant for the interpretation of glacier velocity time-series (paper II&III). It starts with a describtion of the underlying principles of glacier flow, in order to couple velocity products to physical processes. Afterwards, this chapter gives a brief description of material properties and processes of snow and ice that influence glacier flow or because these properties can be sensed specifically by Earth observation satellites. This is followed by an overview of studies related to the measurements of glacier flow in relation to subglacial processes, as well as studies that use velocity products to gain more glaciological understanding. The chapter is finished with an outlook on land surface displacements from space in a broader perspective.

3.1 General physics of glaciers

When over consecutive years snow is able to build up, ice will be formed and due to gravitational pull this ice will flow to lower elevations. At such lower elevations the ice is able to melt and this process is a simplistic view of the glaciological system. A more quantitative view can be formulated through the mass balance, which will be given hereafter.

3.1.1 Mass balance

The mass of a glacier changes through time. Accumulation of water is added to the glacial system through avalanches, wind transport, and precipitation. While ablation is caused by melt, sublimation or evaporation. The net balance at a given time is the sum of gain and loss of these processes over a given point (p). A land terminating glacier (excluding ice loss through calving C) can be expressed as a system of mass conservation as shown in figure 3.1. Every element within the glacier has a density (ρ) and an velocity (u). For such an element, the continuity equation states (Paterson, 1994),

$$\frac{\partial \rho}{\partial t} + \nabla(\rho u) + \beta = 0. \tag{3.1}$$

Where β denotes the production term. This relation can be integrated over a full column, from the surface height (h_s), down to the bottom height (h_b). Integration of the production term results in a composition of the surface net balance (b_s) and the basal melt (b_b) and the velocity term transforms into a flux divergence ($\nabla\vec{q}$), which gives

$$\frac{\partial h}{\partial t} = \frac{\partial}{\partial t}\int_{h_b}^{h_s}(\rho)dz = b_s + b_b + \nabla q, \quad \text{where } q = \int_{h_b}^{h_s}(\rho u)dz. \tag{3.2}$$

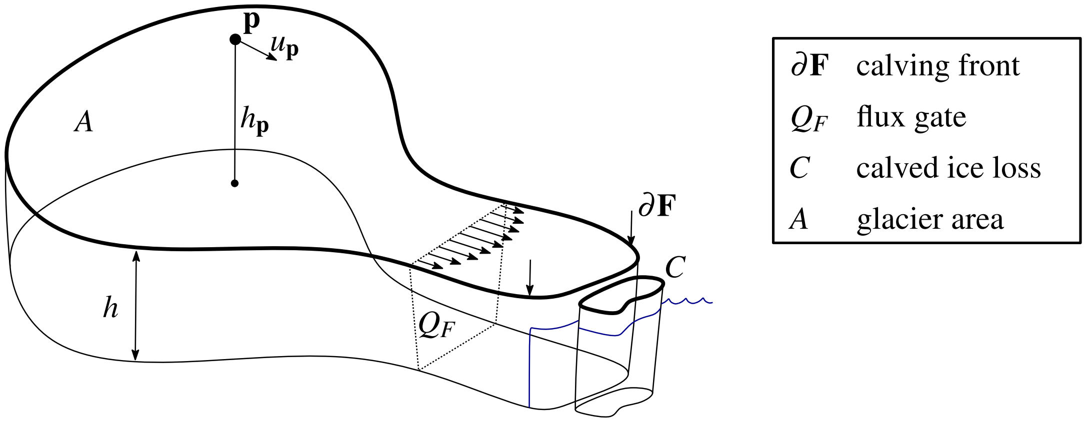

Figure 3.1: Scheme of the mass-balance components of a glacier

If elevation changes over the entire glacier surface (A) are known, than these changes can be related to water mass changes. This is done through multiplication with the density of ice (ρ), resulting in volume change in water equivalent units;

$$\frac{\partial V}{\partial t} = \int_A (\frac{\partial h}{\partial t}\rho)da, \quad \text{similarly } B = \int_A (b_s + b_b)da. \tag{3.3}$$

Now, it is possible to relate mass change to the climatic-basal mass-balance (B) and its glacier-wide integrate flux divergence ($\nabla\vec{q}$) (Cogley et al., 2011),

$$\frac{\partial V}{\partial t} = \frac{1}{A}B + \int_A (\nabla\vec{q})da. \tag{3.4}$$

These prognostic terms on the right hand side of this equation describes the glacier evolution. The first term has an external climate component through the surface mass balance, while the second term relates to the dynamics of the ice (Hagen et al., 2005). This section will briefly highlight aspects concerned with the mass-balance term. Later sections will focus on the second term, the flow of ice and changes thereof.

Different components are aggregated into the term of the mass-balance. The basal component (b_b) can mostly be considered to be a constant or neglected, as not much is known about this component. In many places the geothermal heat flux is low and constant, except for tectonic active regions. The surface component (b_s) combines several processes together. Monitoring of these processes needs complicated instrumentation for correct parametrization. Hence it is of interest to look at correlations with other measurable quantities that seem to exist with mass balance. This in order to get a first-order view of processes which are of importance for glacier behaviour, for example the link to elevation, as can be seen in figure 3.2. A linear trend with elevation can be seen, though the slope is different from gentle, as the dry White glacier (Antarctica), to steep for the maritime Engabreen (Norway). The bias (the location where the lines cross the axis) of these glaciers are also different. Variation is present from the high-latitude glacier of Nigardsbreen (Norway) to the more equatorial glacier of Tuyuksu (Kazakhstan).

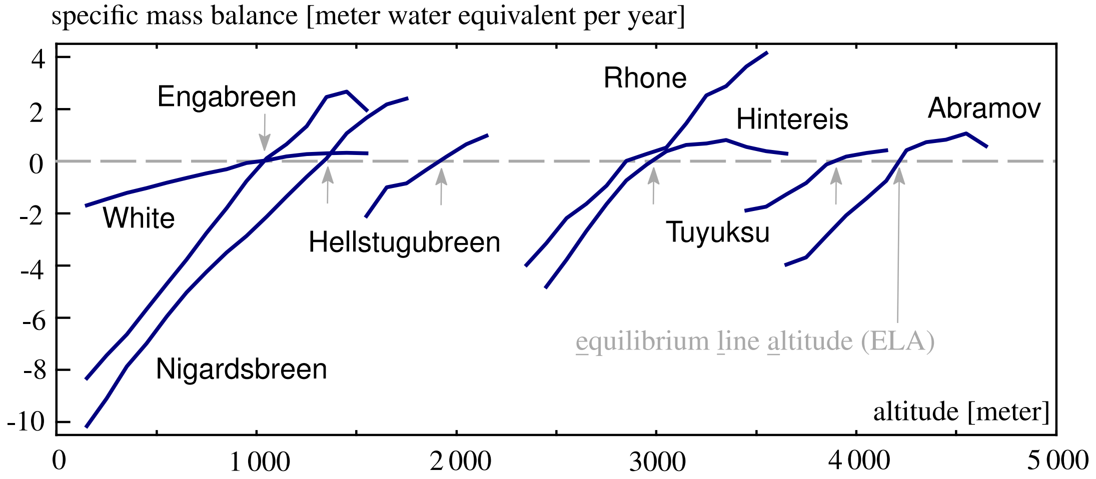

Figure 3.2: Multi-annual mass balance profiles for different glaciers. Modified from Leclercq (2012), with data from world glacier monitoring service (WGMS).

In general, another relation between surface mass balance and climate change seems to exist as well. In a warmer climate, the mass-balance gradient seems to steepen (Dyurgerov and Meier, 2005). This will result in more melt at the snout of the glacier, and more precipitation at the top. Furthermore, an increase in mean temperature is difficult to balance through a surplus in precipitation, thus the net effect will be glacier loss. For the case of Franz-Josef glacier the increase of one degree of temperature needs to be compensated by an increase of precipitation of 30% (Oerlemans, 1997). However, this is dependent on the local climatic setting, as this is a maritime glacier. More continental climates might be more affected by seasonal perturbations, especially in summer (Oerlemans and Reichert, 2000).

The mass balance is affected by the climate, when a change in the climate forcing occurs the glacier icemass needs to come in equilibrium. Hence, there will be a dynamic response on this time dependent forcing. This response time seems to be mainly depended on slope, and can be in the order of several years for steep glaciers (5, Briksdalsbreen) to some decades (35 years, Nigardsbreen) (Oerlemans, 2007). Hence, in principle such changes should be observable in glacier velocity records.

3.1.2 Creep deformation of ice

For a glacier or ice cap, gravity (g, at ± 9.81 m/s^2) is the driving force for flow. The shear stress (ε) exerted on an element within a column of ice can be described by Glen's flow law (Glen, 1952; Steinemann, 1954),

$$\varepsilon = A\tau^n, \quad \text{where } \tau(z) = \rho g(H-z)\tan\alpha. \tag{3.5}$$

Here, ρ is the ice density, typically 910 kg/m^3 and A is the Arrhenius flow coefficient at 1^{16} Pa/yr[1]. Both these parameters are dependent on temperature and pressure. Here for simplicity, they are assumed constant for a typical temperate mountain glacier. The glacier surface slope is given by α, and exponent n is typically given a value of 3. Here, we isolate the horizontal movement of the shear effect out of the column, by neglecting the velocity component perpendicular to the flow direction ($\frac{\partial v}{\partial y}$). Then the vertical velocity gradient ($\frac{\partial u}{\partial z}$) is given by,

$$\frac{\partial u}{\partial z} = 2A[(H-z)\rho g\tan\alpha]^n, \quad \text{because } \varepsilon = \frac{1}{2}\left(\frac{\partial u}{\partial z} + \frac{\partial v}{\partial y}\right). \tag{3.6}$$

Surface velocity is the total velocity over a whole column and found by integration from the bottom to the top of the column,

$$\int_{z_b}^{H} 2A[(H-z)\rho g\tan\alpha]^n \partial z = U = -\frac{2A}{n+2}H\left(\tan\alpha\rho g H\frac{\partial H}{\partial x}\right)^n. \tag{3.7}$$

The equations given above are *diagnostic* equations, modelling the state of a phenomena in respect to others. Another type of equations are *prognostic* equations, describing the state of a

---

[1] One converts to seconds by dividing this coefficient with 31556926, that is, the amount of seconds in a year.

phenomenon over time. The glaciological continuity equation for a glacial column (3.2) can be written with these terms of equation 3.7 which then becomes,

$$\frac{dH}{dt} = -\frac{\partial (HU)}{\partial x} + b. \tag{3.8}$$

Combining both equations results in a partial differential equation, which can predict the state in the next time-step. Thus substitution of equation 3.7 into 3.8, gives

$$\frac{dH}{dt} = \frac{\partial}{\partial x}\left(\frac{2A}{n+2}(\rho g \tan\alpha)^n H^{n+2}\left(\frac{\partial H}{\partial x}\right)^n\right) + b. \tag{3.9}$$

The Arrhenius flow coefficient (A) in equation 3.9 is dependent on temperature. For typical glacier ice values, its viscosity stretches one order of magnitude, as can be seen in table 3.1. In summary, the thermal situation of the full column of ice is important for dictating glacier flow by deformation, as can be seen from equation 3.7. Nonetheless, for general cases one can assume the glacier to be at pressure melting point, then equation 3.7 can be inverted to give an indication of glacier thickness. Results will be reasonable for flat glaciers which resemble an infinitely wide slab, as lateral drag is neglected in this formulation. Estimates from such formulations deviate considerably when applied to high mountain glaciers and errors scale proportionally with the bedrock slope (Le Meur et al., 2004). Also rectilinear ice flow through cylindrical channels have been formulated (Nye, 1965), these formulations might describe valley glaciers more truthfully, but are still simplifications of the complex flow of glaciers.

Water		Ice	
temperature $[^\circ C]$	viscosity $[Pa^{-3}\ s^{-1}]$	temperature $[^\circ C]$	viscosity $[Pa^{-3}\ s^{-1}]$
0	1.765	0	24. 10^{-25}
10	1.285	-10	3.5 10^{-25}
20	0.979	-20	1.2 10^{-25}

Table 3.1: The viscosity of water and ice at different temperatures.

A comprehensive description of glacier flow can be formulated by departing from the mass continuity principle (equation 3.1). In this formulation the relation of the velocity component is given but its form is not specified. Hence if the velocity component is coupled to the force balance, by the property of conservation of momentum, it is possible to take more complete collection of the acting principles into account. The conservation of momentum reads,

$$\rho \frac{d\mathbf{v}}{dt} = \nabla \mathbf{T} + \rho \mathbf{g}. \tag{3.10}$$

The left-hand-side of this equation is the acceleration of velocity over time and can be neglected, as for glaciers it is several orders of magnitude smaller in respect to the terms on the right-hand-side. Here **T** is the (symmetric) stress tensor, which written out fully gives the following systems of equations,

$$\begin{aligned}
0 &= \frac{\partial \tau_{xx}}{\partial x} + \frac{\partial \tau_{xy}}{\partial y} + \frac{\partial \tau_{xz}}{\partial z} + \rho g_x, \\
0 &= \frac{\partial \tau_{yx}}{\partial x} + \frac{\partial \tau_{yy}}{\partial y} + \frac{\partial \tau_{yz}}{\partial z} + \rho g_y, \\
0 &= \frac{\partial \tau_{zx}}{\partial x} + \frac{\partial \tau_{zy}}{\partial y} + \frac{\partial \tau_{zz}}{\partial z} + \rho g_z. \qquad (3.11)
\end{aligned}$$

These fundamental physical laws can be coupled to the material law of Glen, by substitution and inverting of equation 3.5. In such a case, when a steady mass-balance and steady-state velocity field is assumed, these Navier-Stokes equations can arrive at a thickness of creeping ice.

3.2 Material properties of snow and ice

With Earth observation instruments it is possible to observe properties of the surface (optical), and/or near-surface (microwave). These material properties can influence glacier flow behaviour, therefor properties such as density and temperature of snow and ice will be highlighted hereafter.

3.2.1 Snow reflectance

Snow is precipitation of star-like ice crystals, grown in the atmosphere out of water vapor. Snow crystals have various morphologies, where the temperature during formation is the main factor of influence. Freshly precipitated snow is highly porous, and has fragile bindings. If temperature conditions are well below the melting temperature of ice, crystals are highly branched. Such large crystals will undergo fewer transformations, thus dry snow condition will result in a highly spaced snow pack. This low-density material has a high reflectivity, due to easy penetration and low absorption of radiative energy. If conditions are close to the melting point of ice, the snow crystals exhibit more metamorphism. Though decaying processes already start when a snow crystal hits the ground. The branches of the crystals disappear, and the crystal changes to a grain-like structure. The rate of this process is mostly influenced by both temperature and compression of the snow pack. Through time the optical properties of attenuation change, where consecutive melt and freezing are most influential. The size of snow crystals or grains ranges from 50 μm for fresh snow, growing to 1 mm for melting old snow (Wiscombe and Warren, 1980). A large dependency in snow reflection in the visible spectrum is due to grain size as is illustrated in figure 3.3.

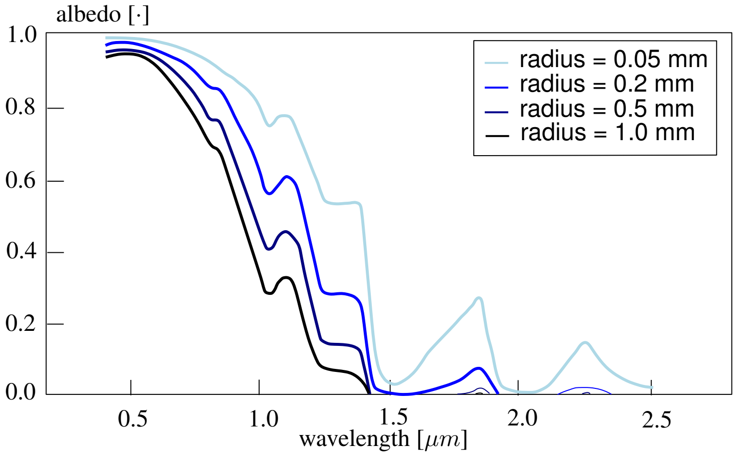

Figure 3.3: The effect of grain size on albedo for different wavelengths, modified from Rees (2006).

While signals in the visible range mostly interact with the surface, microwave signals penetrate into the snowpack and can thus be seen as a volume scatterer. For a dry firn snow pack, reflections at depths up to 30 meters can contribute to the total back-scattered radiation (Zwally, 1977). Accumulation change can thus be estimated through radiative transfer modeling, if an understanding is present about the grain size and temperature. However when water is present the reflectivity of the snow pack in the microwave range changes considerably (see section 2.3.3). Hence the recorded signal losses coherence when phase transitions occur within the snowpack. Consequently, pattern matching is typically done when the snowpack is stable (in winter and/or at high elevations). While melting events typically generate observational gaps for velocity products, though this backscatter information can be used for the validation of firn modelling (Winsvold et al., 2018).

3.2.2 Snow compaction

When snow falls on the higher elevations of a glacier, the snow typically stays all summer. Snow accumulates as time progresses season after season. After many of these iterations, the snow metamorphoses, largely due to the weight of younger snow, and becomes ice. This metamorphism can be seen when an ice core is drilled and one measures its density, as shown in figure 3.4. This figure is from an ice core collected within the Alaska range, where high accumulation rates in the order of several meters per year are common. As seen in figure 3.4, the snow that falls is very light (±200 kg/m^3). Consequently, the conversion or transformation into ice happens for this site around 55 meters (where it has a typical value of ±900 kg/m^3). This is different for glaciers in other climates. For example Holtedahlfonna, an icefield in Svalbard has a much lower annual accumulation of snow. Typically, this icefield has a snow pack of two meters, but the density of the snow is much higher (±350 kg/m^3). Thus, the transition between snow/firn and ice is already found at 20 meters (Sjögren et al., 2007).

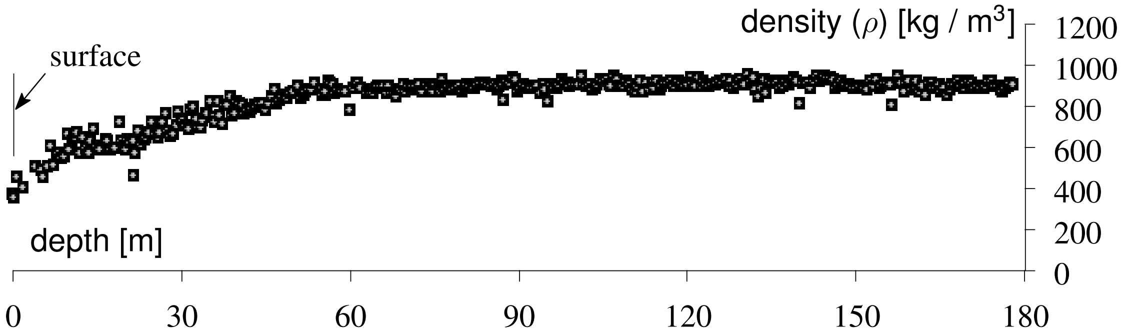

Figure 3.4: Density profile from an icecore of a glacier in central Alaska, adapted from Tsushima et al. (2015).

The difference in density between the two locations is partly because Svalbard has a relatively warmer and maritime climate. Snow crystals are less developed or have gone through metamorphism when they are deposited on the Earth's surface. When crystal melt occurs at the surface and the produced droplets either percolate into the snowpack where they re-freeze and warm the snowpack, or they escape the snowpack and drain as run-off. In the milder climate of Svalbard, melt-freeze cycles are shown to be of great importance for the surface energy balance (van Pelt and Kohler, 2015).

3.2.3 Thermal properties

Refreezing warms the snow-pack but this heat can be lost in winter as cold air drains heat from the glacier surface. Cold air can more easily go through a loose snowpack penetrating as a cold wave (Pfeffer et al., 1991). In the lower part of the glacier, where the snowpack melts in summer, the atmosphere has direct contact with the ice surface. When temperatures drop, this surface drains energy and cools down. This is a slow process, as can be seen from the thermal properties of ice given in table 3.2. Thus when the summer has been warm, the snow melts far up, but this causes the subsurface of the glacier to cool down in winter. One such example is shown in figure 3.5 for Kongsvegen, a glacier just south of Holtedahlfonna.

temperature $[^\circ C]$	thermal conductivity $[W/mK]$	thermal diffusivity $[m^2/s]$
0	2.10	$1.09\ 10^{-6}$
-50	2.76	$1.73\ 10^{-6}$

Table 3.2: Thermal properties of pure ice, taken from Paterson (1994).

The generated firn transforms into ice and is advected through the glacier towards its snout. Because diffusivity and advection are slow processes the thermal regime of a glacier can function as a climate record. For these processes, the timescale to adjust the thermal structure of the glacier to a new climate is in the order of decades to centuries. But in the ablation zone of the glacier, meltwater entrains into the glacier through crevasses or moulins. This water is routed through the glacier by channels, waterfalls and lakes. Heat exchange between the ice and water in such englacial networks can be substantial and the ice reacts by warming to get back into thermodynamic equilibrium, known as cryo-hydrolic warming (Phillips et al., 2010). Most of the meltwater is seasonal, but water can get trapped within the glacier, letting the process continue throughout the winter. Furthermore, englacial networks can be highly distributed, thus even though it is a local effect, ice warming to get into thermal equilibrium can occur on a broad scale. Also trapped water in crevasses can be agents for promotion of ice warming at deeper ranges within the glacial body (Jarvis and Clarke, 1974). Cryo-hydrolic warming is of interest when the melt starts to occur at higher elevation (above the equilibrium line altitude (ELA), figure 3.2). In cases where the ice is cold, the new equilibrium can be reached in the orders of some years to decades. Such warming is of interest as it influences the viscous properties (see section 3.1.2 and table 3.1) and can locally increase the deformation velocity (Phillips et al., 2013).

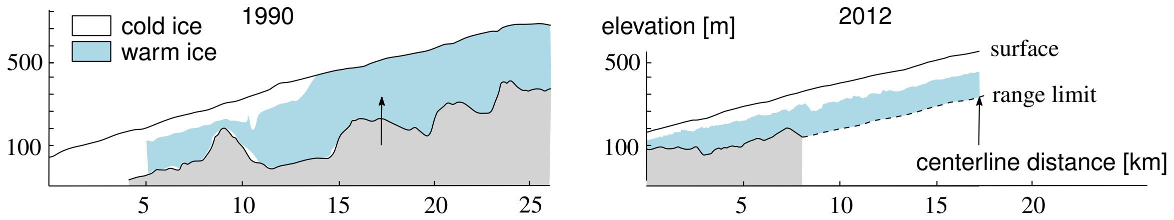

Figure 3.5: Thermal structure over the centerline of Kongsvegen, Svalbard. Left figures modified from Björnsson et al. (1996) and right figure from Sevestre et al. (2015).

3.3 Glacier movement

The governing principles of glacier deformation have been laid out in section 3.1. However, these relations are just one of the components that make up glacier velocity. The second component of glacier flow is the displacement due to slip of ice over the bedrock. For this subject much less information is known, as direct or remote measurements of the basal conditions are sparse. Nevertheless, the literature in respect to sliding laws is rich about this subject. However, these will not be mentioned here, instead an overview of studies are given about conceptual theories or observations of basal processes. Lateron this section connects these concepts, if possible, to observation of glacier surface velocity.

3.3.1 Basal sliding between rock & ice

A second component of the movement of ice is caused by the sliding ice over the bed of the glacier. Glacier sliding depends on a number of bed characteristics. Its end-members are illustrated in figure 3.6. The figure needs to display several dimensions because the ice-bed interaction has much complexity. Basal conditions at each glacier fall within these dimensions and the governing processes can change spatially as well as temporally. Therefor, in the following we describe observations of glacier flow and neglect any modelling efforts.

From a short-term dynamics point of view, the simplest case is a glacier with a frozen bed. Here, the sliding is minimal as the crystal bounds between the rock and ice cause heavy resistance. Nevertheless, sliding has been observed in such glaciers in the range of 0.5 millimeter per day (Echelmeyer and Zhongxiang, 1987). This occurs on macroscopic level where a small film of water seems to exist, making slip possible.

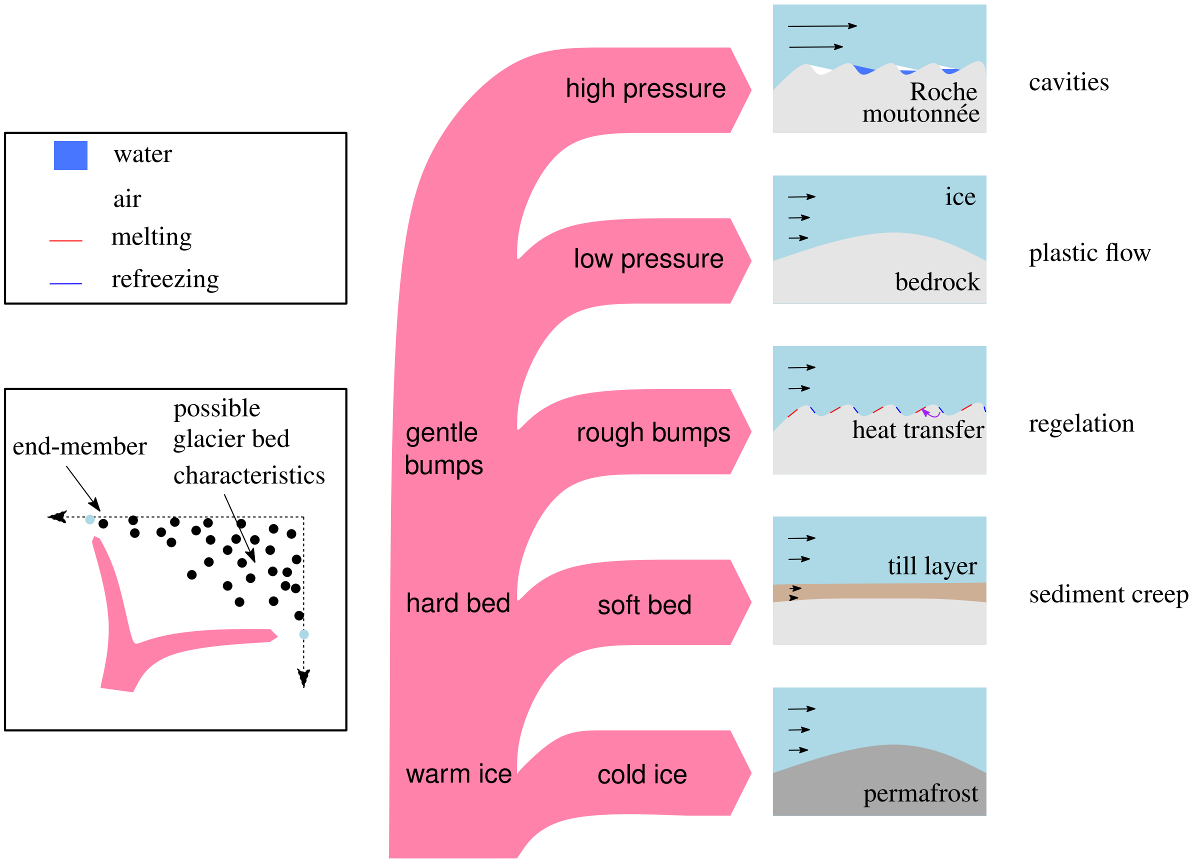

Figure 3.6: End-members of different glacier-bed types and their governing processes.

When ice is temperate other bed characteristics make it possible to increase the basal slip. For example when the glacier lays on top of a layer of sediments, its bonding is less strong as ice. Observations showed that the slip of the glacier interface over the till layer may only be 10%, while the rest of the displacement can be attributed to internal till deformation (Boulton, 1979). The amount of deformation is then dependent on the till-size and geology of the different rocks. When the glacier is on a hard bed, other characteristics start to play a role. For example, when the glacier slides fast, on a steep slope or with a lot of back pressure, such sliding can result in bed separation. Cavities can then start to form. The resistance against the flow of the glacier is then concentrated on the stoss-side, while the lee-side can contain water or air. Hence the pressure increases on such crests on the upstream-facing topography. A section of a cavity can be seen in figure 3.7(a), while its relation with ice thickness, or pressure, is shown in figure3.7(b).

When flow is less fast and thus pressure is low, ice is able to enclose troughs, which are the sections at the lee-side of bumps with respect to the flow direction. In such a case the roughness of the topography becomes of importance. If the topography has obstacles with a natural length

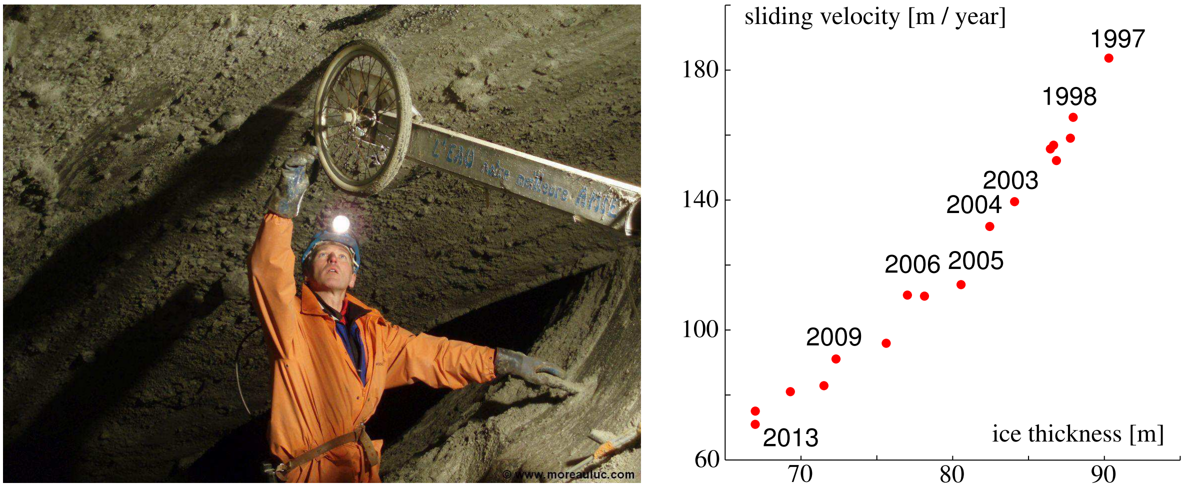

(a) Odometer in a cavity under the Argentière glacier.

(b) measurements of the basal odometer

Figure 3.7: a) shows an installation to measure velocity underneath a glacier, photo by L. Moreau. In (b) these measurements over the years are set against the thickness of the glacier above this installation, graph modified from Vincent and Moreau (2016).

less than 0.5-1.0 meters in dimension, regelation dominates (Kamb and LaChapelle, 1964). Then ice is melted on the high pressure stoss-side, and the resulting water will creep along the obstacle. When it arrives in the low pressure zone (lee-side) it will refreeze. The resulting released heat will transfer through the obstacle back to the stoss-side. When the bedrock bumps have longer oscillations this heat transfer cannot occur, and plastic flow governs ice movement at the glacier base.

3.3.2 Effects of water at the glacier bed

The section given above describes the somehow static configuration of the glacier bed. However, there is an important dynamic influence on the glacier sliding, which is water and especially changes thereof. Therefore, in the following, a similar overview will be given but now with an emphasis on subglacial hydrology.

Cavitation, mentioned above, describes a configuration where the hydrology is included for a very limited extent. But meltwater and the development of the subglacial drainage system play an important role in controlling glacier velocity. The distance which meltwater from the surface has to travel before it reaches the glacial bed is commonly only several ice thicknesses. Supra-glacial water can drain into a crevasse and work its way to the bottom. Through fric-

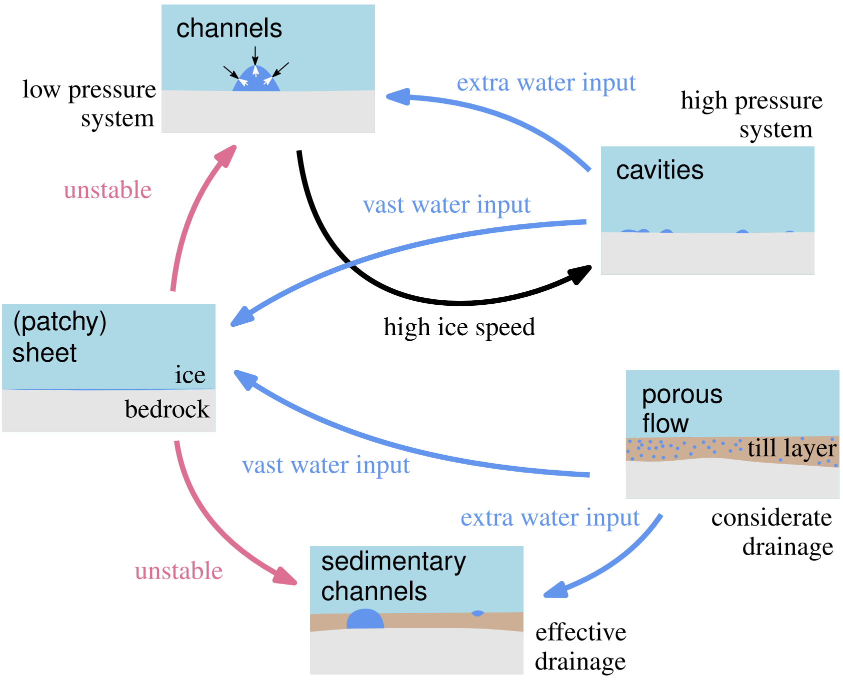

Figure 3.8: Elements of hydrological systems that can occur underneath a glacier, connected with relations to their possible development.

tional heat stemming from the running water such channels can be maintained, even when the crevasse closes again. Closure of the crevasses occurs as glacier ice deforms, however, due to stress from the bedrock topography, the same location at the surface will create new crevasses and new entrances to the bed lets the cycle repeat (Jansson et al., 2007).

At the bed several hydrological elements can exist (Flowers, 2015), as illustrated in figure 3.8. One of these is a sheet of water, which can be of small thickness. This sheet occurs all over the glacier bottom for a temperate glacier bed, as such glaciers are at pressure melting point. Energy for melting basal ice is provided by the geothermal heat flux, but also through loss of potential energy as glaciers flow down-valley (Oerlemans, 2013). When a sheet of water becomes thicker it becomes unstable and will transform towards another hydrological element, as can be seen from the arrow moving away in figure 3.8. As a note, some arrows also arrive at this configuration, which represents a case in which a thick layer of water occurs. This situation is possible when drainage is not able to cope with a large influx of water (flooding) or when the ice is held up by a small selection of clast (Creyts and Schoof, 2009).

Another element of hydrological drainage are channelised systems. Such tunnels form as the water energy is dissipated to melt the ice around it. Water flow speed increases and transforms from laminar into a turbulent flow, making dissipation more effective. The resulting energy loss is used for melting and as such can form channels. Their stability is dependent on the relation between overburden pressure of the ice and the water pressure in the channel to resist closing. At a larger scale, the formation of a channel network is promoted by pressure differences. Different channels will have different effective pressures, due to discharge capacity and the collecting area. Consequently, due to these pressure differences between neighbouring channels, more efficient and large low-pressure channels will draw smaller channels towards them. Hence, such a process will promote the creation of an arterial network. When such a network is developed it can be very efficient to drain, hence pressure might drop again. Channel closure due to creep goes at a slower rate than ice wall melting, thus channels will sometimes be partially filled. Several cross-sectional shapes for a channel are formulated, apart from a cylindrical, also more elongated and shallow tunnels are inferred. With such a configuration, the hydrological system might be more resistant to diurnal high pressure events as after the event, the system may collapse.

The cavities introduced at the start of this section, can also form a hydrological network. Such a linked cavity system is inefficient as it regroups poorly connected water pockets (vein-like structure). Water will not be able to flow easily through, and can even have different pathways. However, such a network is more stable to perturbations, as high pressure causes better inter-connectivity between cavities. Unlike the tunnel network, this configuration will stay distributed and will not evolve towards a single outlet (Hubbard and Nienow, 1997).

The presence of deformable sediments under the ice is another element that influences subglacial hydrology. This can be due to soft bedrock, or from till on top of hard bedrock. Such a layer under alpine glaciers has been measured through boreholes or from exploration in ice tunnels. A typical thickness for till layers of 0.3 meter was found in Storglaciären, Sweden (Hooke et al., 1997), and 0.35 meter for Ürümqi Glacier, China (Echelmeyer and Zhongxiang, 1987). However, a till layer of more than 2 meter was measured at Black Rapids, Alaska, while from seismic signals a layer of at least 5 meters was estimated (Truffer et al., 2000). Such till layers are typically saturated with water, but water transportation by porous flow has a low capacity favouring high water pressure. Similar to the hard bed case, a tunnel system can develop. The evolution of such channels is more complicated as in addition to ice melt and refreeze, also till is relocated due to the force of flowing water. Transportation and deposition of boulders are, up to a certain size, depending on the capacity of water to carry them.

3.3.3 Observing & interpreting glacial motion

The above-given bed configurations and hydrological systems provide a framework to interpret glacial motion. In the following section, several studies will be highlighted that have sensed certain motion events or characteristics, which can be used to infer the latent variables at the bed. The selection of studies will go from detailed studies to rough correlations at glacier, basin or regional scale.

Field measurements have shown a positive correlation between water pressure and velocity (Müller and Iken, 1973; Iken and Bindschadler, 1986). Maximum velocities coincide with maximum water pressure. Hence these short-lived velocity increases were thought be due to bed lubrication, lifting the ice. During short-lived events, such as diurnal forced meltwater, the glacier can experience uplift in the order of several centimetres. However, velocity is only affected when the excess of water is able to drown sticky spots over a glacier length of at least four ice thicknesses (Mair et al., 2001). In such a way, early spring rain events can have a significant effect on glacier velocity, as meltwater can flood large parts of the bed due to the lack of sufficient discharge.

In summer, when the moulins and pathways to the glacier bed are well developed, the diurnal velocity cycle can still be observed, while later in the season such diurnal variations are less likely to have considerable impact, due to a well developed drainage system (Sugiyama and Gudmundsson, 2004). On a shorter time scale, Sugiyama and Gudmundsson (2004) also observe other relations than just linear responses. Water pressure and velocity can take up different relations, suggesting development and different transient glacier flow regimes over the season.

From a flowline perspective, the propagation of melt water can cause pulses of flow increase. For example over Variegated glacier, several mini-surges have been observed, where over a transect of six kilometres, the peak flow travels down-slope with a speed of 300 meters per hour (Kamb and Engelhardt, 1987). At the front of these repeating pulses, water level would drop and speeds would increase due to the mass fronts pressing downslope. The front would come through and water levels would peak. After the pulse passed, ice speed would decay to its previous velocity. Also up-slope propagation of a speed increase can occur, though being of less impact than short-term perturbations like melt/rain events. Such upstream speed increases can occur early in the melt season, and propagate up-slope as temperature rises (paper II). Such transmission has been observed to be in the order of 600 meters per day (Anderson et al., 2004). Within the Wrangell mountains, the lower part of many glaciers seems to speed-up in summer.

This speed increase seems to be present up to the equilibrium line, where in most cases an icefall is located (Armstrong et al., 2017), and due to the chaotic shearing hydrological networks can not develop. Hence hydrologic connectivity between the upper and lower part of the glacier is absent.

Long term trends in glacier velocities can also be seen. For example, on seasonal scale some relations seem to be present in the upper part of glaciers. When more early summer melt occurs than this correlates with an increase in velocity. While a more negative winter mass balance resolves in lower velocities (van de Wal et al., 2008). Coupling between summer and winter velocities is also present, where a warm summer is followed by a slower winter season indicating the importance of sub-glacial network development. Over several decades, glacier velocity seems to decrease at the snout and middle part while the upperpart can see an increase in speed, which might be due to more melt water being able to reach the bed, in combination with longer periods of positive temperatures at these elevations (Thomson and Copland, 2017). Similarly, sparse sampling over the globe from snapshots velocities with a decadal separation show in general slower velocities for land terminating glaciers (Heid and Kääb, 2012b). These measurements have mostly been derived at the snouts, hence mostly been affected by a decrease in ice thickness.

When looking over a large region, the velocity of different glaciers over several years can be grouped together, as can be seen in figure 3.9. Here different flow regimes can be identified, where not only summer speed-ups occur but a change in hydrological regime might be present. However one should take caution as the glaciers of figure 3.9 are marine-terminating outlet glaciers, where the disappearance of ice melange within the fjord in spring can function as a driver for speed increase at a glacier front (Howat et al., 2010). Hence, the level of complexity for such glaciers is far more advanced, as ocean circulation and calving are processes connected to the force balance of the glacier and so to its velocity. As the glacier retreats and changes to a land-terminating type, its velocity regime also changes, or simplifies. This shift in glacier type can also be seen in longer velocity time-series, where after the retreat and type-shift a slowdown at the front is occurring (Millan et al., 2017).

3.3.4 Stress transfer

The components of creep and slip can be formulated into a general force balance. This makes it possible to relate velocities estimated at the surface to basal friction and pushing and pulling

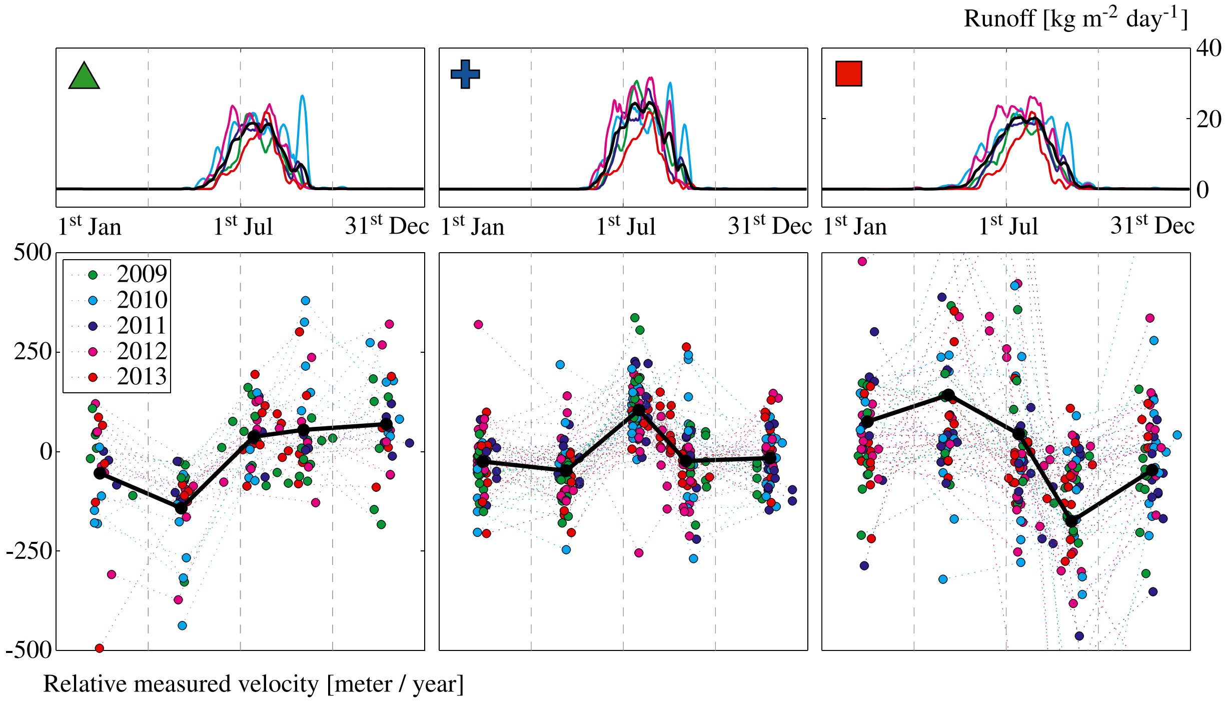

Figure 3.9: Different velocity regimes observed at outlet glaciers along the coast of Greenland, adopted from Moon et al. (2014).

within the glacier. For a full account and derivation see van der Veen (2013). Here, we simply give the relation between the driving stress (τ_{dx}), the basal drag (τ_b) and the resistive stresses (R_{xy}, R_{xx}), that describe the two dimensional force balance,

$$\underbrace{-\rho g H \tan\alpha}_{\text{driving stress}} = \tau_b - \underbrace{\frac{\partial}{\partial x}\int_b^H R_{xy} dz}_{\text{lateral drag}} - \underbrace{\frac{\partial}{\partial x}\int_b^H R_{xx} dz}_{\text{push/pull}}. \tag{3.12}$$

Here, the lateral drag derives from the resistive forces of the valley flanks or from the neighbouring slower/faster moving ice. These forces can be coupled to viscous forces through,

$$R_{xy} = A\varepsilon_{\text{eff}}^{1/(n-1)}\varepsilon_{xy}, \quad R_{xx} = A\varepsilon_{\text{eff}}^{1/(n-1)}\varepsilon_{xx} + R_{zz}, \quad \text{where} \tag{3.13}$$

$$\varepsilon_{\text{eff}}^2 = \frac{1}{2}\left(\varepsilon_{xx}^2 + \varepsilon_{yy}^2 + \varepsilon_{zz}^2\right) + \varepsilon_{xz}^2 + \varepsilon_{xy}^2 + \varepsilon_{yz}^2 \tag{3.14}$$

When the surface velocities and ice thickness are known, it is possible to invert this relation and solve for the basal drag (van der Veen and Whillans, 1989). For short-term force variation, the effects of tidal waves can be seen on floating ice tongues (Minchew et al., 2017), as the basal drag is minimal. For seasonal variations, the sensitivity in surface flow change can have its effect up to ten times the ice thickness (Price et al., 2008). However, icefalls can function as a barrier for such stress transfers (Durkin et al., 2017). For yearly and longer climatic fluctuations diffusion within a glacial body has a stabilizing effect. Local positive mass balance will increase the slope and mass will propagate downwards, while a negative mass balance reduces the flux and stabilizes the glacier. However, this is not the case for thin glaciers or for tide-water glaciers that are close to floatation. For these, perturbations can result in up-glacier propagation of thinning (Pfeffer, 2007).

An example of a large perturbation in the glacial force balance has been the recent reaction of glaciers draining into the Larsen-B iceshelf, Antarctica. The ice shelf system disintegrated in a short period of time, causing an imbalance as its buttressing effect for the glaciers was removed. Velocities of the surrounding glaciers increased up to sixfold (Scambos et al., 2004). Eventually the increased downward mass transport will result in surface lowering and thus a reduced surface slope (α), meaning a lowering of the driving stress. This will bring the force balance back to equilibrium.

3.3.5 Effects of local stress variation in glacier ice

The use of a high resolution velocity product can be used to assess properties of glacier ice and reconstruct its underlying mechanism. In the following several examples will be given that exploit the spatial variation of velocity estimates to get a better understanding of the ice properties and its dynamics through interaction with water or mechanical forcing. Most of these examples are located on ice shelves as at these locations ice velocity can be easily extracted from space, and ice properties are fairly homogenous in respect to mountain glaciers.

Glen's flow law (equation 3.5) is a general formulation for ice creep, however ice crystals have a laminar structure and thus sliding occurs along the basal plane. Deposition of snow is random, but consecutive build-up of pressure changes the crystalline axes towards the direction of compression, hence glacier ice has anistropic behavior. Furthermore, marginal shear zones are able to reorient such c-axes. Velocity products and distribution of emerged particle ages can help to constrain anisotropic modelling of ice dynamics (Zwinger et al., 2014), which can help in ice core interpretation. Also other properties are able to changes the rheology, such as differences in density, contamination (sea-salt or rocks) or water content. These spatial differences can occur due to basal refreezing, which warms the surrounding ice, or through changes in accumulation rates influencing the density profile (Rommelaere and MacAyeal, 1997).

Spatially varying melt rates occur underneath ice shelves, where exiting basal meltwater or variable icethickness can create the start of longitudinal channels. These channels can extent over the full ice shelf and their cross-sectional size is between several hundreds of meters to a few kilometers. Such subglacial ice shelf channels are forced to be in hydrostatic equilibrium, hence surface depressions make it possible to identify these channels. These channels are dynamic features as through iceflow such channels are advected, as well as changes in circulation or local melting and refreezing occurs. Excess melt of these channels result in depressions, but due to the hydrostatic balance also draws ice towards the channels which translates into transverse strain rates, which can be observed (Drews, 2015). Consequently, a better understanding of ice-ocean interaction can be extracted from high temporal remote sensing. Inactive melt-channels will close and the velocity field will equalize, while others will sustain shear-rates in the velocity pattern and thrive to be in balance with the channels subglacial mass-balance.

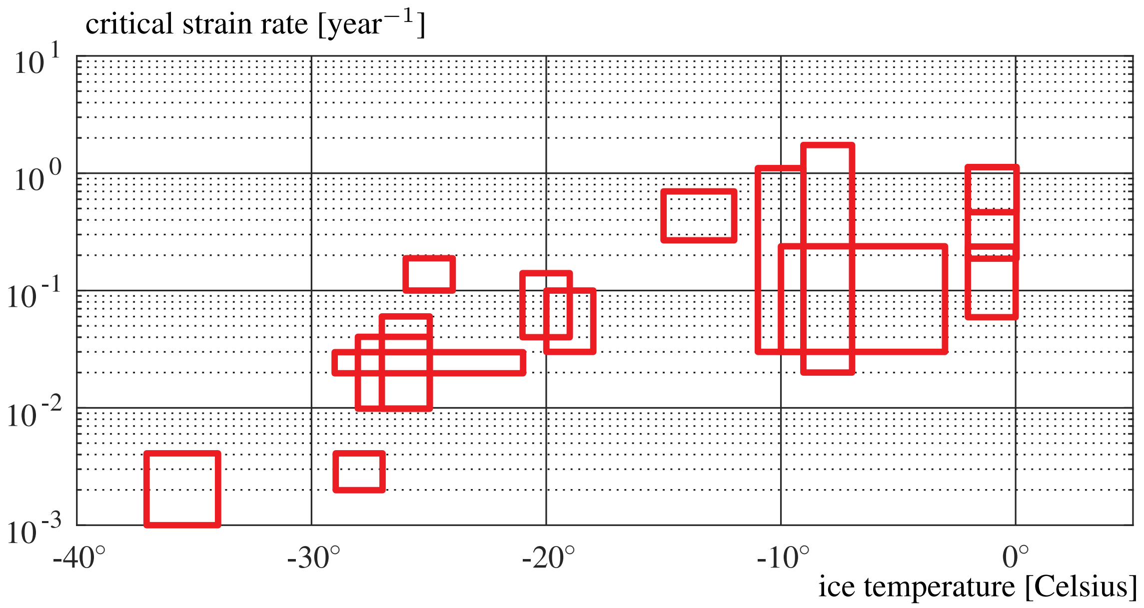

Figure 3.10: Data review of critical strain rates where crevasses occur on glaciers, adopted from (Colgan et al., 2016) with data of Vaughan (1993).

The velocity field changes spatially through widening or narrowing, bedrock bumps or overdeepenings, accumulation or ablation differences along the principle glacier flow line. All these situations cause differential speed across a glacier, which can change the reaction of the ice from ductile to brittle bahaviour. When a critical stress is exceed a crevasses can emerge, though this depends on temperature (figure 3.10). The direction of such fractures are directed perpendicular to the principle stress. In this manner, the crevasse pattern over time can be used to investigate if the flow regime has changed (Etzelmüller et al., 1993). Similarly, through exploitation of the temperature dependence, strain rates from velocities can give a hint about the thermal type of a glacier. But crevassing is not simply a result of glacier motion, it is an integral part of the energy balance of the glacier system. For example, at the marginal zones of ice streams extensive shear and thus crevasses occurs, which releases heat. This heating again couples back to the viscosity of the ice, making shear easier, getting in thermo-mechanical equilibrium (Echelmeyer et al., 1994).

3.4 Geomorphology of glacier flow

3.4.1 Concepts of flow

Analysis of flow fields can provide a quick overview of the complexity or structure of specific glacier flow. Various mathematical formulations to describe flow exist and are described below. This is of importance because with the following concepts, glacier flow and flow-change can be read in the landscape through simple geomorphological interpretation.

- A streamline is a connected curve based on a velocity field at a fixed point in time. When the flow is stable, this corresponds to a trajectory of a particle. Because glaciers are typically not stable in flow, streamlines are not directly observable. Consequently, recordings of flow are only able to reconstruct this concept. Geomorphologic recordings of streamlines are bedrock features and can be of micro scale, such as grooves and striations or of macro scale, such as drumlins as shown in figure 3.11(a).
- A streakline is a set of points which have all passed through a specific point at some instance in time. A good example of such a concept on a glacier is the medial moraine, see figure 3.11(b), as two or more glaciers converge, rocks from intermediate outcrops are entrained. When the flow regime changes, the position of the medial moraine changes accordingly with the ice. This is most clearly seen when tributary glaciers surge producing looped moraines.
- A pathline is the trajectory a particle takes as it moves within a flow system. When the flow is unstable, it is thus dependent on the time of deployment. A pathline is difficult

to find in the landscape. It needs to set its mark along the way, otherwise there is no recording. Nonetheless, examples of geomorphologic features, which are pathlines, are chatter marks (at micro-scale), or the down-valley damage of a glacial outburst flood (on macro-scale) or ice-plough marks (figure 3.11(c)).

- A timeline is a fixed set of connected points, which originate or are deployed at the same time in a (curvi-)linear fashion. On a glacier, ogives are clear demarcations of such timelines (figure 3.11(d)). The annual bright and dark bands of ice underneath an icefall move down-glacier and due to differential flow of the ice transform from bands into horseshoe shape features generating a natural isochronic map.

With these concepts, glacier flow and flow-change can be interpreted from geomorphological interpretation. The data used in this study uses remote sensing recordings, nevertheless, the features given above and shown in figure 3.11, can in some occasions function as verification.

3.4.2 Observing other types of flow at different timescales

For glacial studies, the different sampling strategies of satellite systems can observe different glacial processes. Examples of various glacier processes are illustrated in a Stoffel diagram in figure 3.12, showing the spread of spatial extent in relation to the temporal occurrence of the phenomena. All the different phenomena listed follow, wholly or loosely, the similarity constrain, hence it is possible to track it using image matching. The symbols illustrate the score of the phenomena related to the Deborah-number, describing the observability of the signal. This merit is rooted from rheology, describing the amount of relaxation over the time of observation (Reiner, 1964). Many of the listed processes are observable today from satellites, with an exception of tidal-fluctuations, and post glacial rebound. For such processes, InSAR-technology is more suited than image matching.

The shortcoming of the Deborah-number is its linearity as it assumes constant displacement. For some cases this holds, where continuous forces or oscillating systems influence the movement of the object. One example of such a natural phenomenon is a tidal bore (figure 3.13(b)). This phenomenon is the result of a change in flux between the river output and tidal input into an estuary. With high-tide the incoming seawater overflows the constant river outflow, creating a wave. The tidal magnitude and its timing can be estimated precisely on the minute. Hence, this flow phenomena can be observed with sufficient planning.

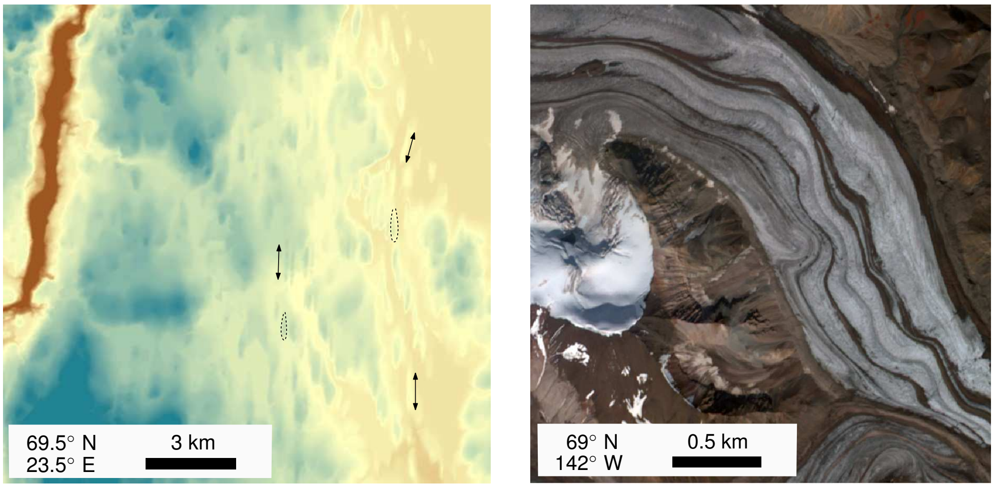

(a) drumlins (b) looped morraines

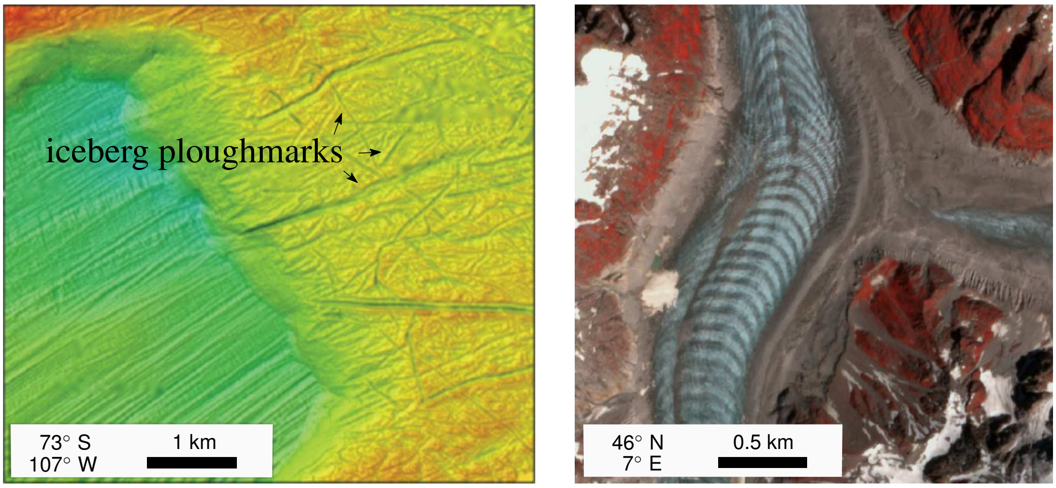

(c) iceberg ploughmarks (d) ogives

Figure 3.11: Observable flow structures on or by glaciers, from left to right:(a) In an elevation model a field of drumlins in Finnmarksvidda, northern Norway, stand out. These are remnants of an icesheet which once was. (b) A moraine band is a form of a streakline, this example is an satellite acquisition from Lime glacier in the Wrangell's mountains, Alaska. (c) An example of a pathline is the bed topography which reveals iceberg ploughmarks (Anderson and Jakobsson, 2016) in an elevation model over the ocean bottom of Pine Island Bay, West Antarctica. (d) Mer de glace has clear distinct bands of bright and dark ice called ogives, there are nice examples of timelines. The image is from an optical spaceborn acquisition.

On the other end of the spectrum are phenomena that are chaotic, or at least of complex nature. These processes are for example rock avalanches and rock fall. An example is shown

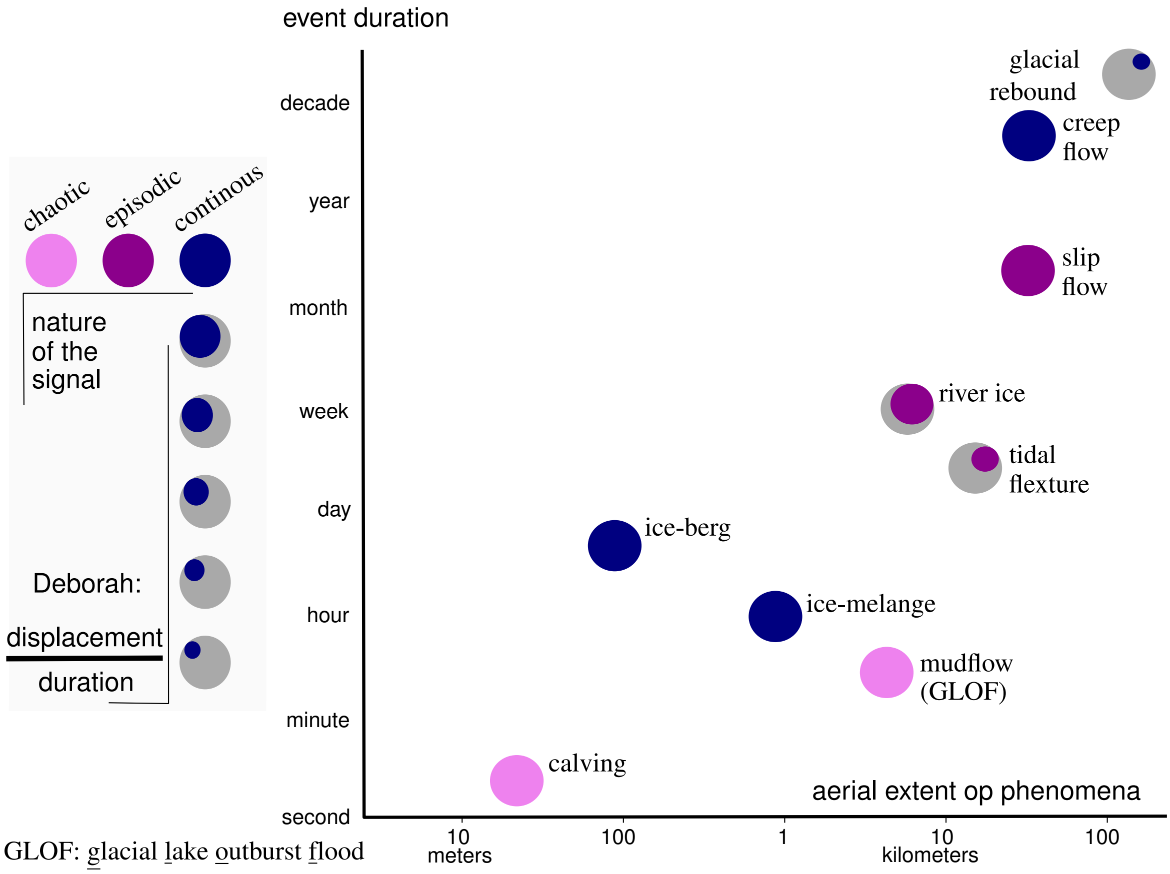

Figure 3.12: Stoffel diagram of the occurance, duration and extent of different glacial events or glacier related processes.

in figure 3.13(a), where a dust cloud of a large rockfall is captured by an overpassing Dove satellite. Monitoring or surveying such phenomena is far more difficult, as the timing or at all its certainty of occurrence is unknown. Between these extremes there are a wealth of phenomena, for which most of them are a mixture of continuous and chaotic behavior (see legend in figure 3.12). The freeze-up and break-up of river ice is such an example. One might be able to predict the occurrence of such events with a certain degree of some days to weeks. But higher temporal resolutions will involve more knowledge and the process becomes too complex.

In the (near) future we will see more recordings of processes that have a chaotic behaviour. This is simply due to the fact that an increasing amount of data will be collected by more satellites. This will have an effect on understanding natural processes, but will to a larger extent be of value for rapid response. Natural hazard management will benefit from these sensors and be able to compose rough inventories for disaster relief like earthquakes (Kääb et al., 2017), floods or avalanches. These types of disasters can ignite other problems, hence satellite analysis can

(a) accidental (rock failure)

(b) predictable (tidal bore)

Figure 3.13: Natural phenomena that have different characteristics by means of their predictability in timing of occurrence.(a) A rock failure and its corresponding cloud at PizCengalo in the Bergalgia range (46.3°N 9.6°E), was accidentally recorded by an overpassing Dove satellite. (b) The monthly occurrence of a tidal bore at Severn inlet (51.8°N 2.4°W ,this time on the 26th of June 2017) was recorded by one of the Doves of the Planet constellation.

greatly reduce further damage when anticipation is possible. A sneak preview into what such a future will look like, is possible through the means of present day meteorological satellites.

In the summer of 2016 on the Tibetan Plateau, a rare natural disaster happened; a large part of a glacier came loose and overrun several herders and their yaks. The first collapse of the lower part of the glacier occurred on the 17th of July 2016. 70 million m^3 of ice detached from the glacier and spread out after it came out of its narrow valley. After the collapse was over, after just some minutes, the resulting deposited ice had covered 105 km^2 (Tian et al., 2017; Kääb et al., 2018). This deposit can be detected from low resolution imagery as in figure 3.14. On the 21st of September of the same year the neighbouring glacier collapsed as well. The magnitude of the event was of similar size, leaving a similar deposit up to the lake edge, as can be seen in figure 3.14.

This event is of such an order that it is possible to detect it by an Indian meteorological satellite. This INSAT-3D is a geostationary satellite (an orbit of ±35 786 km) and senses a large part of the globe every 30 minutes. Consequently, processes on the Earth's surface and the atmosphere can be studied. The one-kilometer resolution of the instrument on this satellite used here is not yet at the resolution that it could be of very much use for mountain glaciers. But with the prospective GeoSat (figure 2.13), with a resolution of 50 meters, more detailed analysis can be made. For instance melting events or large movements can be studied in detail in space and time. But also change detection techniques will be improved, as more imagery increases the

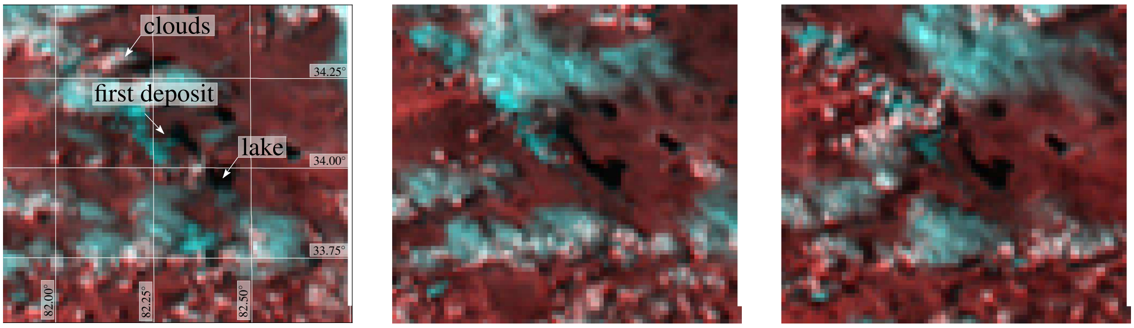

(a) 20 Sep 2016 08:00 (b) 20 Sep 2016 08:30 (c) 20 Sep 2016 09:00

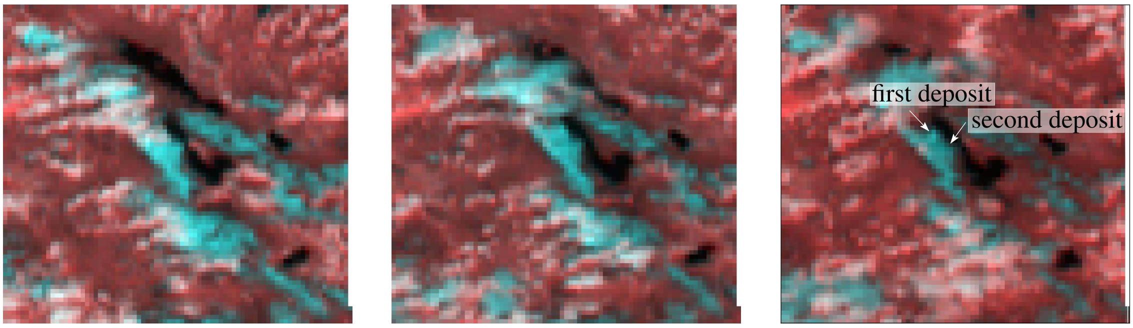

(d) 21 Sep 2016 05:00 (e) 21 Sep 2016 05:30 (f) 21 Sep 2016 06:00

Figure 3.14: False color composite (SWIR-SWIR-VIS) of Aru glacier in Western Tibet, acquired by INSAT-3D.

sample size and thus the confidence of the results.

4 Methods

4.1 Design issues

Algorithms for using two repeat images in time to extract a displacement field are well established (Westerweel, 1997; Cyganek and Siebert, 2011). However, the post-processing to clean and filter datasets is not well developed, especially considering the explosion of Earth observation data in current years. In the following section, tools are highlighted to look into these aspects. One important consideration is the underlying design principle of this thesis; it is to process large volumes of images in bulk and thus algorithms need to be able to scale-up. Therefore, the philosophy taken here is to use only imagery and exclude auxiliary data. The rationale for the latter is simple; if any error is present within the auxiliary data this will influence the processing. Hence auxiliary data enforces a dependency and more importantly, it can introduce a bias which might not be discoverable. Moreover, by implementing a stand-alone tool, one is able to test its full capacity and get a good idea about the limitations of the developed method. Coupling with other algorithms or other dependencies would make such testing more cumbersome. This strategy is also taken for paper I,II&III.

A second consideration to take into account is the aim of optical satellite missions, these are often designed for specific goals, think of agricultrual monitoring, emergency response, greenhouse gas, etc. Processes occurring in the cryosphere are often not the main objective, though exceptions exist (ICESat, CryoSat). This thesis can thus be seen as an opportunistic attempt to extract as much information as possible out of these sensor systems.

If the aim is to use auxiliary data to a minimal extent, one should concentrate post-processing approaches towards material properties of the subject, such as the flow characteristics of ice. The viscosity of a material describes the “stickiness” of a medium. In this aspect ice is very special as over longer timescales it flows like honey, however at small time scales it is brittle. If we would lower the viscosity, a more fluid liquid appears, such as water. Equivalently, higher values describe stiff materials such as polymers (plastics). Now it is of interest to study the research fields which analyze these endmembers: fluids and solids, in order to barrow ideas. On the one hand particle image velocimetry deals with the analysis of fluids. While on the other hand, the field of computer vision works on incorporating human perception of objects into algorithms. Although both fields have different challenges and goals, it is a benefit to dive into both subjects. Because ice is in between both fundamental research fields, and thus many topics overlap. Therefore, both research fields will be introduced in order to place remote sensing of glacier dynamics into perspective.

4.1.1 Displacement measurements in computer vision

Computer vision is a broad and vivid field of study within artificial intelligence. Early research focused on mimicking the processes occurring in the animal or human brain. Simplifying our visual abilities into elementary units, like flip-flops, resulting in artificial neural networks. For pattern matching, two main branches emerged: optical flow and structure-from-motion (SfM). Because both problems are ill-posed the outcomes are infinite, hence these subjects are still active fields of research, though its advances are mostly computational improvements or solutions for specialized cases.

In recent years, algorithms for mining and discovery within large volumes of structured data have become popular. However, in this thesis none of these approaches in pattern recognition will be investigated. An analogy for big data can be made with gold digging, where washing a river bed in the hope for a nugget. It is based on luck and extensive labour composed of simple operations. While on the other hand, the type of work in this thesis might be more comparable with coal mining because when we know what a system is like, success is greatly enhanced. Therefore, when methods from computer vision are used, they will have a functional model.

The field of Earth observation has changed due to the opening of the Landsat archive and the launch of the Copernicus program. Consequently, remote sensing becomes more data intensive and less controlled. This is exactly the type of research problems where computer vision is working on. Hence, methodologies in model fitting and applying robust statistics are common tools within this domain and therefor of interest when large collections of data are processed.

4.1.2 Flow measurements in fluid mechanics

The other field of research, which is extensively touched upon in this thesis, is experimental fluid mechanics. Within this field one uses a fixed laboratory setup, which is rich in data collection. Practically this means that a proper measurement design is deployed and sampling has been done in regular intervals, with great redundancy. Hence robust statistics is less important here, as iteration of design can create a clean and workable dataset. In a typical setup, fluid velocities are measured in a water tank, where particles are lighted by a sheet, as shown in figure 4.1(a). The technique is called particle image velocimetry (PIV).

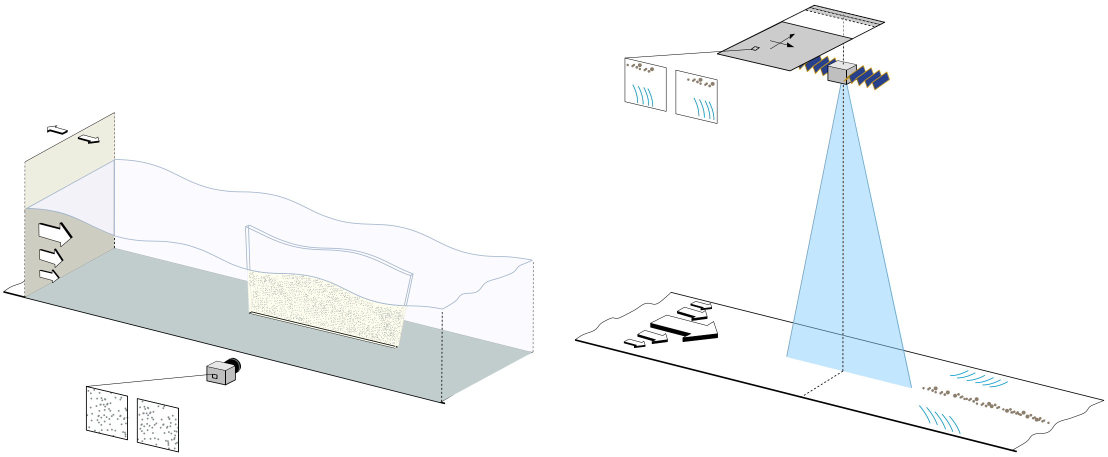

(a) Measurement setup for fluid displacement estimation in a water tank

(b) Configuration of optical remote sensing over moving glaciers

Figure 4.1: The similarity between acquisition configurations for (a) fluid mechanics in a laboratory and (b) spaceborne remote sensing of a glacier. Both analyze movements within a plane, either within a thin light sheet or at the Earth's surface. Figure (a) modified from Raffel et al. (2013)

The set-up of this design is very similar to the configuration of a normal satellites overpass, see figure 4.1(b). Combined with an increase in satellites, such techniques use in fluid mechanics can be transformed to glacier flow analysis. However, in laboratory experiments the surroundings and the subjects under study are controlled. For example, the tracers in the tank need to be steered and distributed evenly. However, this is not the case with a glacier, where the features observable depend on the spectral, radiometric, and spatial resolution of the sensor. Thus only by combining the merits of both the fields of computer vision and experimental fluid mechanics, big advancement can be made in modern day Earth observation. Hence, throughout this thesis methodologies from both fields will be used.

4.1.3 Strategy for glacier flow estimation

Displacement estimation from satellite imagery can be very challenging due to the changing appearance of features on a glacier. Most estimation procedures use brute force and are ad-hoc, largely because the features searched for are configurations which can be coherent, but not necessarily the dominant signal within an image. Though this strategy is highly developed and the main angle of attack in computer vision where interest point operators are used to detect junctions, and descriptors to find similarity. The following sections will mostly be concerned with standard (naive) image matching, as this is the common approach today. However, some explorations have been done into the feature matching technique (paperII). The rest of this chapter will follow the different building blocks of optical remote sensing of glacier flow, from pre-processing of satellite imagery all the way to applications for velocity fields of glaciers.

4.2 Pre-processing

A brief overview of repeat image matching is necessary so the importance of pre-processing and later adjustments is clear. Image matching is the central building block for estimating displacements and consists of a chain of procedures. Its core and details will be explained later in section 4.3.1, but for now it is of importance to understand what the concept is and why the following part is relevant. Figure 4.2 shows a schematic of the step-wise procedures in image matching. Two images acquired in time (t_1 & t_2) are compared by taking subset(s) or templates of one image and to search within a predefined area of the second image. At every position the similarity is estimated between the two images resulting in a score. After each candidate location is visited, the correlation surface is analyzed and the highest value is taken to be the displacement between time t_1 and t_2. This procedure can be separated into small steps with different implementations. Where the first step is pre-processing, the subject of this section. The goal in this step is to emphasis the terrain signal within the imagery as precise and similar as possible without impacting on the positions of the spatial intensity variations because this might improve the ability to distinguish different candidate displacements in the correlation space.

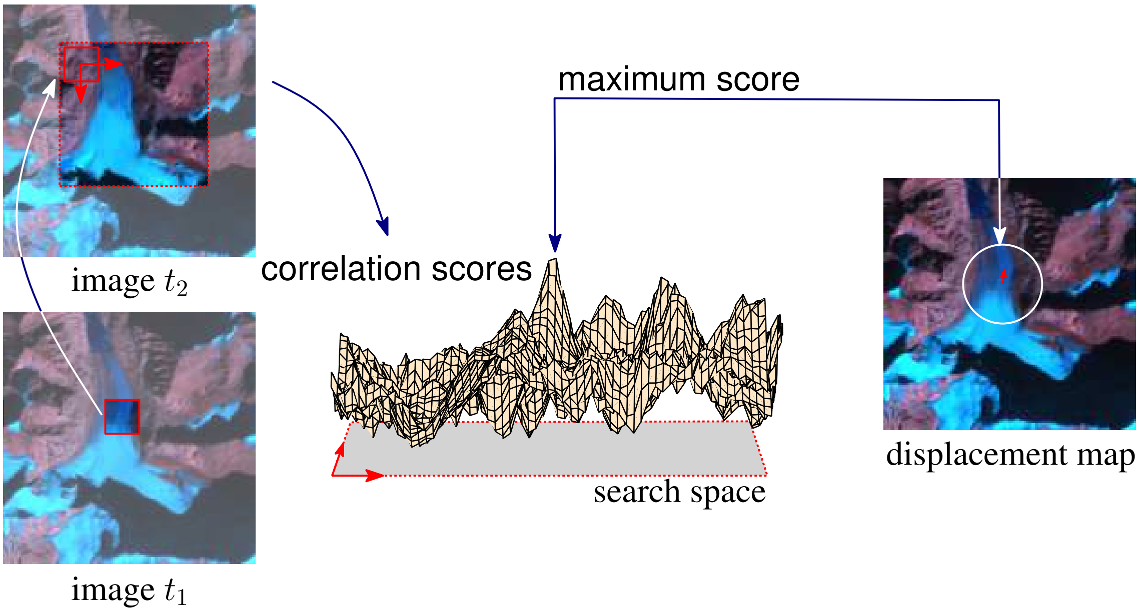

Figure 4.2: Schematic of the basic principle of pairwise image matching.

4.2.1 Pattern enhancement

Image matching on glaciers can be challenging due to surface features characteristics which have a wide range of reflectances; the upper-part of a glacier may have very bright reflecting snow while the lower part could have low reflecting debris. The dynamic range of sensors on present-day satellites, such as Landsat 8 and Sentinel-2, is 12-bit. This is an improvement compared to the older generation Landsat sensors which have a low radiometric range of 6 to 8-bit. Thus, the newer sensors are resulting in better displacement coverage (Jeong and Howat, 2015; Fahnestock et al., 2016; Kääb et al., 2016) where the older sensors saturate with the highly reflective snow (Dowdeswell and McIntyre, 1986; Hall et al., 1988). In the following, we highlight different approaches to increase the information content within Earth observation imagery in order to improve matching capabilities of glaciated surfaces.

4.2.2 Filter banks

A template used for image matching can be composed from the original digital numbers (DN), but may also be a part of an image convoluted through a filterbank (Ahn and Howat, 2011). In this manner, features with a certain spatial frequency or orientation can be stressed over other elements within the template. Typically, the first derivative is used for such cases. The approximation of the derivative at a pixel within the imagery is done through local operators. The smallest kernel to do so is Richards ($\left[\begin{smallmatrix}-1 & 0\\ 0 & 1\end{smallmatrix}\right]$). However, this kernel will estimate the derivative on a staggered grid, which is situated in between the pixel locations. Therefore one commonly uses a Prewitt or Sobel kernel as backbone for derivative estimation (Dehecq et al., 2015). These kernel operators are expressed as,

$$\mathbf{G}_x = \underbrace{\begin{bmatrix}-1 & 0 & 1\\ -1 & 0 & 1\\ -1 & 0 & 1\end{bmatrix}}_{\text{Prewitt}}, \quad \mathbf{G}_x = \underbrace{\begin{bmatrix}-1 & 0 & 1\\ -2 & 0 & 2\\ -1 & 0 & 1\end{bmatrix}}_{\text{Sobel}}, \quad \mathbf{G}_x = \underbrace{\begin{bmatrix}-3 & 0 & 3\\ -10 & 0 & 10\\ -3 & 0 & 3\end{bmatrix}}_{\text{Scharr}}, \quad \mathbf{G}_x = \underbrace{\begin{bmatrix}-17 & 0 & 17\\ -61 & 0 & 61\\ -17 & 0 & 17\end{bmatrix}}_{\text{Kroon}}.$$

Alternative operators such as Scharr (2007) and Kroon (2009) are interesting as they are less sensitive to quantization, that is the ability to be invariant towards orientation of the image grid. This is of interest as the information transformed needs to be translated without prepossession. To illustrate this importance, two scenes over Hendrickson Glacier in Alaska from Landsat 7 and EO-1 are analyzed, as these were taken roughly at the same time. Landsat 7 has an 8 bit radiometry while EO-1 has 10 bit resolution. For both the local orientation ($\mathrm{sgn}(\tan^{-1}(\mathbf{G}_x \star \mathbf{I}/\mathbf{G}_y \star \mathbf{I}))$) has been calculated with different kernels (figure 4.3).

In this plot the advantage of a higher radiometric resolution is clearly visible as a smooth distribution of gradient orientations with two peaks (lower row) is resulting from the EO-1 image. Two peaks are less apparent for the lower radiometric resolution (upper row), especially using the simple, but popular, Prewitt and Sobel operators. Here, a preference for whole angles is present because of the quantization bias. The Scharr and Kroon kernel seems to be the best operator for this sample. It is therefore preferred to use these kernels, especially when low radiometric data is used.

4.2.3 Band ratios

The dominant features on a mountain glacier are snow, ice, water and rocks. The rocks on a glacier come from the surrounding mountains through plucking, thawing or avalanches. These mountains can be composed of multiple geological layers with different minerals within. Because a glacier can cut through these layers, the reflectivity of rocks in and on glaciers is spatially highly diverse. In general, the spectral response of rocks is fairly stable in the visible spectrum. Their discriminative power is more present in the short wave and even more in the

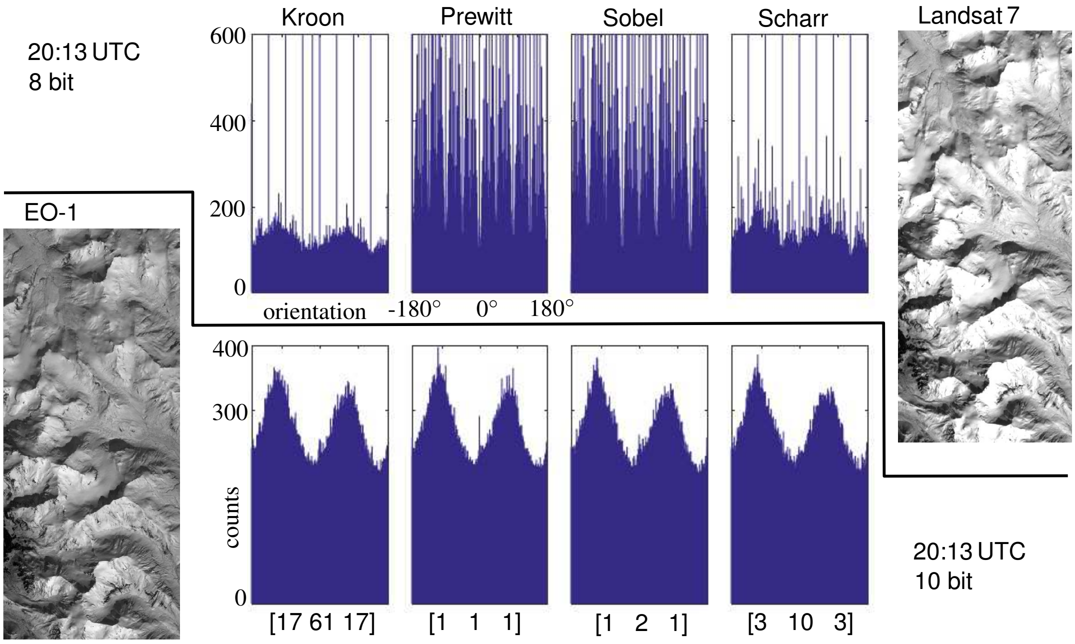

Figure 4.3: Two acquisitions on the 17th of April 2002 over Hendrickson glacier, Alaska. Landsat 7 and EO-1 have different radiometric resolutions. The local orientation estimation of the intensities is done by different kernels, resulting for some estimations into systematic artifacts, as can be seen in the histograms.

thermal range (Ninomiya et al., 2005; Casey et al., 2012). The importance of knowing what type of lithology is present can improve performance of the image matching. Because when a spectral band is selected that is sensitive to the dominant geology, contrast of the surface signal will be higher (Redpath et al., 2013).

Snow has a high response in the visible range, but towards longer optical wavelengths absorption strongly increases, see figure 4.4. With this strong decrease in reflectance a second superimposed signal becomes distinguishable, this signal is highly influenced by grain size (Warren, 1982). For snow the grain size depends on the temperature during creation, as well as the amount of melt since deposition, also known as aging of the snowpack. Another agent which influences the spectral response of snow and ice is the deposition and incorporation of dust. Such particles are transported through the atmosphere, and if the whole snowpack melts away, dust is deposited on the surface, making “dirty ice”.

Most remote sensing instrument, especially the older Landsat sensor family, observe in the visible and shortwave spectrum. For this range there is redundancy in the information content, because bands are correlated (Ingebritsen and Lyon, 1985; Fung and LeDrew, 1987). The intrin-

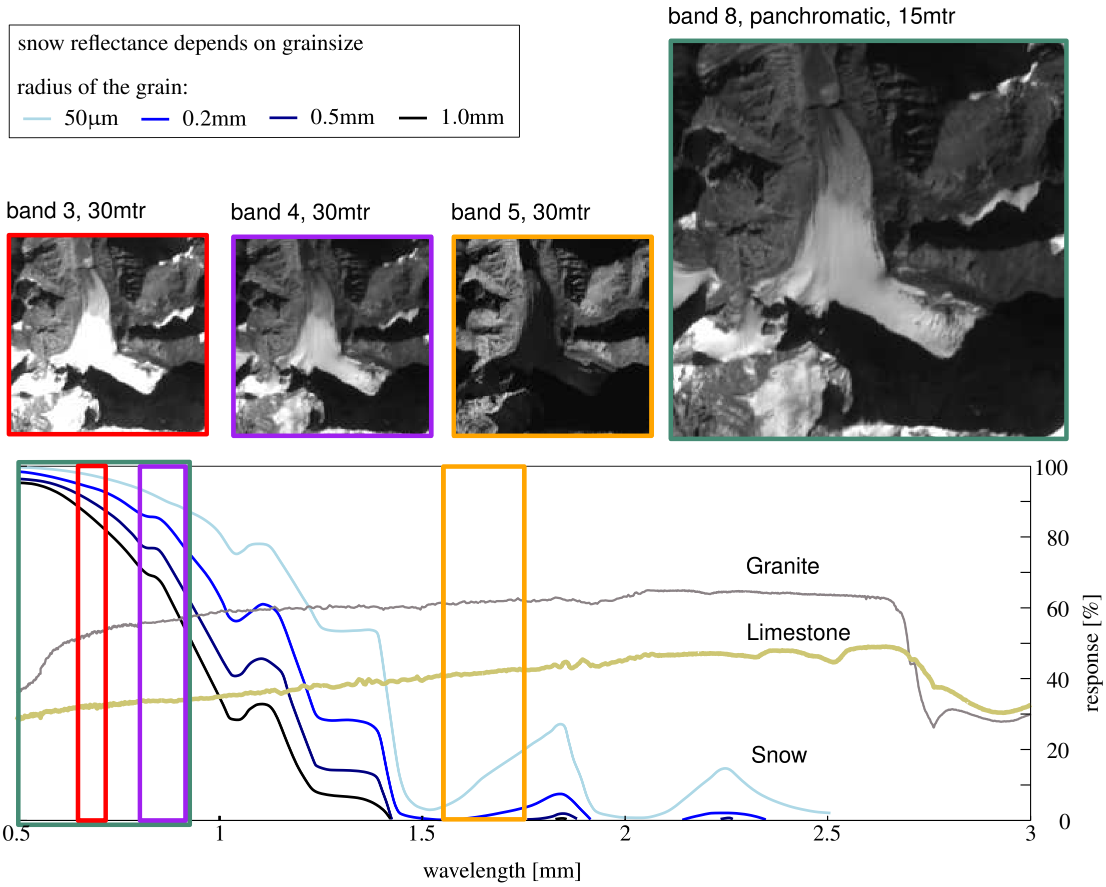

Figure 4.4: Spectral response of different lithology and snow in the visible and short-wave spectrum. The boxes illustrated the range within the spectrum where the bands of Landsat 8 are sensitivity to. The image insets show the different acquisitions of these bands over a glacier.

sic dimensionality (the dimensions needed to describe the dataset) is for the visible to shortwave range in the order of two. This means matching between different sensors, with different band-widths is in essence not problematic. Another consequence of the correlated signals between spectral bands is the small amount of improvement when image matching is done with multiple bands at once. Nevertheless, it is to some degree of importance to select the band with the most information content within. Hence for reliability, bands in the visible range are preferred, as the shortwave spectrum is highly reliant on grain size. Shortwave bands will record changes in grain size and are thus not coherent over time. Within the visible range, the reflectivity of snow is very high, and is able to saturate the sensor. Thus bands within the near infrared are preferred, where snow has less reflectance, and is also not much effected by grain size. For the Landsat system, the panchromatic band is thus a good option, as it is sensitive in the visible and the NIR range, and has the additional advantage that it has a high spatial resolution, which is also of importance for the matching.

Generic methods such as gradient-, orientation-, high pass or Wallis-filters can greatly improve optical matching (Heid and Kääb, 2012a). However, the appearance of a glacier can change considerably, due to snow fall or surface degradation by melt. Thus, feature enhancements working on intensity edges might not select time-coherent features. It can lead to enhancement of temporal surface changes instead of time-invariant features, and thus degrade the temporal image matching.

When glacial surfaces need to be matched under the presence of topography, for example acquired under different sun angels, the shading needs to be removed. For such cases band-ratios can be used making the matching less sensative to illumination variations. This methodology works best when images are radiometrically calibrated and atmospheric conditions are similar or known. Then these terms cancel each other out in band-ratios, namely equation 2.8 is divided by itself, and the surface signal is left:

$$\frac{I_i}{I_j} = \frac{\mathbf{n} \cdot \mathbf{s}\, C \int_\lambda T(\lambda)\, [S(\lambda)\, R(\lambda) + A(\lambda) - L_0(\lambda)]\, d\lambda}{\mathbf{n} \cdot \mathbf{s}\, C \int_\lambda T(\lambda)\, [S(\lambda)\, R(\lambda) + A(\lambda) - L_0(\lambda)]\, d\lambda}. \tag{4.1}$$

This simplified formulation also shows why ratio of multi-spectral bands are so powerful for simple mapping purposes, and thus of common use in Earth observation (Paul, 2000). In case when the illumination geometry is equal ($\mathbf{n} \cdot \mathbf{s} / \mathbf{n} \cdot \mathbf{s} = 1$), relations of reflectance can be directly exploited. When image acquisitions are on the same day, atmospheric conditions are fairly similar, and thus pixel values may be assumed to be affected in like manner. Another approach for normalization is by estimating these parameters through radiative transfer modelling (S, A) and sensor metadata (T, C, L_0). Then the terms right of the topographic terms cancel out or diminish and the topographic estimation can be simplified. Leaving only the reflectivity terms ($R_i(\lambda)/R_j(\lambda)$) in place.

4.2.4 Multi-spectral information transforms

More data-driven approaches for image pre-processing can be chosen, one popular approach is principal component analysis (PCA). This approach has been applied successfully on ice sheets where there is an absence of non-glaciated terrain (Scambos et al., 1992) and the first principle component is dominated by topography (Stearns and Hamilton, 2005). Features related to glacier facies might be observed in the lower principle components (Kääb, 2005). By applying principle component analysis to a superimposed multi-temporal collection of bands, as in Byrne et al. (1980), Dehecq et al. (2015) could improve the matching over high mountain glaciers. However, as already pointed out by Byrne et al. (1980), the use of temporal principle component analysis needs careful assessment, and results of the transform might not be straight forward. Since the sources of variance can be caused by various changes such as in atmospheric conditions, soil moisture, land cover, or sensor calibration. Thus it is of interest to look deeper into this transform, as it is popular and effective, but seem to have shortcomings.

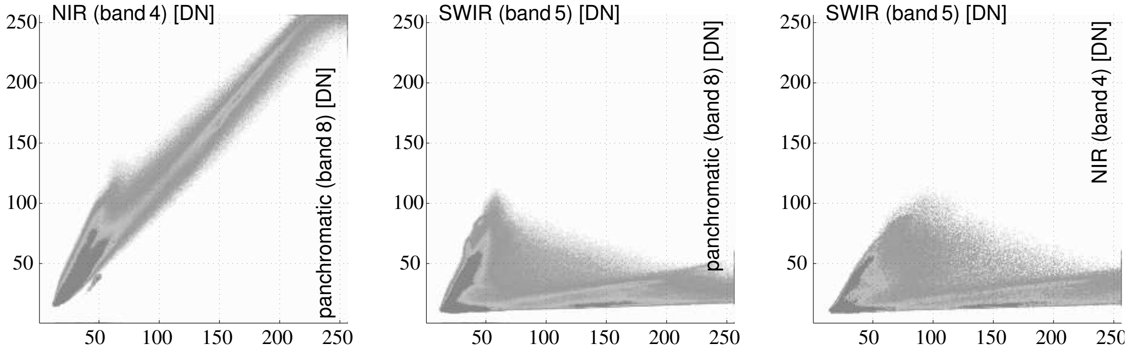

(a) NIR vs Pan (b) SWIR vs Pan (c) SWIR vs NIR

Figure 4.5: Cross-spectral distribution over Franz Josef Glacier, New Zealand. The inter-scene spectral distribution has spread related to different reflecting objects in the image. In (c) the lower lobe is snow/ice, while the steeper lobe is stemming from lithology. This angle of the lobe can also be inferred from figure 4.4; snow has high reflection in the NIR but low in the SWIR, lithology has constant reflection, hence its relation is 1:1. For the lobe with snow reflectance, values seem to concatenate along the edge, indicating that several pixels will be saturated in the NIR and panchromatic band.

Pixel saturation does not only occur in the panchromatic band for older satellite instruments, but most of the time in all first three bands of Landsat (Hall et al., 1988). This saturation is a long-standing problem for glacier mapping, and is related to the gain settings of the instrument (Raup et al., 2000). For Antarctica, the settings can be estimated in advance (Dowdeswell and McIntyre, 1986). However, most continental glacier are situated in the same track as agricultural or vegetated land, where settings in autumn and summer are set to high gain. A robust method should not rely on these overly sensitive bands in the visible range, but rather short wave infrared (SWIR) and near infrared (NIR) bands are preferred for older missions. To look into these specifics, a two dimensional histogram of these two bands over Franz Josef Glacier, New Zealand, is illustrated in figure 4.5(c). This histogram has a similar shape as the panchromatic band (figure 4.5(b)). In both histograms a signal is present in SWIR and absent in the NIR, occurring in multiple imagery. This signal fluctuates from scene to scene, but also from season to season. Through classification we find this signal can be from the lithology, but also from vegetation.

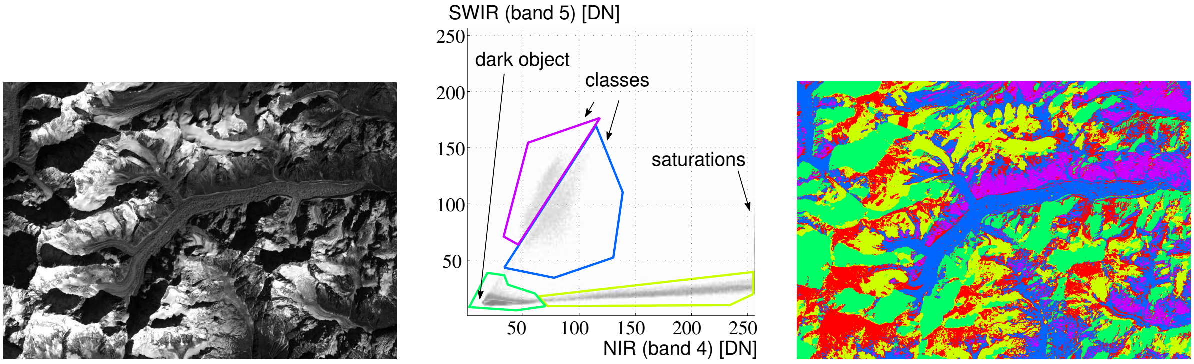

(a) panchromatic scene (b) SWIR vs NIR (c) classification

Figure 4.6: (a) Landsat 7 acquisition on the 26th of December 2000 over Zemu Glacier, Kangchenjunga. (b) Cross-spectral distribution of the SWIR and NIR band of the scene, including a supervised classification denoted by its colored borders. (c) map view of the classification, in red are values outside the selection of the classification, mostly aligning with saturated pixels in the NIR. Other colours correspond roughly to shadows (green), snow and ice (yellow), debris (blue) and vegetation (purple).

The spread of the plot shown in figure 4.5 explains some strong drawbacks to the use of principle component analysis. The origin where both distributions overlap is known as the dark object, and the linear spread in both spectral intensities is due to topographic effects (Conese et al., 1993; Shrestha and Zinck, 2001). Thus when multiple end-members are within a sample set used for such analysis, the characteristics of orthogonality is not present. To better visualize the spread a classification is applied to the cross-specral distribution of a Landsat scene over a Himalayan glacier in figure 4.6. Apart from lithology, a second point of concern is the vegetation class within an image, as this class can change its reflectance characteristics through-out the season (known as the tasseled cap (Kauth and Thomas, 1976)). When sufficient vegetation is within the image, this will ultimately influence the center of mass of the distribution, and thus the directions of the PCA axis. Therefore masking of non-glaciated terrain in the imagery is needed to reduce such dependencies (Sidjak and Wheate, 1999). However as shown by the plots, such deviations exist as well for different lithology, this would imply that similar effects can still occur, but now caused by the amount of snow-cover. In summary, it is not preferred to use the principle component analysis for image matching in high mountain terrain.

While global data driven methods such like principle component analysis capture dominant features, a local approach might highlight signals that are normally less dominant and thus hidden close to the noise (figure 4.5). We adopt some procedures as presented in Socolinsky and Wolff (2002), that merges the local gradient to find the local eigenvector. In their implementation this is used for image fusion, but in our case this integration step is not conducted. The resulting gradient image has therefore a mixed of information content, however because large correlation between bands exist this technique is ideal for saturated data. For each multi-spectral band the gradients and curvatures are estimated. These are combined into a Hessian-matrix and the contrast vector is extracted through single value decomposition (SVD). When there is saturation in one of the bands, no gradient is available, but this does not influence the estimation of the contrast vectors, as these entries in the Hessian are set to zero. To illustrate its performance, the orientation for a Landsat 7 data, similarly to figure 4.3, is estimated with this method and shown in figure 4.7.

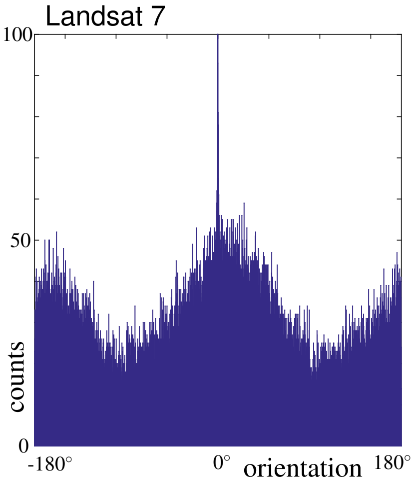

Figure 4.7: Orientation distribution of a Landsat 7 acquisitions taken on the 17th of April 2002 over Hendrickson glacier, Alaska. The histogram is from similar data as of figure 4.3. However now using a multiple bands to reduce the effects of saturation.

There are less counts in this histogram, due to lower resolution of the multi-spectral bands, then with the panchromatic. A single spike can be seen at zero, this is due to no-orientation present in the data. While the rest of the distribution is smooth and has no other spike or preference, as is the case with single band gradients and more resembles the distribution of the EO-1 satellite. The shape of the distribution is different, which is due to the use of a Hessian for the orientation instead of the Jacobian. Nevertheless, the transformation seems to be able to extract information effectively and therefore this transform is preferred here.

4.2.5 Pattern recovery at data voids

A special case in the optical satellite image archive is the malfunctioning of the scan-line-corrector (SLC) on board of Landsat 7. This whiskbroom sensor senses the terrain in scan lines perpendicular to its flight path (section 2.3.1). The SLC is a mechanical device which directs the line-of-sight of one scan line perpendicular to the flightline through a mirror, as the platform flies over, in order to compensate for the sensor motion during the scanning acquisition. The malfunctioning of this mechanism results in data breaks (strips of no data), with grooves cutting up to 1/3 into the image (figure 4.8(b)). These voids are a permanent feature within the imagery and several methods have been proposed to work around this deficiency. The positions of non-value pixels are known, hence infilling with random noise (Warner and Roberts, 2013), has been suggested. The SLC effect can be minimized when normalization of a gradient image is applied (Heid and Kääb, 2012a). Alternatively, the matching can be accompanied by a weighting matrix, specifying the gaps in the template (Ahn and Howat, 2011).

Since its malfunction several studies have been done to bypass this effect and reconstruct a full image again. Procedures differ from multi-temporal (Scaramuzza et al., 2004), multi-sensor approaches or simple interpolation. For glacier displacement estimation, the most reliable is not to introduce data, resulting thus in corresponding voids in the displacement fields, as any methodology relies on assumptions, which can have exceptions, as the example of figure 4.8 demonstrates.

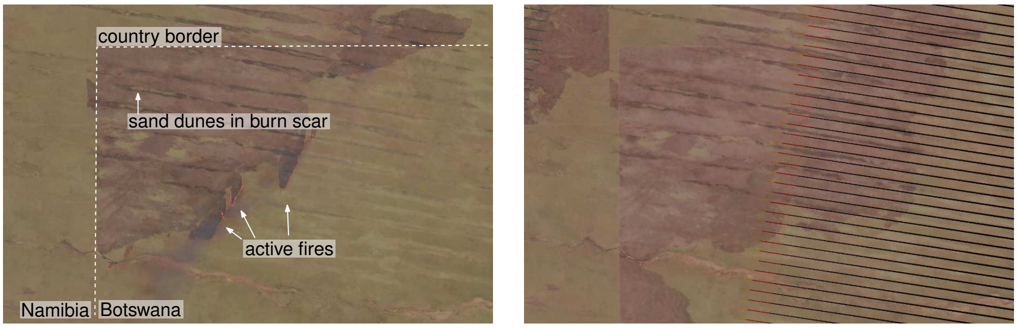

(a) 15th Sep 2017 Landsat 8 (b) 23th Sep 2017 Landsat 7 SLC-OFF

Figure 4.8: Acquisitions over Tsodilo, Botswana. Within this park are elongated repeating sand dunes, this geology is surprisingly in the same orientation as the defect caused by the scan line corrector. Hence, simple infilling of these voids will be very complicated. Also at this time there is a wildfire, see in the left image the orange fire and the gray smoke making a burn scar. The burn scars are a few days later also recorded by Landsat 7, which is shown in the right figure. Here, the extent of burn-scars closely align with the border of Botswana with Khaudum National Park in Namibia (the border is right-angled and in the upperleft). It clearly resembles the difference between shapes and lineations made by the natural and human world. Developing an interpolation scheme that can incorporate all these aspects will be very difficult.

4.3 Processing

4.3.1 Similarity in the spatial domain

The foundation for displacement estimation from optical remote sensing is image matching. It is based on finding a similar template from an image in another image. Typically this similarity measure is implemented through (normalized) cross-correlation and can be formulated in two domains, spatial and frequency. The spatial domain method, visually illustrated in figure 4.2, is mathematically formulated as,

$$\Theta_{pq} = \frac{\sum_{k,l} (\mathbf{I}_p(i+k, j+l) - \bar{\mathbf{I}}_p)(\mathbf{I}_q(k,l) - \bar{\mathbf{I}}_q)}{\sqrt{\sum_{k,l} (\mathbf{I}_p(i+k, j+l) - \bar{\mathbf{I}}_p)^2 \sum_{k,l} (\mathbf{I}_q(k,l) - \bar{\mathbf{I}}_q)^2}}. \tag{4.2}$$

Here Θ_{pq} denotes a score surface at discrete step sizes (k,l). It is calculated by the similarity of two smaller templates ($\mathbf{I}_p$ & $\mathbf{I}_q$). In this formulation, the normalized cross-correlation (NCC) is used in which templates are normalized by their mean intensity (denoted by the overbar), and the intensity spread is taken into account by the lower part of the fraction.

4.3.2 Similarity in the frequency domain

The cross-correlation (CC) can be formulated in the frequency domain as,

$$\rho_{pq} = \mathscr{F}_2^{-1}(\mathscr{F}_2(\mathbf{I}_p)\mathscr{F}_2(\mathbf{I}_q)^*), \tag{4.3}$$

where $\mathscr{F}_2$ represent a two dimensional Fourier transform and $*$ the complex conjugate. The advantage of using the frequency formulation is the computational efficiency that is accomplished using a single multiplication step rather than looping through templates as in the spatial domain method. Several operations are different in their respective domains and can be more efficient, therefor these are listed in table 4.1.

spatial		frequency	
convolution	$f \otimes g$	multiplication	$f \cdot g$
differentiation	$\nabla \vec{v}$	wave number multiplication	$\mathbf{k} \cdot \vec{v}$

Table 4.1: Relations between different operators in the spatial and frequency domain.

Besides computational efficiency, the two approaches result in different correlation surfaces. A demonstration of this is shown in figure 4.9 of a template over an elongated glacial moraine, it provides a difficult case to resolve for image matching. The correlation surface in the spatial domain provides a smooth result with a single peak. While in the frequency method, several sharper peaks emerge, though situated along the same direction. A spatial translation is a Dirac delta in the frequency domain (Leprince et al., 2007). This shows the power of frequency methods, as information of translation over the whole search image-section is taken into account not only the smaller template searched for as used in the spatial-domain solution. In addition, also the similarity scores are high, as can be seen on the scale bar. However, a disadvantage is the transferability of this scale to other correlation surfaces, as no normalization is applied. Therefore, the signal to noise ratio (SNR) is mostly used as a reliable measure using frequency methods.

4.3.3 Deep learning displacements

Artificial neural networks can be used for the estimation of displacements (Rabault et al., 2017). In this way the problem of similarity is transformed to a labeling problem or classification scheme with the (gradient) velocity as classes. Up to now, this has only be implemented in

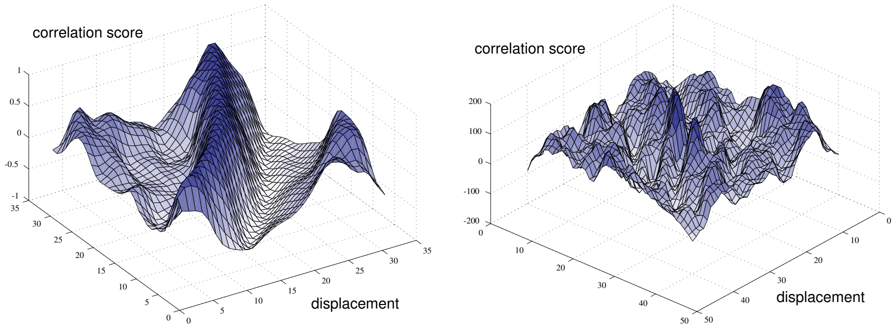

(a) spatial NCC (b) frequency CC

Figure 4.9: Correlation surfaces estimated by NCC (a spatial method) and CC (a frequency method) over an moraine band.

a laboratory setting, where a particle seeded flow is recorded. Hence, such imagery can be replicated by synthetic images and immense training sets can be generated to construct a neural network. Its main advantage is the ability to train complicated flow, which normally would need non-linear optimization (Debella-Gilo and Kääb, 2012b). However, translating this to a real world applications is difficult as the ability to construct a training set is more challenging.

4.3.4 Making similarity more similar

The input for a Fourier transformation can either be real (e.g.: image) or complex (e.g.: gradient of an image or SAR). The resulting transformation is a spectrum highlighting dominant frequencies. Each frequency in the spectrum is described by its intensity and its phase. However, most information is within the phase values (Oppenheim and Lim, 1981). Thus, when images are correlated, that is multiplication in the frequency domain, only the phase information is taken. Another element of importance is the spectral distribution of natural imagery within the Fourier space. Long wavelength signals have larger amplitudes then low-frequency signals. Thus, when this spectrum is normalized, the importance of high frequency signals is amplified. When the frequency vectors are set to unit length, this is called orientation-correlation (Fitch et al., 2002). In the spatial domain this would be somehow similar to high-pass filtering, as is applied in Fahnestock et al. (2016). However, a computer implements a discrete Fourier transformation, thus the frequencies estimated are not continuous, and in order to do so the borders are reflected. This results in a spectrum with a bias towards frequencies along the image axis as large transitions occur there. Pre-processing through periodic decomposition can resolve this (Moisan, 2011).

As already highlighted above, satellite optical imagery often have artifacts, such as gaps, clouds, borders, or saturation. When these artifacts are within the template, the correlation score is reduced. This can be solved through the use of a weighting scheme when spatial cross-correlation is used. However, it is also possible to do this in the frequency domain. In this case, the masks of both templates are also converted to the frequency domain and multiplied. The resulting spectrum is then used to mask frequencies of the original image spectrum, for more details see Padfield (2012). This methodology makes it possible to extract a normalized function of the cross correlation.

4.3.5 Shear and rotation between imagery

The approaches discussed above assume that ice simply translates in rigid fashion, ignoring rotation or shear. To a certain extent these more complicated transformation effects can be dealt with, especially as processing in the spatial domain is robust, as can be seen in figure 4.10. Instead of a simple planar translation, the functional model can be extended to an affine model (Whillans and Tseng, 1995). Through least squares estimation, the two image subsets are adjusted through this transformation, and strain rates can be extracted from its parameters. When incompressibility of ice is assumed also the vertical strain can be estimated from the horizontal components (Debella-Gilo and Kääb, 2012b).

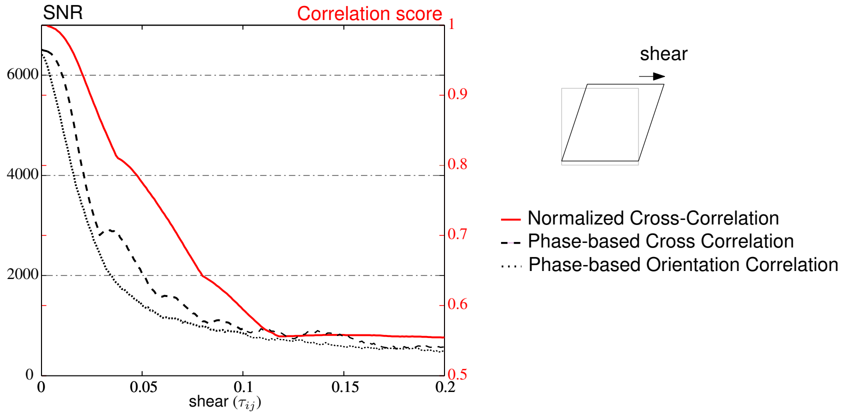

Figure 4.10: Experiment of the sensitivity of different correlation algorithms to shear.

As can be seen from figure 4.10, even CC-based matching procedures are to some extent able to handle some shear. Iterative procedures are also possible, where in a first iteration the displacement is estimated and the resulting displacement field is then used to distort the templates in the next matching iteration (Scarano, 2001). This will resolve in higher correlation scores, though the first initial estimate needs to be correct in order to converge.

To compensate for rotational effects through approaches in the frequency domain, a different formulation of the Fourier domain can be used. Known as Fourier-Mellin, intensities are formulated in polar coordinates instead of a grid resulting in a two-dimensional space spanning orientation and distance. When both images are transformed, the displacement can be estimated similar to equation 4.3, only now the correlation surface span scores for candidates of a relative change in rotation or scale. For our case, the scale parameter will be constant, as the same satellite instruments are used or scaling is known beforehand and our depth of field is slim.

4.3.6 Window size matters

In most cases, the size of the template is set fixed even though the velocity estimation seems to be dependent on the window size in spatial domain methods. Studies have tried to find the optimal window size, for example by finding a tipping point in average velocity (Liu et al., 2012) or through the help of a high-pass filter as noise quantization (Debella-Gilo and Kääb, 2012a). When the template size is big, matching zones of high shear or at glacier snouts (i.e., large displacement-field gradients) is difficult, while when smaller templates are used, not enough information might be within the image section to establish a reliable correspondence. An integrated pyramidal approach is possible (Altena et al., 2015), but such a procedure is computationally expensive. Layered structures as applied in convolutional neural networks have been implemented as a pyramid matching schemes (Revaud et al., 2016). Though such schemes still need simplification and/or small image input not to be overloaded.

4.3.7 High-resolution flow using the time-domain

Difficult situations arise for image matching when the correlation surfaces do not show distinct peaks, either due to a too small window size, or because of complicated flow. Limitations on the size of the support region are imposed because of distortions due to complicated flow or visual coherence loss between acquisitions over time. An extremely example is an icefall, for example, the staircase icefall of Root Glacier in Alaska (figure 4.11(b)) is a challenging case to extract velocity. Here the slope is too steep and the ice too thin to flow as a viscous fluid, thus the surface is full of crevasses and can have calving cliffs. An alternative approach to estimate the velocity from this glacier section is to exploit the temporal dimension when a dense collection of images are available. The idea is that the size of the template can be small, but this is compensated by the support in the temporal dimension. This technique has been introduced in fluid mechanics, and is known as ensemble correlation (Westerweel et al., 2004). Here, a stationary fluid needs to be assumed, therefore the method is only applied in stable fluid flow. For a glacier this assumption can to some degree be valid when the time of year is taken into account. For example, a distinction can be made between summer and winter seasons, separating two different flow regimes. Velocity estimates generated with this methodology can be seen in figure 4.11.

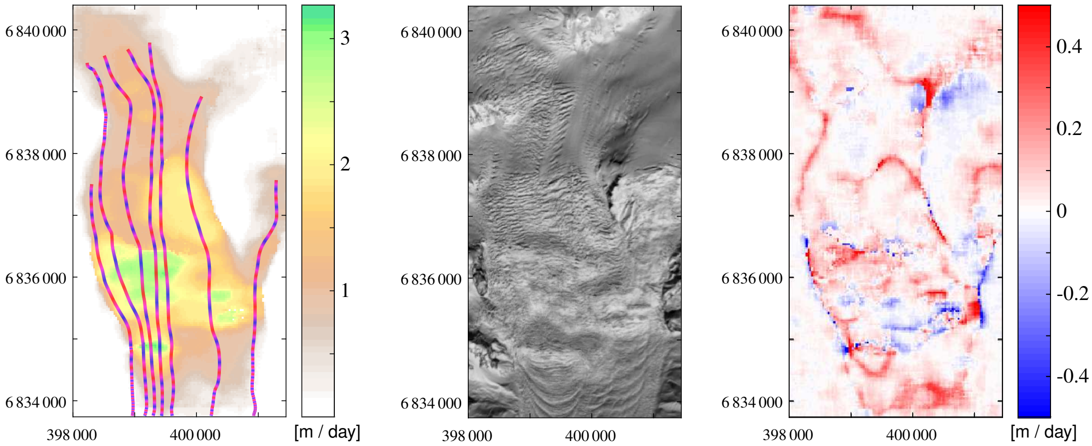

(a) flowpaths and velocity (b) 13^{th} April 2013 (c) seasonal velocity difference

Figure 4.11: Seasonal velocities over the Stairway icefall, part of Root Glacier in the Wrangell Mountains, Alaska, estimated from a collection of Landsat 8 acquisitions, separated in winter and summer scenes. Coloured lines in (a) indicate a seasonal cycle, hence the travel time of a particle through the icefall, a streamline (section 3.4).

4.3.8 Sub-pixel localization

In determining the highest value from the correlation surface, it is possible to estimate a subpixel localization when a small neighbourhood is taken into account. By taking the direct neighbours a parabolic (Argyriou and Vlachos, 2005) or Gaussian function (Nobach and Honkanen, 2005) can be estimated, respectively,

$$\Delta i = \frac{\Theta_{i+1,j} - \Theta_{i-1,j}}{2\left(2\Theta_{i,j} - \Theta_{i-1,j} - \Theta_{i+1,j}\right)}, \quad \Delta i = \frac{\ln\Theta_{i+1,j} - \ln\Theta_{i-1,j}}{2\left(2\ln\Theta_{i,j} - \ln\Theta_{i-1,j} - \ln\Theta_{i+1,j}\right)}. \tag{4.4}$$

This formulation is only in one dimension, but more advanced two dimensional estimations are possible as well. In general, when the spatial domain method is used, this peak is wide (figure 4.9(a)) and the estimation of the peak location can be one order more precise (Debella-Gilo and Kääb, 2011). However, this does not specify the shape of the peak. When the frequency domain method is used, the peaks within the correlation surface are very slim and steep (figure 4.9(b)). Here we formulate a linear formulation to describe the variance of the peak, which also considers the orientation. At a certain location in this search space (i, j) the Gaussian hat can be calculated through,

$$f(i,j) = A \cdot e^{\left(-(a \cdot (i-i_0)^2 + 2b \cdot (i-i_0 \cdot j-j_0) + c \cdot (j-j_0)^2)\right)}. \tag{4.5}$$

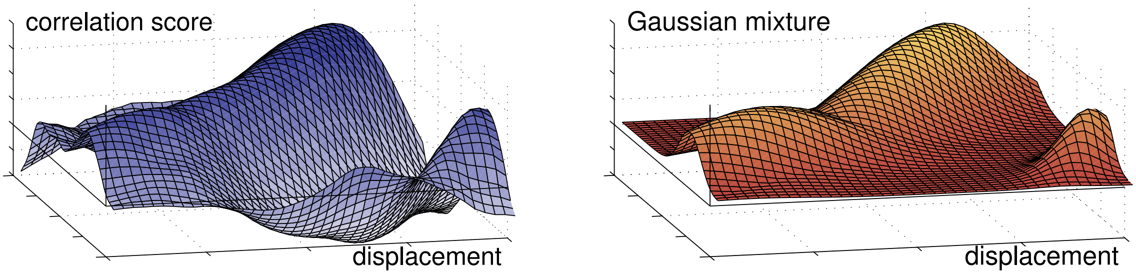

(a) spatial NCC (b) modelled Gaussians

Figure 4.12: (a) Correlation surface as a result of image matching. (b) the modelled Gaussians of the score surface, based on (a).

Here i_0 and j_0 denote the center of the top ($i_0 = i + \Delta i$), A the magnitude and a, b, c are constants. The center of the top can be estimated by a peak finding function (equation 4.4). The rest of the unknowns can be estimated in a second step, and after some rearrangement the following linear system of equations can be constructed:

$$\underbrace{\begin{bmatrix} \ln \Theta_{i-1,j-1} \\ \ln \Theta_{i-1,j} \\ \vdots \\ \ln \Theta_{i+1,j+1} \end{bmatrix}}_{\mathbf{y}} = \underbrace{\begin{bmatrix} 1 & (i\text{-}1\text{-}i_0)^2 & (i\text{-}1\text{-}i_0 \cdot j\text{-}1\text{-}j_0) & (j\text{-}1\text{-}j_0)^2 \\ 1 & (i\text{-}1\text{-}i_0)^2 & (i\text{-}1i_{-0} \cdot j\text{-}j_0) & (j\text{-}j_0)^2 \\ \vdots & \vdots & \vdots & \\ 1 & (i+1\text{-}i_0)^2 & (i+1\text{-}i_0 \cdot j+1\text{-}j_0) & (j+1\text{-}j_0)^2 \end{bmatrix}}_{\mathbf{A}} \underbrace{\begin{bmatrix} \ln A \\ a \\ 2b \\ c \end{bmatrix}}_{\mathbf{x}}. \tag{4.6}$$

This gives the possibility to directly estimate the unknowns through least squares adjustment. Then a, b, c can be reformulated to :

$$\hat{\rho} = -\frac{\hat{x}(2)}{\sqrt{\hat{x}(1) \cdot \hat{x}(3)}}, \quad \hat{\sigma}_i = \frac{\hat{x}(2)}{\hat{x}(1) \cdot 2(1\text{-}\hat{\rho}^2)}, \quad \hat{\sigma}_j = \frac{\hat{x}(2)}{\hat{x}(3) \cdot 2(1\text{-}\hat{\rho}^2)}. \tag{4.7}$$

Such estimations and similar solutions for point estimators (Zeisl et al., 2009) can be of use when co-variances of measurements are needed, as in Brinkerhoff and O'Neel (2017). In such a case probabilistic testing can be applied within block adjustments or other network estimations.

4.3.9 Biased estimates through peak locking

Computational advantages exist to use the frequency domain method over the spatial domain. However, there is one large disadvantage related to a bias inherent from the discretization of the signal and the allocations towards selected frequencies (Fincham and Spedding, 1997). This has an effect when sub-pixel location is estimated, through a parabolic, Gaussian or sinc-function. It causes the correlation score to favour whole integer values over other floating value. This effect, called peak-locking, (shown in figure 4.13) is proportional to the width of the correlation peak (Westerweel, 1997). When simple frequency domain methods are used, due to this effect, the precision of the displacement is in the range of half a pixel, which error estimate is also used in paper I. While spatial domain matching is able to achieve precisions in the order of $1/20$ of a pixel, which is used in paper III. This artifact can be overcome by calculating the sub pixel position directly in the frequency domain through an iterative procedure, see Rösgen (2003); Leprince et al. (2007).

4.3.10 Decision making in image matching

Choosing which candidate is the real displacement within the search space (Θ) is straight forward; the highest peak is the most likely candidate for the real match. However, competing peaks can be enhanced, with the support of neighbouring search spaces in space (Hart, 2000) or time (Altena and Kääb, 2017a). This is done by summation or multiplication of neighboring search spaces. The procedure relies on the assumption that displacement fields are gradual (low shear).

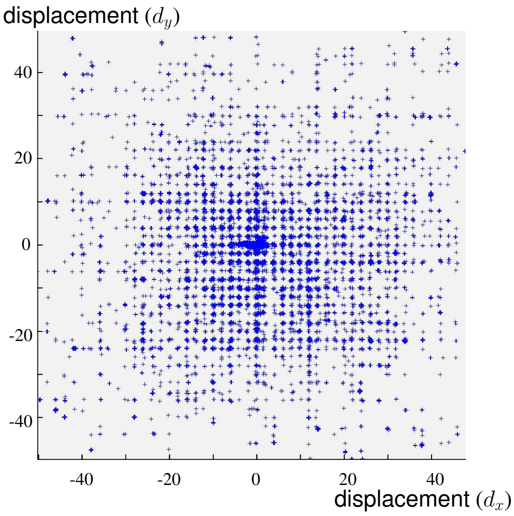

Figure 4.13: Distribution of sub-pixel displacements from frequency domain matching. This is from a typical displacement field, which in a normal case would resemble a smooth distribution (see inset in figure 4.19(b)), but this is not the case. Note the tendency towards whole integer values.

Information about the quality of the displacement-candidate can be extracted from the shape of the peak. The absolute value of the peak ($\Theta_{pq}(i_0, j_0)$) is an indication on success. The curvature or width (σ_i, σ_j) of the correlation peak, gives an indication on its precision. While the ratio between the first and the second peak, gives an indication about the uniqueness of the match in relation to other candidates.

4.3.11 Estimating detailed displacement using optical flow

When the displacement between two surface objects is small, other formulations than image matching (equation 4.3) are able to describe relative displacement. Such alternative approaches can be used for sub-pixel localization, or in the case of slow movement in respect to the acquisition interval. When within an image an intensity has a small displacement, this can be approximated by a first order Tayler expansion,

$$\mathbf{I}_{x+\Delta x, y+\Delta y} = \mathbf{I}_{x,y} + \frac{\partial \mathbf{I}}{\partial x}\Delta x + \frac{\partial \mathbf{I}}{\partial y}\Delta y. \tag{4.8}$$

Where **I** denotes the image, and x and y are the image coordinate axis. When these displacements $(\Delta x, \Delta y)$ are seen over time (t) the optical flow formulation appears, being (Horn and Schunck, 1981).

$$\frac{d\mathbf{I}}{dt} = \frac{\partial \mathbf{I}}{\partial y}\frac{\partial y}{\partial t} + \frac{\partial \mathbf{I}}{\partial x}\frac{\partial x}{\partial t}, \text{ where } \quad \nabla \mathbf{I} \cdot \mathbf{v} + \frac{d\mathbf{I}}{dt} = 0. \tag{4.9}$$

Here the velocities are concatenate together into a vector (**v**) and the first order derivatives simplified by ∇. The second part of this equation is known as the brightness-consistency, where the energy in two imagery should remain the same. The advantage of this formulation is its simplicity and its local formulation. It is possible to estimate the individual displacement for single or small groups of pixels. No large support region, as with pattern matching, is needed. However, the formulation is ill-posed and some regularisation is needed to constrain the estimation (known as the aperture problem). Secondly, the relation is based upon a Taylor approximation, thus the displacements should be within sub-pixel, if not, some pyramid or warping schemes should be applied. Glaciological applications for this technique are sparse, as the brightness consistency constraint cannot be met in practical data collection. Typically, the sun angle changes too much between acquisitions. However this limitation can be bypassed through a formulation of optical flow with second order derivatives (the Hessian, **H**), following Uras et al. (1988):

$$\underbrace{\begin{bmatrix} \frac{\partial^2 \mathbf{I}}{\partial x^2} & \frac{\partial^2 \mathbf{I}}{\partial x \partial y} \\ \frac{\partial^2 \mathbf{I}}{\partial y^2} & \frac{\partial^2 \mathbf{I}}{\partial x \partial y} \end{bmatrix}}_{\mathbf{H}} \underbrace{\begin{bmatrix} \frac{\partial x}{\partial t} \\ \frac{\partial y}{\partial t} \end{bmatrix}}_{\mathbf{v}} = -\nabla \frac{d\mathbf{I}}{dt}. \tag{4.10}$$

The only disadvantage is the use of higher-order derivatives, which need more neighbouring intensities and are typically more sensitive to noise. In paper II we start with the formulation of optical flow and develop a robust implementation, resistant to the shortcomings listed above.

4.3.12 Flow in the frequency domain

There are more formulations that can be of interest to perform in the frequency domain. For example, with these techniques it is possible to infer topography, as will be demonstrated in section 4.5.4. A vector field ($\vec{f}$) can be transformed into the Fourier domain and described as a set of frequencies, with a wave number ($\mathbf{k}$):

$$\vec{f}(\mathbf{x}) \xrightarrow{\mathscr{F}_2} \vec{F}(\mathbf{k}). \tag{4.11}$$

This is similar to polar coordinates formulation (i.e. $x = p\cos\theta, y = p\sin\theta$). From the origin of this spectrum and outwards the wavelength decreases. Hence filters working on the radial distance ($|\mathbf{k}|$) function as high-, band- or low-pass filters and are effective in highlighting glacial surface features within an image. A second property of interest is the de-compositional property of flow fields. An arbitrary flow field ($\vec{\xi}$) can be described as a composition of multiple vector fields; a curl-free (∇E) and a divergence-free ($\vec{W}$) part,

$$\vec{\xi} = (\nabla\vec{\varphi}) + (\nabla \times \vec{a}). \tag{4.12}$$

Where ∇,$\nabla\cdot$ and $\nabla\times$ denote the gradient, divergence and curl operator, respectively. Within the frequency domain this decomposition is a projection of the spectrum perpendicular to the origin. The curl-free part is a projection of the longitudinal component in the frequency domain and the divergence-free part is calculated through a transverse projection in the frequency domain. This Helmholtz-Hodge transformation is thus,

$$\mathscr{H} = -\frac{(\mathbf{k}\cdot F(\mathbf{k}))\mathbf{k}}{|\mathbf{k}|^2}. \tag{4.13}$$

4.3.13 Crevasse detection using the Radon-transform

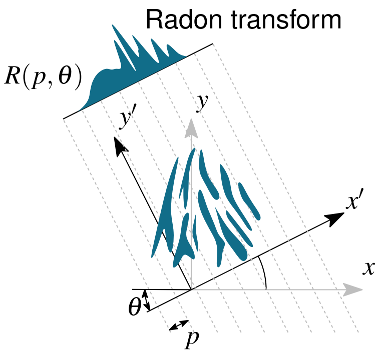

Figure 4.14: Schematic of a Radon transform for a coordinate frame (x', y') rotated by a given angle(θ).

Crevasses in the ice are another feature of ice flow and relate to current and past stress regimes (section 3.3.5). These elongated features have a specific structure, which is well observable in optical imagery. This texture can be detected by applying a Radon-transform. A Radon-transform is a parallel projection, where the coordinate system is rotated and a summation over the axis occurs. It can be formulated as,

$$R(p,\theta) = \int\int I(x,y)\delta(x\cos\theta + y\sin\theta)dxdy. \tag{4.14}$$

Here θ describes the rotation of the coordinate system ($\{x,y\} \rightarrow \{x',y'\}$), δ is a dirac-delta function and p is the axial distance from the origin. The concept of one such projection is illustrated in figure 4.14. When from every angle a transform is made, another image appears (known as sinogram, see figure 4.15). This sinogram will have local maximum variation where the intensities are aligned, as is the case with crevasses. In figure 4.15 the crevasses are both insets and are roughly at right angle of each other. Hence when the variation in the sinogram is assessed for each orientation, the group orientation of the crevassed area can be estimated.

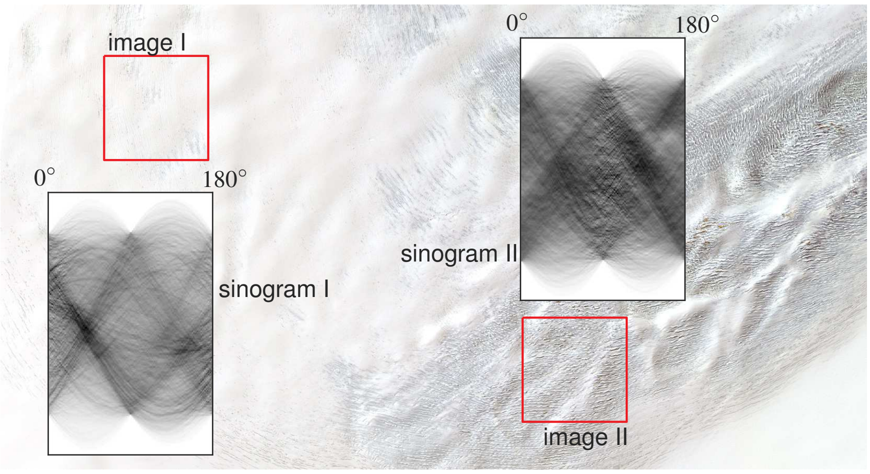

Figure 4.15: RapidEye image over the upperpart of Basin-3, Svalbard. Over this crevassed field, two insets are taken and the Radon-transform is applied for every angle of the halfcircle, resulting in two different sinograms.

Fourier-slice theory says a slice of the Fourier transform at a certain angle and the one-dimensional Fourier transform of a Randon transform are similar (Deans, 2007). Consequently, it is possible to do similar analysis directly in the frequency domain. However, due to the potential incompleteness of images, the Radon transform is preferred. The back-projection of a Radon transform is also possible. Such a formulation at a given angle is then,

$$F_\theta(x,y) = R(x\cos\theta + y\sin\theta, \theta). \tag{4.15}$$

When different Radon transforms from different aspects are present, a simple reconstruction can be obtained through summation, that is

$$F(x,y) = \sum_{\theta=0}^{\pi} F_{\theta}(x,y). \tag{4.16}$$

The Radon transform is related to the Fourier transform, as illustrated in figure 4.16. Here, the frequency domain is denoted by x and y instead of $\mathbf{k}$ to denote the implementation is done in a regular grid. Similarly, the θ and p describe a Fourier transform specified in polar coordinates. The transformation of both Fourier descriptions is done through interpolation. The advantage of this connection is that the high computational efficiency of the Fourier transform can be exploited for the inverse of the Radon transform.

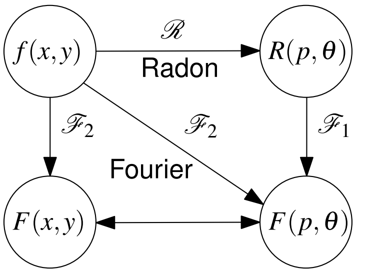

Figure 4.16: Schematic of the relation between the Radon transform ($\mathscr{R}$) and the one and two-dimensional Fourier transform ($\mathscr{F}_x$).

4.4 Post-processing

Displacement fields of glaciers are constructed from image matching, making use of the methods described above. However, these velocity fields include measurements with noise, systematic errors or outliers. Hence to be of use for analysis, post-processing is needed to remove, filter or adjust these products. The content described here forms the backbone of paper III.

Within remote sensing three configurations or groups in time-series analysis can be discriminated, see figure 4.17. State change is the simplest form, where typically abrupt change happens from one state to the other. For example, landslides or lake drainages in which a distinguished prior- and post- situation can be identified. When time-series image data are exploited, this first group can help in creating confidence in the occurrence and timing of a change, as they model a step function.

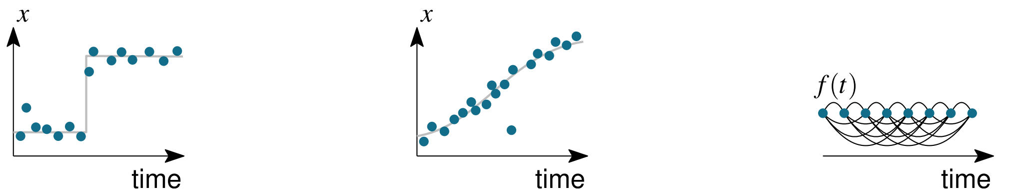

(a) state change (b) independent variable (c) dependent variable

Figure 4.17: Different relations of phenomena under study for post processing. (a)&(b) are properties which can be measured directly, while (c) extracts relational properties and thus several combinations are possible to extract the property.

A second group of estimating change is the direct observation of a variable over time. Think of the albedo of a surface, or other quantitative remote sensing measures. Here the time-series will follow a pattern or trajectory which can be used to detect outliers.

The third group is based on dependent measurements, where a combination of scenes is needed to extract the variable. Relational properties or relative measurements are extracted, an example is photogrammetric reconstruction. Generally, a single-view acquition is not able to reconstruct topography, for this case multiple acquisitions are needed. Because a single measurement is dependent on others, the complexity of combinations will increase when time-series expand. One is able to construct a network, where acquisitions are connected through these dependencies. In this way redundant measurements will be present in the data, and this will be the topic of this section.

Redundant measurements are of interest as they can increase the accuracy of an estimate. When the distribution of measurements is Gaussian the precision increases especially at small sampling sizes ($\sqrt{N}$). An increase in connected measurements also improves the reliability of an estimate. When more measurements are available, the model to work with can be more sophisticated. However this will also increase the sensitivity to outliers. Hence, the amount of success of a method heavily depends on the amount of contamination, that is, measurements which are not describing the flow regime of a glacier but something else (clouds, noise, shadows, etc.). Thus the quality of the data are the main drivers in deciding which post-processing strategy to take.

4.4.1 Characteristics of glacier displacement data

Several post-processing implementations will now be introduced, in order to compare these, the same velocity field will be used over Walsh Glacier in the Saint Elias Mountains. The velocity field is derived from a Landsat 8 image pair in winter with a 16 days interval, as part of the GoLIVE dataset (Scambos et al., 2016). At this time the Walsh glacier has just started its surge (paper III) and because of the winter it is snow-covered and has many shadow-cast features in both scenes. To get an idea of the data, one input image and the magnitude of the derived velocities are given in figure 4.18.

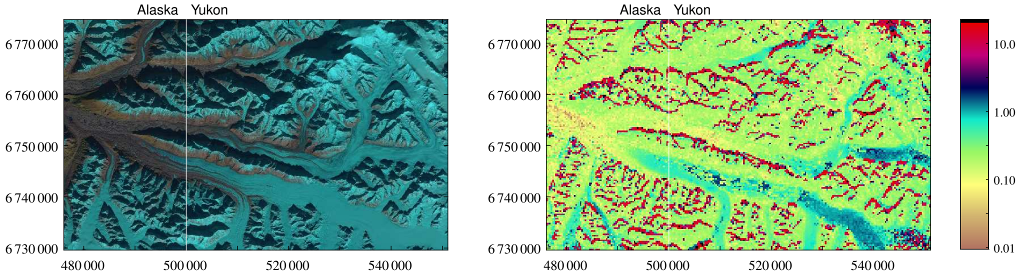

(a) Landsat acquistion

(b) velocity in meters per day

Figure 4.18: Image and velocity data over Walsh Glacier, Alaska-Yukon border. This data is used for post-processing in this section. Figure 4.18(a) is a Landsat8 acquistion from 6th of October 2016, figure 4.18(b) is a displacement field from the GoLIVE dataset, in March 2014.

When an image pair is matched, the resulting vector field can be seen as a distribution. An example of such a distribution is plotted in figure 4.19(a), as a one-dimensional histogram. What becomes apparent in this illustration is that the distribution has large tails and a sharp peak. Hence normal statistical measures might therefore not be sufficient to detect outliers.

When looking at the distribution in two dimensions, such a dataset can also be plotted as a scatter-plot, as in figure 4.19(b), where every vector is represented as a point in space. By eye, three different patterns can be identified within the scatter: first, a major trend is present scattering in one predominant direction, this is systematic error within displacement fields due to the tracing of shadows. Most satellites with optical instruments have a near-polar orbit, hence the local time of an overpass is stable, at this case around 10:00 local time (figure 6.5). Consequently, the azimuth (150°) is stable, but the elevation of the sun changes seasonally. This effect can be small and subtle for rough topography (Berthier et al., 2005), but large apparent displacements occur when the shadows of mountain tops are followed. Such displacements infect the sample because the contrast of the shadow dominates all other information when the shadow is casted on a white snow field. However, this metadata can be used as prior knowledge and thus used in the statistical analysis. Displacements with the same bearing as the sun's azimuth are uncertain members of the glacier displacement cluster.

Secondly, a regular pattern around the border can be observed in the distribution of figure 4.19(b), this is due to a technical issue. The sub-pixel estimation used for the velocity field applies a spline function, hence a neighbourhood needs to be present, which is not the case at the border of the search domain. Consequently, the three rows forming a window around the border have no sub-pixel estimation. When looking at the zoom-in panel more advanced clusters appear. Here, the data stems from the displacement field which has tributaries, turns, etc.

Then, fourth, the final pattern is a random scattering of points covering most area of the two-dimensional histogram, without any coherent structure in the neighbourhood. These points are most presumably not valid displacements, but rather the outliers, i.e. the measurements which are not of interest.

In the following section several relations will be explored. Because glacier displacement is a related property, the assessment for correctness should also be related to its neighbourhood. This neighbourhood can be formulated in different ways, rigid or adaptive. In the adaptive version the neighbourhood is selected through the form of the data. This approach is known as object-based, and segments the data into distinct regions with similar behaviour. Seeding points are initiated to then grow into a region, while updating its statistics and its merger rules (Rosenau et al., 2015; Lüttig et al., 2017). However, as we are dealing with a fluid, this approach is not taken here, as glacial ice has, apart from its boundary, no clear regions. Hence, the rigid procedure is applied here, where a neighbourhood consists of a rectangular window around a point.

4.4.2 Heuristical testing of outliers

As was just shown, a simple scatter plot can already show outliers, however no verdict or impeachment is made. This decision making can be done through the use of statistical measures.

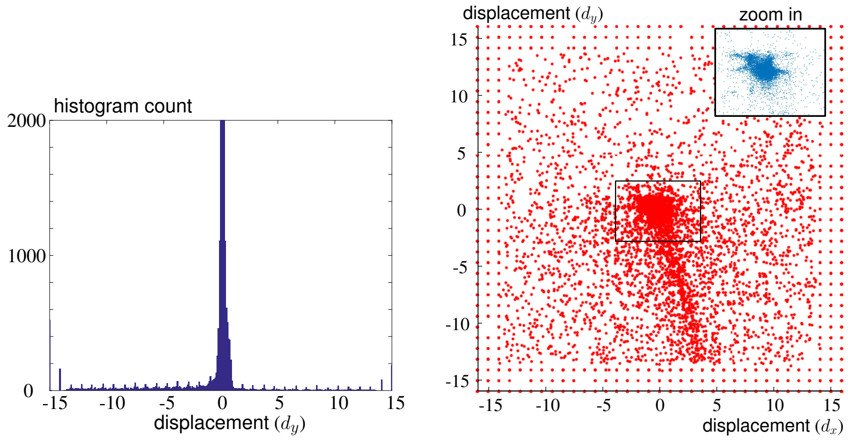

(a) one dimension

(b) two dimensions

Figure 4.19: Examples of distributions of a derived vector field, as in figure 4.18(b).

A simple and effective measure is the so-called Wald-test. It gives a score on the expectation how good a displacement (d_i) falls within the distribution made up by its neighbourhood,

$$w = \frac{(\underline{d_i} - \bar{d}_i)^2}{\mathrm{var}(d_i)}. \tag{4.17}$$

In this case a Gaussian distribution is assumed, then the threshold for w is mostly taken at 3.29, corresponding to 3σ (Baarda, 1968). The neighbourhood can be of variable size, however, most of the times an extended neighbourhood is used, to have a sufficient sample size. However, the displacement measurements are corrupted heavily with gross-errors. Hence, more robust statistical measures might be more suited, and give a more vigorous discordancy test. Thus, if the mean and variance are replaced by the median and median of absolute difference (mad), on gets the Hampel-identifier,

$$h = \frac{|\underline{d_i} - \mathrm{med}(d_i)|}{\mathrm{mad}(d_i)}. \tag{4.18}$$

The statistical heuristics given above are the type of post-processing currently implemented for the filtering of large collections of glacier displacement data (Scherler and Strecker, 2012; Dehecq et al., 2015). This statistical testing is very general and has a limited level of complexity. Therefore it is of interest to look at the performance of other approaches which formulate tighter constraints through flow specific features.

4.4.3 Testing through data-driven methods

The amount of sophistication of post-processing is largely dependent on the a-priori constraints. Statistical measures are abstract properties, where the displacements are seen as a plain distribution. Because of their simplicity these measures are very robust to detect gross-errors. Another approach is to make use of the vast amount of displacement estimates and rely on the property that ice flow has a coherent structure. In such cases the distribution does not have to be known and data driven methods can be used. The benefit is their ability to adopt to different probability functions and, for some, their applicability to higher dimensional datasets.

A simple method building upon the distribution method is the use of a bagplot (Rousseeuw et al., 1999), a bivariate boxplot. Its normal implementation is computational expensive, hence for sake of simplicity the centre is in this implementation given by the median. A second component is the bag (or convex-hull) that contains 50 percent of all displacements. A homogeneous dilation increases the spread of the bag, known as fence, to include a wider range of displacements. The advantage of this method is its adaptability to the spread in different directions. Such a procedure is applied on the Walsh velocity data set and shown in figure 4.20(a). Most of the shadow-cast outliers are removed, but the smaller fluctuations and noise are still present in the data. The drawback of this approach is the assumption of one distribution, while there may be several in the displacement data set.

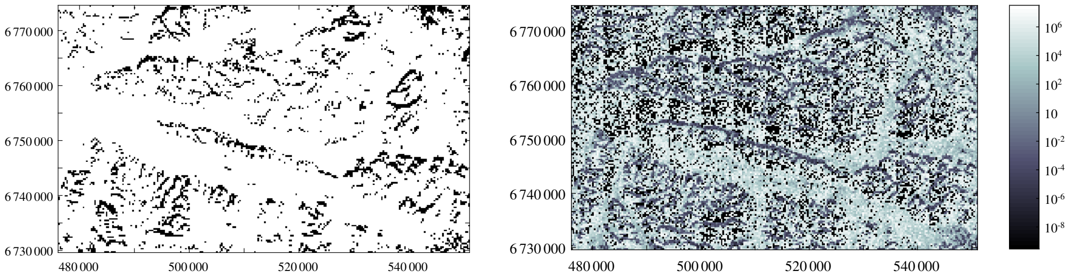

(a) outliers through bagplot (b) angular outlier detection

Figure 4.20: Results of data-driven outlier detection methods over the Walsh dataset of figure 4.18(b).

Another property that can be exploited is the relationship of each point with its neighbours. For example, taking the relative angle between a point in displacement space (d_x, d_y) and its neighbours, an outlier will have a distribution with a tendency towards a certain direction. While an inlier will have no clear favour for direction, as illustrated in figure 4.21(a). This angle-based distribution property can be used to detect outliers (Kriegel et al., 2008), as is done in figure 4.20(b) for the case of the Walsh dataset.

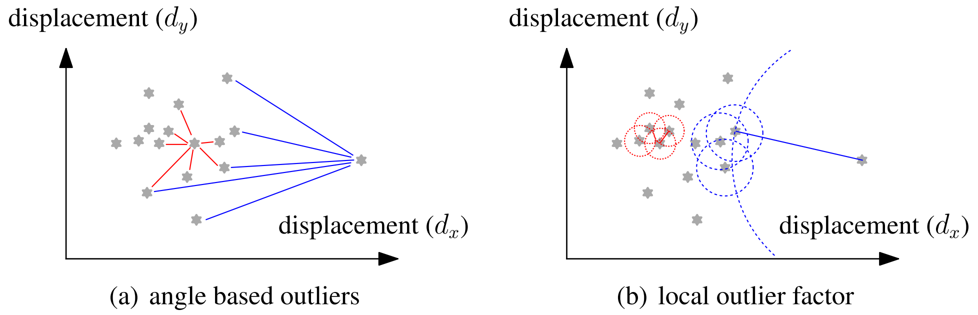

(a) angle based outliers (b) local outlier factor

Figure 4.21: Metrics to describe outliers, by their collection of orientations of relative angles (4.21(a)) between an inlier (red) and an outlier (blue), or through the local density (4.21(b)) of their neighbouring points.

Another mapping to detect outliers is through the use of density. Typically, displacements are grouped together, as can be seen in figure 4.19(b). Therefore, if the distance of the nearest neighbour for each displacement is estimated, the distance of these neighbours can be calculated. This working principle is illustrated in figure 4.21(b) and called local outlier factor (Breunig et al., 2000). The results are shown in figure 4.22(a). Its effectiveness is hampered by the fact that shadow-cast displacements are also grouped together, which is also the case for displacements at the border of the domain, as these do not have a sub pixel position and rounded towards nearest integer value. The latter can be omitted, but still the method can only detect outliers, which are due to coherence loss (random).

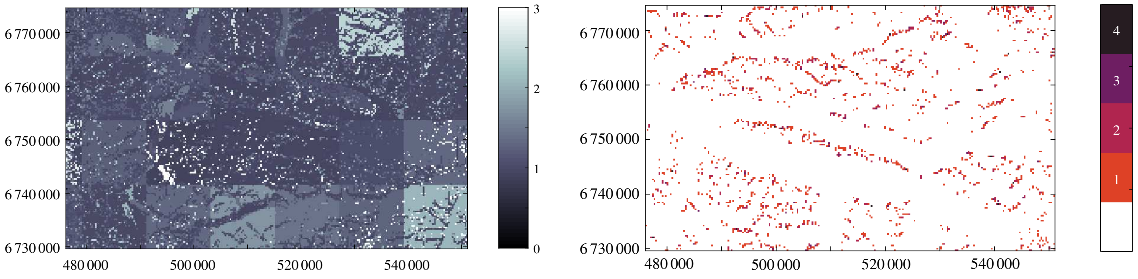

(a) local outlier factor (b) leap frog detection

Figure 4.22: Results of data-driven methods over the Walsh dataset.

4.4.4 Contextual drivers of glacier flow

The local context around a displacement can also be used. When a displacement field over a glacier is estimated, the field can be used to advect particles along. If the velocity field is without any error, the traveled paths will not cross. Thus the lines describing the displacement will not leap-frog over each other. Such an operation is shown in figure 4.22(b). This method is depended on the amount of displacements and the sampling interval, as turns in the flow will also cause crossings. However, the amount of violations in respect to each neighbourhood can be used to detect the outliers. Though, when the neighbourhood is heavily contaminated this procedure will break down.

Most matching approaches described above perform every matching operation completely independent of each other. One methodology that does take the context of its surrounding into consideration during post-processing is relaxation labelling. It drives on the principle that initially certain regions within a dataset have high confidence, which helps to support decision making in their direct surrounding. This context spreads with each iteration step, hence this method is robust to single or small groups of outliers (Price, 1985). Relaxation labelling is a local iterative scheme that uses comparability relationships to enhance coherent interpretations and eliminate inconsistent combinations. A compatibility function (with scores of $[-1 \ldots 1]$) describes the relation between neighbouring locations (i,h) with a certain label (j,k), as illustrated in figure 4.23. The label in our case is a potential displacement vector ($\mathbf{d}$), and its compatibility (c) is solely dependent on the relative angle, such that:

$$c(i,j;h,k) = \frac{\langle \mathbf{d}_{ij}, \mathbf{d}_{hk} \rangle}{\|\mathbf{d}_{ij}\| \cdot \|\mathbf{d}_{hk}\|}. \tag{4.19}$$

Every location will have a selection of labels with an associated likelihood. The correlation coefficient makes it possible to assign *a-priori* weights to this framework, or express relative preference to candidates (Vosselman, 1992). Even a no-match candidate can be included (Wu, 1995), however we omit this as for our case the purpose is to extract a ranking. Transforming the

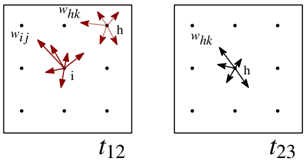

Figure 4.23: Nomencalture of the different symbols used within the relaxation labelling.

correlation scores to membership preferences (w) is done by normalization over all (m) candidates, where the exponent is used to exaggerate the difference between high and low correlation scores (ρ);

$$w_{ij}^{(0)} = \frac{\rho_{ij}^2}{\sum_{j=1}^{m} \rho_{ij}^2}. \tag{4.20}$$

However, this normalization of weights suppresses the absolute confidence of a match. For example, a location with only low correlation scores has similar influence to its neighbour with high correlation score. Hence, the introduction of a neighbourhood confidence coefficient (C) keeps the confidence information by strengthening or weakening importance, in our case based on the correlation coefficient. Furthermore, the convergence of the labelling can be slow, but sped up by a power function (κ) (Kittler and Illingworth, 1985). Then the support (q) can be written as;

$$q_{ij}^{(r)} = \frac{1}{n-1} \cdot \sum_{\substack{h=1 \\ h \neq i}}^{n} C_{ij} \cdot \left(\sum_{k=1}^{m} c(i,j;h,k) \cdot w_{hk}^{(r)} \right), \quad \text{where } C_{ij} = \frac{\rho_{ij}}{\sum\limits_{j=1}^{n} \rho_{ij}}. \tag{4.21}$$

Then at every iteration (r, and within parenthesis) the membership preferences (w) are updated,

$$w_{ij}^{(r+1)} = \left[\frac{w_{ij}^{(r)} \cdot (1 + q_{ij}^{(r)})}{\sum_{j=1}^{m} w_{ij}^{(r)} \cdot (1 + q_{ij}^{(r)})} \right]^{\kappa}. \tag{4.22}$$

Relaxation labelling has not been extensively used in glaciology (Evans, 2000; Altena et al., 2015). However it is an interesting approach as it takes the matching score into account and is non-linear. This can be of benefit for multi-temporal datasets in, for example, the creation of mosaics. Such an example for the Walsh dataset (figure 4.18(b)) from five velocity fields is shown in figure 4.24(b). The voting for the velocity field used in prior examples is shown in figure 4.24(a). The new velocity field has less high velocity outliers, but still these occur scattered through out the mosaic. Over stable terrain, the labelling does work but in these places the matching is in general easier. Patches of correct velocities seem to be apparent in the data, but not at every location. This might be due to an absence of correct velocity in the stack at that position, but the labelling is forced to select an estimate from the stack.

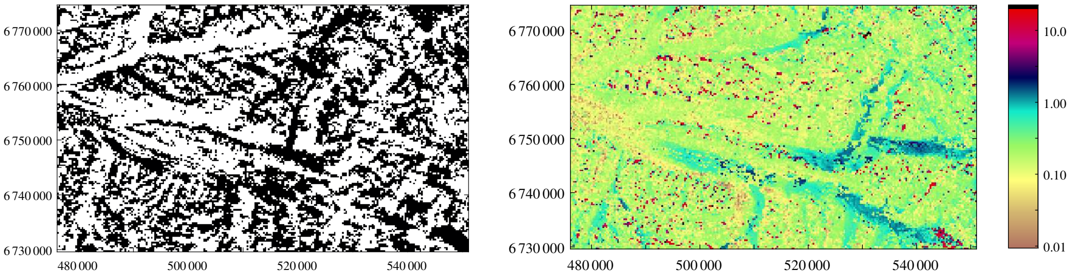

(a) highest vote

(b) mosaic based on relaxation labelling

Figure 4.24: Result of relaxation labelling of five velocity fields over Walsh glacier.

4.4.5 Testing through glacial flow characteristics

The former sections described methods based upon patterns within the data. A second group of approaches are physically-based post-processing procedures for glacier displacement fields, several of these will now be described. Ice is a fluid, hence its flow can be described by the Navier-Stokes equation. This system of equation describes fluid motion through the force interaction caused by pressure, inertia and viscosity. However, for our case only the viscosity is known to some extent and thus the only parameter to constrain surface velocity. The flow resistance of ice (η, molecular or dynamic viscosity) can be related to shear stress (τ), through the Glen-Steinemann's flow law,

$$\eta = \frac{1}{2}\left(A(T)\tau^{n-1}\right)^{-1}. \tag{4.23}$$

Here $A(T)$ is the Arrhenius flow coefficient and dependents on temperature, and where the Glen's flow parameter (n) is set to a constant value of 3. Because the shear stress increases with depth, the velocity magnitude is related to depth ($|u| \propto H^4$ and see equation 3.7). However, with remote sensing only the surface velocity can be observed and for most glaciers the ice thickness is unknown. But for iceshelfs and icestreams the depth-to-width ratio reverses and slope decreases (Truffer and Echelmeyer, 2003). Therefore, the horizontal velocity component becomes more important. Consequently, the viscosity can be reduced to a formulation which only includes planar velocity terms (MacAyeal, 1989),

$$\eta = \frac{1}{2}A(T)^{-1./n}\left(\frac{1}{4}\left(\frac{\partial U}{\partial Y}+\frac{\partial V}{\partial X}\right)^2+\frac{\partial U}{\partial X}\frac{\partial V}{\partial Y}+\frac{\partial^2 U}{\partial X^2}+\frac{\partial^2 V}{\partial Y^2}\right)^{\frac{1-n}{2n}}. \tag{4.24}$$

Another relation that describes the mechanical fluid forces is the Burgers' equation,

$$\begin{aligned} \frac{\partial U}{\partial t} + U\frac{\partial U}{\partial x} + V\frac{\partial U}{\partial y} &= \frac{1}{\mathrm{Re}}\left(\frac{\partial^2 U}{\partial x^2} + \frac{\partial^2 U}{\partial y^2}\right), \\ \underbrace{\frac{\partial V}{\partial t} + U\frac{\partial V}{\partial x} + V\frac{\partial V}{\partial y}}_{\text{advection}} &= \underbrace{\frac{1}{\mathrm{Re}}\left(\frac{\partial^2 V}{\partial x^2} + \frac{\partial^2 V}{\partial y^2}\right)}_{\text{diffusion}}. \end{aligned} \tag{4.25}$$

Here Re stands for the Reynolds-number, which is a scale-free parameter to relate different fluid problems to one and another. A simple estimate of its order can be done through,

$$\mathrm{Re} = \frac{\bar{U}z}{\nu}. \tag{4.26}$$

Here in the numerator z is depth or characteristic length and $\bar{U}$ the mean velocity. In the denominator is the kinematic viscosity (ν), which is dependent on density (ρ), that is $\eta = \nu/\rho$. For example taking the case for the Grosser Aletsch Glacier, Switzerland, (Deeley, 1908), the ρ is 0.9177 m^3 /kg, $\bar{U}$ is 4.7×10^{-5} m/s, z is 450 m and ν of 2×10^{13} kg/m s^2. Because of this high viscosity the Reynolds number becomes a very small number. For glacier displacements this is very problematic, as this inverse Reynolds term blows up the diffusion part of the Burgers' equation. Furthermore, the equation is non-linear so difficult for test directly. A third relation which can be formulated is the assumption of ice incompressibility, which gives,

$$\frac{\partial U}{\partial x} + \frac{\partial V}{\partial y} + \frac{\partial W}{\partial z} = 0. \tag{4.27}$$

When stable flow is assumed, the velocity does not change over time and the last term on the left hand side becomes zero. Else, this vertical term is still small, nevertheless it will increase when rapid change is occurring as in a glacier surging. The relations given above are advanced fluid formulations, however they are special cases of the more complicated Navier-Stokes equations. In order to be of use in the post-processing of velocity fields, these need to be formulated into a testing scheme. The idea for this case is to write these equations into a linear fashion, or into a linearized version. Then, these relations can be tested and outliers might become visible. Therefore, the first step in this procedure is to write the spatial strain and stress as a linear combination. Ideally with corresponding variance estimates ($\mathbf{Q}_y$, i.e.: equation 4.7),

$$\begin{bmatrix} u_{i,j\text{-}1} \\ u_{i\text{-}1,j} \\ u_{i+1,j} \\ u_{i,j+1} \\ v_{i,j\text{-}1} \\ v_{i\text{-}1,j} \\ v_{i+1,j} \\ v_{i,j+1} \end{bmatrix} = \begin{bmatrix} \text{-}1 & 0 & 0 & 1 & 0 & 0 & 0 & 0 \\ 0 & \text{-}1 & 1 & 0 & 0 & 0 & 0 & 0 \\ 0 & 0 & 0 & 0 & \text{-}1 & 0 & 0 & 1 \\ 0 & 0 & 0 & 0 & 0 & \text{-}1 & 1 & 0 \end{bmatrix} \begin{bmatrix} \partial u_{i,j}/\partial x \\ \partial u_{i,j}/\partial y \\ \partial v_{i,j}/\partial x \\ \partial v_{i,j}/\partial y \end{bmatrix}, \quad \mathbf{Q}_y = \begin{bmatrix} \sigma_0^2 \mathbf{I} & \rho \mathbf{I} \\ \rho \mathbf{I} & \sigma_0^2 \mathbf{I} \end{bmatrix}. \tag{4.28}$$

Here, for simplicity the values within the design matrix are ones, however these should be scaled according to their respective grid spacing. Furthermore, the entries within the covariance matrix can be taken from the Gaussian hat estimation, as described in equation 4.7. The matrix formulation in equation 4.28 can be used to describe incompressibility (4.27) as a linear system of equations. In such a case the last term becomes zero and can directly be estimated by summing the first and last columns of the design matrix. This equation is an implicit form, hence the incompressibility can be formulated as an conditioned linear model,

$$\mathbf{B}^{\top} \underline{\mathbf{y}} = \underline{\mathbf{t}}. \tag{4.29}$$

Then this relation can be used to do testing, following Teunissen (2000):

$$\underline{\hat{\mathbf{e}}} = \underbrace{\mathbf{Q}_y \mathbf{B} \left(\mathbf{B}^{\top} \mathbf{Q}_y \mathbf{B} \right)^{-1} \mathbf{B}^{\top}}_{P_{Q_y B}} \underline{\mathbf{y}}, \quad \mathbf{Q}_{\hat{e}} = P_{Q_y B} \mathbf{Q}_y. \tag{4.30}$$

In a similar way the MacAyeal-approximation for iceshelfs can be formulated, moving all known parameters to one side,

$$\eta = \frac{1}{2} A(T)^{\text{-}1/n} \left(\frac{1}{4} \left(\frac{\partial U}{\partial y} + \frac{\partial V}{\partial x} \right)^2 + \frac{\partial U}{\partial x} \frac{\partial V}{\partial y} + \left(\frac{\partial U}{\partial x} \right)^2 + \left(\frac{\partial V}{\partial y} \right)^2 \right)^{\frac{1-n}{2n}}, \tag{4.31}$$

$$\left(\frac{2\eta}{A(T)^{\text{-}1/n}} \right)^{\frac{2n}{1-n}} = \frac{1}{4} \frac{\partial U}{\partial y} \frac{\partial U}{\partial y} + \frac{1}{2} \frac{\partial U}{\partial y} \frac{\partial V}{\partial x} + \frac{1}{4} \frac{\partial V}{\partial x} \frac{\partial V}{\partial x} + \frac{\partial U}{\partial x} \frac{\partial V}{\partial y} + \frac{\partial U}{\partial x} \frac{\partial U}{\partial x} + \frac{\partial V}{\partial y} \frac{\partial V}{\partial y}, \tag{4.32}$$

$$\left(\frac{2\eta}{A(T)^{-1/n}}\right)^{\frac{2n}{1-n}} = \frac{1}{4}\frac{\partial U}{\partial y}\frac{\partial U}{\partial y} + \frac{\partial U}{\partial x}\frac{\partial U}{\partial x} + \left(\frac{1}{2}\frac{\partial U}{\partial y} + \frac{1}{4}\frac{\partial V}{\partial x}\right)\frac{\partial V}{\partial x} + \left(\frac{\partial U}{\partial x} + \frac{\partial V}{\partial y}\right)\frac{\partial V}{\partial y}. \quad (4.33)$$

This relation stays non-linear, hence linear testing is not possible. However, the estimation of the derivatives can be done with different kernels. Hence, these filter banks will be used to assess the different velocities. The concept behind this approach is that if an outlier exists, it will directly contaminate the estimate. But the opposite is also true; when all estimates are correct the estimate will be close to the expected viscosity term. Hence, derivatives can be formulated through different kernels. When a correct estimate is calculated, the contributing measurements can be traced back through the design matrix of equation 4.28. Such measurements are then flagged as correct. This approach is different from normal practice, as it is an optimistic view rewarding inliers instead of hunting for outliers.

The advantage of such formulation is their relation to the physical world. Parameters such as the viscosity, even though it changes with temperature and pressure, can be adjusted to a range that makes physical sense. For both functions the result for the Walsh dataset are shown in figure 4.25. The iceshelf testing is done on a glacier section, hence not many inliers can be expected. Nevertheless, the influence of a single outlier can be seen, as patches of correct estimates are crossed by elongated inlets or crosses. These patterns are less apparent when the incompressibility is tested, where much of the shadow-cast velocities are excluded. Also some on-glacier outliers are detected.

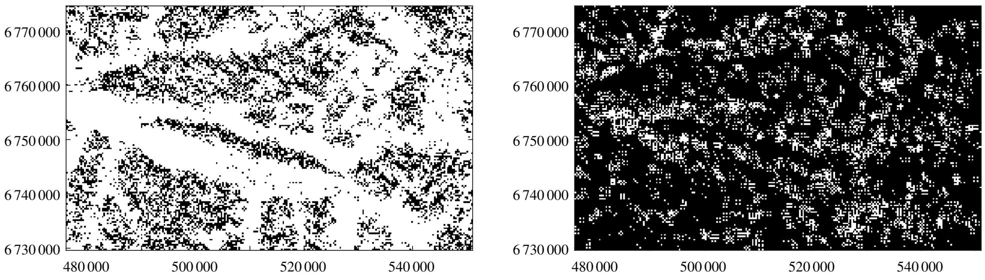

(a) incompressibility (b) iceshelf viscoscity

Figure 4.25: Testing of the incompressibility and iceshelf property, over the Walsh displacement dataset (figure 4.18(b)). Black indicates disagreement, while white means agreement between model and measurements.

Another approach, is to iterate to a solution given by a velocity and a model, such as Burgers (4.25). It is similar to a Navier-Stokes assimulation as given by Maksymiuk et al. (2016). Again it is not possible to do straightforward testing because of the non-linear Navier-Stokes relation, however it is possible to iteratively optimize the measurements to be in accordance with the fluid model. For such an approach it is possible to use alternating least squares. This is an iterative scheme that subdivides the unknowns in two groups, being part of the design matrix and another being part of the unknowns. After estimation of the unknowns, the roles are reversed (or alternated) and the other group is estimated.

4.4.6 A voting scheme through the Hough-transform

The velocity estimation can be formulated as a system of equations as in equation 4.29, see paper I. However, such linear least-squares formulations are very sensitive to multiple outliers. Another strategy is thus a voting scheme, where a functional model is used and the option with the most agreement is chosen. For example, such voting can be done through <u>ran</u>dom <u>s</u>ampling <u>a</u>nd <u>c</u>onsensus (RANSAC), a trial and error approach. However, another option is to discretise the parameter space, and use this as a voting space. This is known as the Hough-transform. Thus for a simple network of three images and three estimated displacements from them, the network will have the following equations:

$$\begin{aligned} y_{12} &= x_a + 0, \\ y_{23} &= 0 + x_b, \\ y_{13} &= x_a + x_b. \end{aligned} \tag{4.34}$$

These are line equations, and can also be formulated differently as polar coordinates,

$$\begin{aligned} y_{12} &= x_a \cos\theta_{12} + x_b \sin\theta_{12}, \\ y_{23} &= x_a \cos\theta_{23} + x_b \sin\theta_{23}, \\ y_{13} &= x_a \cos\theta_{13} + x_b \sin\theta_{13}. \end{aligned} \tag{4.35}$$

The striking aspect is the similarity with equation 4.14. Hence, the whole estimation can be seen as an inverse Radon-transform, where back-projection will result in a similar system. When only a single displacement is measured, there will be a right angle in equation 4.15. But when displacements over a longer time interval are taken, the angle will change and the axis will tilt. Now, the specification of the Radon-transform has a Dirac delta function within, which is a normal distribution with a variance approaching zero. This is an ideal case and for our estimates it is of importance to include some noise, so neighbouring positions in the parameter space get support as well. Therefore, the Dirac function is loosened to a normal distribution with variance, but other distributions are possible as well. Such an example is given in figure 4.26.

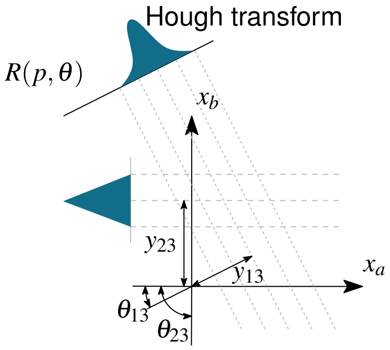

Figure 4.26: Schematic of a Hough transform. However, it can also be seen as a Radon transform, where a coordinate frame (x',y') is rotated by a given angle(θ).

The advantage of this approach is its resistance to multiple outliers and ability to handle large collections of displacement estimates from different time intervals, therefore this approach is used in PaperIII.

4.4.7 Reducing the effect of data-voids in displacement fields

The relations given in the former sections rely on information from the direct neighbourhood, mostly derivatives in both directions. However, remote sensing data is hampered by data voids, complicating steps towards model integration or advanced product generation. If the data has "salt-and-pepper" noise, this can be bypassed through the use of writing the convolution out fully, as is done in section 4.4.5. Different template filters, as described in section 4.2.2, can be used to estimate derivatives.

Morphometric analysis of glacier flow relies on derivatives of flowfields, such as local convergence and divergence (Ng, 2015). Such parameters can help in understanding the genesis of streaklines on icestream, which seem to form through an uneven bed (static) or sticky spots (dynamic over time) within parallel glacier flow (Ely et al., 2017). For such analysis the derivatives need to be as complete as possible, therefor a methodology is presented here which aims towards this goal.

The property exploited in this method is the redundancy of the kernel used to estimate the derivative in each direction. Within the neighbourhood multiple entities are used, thus this re-

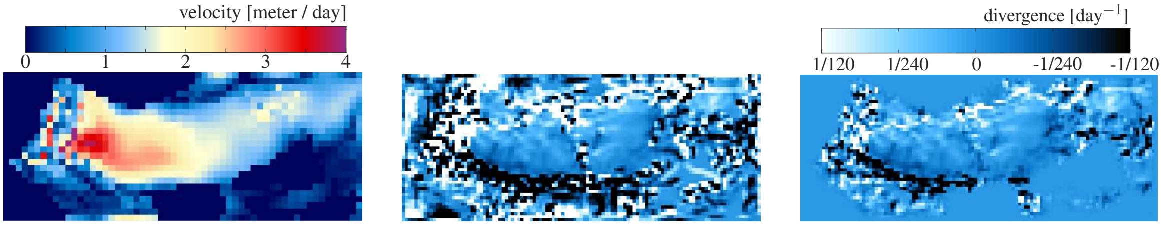

(a) Kronbreen summer speed (b) divergence with noise (c) divergence resistant to noise

Figure 4.27: Incomplete velocity estimate over Kronebreen glacier, Svalbard. For this velocity data the divergence is estimated normally (figure 4.27(b)) and through a method which is, to some extent, resistant to data voids (figure 4.27(c)).

dundancy can be exploited. The distribution of these entities in the kernel can vary, though the result should have a similar amount of energy. For example for a Prewitt kernel (see section 4.2.2) the summation is zero over all entities. However, when gaps occur in the neighbourhood, this energy balance is disrupted. Consequently, this lost energy should be added to one side, or reversely, taken away by the other. When the convolution is written out directly in matrix form, this allocation of energy is done by column-wise operators. If the neighbourhood is out of balance, the kernel is not estimated. An example of such an implementation is shown in figure 4.27. The estimated velocity field has some small outliers within, and these have effect on the surrounding estimates. However improvement is made on a local level. It does not solve all, as when large parts are affected, or the outlier detection is false, fluctuations are still present.

4.5 Applications for glacier surface velocity products

In the following section some applications for velocity fields will be given. The emphasis on these examples is foremostly concentrated on products which can be solely constructed from the methods given above. Other uses of products which can be derived from velocity data are possible, however these applications mostly require topographic or other auxiliary data as well. These will not be covered here for sake of brevity.

4.5.1 Crevasse mapping

When glacier topography (bed and surface) and meteorological information is sufficient, one might be able to use sophisticated fluid mechanical or finite element models to simulate the

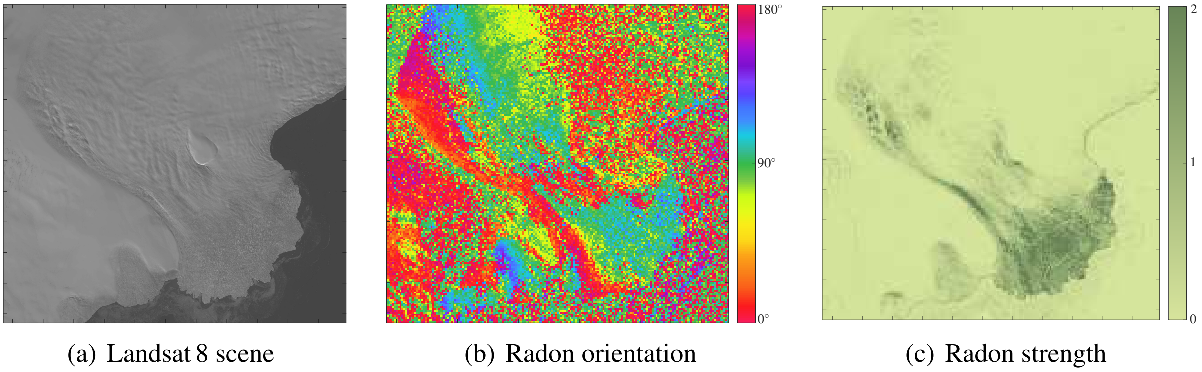

(a) Landsat 8 scene (b) Radon orientation (c) Radon strength

Figure 4.28: Crevasse detection over Basin-3, Svalbard through a Landsat 8 scene using the Radon transform.

dynamics of a glacier. Such models use measurements over time (borehole temperatures, atmospheric forcing, elevation change, velocity) as input to estimate unknown properties of interest, such as basal slip, and ice temperature. However, when all these parameters are included into the model, the possibility to check if a model run is valid becomes limited. Hence, crevasses can be a means to test if the model does represent the observations. Crevasses occur when a certain threshold is passed (depending on strain-rate and temperature (Vaughan, 1993)) and typically seem to last for 1-2 years (Harper et al., 1998). This secondary property of glacier flow is a deliverable of such model runs. So the stress field of a glacier can be extracted from a fluid mechanical model run and checked against the spatial distribution of crevasses. Or for the case with finite element models, the elements which are separated and form a crevasse, need to be in the same orientation as is observed (Gong et al., 2017).

The use of crevasse distribution has up to now only been used in a descriptive way to support theories in glacier dynamics. Extraction of such fields from remote sensing data was done in a manual manner, which is subjective and time consuming. Hence, an automatic workflow is needed if crevasse distributions are used as a validation tool for model output. By the use of the Radon transform (section 4.3.13) this is possible and the results for the Basin-3 glacier, Austfonna, Svalbard, are shown in figure 4.28. The product gives an areal estimate which can be related to mechanical damage, which can be a model output. But no individual crevasses are mapped, if this is needed then another more object-oriented analysis method needs to be implemented, such as for example is demonstrated in Stumpf et al. (2013).

4.5.2 Ogive formation

Ogives are periodic alternating features observable on the glacier surface. Three types of ogives exist: wave-, band- and sedimentary ogives. Wave ogives are topography undulations forming underneath certain icefalls, see figure **??**. The topographic amplitude of these undulations decays exponentially (Nye, 1958). Band ogives are alternating zones of dark and bright ice. It is stipulated that albedo effects further increase the contrast between bright and dark bands (King and Lewis, 1961). Recent high-temporal terrestrial laser measurements seem to confirm this process (Gabbud et al., 2015). Sorting of albedo values seems to take place in the first decade after creation (Anderson et al., 2017), related to the melting and folding structure which is generated by the icefall.

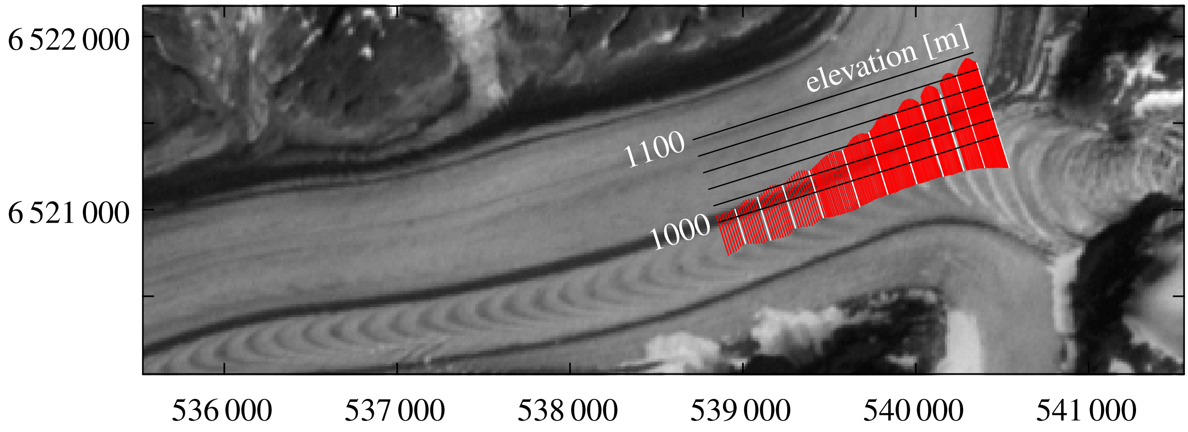

Figure 4.29: Ogives on Vaughan-Lewis glacier, Alaska, observed by Landsat 7. The centerline topography (GPS) in 2001 is shown in red. Data from juneau icefield research program.

The exact drivers of these phenomena are still unclear. Concerning the wave ogives, the seasonal change in glacier velocity through the icefall is suggested to be of influence (Posamentier, 1978). Modelling efforts by Waddington (1986) seem to suggest that multiple icefall characteristics (change in speed, mass balance or width) can be of importance in the formation of wave ogives. While a recent study by Armstrong et al. (2017), found from velocity observations that the summer speed-up only occurs below the icefall, suggesting origin is the variation caused by the snout not the icefall.

In order to get a better understanding of how this process of ogive formation works out, a seasonal velocity field can be useful. Apart from a multi-annual GPS survey (fig. 4.29) also terrestrial photogrammetry has been conducted over Vaughan-Lewis by Rentsch et al. (1990);

Rentsch (1997), hence the icefall seems a good study site. To our best knowledge no temporal velocity variation has been extracted over this icefall or any other, apart from annual or snapshot measurements (Lang, 1997; Welsch, 2000).

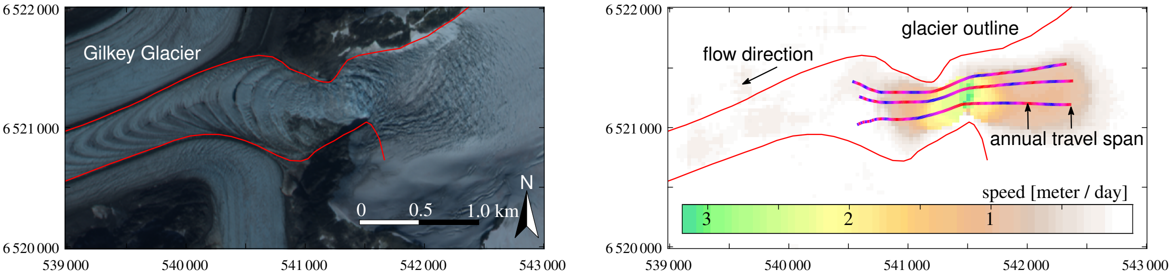

(a) RapidEye image over icefall (b) Icefall summer speed-up

Figure 4.30: Vaughan-Lewis glacier and icefall, Alaska

Matching the velocity over the icefall is much more challenging than on the slow-flowing tongue. Surface features in this part change heavily over time, thus visual coherence is lost. Furthermore, the flow is first converging and then diverging and has strong shear. Thus bulk velocity does not work and smaller template sizes are needed. Therefore, in this specific case we apply pattern matching in the time domain (section 4.3.7), known as ensemble matching (Meinhart et al., 1999). The matching is done with small windows, but for multiple image pairs. The same signal-to-noise can be achieved, as a similar sample set is taken as with single image pair matching. When the flow does not change over the taken stretch of time, it is even possible to extract flow at single pixel resolution (Westerweel et al., 2004).

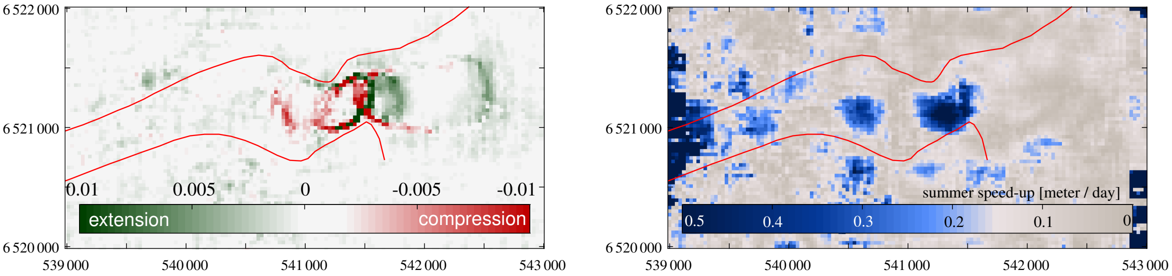

(a) Icefall flow divergence (b) Icefall summer speed-up

Figure 4.31: Flow characteristics and seasonal flow difference of the icefall of Vaughan-Lewis glacier, Alaska

As can be seen in figure 4.30(b), it does take a year for the ice to travel through the icefall, hereafter it decelerates. The time spent in the icefall also has a clear velocity difference, as can be seen in figure 4.31(b). The spatial convergence in figure 4.31(a) is right at the end of this temporal speed up. From this data it seems this location is the origin of the ogive. This strengthens the hypothsis of Posamentier (1978), which associates ogives formation with thrust faulting and associated basal entrainment to generate the dark bands.

4.5.3 Glacier outlines

In principle one can use a velocity field as aid to delineate a glacier outline. Mathematically, the non-glacial area can be formulated as all locations without movement. Practically, this is not feasible with optical remote sensing, as the constructed displacement fields are incomplete, or actual displacements are too small to be observed, as for dead ice. However, displacement information can be a great aid for the detection of calving fronts. Currently, such methods rely on GIS thresholds with slope and elevation (Nuth et al., 2013). Or routing occurs, but again depending on a digital elevation model (Kienholz et al., 2014). Such procedures become troublesome for long outlets or ice shelves, as these are relatively flat and low lying.

However, if glacier front detection is done in a robust and automatic way, this can have several applications. Firstly, it can be of interest for the detection of calving activity. In combination with another algorithm such front detection can be used to construct a pipeline to monitor calving flux (Altena and Kääb, 2017b). Another application could be the detection of glacier snouts. With such a localization it might be possible to automatically monitor glacier length, such as in Usset et al. (2015).

A global approach can be taken to detect glacier fronts where properties of the mass-continuity equation are used. For a land terminating glacier the ice flux is balanced by the mass balance. This is not the case for calving glaciers, where ice flux goes through a gate ($\partial\mathbf{F}$) and the glacier looses mass through calving (figure 3.1). Or similarly, the separation of a calving event redraws the glacier boundary. This simple property is used for this method and is implemented by seeding the glacier with tracers and use the velocity field to spin-up a fluid model, with the viscous properties of ice. By running fast forward into time, the tracers will find their way to the snout of the calving front. Locations are flagged where these tracers cross the glacier outline.

To demonstrate this principle a velocity field of Penckbreen, Spitsbergen, is analysed. An optical image pair was used to extract a displacement field, as can be seen in figure 4.32(b). Here also the end result and the trajectory of a time step of the tracers are shown in figure 4.32(c), in

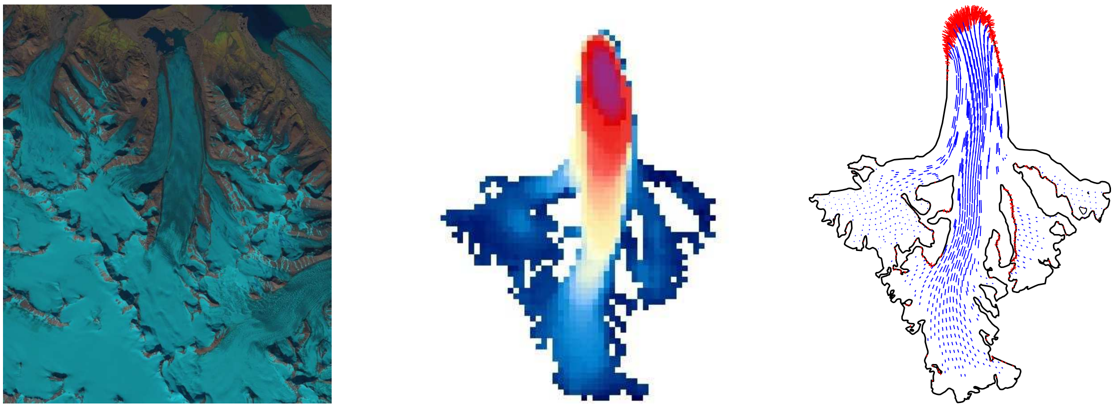
(a) Landsat 8
(b) surface speed
(c) tracers

Figure 4.32: (a) shows a Landsat scene over Penckbreen, Svalbard, on the 2nd of August 2016. (b) highlights the speed of a velocity field, derived from RapidEye imagery from autumn 2016 & 2017. (c) shows a time-step within the seeded fluid model run. Here the tracer movements are in blue, while tracers in red have moved out of the glacier outline.

blue, when their location is within the glacier boundary and red when this is not the case. The big advantage of this method is its simplicity and the use of a single data source. Therefore, error propagation is minimal or at least less dependent on local of single errors.

4.5.4 Glacier depth

For many glaciers the bed topography is unknown, however this is of great interest for fresh water inventories and potential lake reservoirs after glacier recession (Linsbauer et al., 2016). Also a detailed map of the bed is of interest for glacier modelling, as glacier flow models sophisticate and change from flow lines, to describe ice flow in three dimensions. Estimating glacier topography from remote sensing has been done with the help of simplified models (Gantayat et al., 2014), or involving sophisticated inverse modeling (Fürst et al., 2017). The first strategy is incapable of extracting sufficient detail and assumes the glacier is in steady state, which is difficult to justify. The latter method needs reliable data from different sources. When any of these have an error, the source is difficult to trace back. Secondly, meteorological data is also needed and not always available or of sufficient quality. Though, error propagation can be monitored when the glacier bed topography can be estimated directly from a velocity field. Secondly, the meteorological data can be used to bootstrap other parameters within the modelling effort.

Glacier ice is a viscous fluid, hence it obeys the laws of fluid mechanics. For example in the case of Kronebreen glacier, its ice comes from the Holtedahlfonna (300km^2) and Infantfonna (100km^2) icefields and is funnelled through a valley of roughly four kilometers in width. Therefore, the ice speed increase as it enters from the wide icefield into the narrow valley. Similarly, this is the case for the depth of a glacier. The subglacial topography pushes the ice in or outwards of its flowline. If we make use of this concept of horizontal displacements (dv/dy, which is neglected in equation 3.6) we might be able to extract the topographic signal of the bed from a single velocity field. A similar approach has been taken by O'Neel et al. (2005), however restricting themselves to flowlines, later interpolating back to a grid.

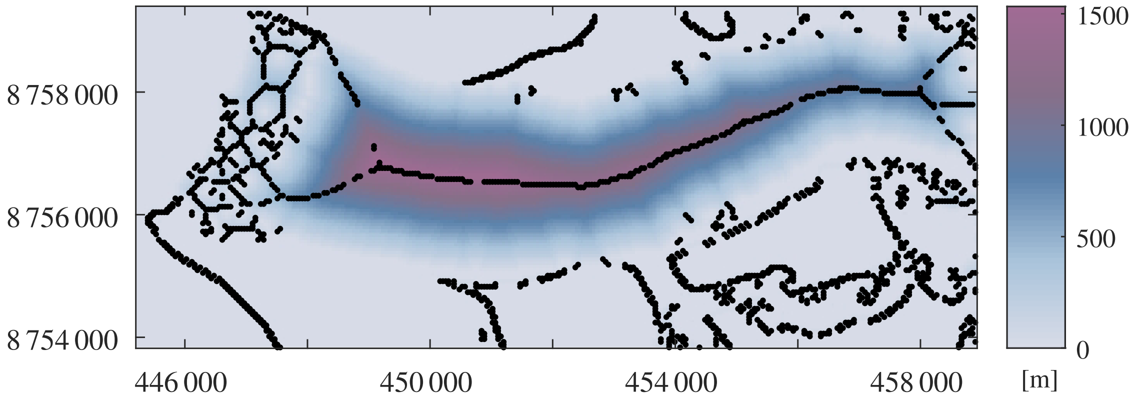

Figure 4.33: From non-glacial terrain and slow flowing a distance function is calculated for a velocity field over Kronebreen, Svalbard. The black dots indicate points of convergence of this transform. These are used to find corridors of flow, see figure 4.34.

For this case we use the Helmholtz-decomposition. It describes a velocity field by means of two components, one which is curl-free and one which is divergence-free, see equation 4.12 and further. This decomposition is done in the frequency domain, making use of the fast Fourier transform (FFT). Consequently, the boundary conditions are periodic. This aspect is of importance and constrains the applicability. Because of the transformation into the frequency domain, the velocity field is within a toroidal topology. Hence, the glacier needs to have reflective boundaries, which is the case when for example the channel is of constant width. Furthermore, the velocity distribution across the border should be similar (obeying the reflection property).

In order to find such sections a velocity field is first estimated. The slow moving part of the velocity field can be selected and form a boundary. This boundary is filled inwards, through an infilling procedure, until the whole domain is filled-up. The infilling results in a distance transform where local maximum distances form a skeleton, see figure 4.34. It are these skeleton

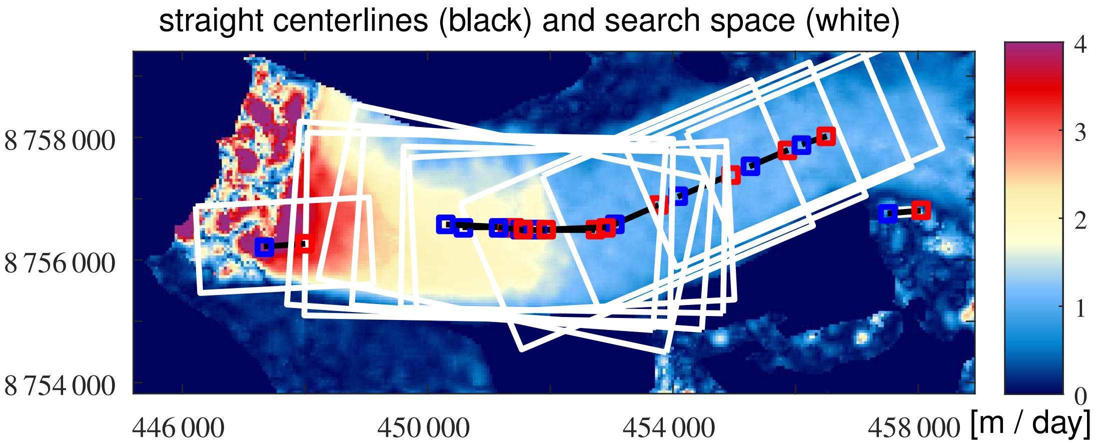

Figure 4.34: Rectangles which align with the flow of Kronebreen, these are along centerline points as from figure 4.33.

cells, which have a given width metric. If multiple skeleton cells with the same width metric are on a line, then one is in a corridor. For example, in figure 4.34 multiple candidate squares are plotted for the outlet of Kronebreen. These rectangles can be seen as search areas, where a square matrix can migrate along. At every step of such a migration, the velocities at the front and the end of the square are compared against each other. With such a procedure it is possible to find a section of a velocity field which is square and conserves energy, hence is reflective. The resulting transform can then be calculated, and is shown together with the real topography in figure 4.35.

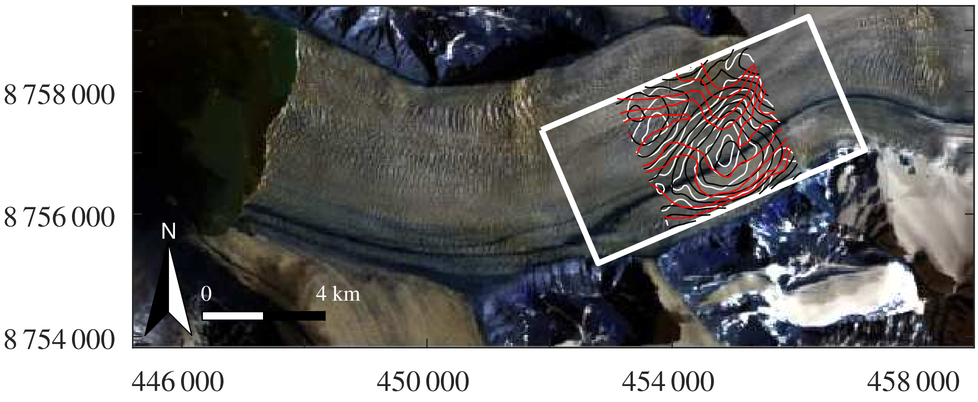

Figure 4.35: Square domain with estimated integrated curl-free (irrotational in black) and (divergence-free) vector field (solenoidal in white). Contourlines of the glacier topography are given in red and have an interval of 20 meters. Data courtesy K. Lindbäck, Norwegian Polar Institute.

The curl-free estimate is perpendicular to the contours of the topography. Meaning the decomposition is able to extract the spatial pattern of the bedrock topography. However, this is only a correlation, a relative and absolute scaling is needed to transform to a metric scale. This can be done by calibration with tracks from a ground penetrating radar (GPR). Typically, these are collected along profiles, but to extract the bedrock topography, dense grids need to be driven. Driving such grid profiles on snow scooters or skies is dangerous, especially on fast flowing glaciers with crevasse fields. Secondly, the post-processing of the data is very labor intensive. Thus this methodology can complement such work and saves labor.

A second approach to calibrate this decomposition is the use of the level of detail of the bedrock topography. Wavelength in the order of one ice thickness are able to influence the surface velocity (Gudmundsson and Raymond, 2008). Thus ice thickness serves as a low-pass filter, hence, the inference of the bed derived from the velocity field has a reduced spectrum. This cut-off frequency can be used in this case, to translate to a scaling, and directly get an estimate of depth. In this way, this method is able to generate bed topography, independently from other data sources, and can therefor be used as a fast check for model output or initial guess.

5 Summary of research

This chapter provides a summary of the papers and key results of this dissertation. For some of the summaries auxiliary material is presented as well, making the broader implications of this work more explicit.

5.1 Extracting glacier velocity from different orbits

Paper I - *Elevation change and improved velocity retrieval using orthorectified optical satellite data from different orbits. Altena & Kääb. Remote Sensing.*

When the first satellite of the Sentinel-2 constellation, Sentinel-2A was launched, initial tests revealed large surface displacements over mountainous terrain in mainland Norway (Kääb et al., 2016). These displacements are artificial, stemming from the use of an inaccurate digital elevation model for orthorectification. These orthorectification errors are more clearly visible in Sentinel-2 data in comparison to orthorectified Landsat imagery, mainly because the Sentinel-2 sensor has a wide field of view and a higher spatial resolution of 10 meters (Gaudel et al., 2017). The offsets are magnified further through the use of an elevation model which has a lower quality above 60°North, since the SRTM data used for it is not covering high latitudes. To overcome these deficiencies, in this study we develop a matching methodology that is more independent of the orthorectification process and the potential offsets in the repeat images.

A second reason to develop such a method is the flexibility to process velocity fields independent of the satellite sensor. In such a case, analysis will be easier and more data can be extracted from the available remote sensing archives. While efforts for radiometric and geometric harmonization are in progress for Sentinel-2 and Landsat 8, this is not the case for many other commercial and/or older satellite systems. Therefore, older and other data can be used (e.g. figure 5.1, where data from the Indian IRS-R2 is used), without the complication of cross-

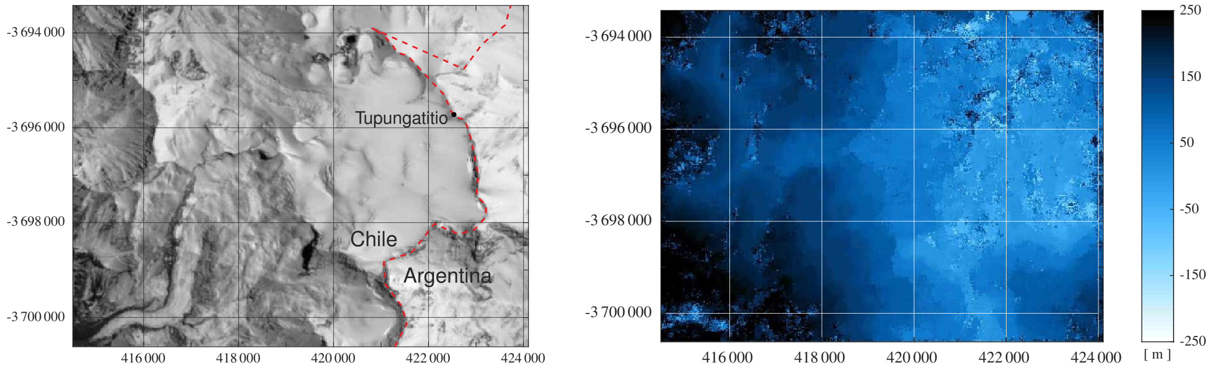

(a) Resourcesat-2 LISS-3 (b) across-track displacement

Figure 5.1: An acquisition over the Southern Andes, which was matched against another IRS-R2 scene in a different orbit. Both scenes are orthorectified imagery based on the SRTM90 dataset. Figure 5.1(b) shows the resulting cross-track displacements, that reflect the higher detailed real topography that is not captured by the SRTM90 elevation model.

calibration of systems.

Furthermore, we introduced a computationally fast triplet-matching scheme, through the exploitation of properties in the frequency domain. This allows calculation of displacement for all three images simultaneously. In this way triangle-closure (for outlier filtering) is immediately integrated rather than as a post-processing step providing efficient and robust results. Finally, we developed a simple projection operator to enable displacement measurements with different imagery from different orbits without the need for three images or precise knowledge of the flown orbits.

After this study, and partially based on it, the orthorectification of Sentinel-2 over Norway has improved considerably. A high quality elevation model from the Norwegian mapping agency is now used for the orthorectification. This improvement in mainland Norway shows the potential for reprocessing of the entire Arctic using a newly released highly detailed elevation model (e.g. ArcticDEM). This would reduce the artificial offsets considerably, allowing more precise and widespread use of the imagery for terrain dispacements. The method here will allow harmonization to old and new sensors, especially those where orthorectification is done with an unknown, bad quality or outdated digital elevation model.

5.2 Observing seasonal changes in glacier flow

Paper II - *Weekly glacier flow estimation from dense satellite time series using adapted optical flow technology. Altena & Kääb. Frontiers in Earth Science.*

Recently, an increase of satellite observations enable daily or sub-weekly high resolution satellite acquisitions over a certain location. For example, the twin constellation of Sentinel-2 provides repeat acquisitions of 5 days within orbit or even better (figure 5.2), or the promising fleet of micro-satellites from Planet Doves with daily repeat. For glaciologists, this enables observation of short-term glacier velocity changes. Current methods using template matching (section 4.3.1) may not be able to detect small displacements and are ineffective for large collections of imagery due to its pair-wise calculation structure. We explored an alternate method, called optical flow (section 4.3.11), that may easier estimate small movements.

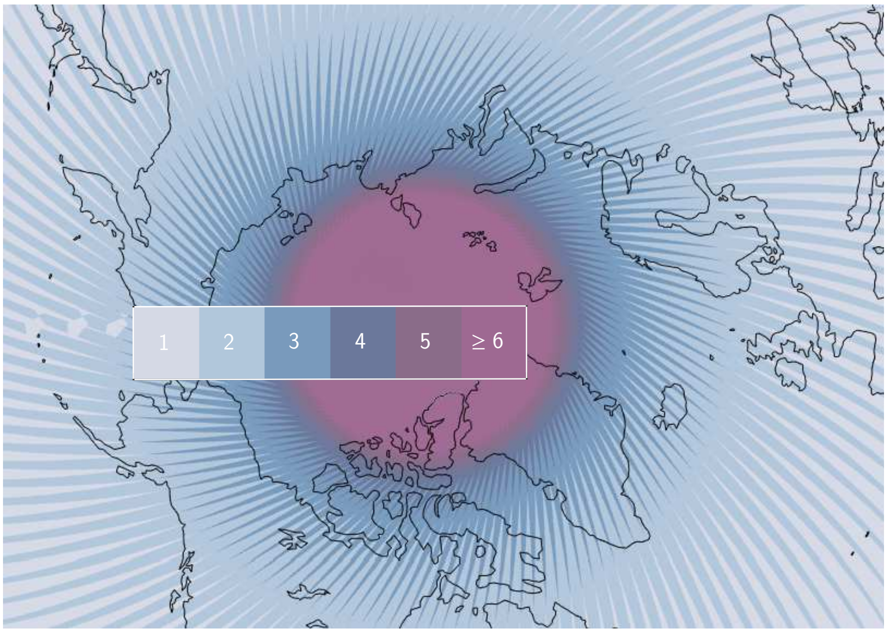

Figure 5.2: Amount of times a point can be seen from different orbits by Sentinel-2. The revisit time of this constellation is now every five days, so daily glacier flow estimation is feasible in the High Arctic, if terrain correction is sufficient (paper I).

Two approaches are tested, one based on stacking that constructs a space-time slice, and another by the selection of a smaller sample set based on features. A pilot dataset was used, from the SPOT5 satellite, which after servicing for several years, was succeeded by newer versions, and thus de-orbited. Through the SPOT5-Take5 initiative, it was set in a high repeat orbit with a revisit time of 5-days over a selection of sites. An ideal dataset for exploring methods for data which is nowadays available.

One advantage of optical flow methods, or detection of slant angles in space-time, is its simplicity. A clear picture of the glacier velocity evolution can be extracted very fast provided a dense time series with limited cloud cover. In our paper we demonstrate the ability to extract an upstream migration of speed increase on Kaskawulsh Glacier, Yukon (figure 7, paperII). Similarly, Armstrong et al. (2017) found a clear seasonal velocity difference between the upper and lower sections of several glaciers within a mountain range. Their data seems to show that icefalls are a typical hydrological barrier for the sub-glacial routing of the melt water. Hence by combining this knowledge and our methodology, we might be able to generate a larger spatial coverage of the seasonal glacier velocity variations related to melt water and progress our understanding of glacier dynamics at glacial scales.

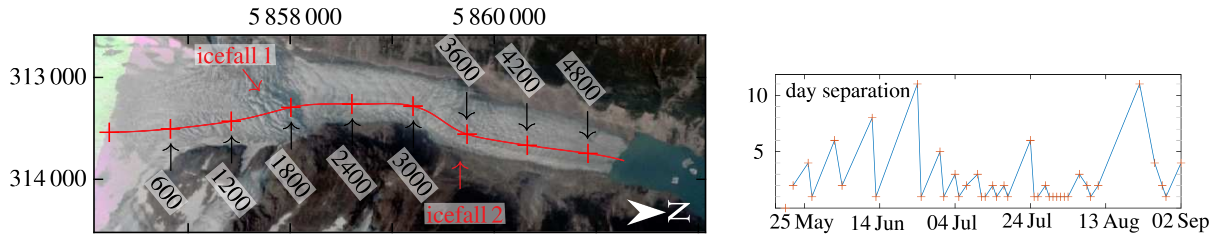

(a) Sir John Abott

(b) acquisitioin statistics

Figure 5.3: Flowline over the lower part of John Abott glacier, British Columbia, used for the analysis for seasonal flow change. Figure 5.3(b) shows the revisit statistics of cloud free imagery from the PlanetScope and RapidEye constellation in 2017.

An interesting example is of a glacier that has two icefalls; John Abott glacier in British Columbia. The two icefalls generate independent ogive trains that superimpose on the glacier snout. Currently the processes forming the ogives are starting to be tested (section 4.5.2). In this example 41 images from PlanetScope and RapidEye data over a 105 days interval were used (figure 5.3(b)). Not every day the glacier is sensed, as clouds obscure the surface, and the PlanetScope constellation was not fully operational at that time. Nevertheless, as can be seen on the revisit statistics in figure 5.3(b), for a large part of the summer season the glacier is observed.

When we look at the results in figure 5.4, at the lowest point of the glacier, the spring velocity is clearly different than the mid-summer steady flow. Above the lower icefall, velocities re-

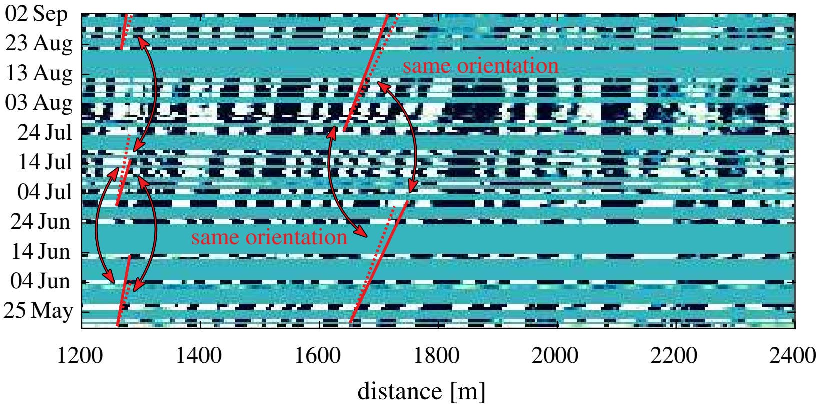

(a) space-time image for the higher icefall

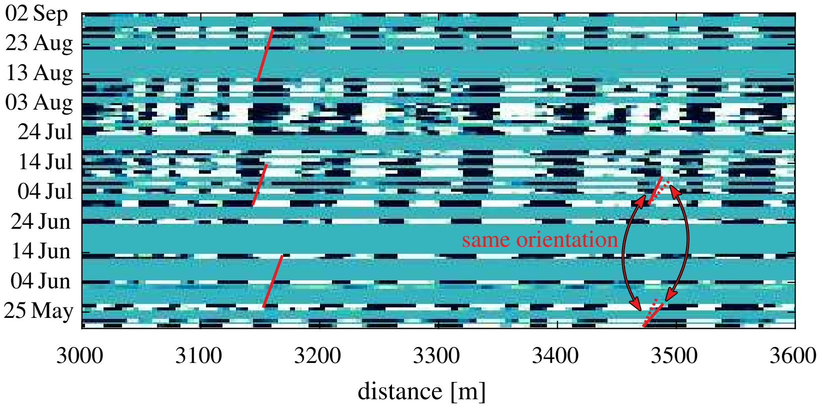

(b) space-time image for the lower icefall

Figure 5.4: Space-time images along flowline, as given in figure 5.3(a). It shows the displacement over time along the flowline. Because of cloud cover, the coverage is incomplete, therefore red lines are drawn to interpret the speed changes. Note the horizontal scale of figure 5.4(a) is two times smaller than figure 5.4(b).

main constant suggesting the icefall functions as a barrier. Around the higher icefall, a different regime seems to be present. A clear but subtle velocity change occurs through time and also propagates up-glacier, but only in mid-summer. Down-glacier from both icefalls are ogives, and these observations might suggest two different mechanisms that result in the same phenomena. Either the snout pulls the ice at the base, while the icefall flows steady, as seem to occur in the lower icefall. At the upper icefall, the icefall increases in speed between winter and summer, though its snout is steadily flowing. Analysis like these for more glaciers might give a better insight and a more clear picture. Whatever the outcome, through our study it is now possible to do these kind of studies and exploit the enormous collection of Earth observation data.

The method proposed in this study is an effective tool to grasp the essence of governing ice flow of a glacier under study. Upscaling is hampered by manual intervention, as operations like drawing lines are needed to extract information. Though it is very efficient as interpretation can be done simultaneously. Hence, the method is a very effective tool for quick assessments and hypothesis formulation.

5.3 Semi-monthly velocities over mountain ranges in Alaska and Canada

---

Paper III - *Extracting recent short-term glacier velocity evolution over Southern Alaska from a large collection of Landsat data. Altena et al. The Cryosphere Discussions.*

The European Union's Copernicus initiative aims at availability of climate related data from satellite observations. For some disciplines, such as meteorology, this represents a simple continuation of monitoring practices that are already available. However, this level of operation has not been achieved yet in the field of glaciology. Here remote sensing has still been operating on an opportunistic approach (Paul et al., 2015), hence in the field of high mountain glacier remote sensing the Copernicus objective is challenging to reach.

For glacier velocity fields, the quality of the product is of sufficient precision, with reliability being the greatest drawback and of major importance for an operational product. A first step towards such a product has been the set-up of a service by the national snow and ice datacenter (NSIDC). For this project "global land ice velocity extraction from Landsat 8" (GoLIVE), image pairs were matched and the results, without quality control, were placed in a repository for further use by others (Scambos et al., 2016). This has been a great step forward as it pushed the research emphasis away from matching and towards post-processing of such velocity fields. Similar initiatives have also emerged for Sentinel-1 data, where velocity fields over Greenland are available through portals (Nagler et al., 2015).

This paper aims to extract a complete semi-monthly time-series of glacier velocities by combining a large collection of velocity fields over varying time-spans. The resulting dataset can be used to identify dynamics over a large area (at the scale of mountain ranges). To this avail, we construct a post-processing scheme that exploits a geometric contraint (introduced in paper I) instead of using the correlation score (a measure of similarity). This allows the detection and filtering of outliers and inconsistencies. Another important aspect is the incorporation of a decision scheme. Here the data is placed into a voting scheme (section 4.4.6), while else testing would be applied. The advantage of such a strategy is its lower sensitivity to outliers. A main disadvantage of the voting scheme is the discretisation of the parameter space. This exponentially grows with the amount of parameters to be estimated.

As an example, we choose to construct a velocity time-series of the Saint Elias and its neighbouring mountain ranges over a period from 2013 until 2017 with a monthly interval. The resulting time-series captures several patterns of glacier dynamics including the timing of multiple surges over a vast region. These types of big-data sets will be more and more common in the future, enabling a better characterization of dynamical patters with high temporal resolution. Importantly, the post-processing scheme introduced here is independent of sensors, all types of optical sensors or even velocities from SAR can be used.

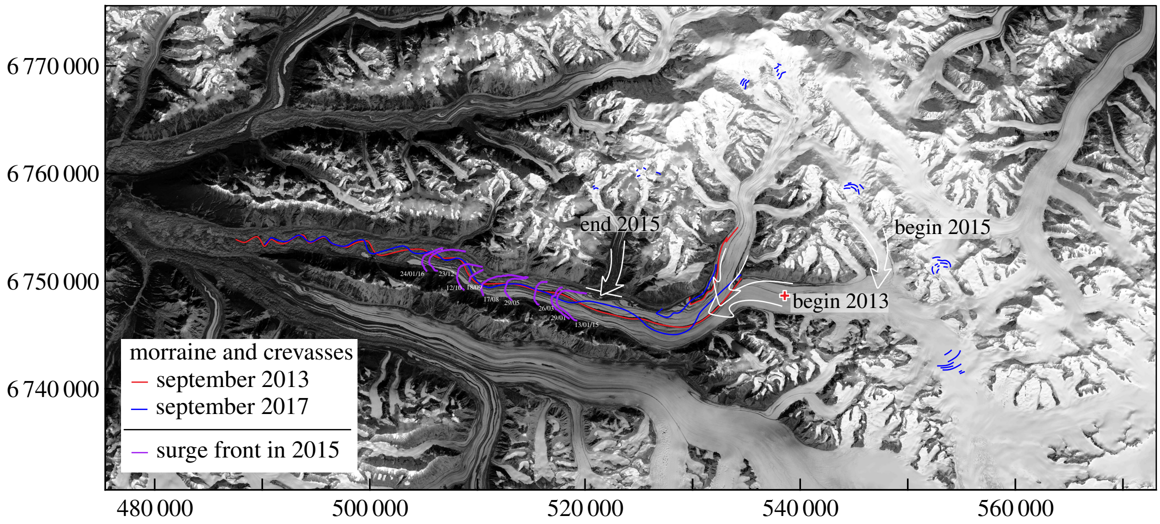

Figure 5.5: Chronology of surge history at the Walsh glacier system, Saint Elias Mountains. Stemming from the time series of the GoLIVE daset presented in paper III.

The synthesized velocity time-series over the Saint Elias and its neighbours give a fast and complete picture of complicated flow interactions. For example, the recent surge event that occurred over Walsh glacier is well documented with this dataset and several of its components can be identified making it possible to work out a chronology of its glacier dynamics. The initiation point of the surge can be identified, as well as the downward propagation of the surge front. The timeline is further enriched by the timing of releases of tributary glaciers, both in downstream direction as well as the upper parts of the glacier. Landsat acquisitions before and after the event can be used to verify and map the extent of crevasses and moraines. Not all tributaries within this basin have been triggered by this main surge event. The increase in slope, due to lowering of the main surge might be a trigger for these exceptions. Another aspect might be the thickness of tributary glaciers and thus their connectivity and associated pulling force caused by the main surge. To answer such questions, modelling is needed, however, the spatial-temporal information within this data-set give strong handholds to constrain such modelling efforts.

6 Conclusions & Opportunities

The focus of this thesis is on the extraction of glacier velocity time-series from optical satellites. Within a short period of time, this niche within the field of glaciological research has grown from sporadic case studies to large-scale processing. This is due to the availability of imagery and velocity fields over the entire globe. Spaceborne missions have also changed the way in which studies are conducted (figure 2.3). Single sensor results advance to harmonization with various constellations of satellites. Many of the methods presented in this thesis will contribute to easier and more robust extraction of repeat image derived displacement for a better insight into glacier dynamics.

6.1 Advances in computing

A number of advances in processing are required to fully utilize the ever increasing archive of satellite optical images. Importantly, we present a method in paper I to estimate surface velocity independent of orthorectification. This enhances opportunities for glacier velocity studies as imagery from any orbit can now be used. In light of natural phenomena with even slower movements, the need to be independent of constellation or orbit becomes even more pronounced (Stumpf et al., 2018). Our proposed method is essential for the harmonization between satellite systems, both for older and newer constellations, as these are not always in the same orbit.

The introduction of triplet matching in paper I is an advantage over current implementations, many of which attempt to improve image matching by an additional building block within the pipeline. Our implementation has checks and balances built within, effectively using the information content. Additionally, implementation in the frequency domain ensures short processing times.

The advantage of including a third acquisition into the velocity estimation has also a drawback. It requires that the image is free of clouds during all three acquisitions. Therefore, chances for successful matches are reduced compared to image couples. Importantly, this problem diminishes when a multitude of imagery is included (n). The probability of a successful set ($P_{m\odot}$) is given by Ju and Roy (2008). Extending this to a triplet case, the probability can be calculated through,

$$P_{m\odot} = \Pi_{j=1}^{m} P(1 - \Pi_{i=j}^{n} p_i). \tag{6.1}$$

Here, m denotes the amount of cloud-free imagery needed for the matching. This relation is illustrated for several probabilities (p_i) in figure 6.1. The upper bound of 60% is the case for continental climates, while the lower bound is typical for maritime glaciers. This relation shows that triplet matching thrives on large collections for regions with low cloud-free potential, a situation which is now possible with all available sensors in space.

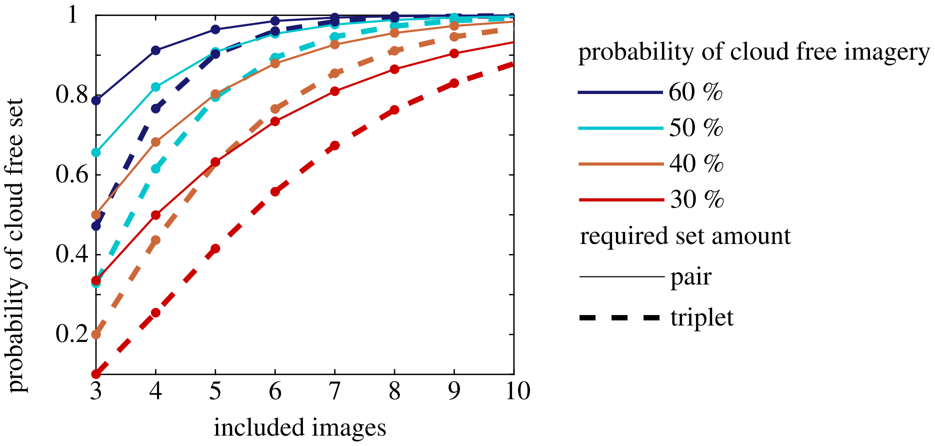

Figure 6.1: Success-rate of a feature being observed in relation to cloud cover and amount of acquisitions.

The post-processing of velocity fields is traditionally based on simple or robust spatial statistics. Our contribution to this aspect (paper III) is the implementation of a robust functional model. The configuration of the different timespans are included into the model, composing a network which can be tested or voted for.

Research with Sentinel-2 and PlanetScope imagery has contributed to the acceptance of the data for product development within the Earth observation community (Kääb et al., 2016, 2017)&paper I. Sentinel-2 is a continuation of the SPOT legacy and in some respects an improvement over the Landsat legacy. A calibration and validation phase has been done to provide standard products. While for the PlanetScope data a calibration campaign with test sites is too labor intensive. It is not possible to test and compare one sensor and extrapolate towards the others, since the concept relies on the constellation of many micro-satellites that are constantly replenished. Therefore, this Earth observation innovation has received some scepticism, especially within the quantitative remote sensing community. To gain confidence, we implemented and demonstrated the photometric capabilities of the system to improve adoption and acceptance in the scientific community (Altena et al., 2017). Photometry extracts topography through changes in the sun angle (section 2.3.5) and heavily depends on the radiometric quality of the system and its calibration procedures. Without calibration, photometry is still possible with PlanetScope data, ensuring the possibility of many more simpler methods as well.

6.2 Glaciological contribution

At the start of this PhD, research on glacier velocity was mostly conducted on case specific events. Multi-annual mapping efforts started to emerge describing large spatial extents. Our contribution within this aspect is towards an increase in detail over time (paper II). Also we have been able to extract information at an inter-seasonal resolution over a large areal extent (paper III). Consequently for example, the propagation of surges can be analysed, not only in a flowline fashion, but for the full aerial extent.

The level of process understanding through inferences from velocity data alone is limited. Hence, many demonstrations within this work are mostly of great help for identifying regions of interest in space and time. However before this thesis had been written, the extraction of temporal flow over icefalls, for instance had not been demonstrated from space. Furthermore, surges were seen as special events, but with our time-series at a mountain range scale, one instantaneously can see that such dynamics is rather the normal state in some glaciated regions. Surges and speed-ups are found all over the mountain ranges of Southern Alaska for a period of just four years.

6.3 Outlook

6.3.1 Data recovery

Since the 1960's satellites have been observing the Earth with optical cameras. Because the oldest reconnaissance (spy) cameras had a stereo configuration, they are importnat for long-term glacier volume change assessments (Bolch et al., 2011). The reconstructed topographies are snapshots and therefore do not depend on satellite revisit times. Though multi-temporal imagery is needed for glacial velocity estimation, unfortunately consistent temporal acquisitions are mostly absent for this type of data. Another important historical data source for glaciology is the Landsat legacy, which now has been continuously running for 42 years. Its acquisitions can be of great use for decadal-scale analysis of glacier flow. It is thus the only consistent data source for long term world wide glacier flow change analysis.

Most of the imagery collected early in the Landsat legacy were downloaded and stored directly at local ground stations. The Landsat data required a paid license at this time and thus most acquisitions are stored on tapes at these facilities. In recent years, an effort has been taken to centralize, recover, convert, store and make these data web enabled (Wulder et al., 2016). Consequently, more data from the thematic mapper (TM) and newer (Landsat 4 and higher), is gradually becoming publicly available.

For the older multi spectral scanner (MSS) instrument, the recovery of the data can be more challenging, as the instruments on the oldest Landsat satellites are less accurate due to less precise orbits; within two kilometers for Landsat 1-3 and one kilometer for Landsat 4-5. Georeferencing needs to be solved on data that is of medium spatial resolution (68 m x 83m) and imagery with low radiometric resolution (6 bit). Therefore, these challenges for snow-covered or glaciated places result in many unused acquisitions. Today, advances in processing power and automation have made it possible to recover saturated data and reprocess the georefencing of this data (Saunier et al., 2017).

These datasets are of great interest for glaciology, however these campaigns are not spatially and temporally as complete and coherent as present campaigns. Extracting velocity records from these missions is challenging as imagery from different orbits (with low locational precision), with high potential saturation or artifacts. With the techniques presented in section 4.2 and paper I, this information might be possible to extract. Finally, it is not only velocity data which can be extracted from the older Landsat data, it can also be used for detection of transient

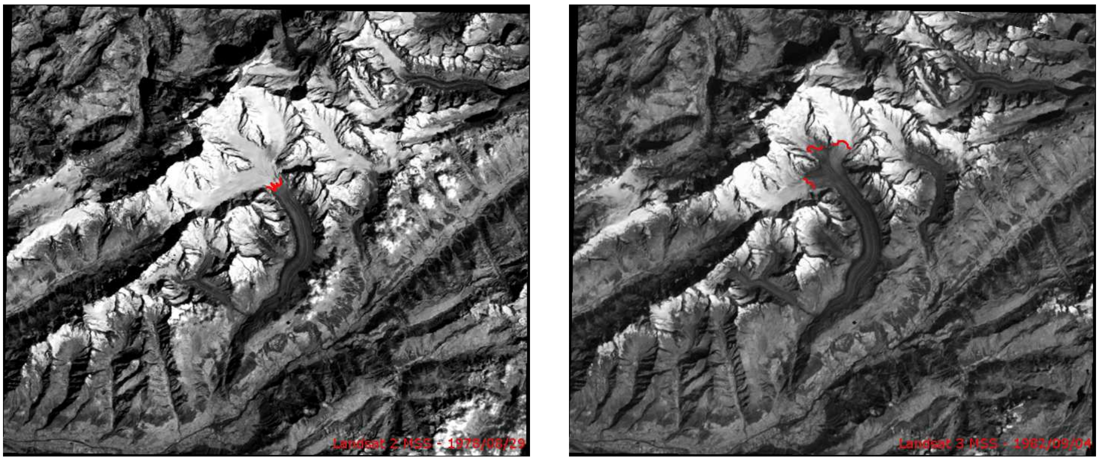

(a) 29th Aug 1978, Landsat 2 (b) 4th Sep 1982, Landsat 3

Figure 6.2: Snowline detection for Aletsch glacier, Switzerland. Imagery courtesy S.Saunier, Telespazio.

snowlines (figure 6.2) and mapping decadal glacier or snow cover change. The elevation of the transient snowline or the spatial distribution of snow cover can be used as a proxy for the glacier mass-balance (Østrem, 1975; Rabatel et al., 2017). Such information can be complementary to stake measurements and help to assess to what extent glacier mass balance models are able to describe complicated spatial variability which is present at the glacier surface. Abstract formulations in models for processes that influence the snowmelt, such as direct solar radiation in respect to effective horizon (Hock and Holmgren, 2005), or precipitation patterns due to airflow dynamics (Schuler et al., 2007), can be assessed.

6.3.2 Post-processing

From a computational point of view, our large scale post-processing scheme with a discrete search space implementation is ineffective. Hence, development of a more computationally efficient implementation of our scheme has the potential to allow operational processing with the rapid pace of current acquisitioning by satellites.

The opening of the archives of the Landsat legacy in 2007 and the recent addition of the suit of Sentinel satellite fleet set in operation by the Copernicus program provides an amazing collection of imagery. The GoLIVE dataset (Scambos et al., 2016) is a service built on top of these datasets to produce glacier velocity fields with diffent time intervals, and is publicly available.

With a proper post-processing, clean and more complete velocity products will become available. Consequently, the coupling to models will be made, also towards implementation into thematic exploitation platforms, therefor reaching a broader audience.

6.3.3 Process modelling

From a product point of view some future direction in the post-processing can be envisioned. This became apparent at the end of the post-processing chapter where the sophistication of the model increased considerably and exploited fluid properties were tested. A similar procedure has been developed by Maksymiuk et al. (2016) incorporating the full Navier-Stokes equations. It is envisioned that this direction of coupling of remote sensing data and sophisticated fluid models will increase. Remote sensing data will not only be used to kickstart a model, but feedback in the form of testing and adjustment will be established. In this way, spurious velocity data can be removed in which the procedures in section 4.4 are a first attempt in this coupling, though with simple models and fluid properties. However, such random sampling and consensus type of testing is a first step.

From a modelling point of view, the multi-temporal velocity fields can enhance the degree of sophistication of glacier thickness estimation. Because patterns within the flow field of the glacier can be caused by flow disturbances transmitted through the ice. Henceforth velocity fields are useful measurements for bed inferences, though such reconstructions are difficult. Small scale flow variation can be related to bedrock topography (bumps) and changes in friction (sticky spots). Especially at fast flowing glaciers, this transmission is apparent, though not all features have effect. Along flow features of any size, such as troughs or stripes have minimal effect, as well as features smaller than two ice thicknesses (Thorsteinsson et al., 2003; Armstrong et al., 2016). Secondly, parameter estimates can compensate each other when inverting for friction and bedrock, hence regulation is needed (Mosbeux et al., 2016).

A velocity field and a sparse collection of ice thickness measurements can also be used together with the mass-continuity (see equation 3.2) to estimate bedrock topography (Farinotti et al., 2009; Morlighem et al., 2011). These methods solve the continuity equation through flux-gates or along flowlines (McNabb et al., 2012). However, assumptions need to be made to convert from surface velocities to depth average values. Also the divergence need to be constrained as viscous properties are not present in the continuity equation.

Another implementation will be directed towards data-driven modelling, where Kalmann-filters are implemented together with ensemble runs. This makes it possible to include irregular measurements into a model run. Remote sensing data can be used to bootstrap the parameter space. Here remote sensing measurements have a different function than measurements have normally, as these typically have continuous sampling. This is not possible for remote sensing data, hence, such schemes are important to be developed in the near future. Such framework are in place for snow-cover mapping and snowpack modelling (Charrois et al., 2016), though still at a stage where proof-of-concepts are based upon synthetic data.

Assimilation of glacier velocity implies the model is able to describe the transient behavior of flow. However, sliding or friction behavior over time is not yet captured within a sliding law (which is one of the reasons why it is not covered in this work). To a great extent this is due to the complicated interaction of water input under the glacier (see section 3.3.2). But with current large collections of velocity data, such exploratory work towards such a sliding law might be fruitfull.

6.3.4 Pattern recognition

One strategy in this thesis has been to use the physical properties, known from field-studies and modelling, to aid in the processing of Earth observation data. For example, knowing the viscous behaviour of ice, we can test the individual estimates in a displacement field of a glacier (section 4.4.5). The use of data-driven approaches can be another gateway to gain knowledge. For such methods large collections of data is needed and this is the case for Earth observation as satellite imagery will continue to be collected from ever more constellations and platforms. Especially arteficial neural networks have gained popularity as a discovery tool in the last couple of years, and are now starting to be used on geospatial data as well. One such application might be the discovery of certain features of interest, such as supra-glacial lakes illustrated in figure 6.3. Currently, this tool is limited to features of a similar fixed form, though, it might be possible that such descriptors will become better in describing free-form objects, for example through construction of large training-sets. Experiments in this direction, though based on feature engineering, have been conducted for streaklines in relation to surge activity (Herreid and Truffer, 2016).

Similar to imagery, velocity fields can also take advantage of such descriptors in combination with pattern recognition procedures. Think of interpretation of flowlines over time, or

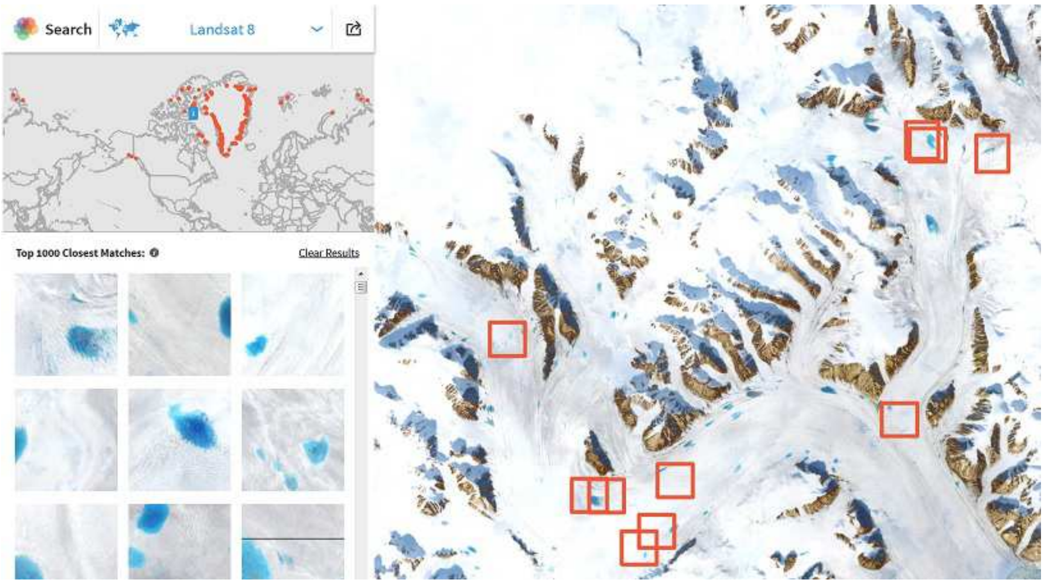

Figure 6.3: Meltpond localization based on image descriptors. The example procedure returns the 1000 most similar templates from a high resolution dataset that covers the entire Earth's surface. Screenshot from GeoVisual search by Descartes Labs.

grouping of certain events in space and time. Experiments with such procedures are currently explored (Nguyen et al., 2017), and will certainly continue in the future.

One direction which can be of interest in the discovery of patterns in space and time is the formulation of ice crystal trajectories. These can be constructed from multi-temporal velocity fields and are unique in space and time and of multitude. Within such a space these trajectories can be seen as entities and as such periodic patterns and flocks can be searched for (Laube et al., 2005). Flocks of such trajectories might co-align with seasonal variation, while meetings or convergence might represent a surge or quiescent phase (Gudmundsson and van Kreveld, 2006). Some robustness might be introduced by permitting trajectories to leave or join the flock (Kalnis et al., 2005).

6.3.5 Big implications caused by small satellites

Recently, to exploit the extra space available in space carriers launches, a rise in lower cost, micro satellites is set in orbit. For example, a regular destination for space rockets is the international space station as scientific instrumentation and crew provisions needs to be carried to it. Such regular scheduled flights are a secure opportunity to get cubesats into space. However, with an orbital inclination of 51.6 degrees, cubesats orbits travel in opposite direction of timezones and will not fly over high latitudes. Therefore, it is not the most optimal orbit for Earth observation, but the temporal repeatability of images acquired provides an immense potential for understanding rapidly changing features or processes.

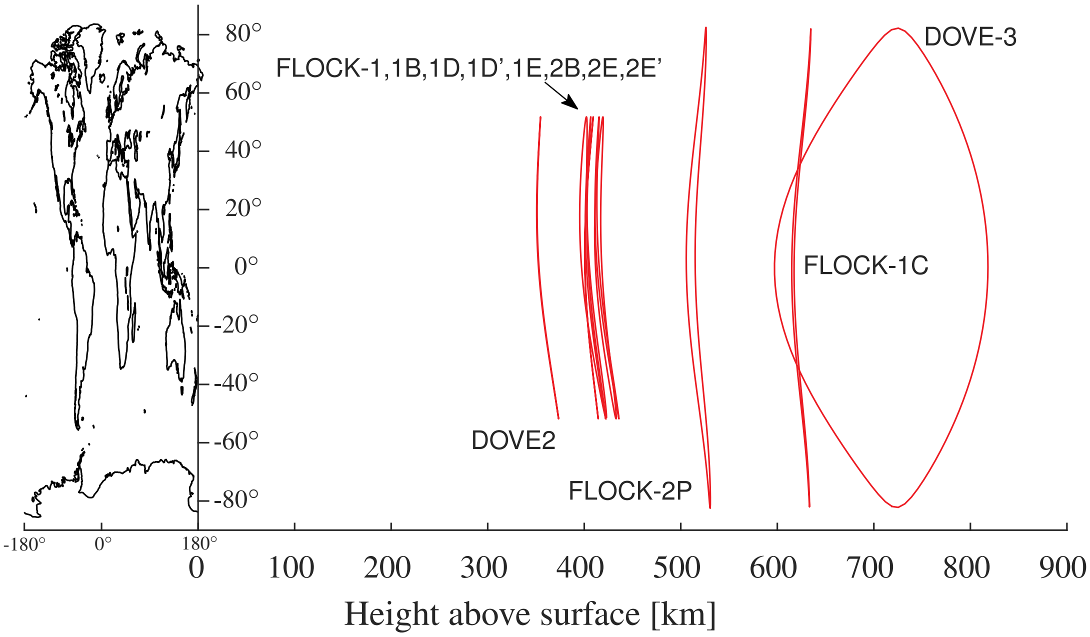

Figure 6.4: Different orbits of Planet cubesats, before the full constellation in sun-synchronous orbit was put into place.

During the period of this thesis, the deployment of cubesats into space has increased significantly (figure 2.5). While a decade ago these cubesats were technology demonstrations, now the majority has an optical systems in the visible range as payload (Poghosyan and Golkar, 2017). However, the opportunities for Earth observation with small satellites have not been limited to this kind of sensor. Many applications which seemed infeasible half a decade ago (Selva and Krejci, 2012), are now operational systems. Since these sensors will be of interest for observing glaciers and other cryospheric processes, some recent advances are highlighted here to close off this part of the dissertation.

spectral satellites Several hyperspectral missions are currently built and some constellations are set into orbit. Currently, the Argentinian company of Satellogic has three satellites in orbit and plans to build a full constellation. A similar plan is set forth by the Canadian company of Northstar. Both instruments operate in the visible domain relying on silicon photo-sensitive cells. For recording the short-wave infrared wavelengths, dedicated cells that require cooling must be used. While such sensors will be available soon, currently only hyperspectral missions controlled by space agencies use the technology (EnMap and HyspIRI). One mission that does operate in this spectrum is the greenhousegas satellite (GHGSat), built to monitor emissions at large industrial sites to a precision of roughly 1% of the atmospheric background level. A similar microsatellite constellation for methane monitoring is envisioned by the company Bluefield. Their market is to compile estimates of trace gases and couple these to regulations set forth by the Paris agreement. Such spectral measurements for trace gases are also envisioned by the company of Koolock in USA and Promethean labs in Canada.

microwave satellites Another market where small satellites are emerging and constellations of satellites are deployed is in the microwave spectrum. The Finish company Iceye has launched their first X-band microwave satellite in orbit this January. Also the US company Capellaspace is in an advanced state of deploying a similar constellation. From military business, the Trident Space company has announced plans for a constellation, as well as, the company of XpressSAR. These systems will boost research and will be as innovative as currently happens in the optical market. Furthermore, synergy between optical and microwave satellites will further increase within the field of glaciology (Winsvold et al., 2018). For the most part, ultra dense time-series with microwave data will see a large boost in use, as such data has not been as easily accessible as is now the case with Sentinel-1.

Methodological innovation will come from combining satellites. For instance, the SAOCOM-1A&B satellites scheduled for launch by the Argentine space agency (CONAE) will fly in formation with the SAOCOM-CS satellite from the European space agency, which makes it possible to exploit tomographic techniques, a potential for subglacial topography extraction (Tebaldini et al., 2016).

optical satellites from different orbits and countries Many of the small satellite deployments are rooted from projects initiated by governmental agencies (NASA, JAXA, ESA, ...). When expertise and a profitable concept is at a sufficient level, valorization happens within the commercial markets. A good example is the optical constellation market, where multiple players are competing for a majority of the market share. At the time of writing, competition is large in the United States. However, other countries have started exploring this market as well. There can evolve a repetition in history, as similar to the known Landsat-program, other countries have their own Earth observation programs. Their efforts and achievements can't be unnoticed either, think of CBRES (China-Brazil), ALOS (Japan), IRS (India), etc. Therefore, because of political will to sovereignty, one might expect these new constellations to be less affected by the dominance of the US market forces. Hostile takeovers or abort-of-mission will be less likely, hence it is of interest also to list initiatives from these countries, and their efforts to ramp-up optical constellations.

For example in Japan, Axel space has launched a first small optical satellite, with the aim of a full constellation. The first cubesat test flights with optics have been launched by Zhejiang Lizhui Electronic Technology from China. Similarly, Argentina has several commercial satellites in orbit from the company of Satellogic. Finally, the Canadian-Spanish company of Deimos aims at a daily coverage as well, in combination with SAR to detect clouds before acquisition of optical images. What is possible with such new satellite systems in respect to the cryosphere is given in the following.

general trends in orbit configuration and opportunities for the Cryosphere Besides more launches, a tendency over the last decades is a steady increase in satellites' lifetime (longevity) (Belward and Skøien, 2015). Therefore, there will be less interest in populating the morning crosses at a sun-synchronous orbit. Other times of the day will be explored, as well as low inclination orbits, to facilitate multiple overpasses over one day (cadence). This can be seen by the current distribution of satellites in sun-synchronous orbit, illustrated in figure 6.5. In this plot only a selection of satellites are highlighted as the gross amount of these is situated at 10:00 local equator crossing time.

The amount of small and micro-satellites is likely to grow even further, as the cost of production decreases. Another advantage of deploying multiple small satellites is risk reduction and more strategic capacity. If malfunction happens in a multi-satellite constellation, this will only lead to soft degradation of the performance.

The design of the satellites will advance towards more autonomous systems, as this will ease the transmission bottleneck to ground stations (Sandau, 2010) and help in formation flying (figure 2.6). For the analysis and product development this will stress importance of automated cross-registration of different sensors and between constellations. Calibration and harmonization of such systems is needed, as validation programs with ground samples will be infeasible

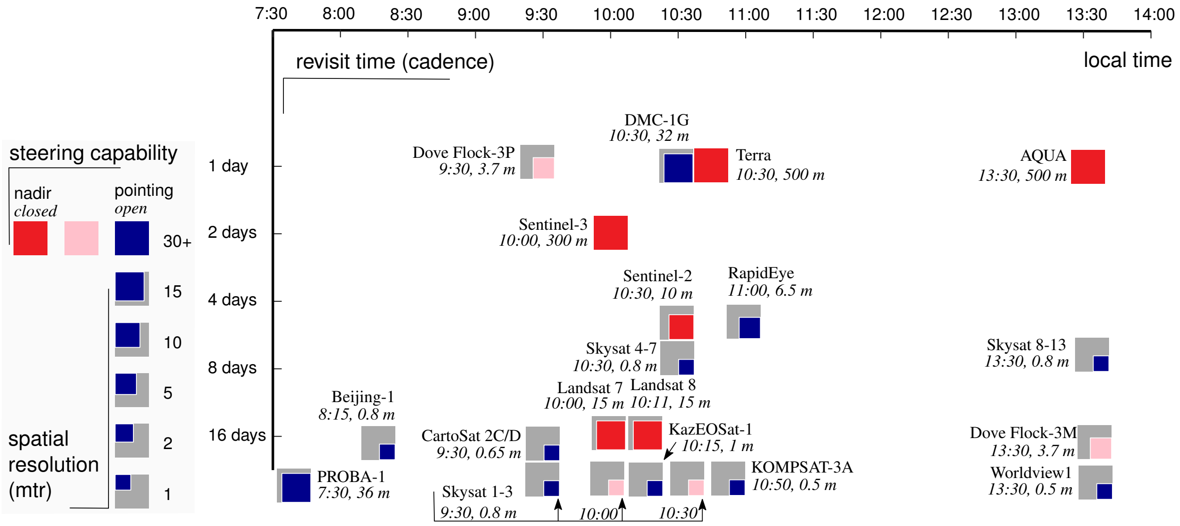

Figure 6.5: A selection sun-synchronous earth observation satellites and their different equatorial cross-over times are illustrated against revisit rate and spatial resolution.

for all sensors. However, the increased cross-overs and overlap of different systems give opportunities for automated cross-calibration efforts.

The increased cadence within one day can provide information complementary to glacier velocities. For example, the timing of lake level changes can be mapped at short-time intervals (Cooley et al., 2017), and can be related to the connections within the hydrological network under the glacier (Miles et al., 2017). This high resolution and dense sampling from micro-satellites is for example, capable to detect growth and decline of supraglacial lakes (figure 6.6).

The increased high-resolution sensing of the cryosphere will also make it possible to observe other movements. Especially, frontal glacial dynamics, such as crack propagation, ice shelf disintegration and iceberg calving. The interaction of glacier velocity and ice calving is of great interest but systematic measurements have been limited in time and space. In this case optical satellite imagery can help out, as daily ice-loss can be estimated automatically (Altena and Kääb, 2017b).

At daily time scales, observing large calving events can give insight into the specific ice-mechanical processes at work. Initiation of such dynamics can be triggered by subtle events, such as far-away earthquakes or lake level fluctuations due to rain (Dykes et al., 2017). The stress regime caused by the general flow of the glacier can be measured by traditional means,

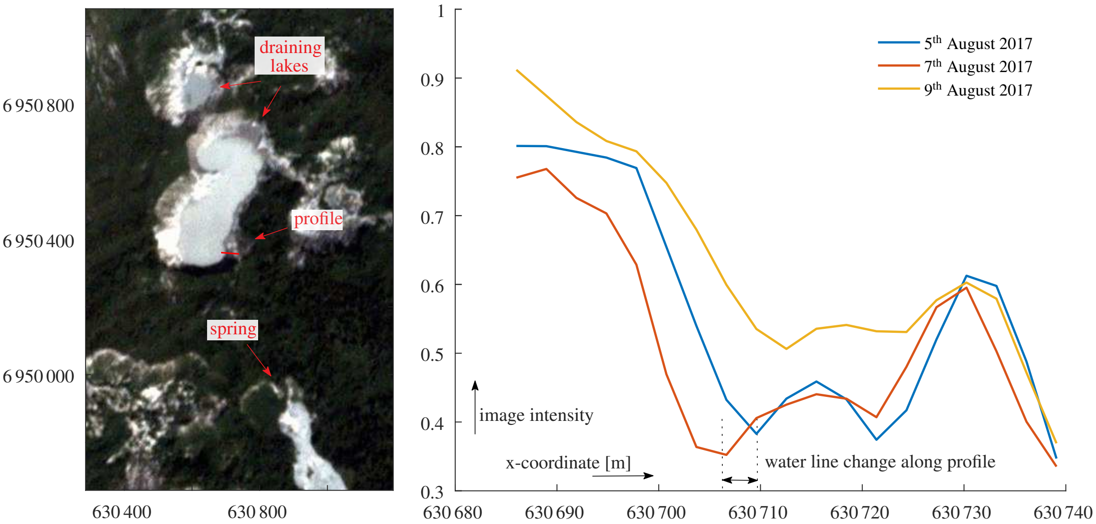

Figure 6.6: High-repeat Planet imagery makes it possible to use an optical ruler to assess the supraglacial lake filling and draining at the snout of Ruth glacier, Alaska.

and function as a baseline for spin up, while the high resolution data can be used to describe the stress regime for a detailed frontal part of the glacier, which can then be modelled (Jouvet et al., 2017). However, for such detailed studies more information such as the basal topography is helpful, such as water levels in the cracks and crevasse depth. Nevertheless, the essential component, that is the local stress regime prior to the event, can be extracted from satellite imagery and optical flow (paper II). For example such a displacement field is shown for a large calving event in figure 6.7.

The examples shown above demonstrate new applications that are now in reach. Movements at different spatial and temporal scales can now be observed with the vast collection of optical satellite systems in space. The methods introduced in this part of the dissertation and the research in the next part, will contribute to more easy information extraction. Bringing the opportunity to increase our understanding of what happens in the vast changing cryosphere.

6.3.6 Requirements for future satellite missions

The advanced land imager (ALI) instrument onboard the EO-1 satellite, has been the demonstration instrument for Landsat 8. It introduced instruments with a large radiometric range, which made it ideal for capturing small details on the snow surface (Bindschadler, 2003). This advanced bit depth makes it possible to extract reliable displacements at the snowcovered upperpart of glaciers and icesheets. Which is partly why current satellites like Landsat 8 (Jeong and Howat, 2015), or Sentinel-2 (Kääb et al., 2016) generate superior results in respect to older

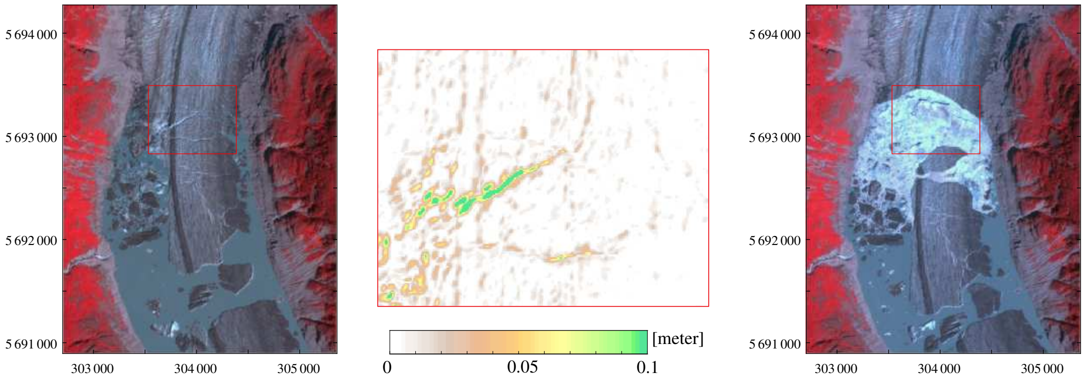

(a) July 4th 2017 (b) displacement from 3-4 July (c) July 6st 2017

Figure 6.7: Lake calving event at SilverThrone glacier into its pro-glacial lake, British Columbia as seen through the Planet constellation.

satellites. Increasing the bit depth further might not be an urgent need for pattern matching, as the gross signal of the surface is captured.

The spectral sensitivity is another component for the instrumentation design. A clear limitation for both Sentinel-2, PlanetScope and other multi-spectral imagery is their poor detection ability of cloud cover. Algorithms highly rely on the thermal bands (Zhu and Woodcock, 2012), this is especially of importance in snow-covered terrain. Currently, when thermal data is lacking cloud cover algorithms work with the coherence in the temporal domain (Hagolle et al., 2010), which is not an option when estimating displacement. Furthermore, such algorithms rely on accurate elevation models for the shadow casting, which is neither ideal for the cryosphere as terrain models are of low quality as they are in high mountains. Experimentation with machine learning is current research, but it is better to incorporate thermal bands into the design.

The geolocation of the imagery is of utterly importance. Especially for spaceborne glacier velocity estimation, as errors are a combination of absolute geo-referencing accuracy and the quality of the digital elevation model. The procedure presented in paper I is able to estimate velocity independent of errors in the elevation model. The method is a work around and helpfull for large scale processes, but still highly dependent on the absolute geo-referencing of the product. One step in the right direction occurs when the global reference image from Sentinel-2 imagery is created. This will increase the relative geolocation, but ideally such block-adjustments will be created with higher resolution satellite systems. Consequently, methods as shown in paper II will be more accurate and it will be possible to extract better and more precise information on glacier flow change.

The availability of low level product is essential to exploit the potential of multi-sensor integration. Because the movement of the solar array of a satellite can cause oscillations, this shaking will propagate into the acquisition, called jitter (Ayoub et al., 2008). For example, the Sentinel-2 satellite has two oscillations: one at 0.84Hz with an amplitude of 50 microradians, one at 0.03Hz with an amplitude of 100 microradians (Dechoz et al., 2015). On-board sensors can estimate the attitude and thus when higher level imagery is created, these artifacts can be compensated for. However, errors might be created within the product generation, or for specific areas, ground control might be better than the global product provided by the space agency. If for certain applications a very high accuracy is needed, it is beneficial to get the raw imagery, metadata and instrument readings. Also raw imagery is available for the PlanetScope imagery (see figure 2.8), this makes it possible to do photogrammetry or in-house orthorectification. An example of such processing with low-level products, in this case with Landsat 8 and Sentinel-2, has been demonstrated by Stumpf et al. (2018). Here the application was rock slope movement, where the location of the area of interest is well known and the spatial extent is very limited. This is not practical for large scale glacier monitoring, but for site specific analysis this can be of great value. Such co-registration pipelines make it possible to merge different sensors, thus providing low-level products is essential and make possible to push the frontier of Earth surface monitoring.

Remote sensing has been thriving on signals of opportunity, but in recent years it has migrated towards an asset in space. Multi-sensor observation systems are now in orbit which can sense the cryosphere at regular intervals (Drinkwater, 2014). Especially the Copernicus program is contributing towards this effort through its Sentinel missions, which are orchestrated with each other to enhance their extractable information content. Such harmonization efforts is of great benefit from a monitoring perspective. However, the constellation of Planet has shown to be very effective as well. Their development process was part of the build-up of their constellation, known as agile space. Consequently, unexpected products where possible to generate (Altena et al., 2017), which were only possible through early feedback loops between scientists and the satellite development team. It is therefore of importance to include several degrees of freedom in the design and thus give capacity to the system to adapt or evolve.

Complication with spaceborne velocity estimation through SAR imagery occurs during the melt season, as water in the snow-pack change the scattering properties and coherence in the signal gets lost. Similarly in winter optical imagery is less ideal for pattern matching as the surface is mostly homogeneously covered with snow. Merging the merits of both sensors is thus evident, however, matching optical to SAR imagery is challenging.

Firstly in order to apply pattern matching, the acquisition geometry need to be set to a common vantage point. Attempts to do so commonly orthorectify the SAR imagery (see figure 2.2). However the visual imagery can also be brought to the side-looking vantage point of the SAR (Palubinskas et al., 2010). Practically this would translate into matching the unrectified outer edge of the wide looking sentinel-2 imagery, or making use of the steerable capabilities of satellites (see figure 6.8). If a common vantage point is established, the imagery are still very different and resolution issues still apply. The SAR signal is dependent on the reflectivity of a material and its cross-sectional area, where the illumination is in the line-of-sight. For optical the illumination is side-looking as well, but has a different aspect. Hence a final strategy to merge both imagery is to make the optical imagery invariant to illumination. This can be done by generating an elevation model and creating a hillshade in SAR geometry. Consequently, the two datasets will be in the same geometry and to some extent have the same information content within.

Hence, this topic is still work in progress, thus for the harmonization of both sensors the most practical is to merge velocity products rooted from either system. This can be done by directly merging the products to fill temporal gaps (Strozzi et al., 2017), mosaicking (Joughin et al., 2018), or through post-processing with a framework as presented in paper III. Future harmonization might exploit the difference in nature for both sensors. For example, making use of the line-of-sight velocity from interferometric SAR and the high resolution planar displacements from optical to extract high resolution three dimensional surface displacements.

The rapid evolution of space technology and advances in off-the-shelf electronics have transformed the field of Earth observation(see figure 2.4). (Sub-)daily acquisitions are and will be collected with optical and SAR satellites. Hence the amount of data for this type seems sufficient to generate surface changes. However bulk movement can also be estimated by satellites, by measuring changes in the Earth gravity field. Such single or tandem satellite systems are able to resolve monthly mass changes on coarse spatial scale (Wouters et al., 2014). This is an independent measurement and can therefor be used complementary to the visual signals. If such a system is deployed in a cubesat fashion ($>$ 100 satellites), it might be able to enhance resolution in space or time. Then it is not only possible to extract ice mass loss over time which

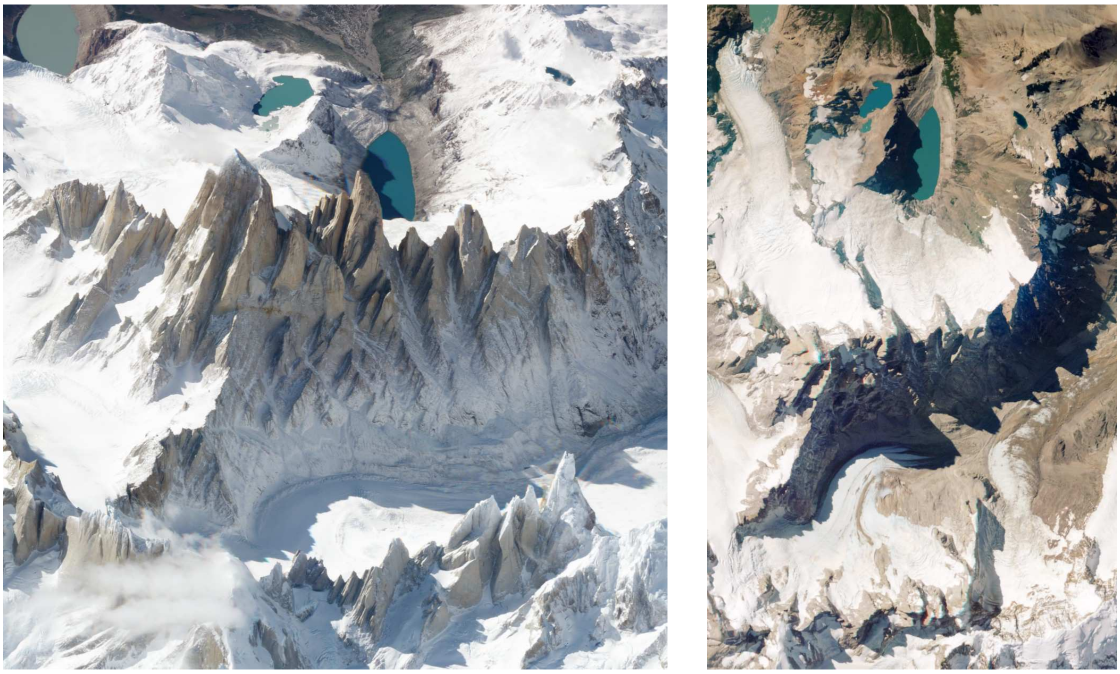

(a) sideward looking (oblique)

(b) downward looking (nadir)

Figure 6.8: Spaceborne imagery of Fritz Roy, Patagonia. (a) Oblique view taken by a SkySat satellite. (b) Typical nadir view image taken by RapidEye. Image courtesy Planet Labs, Inc.

is related to the atmosphere, but also look at glacier dynamics related to hydrolic and geometric properties. Fortunately, gravity is not only of interest to glaciologist, but if such constellations are in orbit, it might be possible to resolve such changes more rapidly and come to a near-real-time solution, instead of current half a year processing and release times. This opens the door for other applications, such as drought warning and food security, two subject of the united nations sustainable development goals.

References

Abdel-Aziz Y and Karara H (2015 (&1971)) Direct linear transtransform from comparator ccoordinate into object space ccoordinate in close-range photogrammetry. *Photogrammetric Engineering & Remote Sensing*, **81**(1), 103–107

Ahn Y and Box J (2010) Glacier velocities from time-lapse photos: technique development and first results from the Extreme Ice Survey (EIS) in Greenland. *Journal of Glaciology*, **56**(198), 723–734

Ahn Y and Howat IM (2011) Efficient automated glacier surface velocity measurement from repeat images using multi-image/multichip and null exclusion feature tracking. *IEEE Transactions on Geoscience and Remote Sensing*, **49**(8), 2838–2846

Altena B (2009) *Assesment of glacier DTM's from ALOS PRISM triplet detector*. Hogeschool Utrecht Bsc Thesis

Altena B and Kääb A (2017a) Elevation change and improved velocity retrieval using orthorectified optical satellite data from different orbits. *Remote Sensing*, **9**(3), 300

Altena B and Kääb A (2017b) Glacier ice loss monitored through the Planet cubesat constellation. In *9th International Workshop on the Analysis of Multitemporal Remote Sensing Images (Multi-Temp)*, 1–4, IEEE (doi: 10.1109/Multi-Temp.2017.8035235)

Altena B, Kääb A and Nuth C (2015) Robust glacier displacements using knowledge-based image matching. In *Analysis of Multitemporal Remote Sensing Images (Multi-Temp), 2015 8th International Workshop on the*, 1–4, IEEE (doi: http://dx.doi.org/10.1109/Multi-Temp.2015.7245790)

Altena B, Mousivand A, Mascaro J and Kääb A (2017) Potential and limitations of photometric reconstruction through a Flock of Dove cubesats. *ISPRS International Archives of Photogrammetry Remote Sensing and Spatial Information Sciences*, **XLII-3-W3**, 7–11 (doi: 10.5194/isprs-archives-XLII-3-W3-7-2017)

Andersen M, Stenseng L, Skourup H, Colgan W, Khan SA, Kristensen SS, Andersen S, Box J, Ahlstrøm A, Fettweis X et al. (2015) Basin-scale partitioning of Greenland ice sheet mass balance components (2007–2011). *Earth and Planetary Science Letters*, **409**, 89–95

Anderson J and Jakobsson M (2016) Grounding-zone wedges on Antarctic continental shelves. *Geological Society, London, Memoirs*, **46**(1), 243–244

Anderson N, Loso MG, Armstrong W, Altena B and Girbacea R (2017) Morphology, deformation, and seasonally varying velocity of ogives on Root glacier, Alaska. *In preparation*

Anderson RS, Anderson SP, MacGregor KR, Waddington ED, O'Neel S, Riihimaki CA and Loso MG (2004) Strong feedbacks between hydrology and sliding of a small alpine glacier. *Journal of Geophysical Research: Earth Surface*, **109**(F3)

Argyriou V and Vlachos T (2005) Performance study of gradient correlation for sub-pixel motion estimation in the frequency domain. *IEEE Proceedings-Vision, Image and Signal Processing*, **152**(1), 107–114

Armstrong W, Anderson R, Allen J and Rajaram H (2016) Modeling the WorldView-derived seasonal velocity evolution of Kennicott Glacier, Alaska. *Journal of Glaciology*, **62**(234), 763–777

References

Armstrong WH, Anderson RS and Fahnestock MA (2017) Spatial patterns of summer speedup on South central Alaska glaciers. *Geophysical Research Letters*, **44**, 1–10 (doi: 10.1002/2017GL074370)

Ayoub F, Leprince S, Binet R, Lewis KW, Aharonson O and Avouac JP (2008) Influence of camera distortions on satellite image registration and change detection applications. In *Geoscience and Remote Sensing Symposium, 2008. IGARSS 2008. IEEE International*, volume 2, II–1072, IEEE

Baarda W (1968) *A testing procedure for use in geodetic networks*. Rijkscommissie voor Geodesie

Belward AS and Skøien JO (2015) Who launched what, when and why; trends in global land-cover observation capacity from civilian Earth observation satellites. *ISPRS Journal of Photogrammetry and Remote Sensing*, **103**, 115–128

Berger M, Moreno J, Johannessen JA, Levelt PF and Hanssen RF (2012) ESA's sentinel missions in support of Earth system science. *Remote Sensing of Environment*, **120**, 84–90

Berthier E, Vadon H, Baratoux D, Arnaud Y, Vincent C, Feigl K, Remy F and Legresy B (2005) Surface motion of mountain glaciers derived from satellite optical imagery. *Remote Sensing of Environment*, **95**(1), 14–28

Bindschadler R (2003) Tracking subpixel-scale sastrugi with advanced land imager. *IEEE transactions on geoscience and remote sensing*, **41**(6), 1373–1377

Bindschadler R and Vornberger P (1994) Detailed elevation map of ice stream C, Antarctica, using satellite imagery and airborne radar. *Annals of Glaciology*, **20**(1), 327–335

Bindschadler R, Skvarca P and Scambos T (1994) Surface-velocity field of the northern Larsen ice shelf, Antarctica. *Annals of Glaciology*, **20**(1), 319–326

Bindschadler R, Scambos T, Rott H, Skvarca P and Vornberger P (2002) Ice dolines on Larsen ice shelf, Antarctica. *Annals of Glaciology*, **34**(1), 283–290, ISSN 0260-3055

Bjørk AA, Kjær KH, Korsgaard NJ, Khan SA, Kjeldsen KK, Andresen CS, Larsen NK and Funder S (2012) An aerial view of 80 years of climate-related glacier fluctuations in southeast Greenland. *Nature Geoscience*, **5**(6), 427–432

Björnsson H, Gjessing Y, Hamran S, Hagen JO, Liestøl O, Pálsson F and Erlingsson B (1996) The thermal regime of sub-polar glaciers mapped bu multi-frequency radio-echo sounding. *Journal of Glaciology*, **42**(140), 23–32

Bolch T, Pieczonka T and Benn D (2011) Multi-decadal mass loss of glaciers in the Everest area (Nepal Himalaya) derived from stereo imagery. *The Cryosphere*, **5**(2), 349–358

Borstad C, McGrath D and Pope A (2017) Fracture propagation and stability of ice shelves governed by ice shelf heterogeneity. *Geophysical Research Letters*, **44**(9), 4186–4194

Boulton G (1979) Processes of glacier erosion on different substrata. *Journal of glaciology*, **23**(89), 15–38

Breunig MM, Kriegel HP, Ng RT and Sander J (2000) Lof: identifying density-based local outliers. In *ACM sigmod record*, volume 29, 93–104, ACM

Brinkerhoff D and O'Neel S (2017) Velocity variations at Columbia glacier captured by particle filtering of oblique time-lapse images. *arXiv preprint arXiv:1711.05366*

Byrne G, Crapper P and Mayo K (1980) Monitoring land-cover change by principal component analysis of multitemporal Landsat data. *Remote Sensing of Environment*, **10**(3), 175–184

Casey K and Kääb A (2012) Estimation of supraglacial dust and debris geochemical composition via satellite reflectance and emissivity. *Remote Sensing*, **4**(9), 2554–2575

Casey K, Kääb A and Benn D (2012) Geochemical characterization of supraglacial debris via in situ and optical remote sensing methods: a case study in Khumbu Himalaya, Nepal. *The Cryosphere*, **6**(1), 85–100

Charrois L, Cosme E, Dumont M, Lafaysse M, Morin S, Libois Q and Picard G (2016) On the assimilation of optical reflectances and snow depth observations into a detailed snowpack model. *The Cryosphere*, **10**, 1021–1038

Cogley J, Hock R, Rasmussen L, Arendt A, Bauder A, Braithwaite R, Jansson P, Kaser G, Möller M, Nicholson L and Zemp M (2011) Glossary of glacier mass balance and related terms. Technical Report 86, International Association of Cryospheric Sciences, UNESCO-IHP, Paris, France

Colgan W, Rajaram H, Abdalati W, McCutchan C, Mottram R, Moussavi MS and Grigsby S (2016) Glacier crevasses: Observations, models, and mass balance implications. *Reviews of Geophysics*, **54**(1), 119–161

Conese C, Maracchi G and Maselli F (1993) Improvement in maximum likelihood classification performance on highly rugged terrain using principal components analysis. *International Journal of Remote Sensing*, **14**(7), 1371–1382

Cooley SW, Smith LC, Stepan L and Mascaro J (2017) Tracking dynamic Northern surface water changes with high-frequency Planet cubesat imagery. *Remote Sensing*, **9**(12), 1306

Creyts TT and Schoof CG (2009) Drainage through subglacial water sheets. *Journal of Geophysical Research: Earth Surface*, **114**(F4)

Cuffey K and Paterson W (2010) *The physics of glaciers*. Academic Press

Cyganek B and Siebert JP (2011) *An introduction to 3D computer vision techniques and algorithms*. John Wiley & Sons

dAngelo P, Máttyus G and Reinartz P (2016) Skybox image and video product evaluation. *International Journal of Image and Data Fusion*, **7**(1), 3–18

Davidson G and Nye J (1985) A photoelastic study of ice pressure in rock cracks. *Cold Regions Science and Technology*, **11**(2), 141–153

Davis BA, Brewer S, Stevenson AC and Guiot J (2003) The temperature of Europe during the Holocene reconstructed from pollen data. *Quaternary Science Reviews*, **22**(15), 1701–1716

de Loor G (1993) *Land observation by remote sensing: theory and applications*, volume 3 of *Current topics in remote sensing*, chapter Physical characteristics of remote sensing information, 35–50. Pudoc Wageningen

Deans S (2007) *The Radon transform and some of its applications*. Courier Corporation

Debella-Gilo M and Kääb A (2011) Sub-pixel precision image matching for measuring surface displacements on mass movements using normalized cross-correlation. *Remote Sensing of Environment*, **115**(1), 130–142

Debella-Gilo M and Kääb A (2012a) Locally adaptive template sizes for matching repeat images of Earth surface mass movements. *ISPRS Journal of Photogrammetry and Remote Sensing*, **69**, 10–28

Debella-Gilo M and Kääb A (2012b) Measurement of surface displacement and deformation on mass movement using least squares matching of repeat images. *Remote Sensing*, **4**, 43–67

References

Dechoz C, Poulain V, Massera S, Languille F, Greslou D, de Lussy F, Gaudel A, L'Helguen C, Picard C and Trémas T (2015) Sentinel-2 global reference image. In *Image and Signal Processing for Remote Sensing XXI*, volume 9643, 96430A, International Society for Optics and Photonics

Deeley R (1908) The viscosity of ice. *Proceedings of the Royal Society of London. Series A, Containing Papers of a Mathematical and Physical Character*, **81**(547), 250–259

Dehecq A, Gourmelen N and Trouvé E (2015) Deriving large-scale glacier velocities from a complete satellite archive: Application to the Pamir–Karakoram–Himalaya. *Remote Sensing of Environment*, **162**, 55–66 (doi: 10.1016/j.rse.2015.01.031)

Dehecq A, Millan R, Berthier E, Gourmelen N, Trouvé E and Vionnet V (2016) Elevation changes inferred from TanDEM-X data over the Mont-Blanc area: Impact of the X-band interferometric bias. *IEEE Journal of Selected Topics in Applied Earth Observations and Remote Sensing*, **9**(8), 3870–3882

Doan D, Zimmerman R, Leung L, Mason J, Parsons N and Shahid K (2017) Commissioning the worlds largest satellite constellation. In *Proceedings of Small Satellite Conference*, AIAA Utah State University

Dowdeswell JA and McIntyre N (1986) The saturation of Landsat MSS detectors over large ice masses. *International Journal of Remote Sensing*, **7**(1), 151–164

Dozier J and Painter T (2004) Multispectral and hyperspectral remote sensing of alpine snow properties. *Annual Review of Earth and Planetary Sciences*, **32**, 465–494

Drews R (2015) Evolution of ice-shelf channels in Antarctic ice shelves. *The Cryosphere*, **9**(3), 1169–1181

Drinkwater M (2014) *Cryosphere and Polar Region Observing System*, 91–98. Springer New York, New York, NY, ISBN 978-0-387-36699-9 (doi: 10.1007/978-0-387-36699-9_25)

Durkin WJ, Bartholomaus TC, Willis MJ and Pritchard ME (2017) Dynamic changes at Yahtse glacier, the most rapidly advancing tidewater glacier in Alaska. *Frontiers in Earth Science*, **5**

Dykes R, Brook M and Lube G (2017) A major ice-calving event at Tasman glacier terminus, Southern Alps, 22 February 2011. *Journal of the Royal Society of New Zealand*, **47**(4), 336–343

Dyurgerov MB and Meier MF (2005) *Glaciers and the changing Earth system: a 2004 snapshot*, volume 58. Institute of Arctic and Alpine Research, University of Colorado Boulder

Echelmeyer K and Harrison W (1990) Jakobshavns Isbræ, West Greenland: Seasonal variations in velocity-or lack thereof. *Journal of Glaciology*, **36**(122), 82–88

Echelmeyer K and Zhongxiang W (1987) Direct observation of basal sliding and deformation of basal drift at sub-freezing temperatures. *Journal of Glaciology*, **33**(113), 83–98

Echelmeyer K, Harrison W, Larsen C and Mitchell J (1994) The role of the margins in the dynamics of an active ice stream. *Journal of Glaciology*, **40**(136), 527–538

Ely J, Clark C, Ng F and Spagnolo M (2017) Insights on the formation of longitudinal surface structures on ice sheets from analysis of their spacing, spatial distribution, and relationship to ice thickness and flow. *Journal of Geophysical Research: Earth Surface*, **122**(4), 961–972

Etzelmüller B, Vatne G, Ødegârd RS and Sollid JL (1993) Mass balance and changes of surface slope, crevasse and flow pattern of Erikbreen, northern Spitsbergen: an application of a geographical information system (GIS). *Polar Research*, **12**(2), 131–146

Evans AN (2000) Glacier surface motion computation from digital image sequences. *IEEE Transactions on Geoscience and Remote Sensing*, **38**(2), 1064–1072

Fahnestock M, Bindschadler R, Kwok R and Jezek K (1993) Greenland ice sheet surface properties and ice dynamics from ERS-1 SAR imagery. *Science*, **262**, 1530–1530

Fahnestock M, Scambos T, Moon T, Gardner A, Haran T and Klinger M (2016) Rapid large-area mapping of ice flow using Landsat 8. *Remote Sensing of Environment*, **185**, 84–94 (doi: 10.1016/j.rse.2015.11.023)

Faillettaz J, Funk M and Vagliasindi M (2016) Time forecast of a break-off event from a hanging glacier. *The Cryosphere*, **10**(3), 1191–1200

Farinotti D, Huss M, Bauder A, Funk M and Truffer M (2009) A method to estimate the ice volume and ice-thickness distribution of alpine glaciers. *Journal of Glaciology*, **55**(191), 422–430

Fincham A and Spedding G (1997) Low cost, high resolution DPIV for measurement of turbulent fluid flow. *Experiments in Fluids*, **23**(6), 449–462

Fitch A, Kadyrov A, Christmas WJ and Kittler J (2002) Orientation correlation. In *Britisch Machine Vision Conference*, 1–10

Flowers GE (2015) Modelling water flow under glaciers and ice sheets. *Proceedings of the Royal Society of London - A*, **471**(2176), 20140907

Förstner W and Wrobel B (2016) *Photogrammetric Computer Vision*, volume 11 of *Geometry and Computing*. Springer (doi: 10.1007/978-3-319-11550-4_13)

Foster C, Hallam H and Mason J (2015) Orbit determination and differential-drag control of Planet labs cubesat constellations. *AIAA/AAS Astrodynamics Specialist Conference*, (15-524)

Fung T and LeDrew E (1987) Application of principal components analysis to change detection. *Photogrammetric engineering and remote sensing*, **53**(12), 1649–1658

Fürst JJ, Gillet-Chaulet F, Benham TJ, Dowdeswell JA, Grabiec M, Navarro F, Pettersson R, Moholdt G, Nuth C, Sass B et al. (2017) Application of a two-step approach for mapping ice thickness to various glacier types on Svalbard. *The Cryosphere*, **11**(5), 2003

Gabbud C, Micheletti N and Lane S (2015) Lidar measurement of surface melt for a temperate Alpine glacier at the seasonal and hourly scales. *Journal of Glaciology*, **61**(229), 963–974

Gantayat P, Kulkarni A and Srinivasan J (2014) Estimation of ice thickness using surface velocities and slope: case study at Gangotri glacier, India. *Journal of Glaciology*, **60**(220), 277–282

Gardner AS, Moholdt G, Scambos T, Fahnstock M, Ligtenberg S, van den Broeke M and Nilsson J (2018) Increased west Antarctic and unchanged east Antarctic ice discharge over the last 7 years. *The Cryosphere*, **12**(2), 521–547 (doi: 10.5194/tc-12-521-2018)

Gaudel A, Languille F, Delvit J, Michel J, Cournet M, Poulain V and Youssefi D (2017) Sentinel-2: Global reference image validation and application to multetemporal performances and high latitude digital surface model. *International Archives of the Photogrammetry, Remote Sensing & Spatial Information Sciences*, **42** (doi: 10.5194/isprs-archives-XLII-1-W1-447-20)

Gilbert A, Vincent C, Wagnon P, Thibert E and Rabatel A (2012) The influence of snow cover thickness on the thermal regime of Tête Rousse Glacier (Mont Blanc range, 3200 m asl): Consequences for outburst flood hazards and glacier response to climate change. *Journal of Geophysical Research: Earth Surface*, **117**(F4)

References

Giordan D, Allasia P, Dematteis N, DellAnese F, Vagliasindi M and Motta E (2016) A low-cost optical remote sensing application for glacier deformation monitoring in an alpine environment. *Sensors*, **16**(10), 1750

Girod L (2018) *Improved measurements of cryospheric processes using advanced photogrammetry*. Ph.D. thesis, University of Oslo

Glen J (1952) Experiments on the deformation of ice. *Journal of Glaciology*, **2**(12), 111–114

Goldstein RM, Engelhardt H, Kamb B and Frolich RM (1993) Satellite radar interferometry for monitoring ice sheet motion: application to an Antarctic ice stream. *Science*, **262**, 1525–1525

Gong Y, Zwinger T, Åström J, Altena B, Schellenberger T, Gladstone R and Moore JC (2017) Simulating the roles of crevasse routing of surface water and basal friction on the surge evolution of Basin 3, Austfonna ice-cap. *The Cryosphere Discussions*, **2017**, 1–23 (doi: 10.5194/tc-2017-180)

Gray A, Short N, Mattar K and Jezek K (2001) Velocities and flux of the Filchner ice shelf and its tributaries determined from speckle tracking interferometry. *Canadian Journal of Remote Sensing*, **27**(3), 193–206

Grodecki J and Dial G (2003) Block adjustment of high-resolution satellite images described by rational polynomials. *Photogrammetric Engineering & Remote Sensing*, **69**(1), 59–68

Gudmundsson GH and Raymond M (2008) On the limit to resolution and information on basal properties obtainable from surface data on ice streams. *The Cryosphere*, **2**(2), 167–178 (doi: 10.5194/tc-2-167-2008)

Gudmundsson J and van Kreveld M (2006) Computing longest duration flocks in trajectory data. In *Proceedings of the 14th annual ACM international symposium on Advances in geographic information systems*, 35–42, ACM

Guindon B (1990) Development of a Shape-from-Shading technique for the extraction of topographic models from individual spaceborne sar images. *IEEE transactions on Geosciences and Remote Sensing*, **28**(4), 654–661

Gupta R and Hartley RI (1997) Linear pushbroom cameras. *IEEE Transactions on pattern analysis and machine intelligence*, **19**(9), 963–975

Hagen JO, Eiken T, Kohler J and Melvold K (2005) Geometry changes on Svalbard glaciers: mass-balance or dynamic response? *Annals of Glaciology*, **42**(1), 255–261

Hagolle O, Huc M, Pascual DV and Dedieu G (2010) A multi-temporal method for cloud detection, applied to formosat-2, venμs, landsat and sentinel-2 images. *Remote Sensing of Environment*, **114**(8), 1747–1755

Hall DK, Chang AT and Siddalingaiah H (1988) Reflectances of glaciers as calculated using Landsat-5 Thematic Mapper data. *Remote Sensing of Environment*, **25**(3), 311IN1313–312321

Hanssen RF (2001) *Radar interferometry: data interpretation and error analysis*, volume 2. Springer Science & Business Media

Harper JT, Humphrey N and Pfeffer WT (1998) Crevasse patterns and the strain-rate tensor: a high-resolution comparison. *Journal of Glaciology*, **44**(146), 68–76

Hart D (2000) PIV error correction. *Experiments in Fluids*, **29**(1), 13–22

Haug T, Kääb A and Skvarca P (2010) Monitoring ice shelf velocities from repeat MODIS and Landsat data–a method study on the Larsen C ice shelf, Antarctic Peninsula, and 10 other ice shelves around Antarctica. *The Cryosphere*, **4**(2), 161–178

Heid T and Kääb A (2012a) Evaluation of existing image matching methods for deriving glacier surface displacements globally from optical satellite imagery. *Remote Sensing of Environment*, **118**, 339–355

Heid T and Kääb A (2012b) Repeat optical satellite images reveal widespread and long term decrease in land-terminating glacier speeds. *The Cryosphere*, **6**(2), 467–478

Herreid S and Truffer M (2016) Automated detection of unstable glacier flow and a spectrum of speedup behavior in the alaska range. *Journal of Geophysical Research: Earth Surface*, **121**(1), 64–81

Hock R and Holmgren B (2005) A distributed surface energy-balance model for complex topography and its application to Storglaciären, Sweden. *Journal of Glaciology*, **51**(172), 25–36

Hodge S (1974) Variations in the sliding of a temperate glacier. *Journal of Glaciology*, **13**(69), 349–369

Höfle B, Geist T, Rutzinger M and Pfeifer N (2007) Glacier surface segmentation using airborne laser scanning point cloud and intensity data. *International Archives of Photogrammetry, Remote Sensing and Spatial Information Sciences*, **36**(Part 3), W52

Hooke RL, Iverson NR, Hanson B, Jansson P and Fischer UH (1997) Rheology of till beneath Storglaciären, Sweden. *Journal of Glaciology*, **43**(143), 172–179

Horn BK and Schunck BG (1981) Determining optical flow. *Artificial Intelligence*, **17**, 185–203

Howat IM, Joughin I, Tulaczyk S and Gogineni S (2005) Rapid retreat and acceleration of Helheim glacier, east Greenland. *Geophysical Research Letters*, **32**(22)

Howat IM, Box JE, Ahn Y, Herrington A and McFadden EM (2010) Seasonal variability in the dynamics of marine-terminating outlet glaciers in Greenland. *Journal of Glaciology*, **56**(198), 601–613

Hubbard B and Nienow P (1997) Alpine subglacial hydrology. *Quaternary Science Reviews*, **16**(9), 939–955

Huss M and Hock R (2018) Global-scale hydrological response to future glacier mass loss. *Nature Climate Change*, 1758–6798 (doi: 10.1038/s41558-017-0049-x)

Iken A and Bindschadler RA (1986) Combined measurements of subglacial water pressure and surface velocity of Findelengletscher, Switzerland: conclusions about drainage system and sliding mechanism. *Journal of Glaciology*, **32**(110), 101–119

Immerzeel WW, Van Beek LP and Bierkens MF (2010) Climate change will affect the Asian water towers. *Science*, **328**(5984), 1382–1385

Ingebritsen S and Lyon R (1985) Principal components analysis of multitemporal image pairs. *International Journal of Remote Sensing*, **6**(5), 687–696

Iverson NR and Petersen BB (2011) A new laboratory device for study of subglacial processes: first results on ice–bed separation during sliding. *Journal of Glaciology*, **57**(206), 1135–1146

Jansson P, Näslund JO and Rohde L (2007) Ice sheet hydrology: a review. Technical Report TR-06-34, Svensk Kärnbränslehantering AB

Jarvis GT and Clarke GK (1974) Thermal effects of crevassing on Steele glacier, Yukon territory, Canada. *Journal of Glaciology*, **13**(68), 243–254

Jeong S and Howat IM (2015) Performance of Landsat 8 Operational Land Imager for mapping ice sheet velocity. *Remote Sensing of Environment*, **170**, 90–101

Jóhannesson T, Raymond C and Waddington E (1989) Time–scale for adjustment of glaciers to changes in mass balance. *Journal of Glaciology*, **35**(121), 355–369

References

Joughin I, Smith BE and Abdalati W (2010) Glaciological advances made with interferometric synthetic aperture radar. *Journal of Glaciology*, **56**(200), 1026–1042

Joughin I, Smith B and Howat I (2017) A complete map of Greenland ice velocity derived from satellite data collected over 20 years. *Journal of Glaciology*

Joughin I, Smith BE and Howat IM (2018) A complete map of Greenland ice velocity derived from satellite data collected over 20 years. *Journal of Glaciology*, **64**(243), 1–11

Jouvet G, Weidmann Y, Seguinot J, Funk M, Abe T, Sakakibara D, Seddik H and Sugiyama S (2017) Initiation of a major calving event on the Bowdoin glacier captured by UAV photogrammetry. *The Cryosphere*, **11**(2), 911

Ju J and Roy DP (2008) The availability of cloud-free Landsat ETM+ data over the conterminous United States and globally. *Remote Sensing of Environment*, **112**(3), 1196–1211

Kääb A (2005) *Remote sensing of mountain glaciers and permafrost creep*, volume 48. Geographisches Institut der Universität Zürich, ISBN 3855432449

Kääb A, Lefauconnier B and Melvold K (2005) Flow field of Kronebreen, Svalbard, using repeated Landsat 7 and ASTER data. *Annals of Glaciology*, **42**(1), 7–13

Kääb A, Bolch T, Casey K, Heid T, Kargel JS, Leonard GJ, Paul F and Raup BH (2014a) Glacier mapping and monitoring using multispectral data. In *Global Land Ice Measurements from Space*, 75–112, Springer

Kääb A, Girod L and Berthling I (2014b) Surface kinematics of periglacial sorted circles using structure-from-motion technology. *the Cryosphere*, **8**, 1041–1056 (doi: 10.5194/tc-8-1041-2014)

Kääb A, Winsvold S, Altena B, Nuth C, Nagler T and Wuite J (2016) Glacier remote sensing using Sentinel-2. Part I: Radiometric and geometric performance, and application to ice velocity. *Remote sensing*, **8**(7), 2072–4292 (doi: 10.3390/rs8070598)

Kääb A, Altena B and Mascaro J (2017) Coseismic displacements of the 14 November 2016 Mw7.8 Kaikoura, New Zealand, earthquake using an optical cubesat constellation. *Natural Hazards and Earth System Sciences Discussions*, **2017**, 1–18

Kääb A, Leinss S, Gilbert A, Bühler Y, Gascoin S, Evans S, Bartelt P, Berthier E, Brun F, Chao WA, Farinotti D, Gimbert F, Guo W, Huggel C, Kargel J, Leonard G, Tian L, Treichler D and Yao T (2018) Massive collapse of two glaciers in western Tibet in 2016 after surge-like instability. *Nature Geoscience*, (1752-0908) (doi: 10.1038/s41561-017-0039-7)

Kalnis P, Mamoulis N and Bakiras S (2005) On discovering moving clusters in spatio-temporal data. In *SSTD*, volume 3633, 364–381, Springer

Kamb B and Engelhardt H (1987) Waves of accelerated motion in a glacier approaching surge: the mini-surges of Variegated glacier, Alaska, USA. *Journal of Glaciology*, **33**(113), 27–46

Kamb B and LaChapelle E (1964) Direct observation of the mechanism of glacier sliding over bedrock. *Journal of Glaciology*, **5**(38), 159–172

Kargel JS, Leonard GJ, Bishop MP, Kääb A and Raup B (eds.) (2014) *Global Land Ice Measurements from Space*. Geophysical Sciences, Springer, 1 edition (doi: 10.1007/978-3-540-79818-7)

Kauth RJ and Thomas G (1976) The tasselled cap–a graphic description of the spectral-temporal development of agricultural crops as seen by Landsat. In *Proceedings of the Symposium on Machine Processing of Remotely Sensed Data*, 159

Kenner R, Bühler Y, Delaloye R, Ginzler C and Phillips M (2014) Monitoring of high alpine mass movements combining laser scanning with digital airborne photogrammetry. *Geomorphology*, **206**, 492–504

Kienholz C, Rich J, Arendt A and Hock R (2014) A new method for deriving glacier centerlines applied to glaciers in Alaska and northwest Canada. *The Cryosphere*, **8**(2), 503–519

King C and Lewis W (1961) A tentative theory of ogive formation. *Journal of Glaciology*, **3**(29), 913–939

Kittler J and Illingworth J (1985) Relaxation labelling algorithmsa review. *Image and Vision Computing*, **3**(4), 206–216

Kodde M, Pfeifer N, Gorte B, Geist T and Höfle B (2007) Automatic glacier surface analysis from airborne laser scanning. *International Archives of the Photogrammetry, Remote Sensing and Spatial Information Sciences*, **36**(3/W52), 221–226

König M, Winther J and Isaksson E (2001) Measuring snow and glacier ice properties from satellite. *Reviews of Geophysics*, **39**, 1–27

Korsgaard NJ, Nuth C, Khan SA, Kjeldsen KK, Bjørk AA, Schomacker A and Kjær KH (2016) Digital elevation model and orthophotographs of Greenland based on aerial photographs from 1978–1987. *Scientific data*, **3**, 160032

Kos A, Amann F, Strozzi T, Delaloye R, Ruette J and Springman S (2016) Contemporary glacier retreat triggers a rapid landslide response, Great Aletsch glacier, Switzerland. *Geophysical Research Letters*, **43**(24)

Kraaijenbrink P, Meijer S, Shea J, Pellicciotti F, De Jong S and Immerzeel W (2016) Seasonal surface velocities of a himalayan glacier derived by automated correlation of unmanned aerial vehicle imagery. *Annals of Glaciology*, **57**(71), 103–113

Kriegel HP, Zimek A et al. (2008) Angle-based outlier detection in high-dimensional data. In *Proceedings of the 14th ACM SIGKDD international conference on Knowledge discovery and data mining*, 444–452, ACM

Krimmel R and Meier M (1975) Glacier applications of ERTS images. *Journal of Glaciology*, **15**(73), 391–402

Kroon D (2009) Numerical optimization of kernel based image derivatives. *Short Paper University Twente*

Lang M (1997) Geodetic activities during the 1997 Juneau icefield research program field season. Survey report, Bundeswehr University Munich

Laube P, van Kreveld M and Imfeld S (2005) Finding REMO-detecting relative motion patterns in geospatial lifelines. In *Developments in spatial data handling*, 201–215, Springer

Le Meur E, Gagliardini O, Zwinger T and Ruokolainen J (2004) Glacier flow modelling: a comparison of the Shallow Ice Approximation and the full-Stokes solution. *Comptes Rendus Physique*, **5**(7), 709–722

Leclercq P (2012) *Glacier fluctuations, global temperature and sea-level change*. Ph.D. thesis, Utrecht University

Lefauconnier B, Hagen JO and Rudant JP (1994) Flow speed and calving rate of Kongsbreen glacier, Svalbard, using SPOT images. *Polar Research*, **13**(1), 59–65

Lemke P, Ren J, Alley R, Allison I, Carrasco J, Flato G, Fujii Y, Kaser G, Mote P, Thomas R et al. (2007) Observations: changes in snow, ice and frozen ground. *Climate change*, 337–383

Leprince S, Barbot S, Ayoub F and Avouac JP (2007) Automatic and precise orthorectification, coregistration, and subpixel correlation of satellite images, application to ground deformation measurements. *Geoscience and Remote Sensing, IEEE Transactions on*, **45**(6), 1529–1558

References

Linsbauer A, Frey H, Haeberli W, Machguth H, Azam M and Allen S (2016) Modelling glacier-bed overdeepenings and possible future lakes for the glaciers in the HimalayaKarakoram region. *Annals of Glaciology*, **57**(71), 119–130

Liu H, Wang L, Tang SJ and Jezek KC (2012) Robust multi-scale image matching for deriving ice surface velocity field from sequential satellite images. *International journal of remote sensing*, **33**(6), 1799–1822

Lliboutry L and Reynaud L (1981) Global dynamics of a temperate valley glacier, Mer de Glace, and past velocities deduced from Forbes bands. *Journal of Glaciology*, **27**(96), 207–226

Lüttig C, Neckel N and Humbert A (2017) A combined approach for filtering ice surface velocity fields derived from remote sensing methods. *Remote Sensing*, **9**(10), 1062

Lutz A, Immerzeel W, Shrestha A and Bierkens M (2014) Consistent increase in high Asia's runoff due to increasing glacier melt and precipitation. *Nature Climate Change*, **4**(7), 587

MacAyeal DR (1989) Large-scale ice flow over a viscous basal sediment: Theory and application to ice stream b, Antarctica. *Journal of Geophysical Research: Solid Earth*, **94**(B4), 4071–4087

Mair D, Nienow P, Willis I and Sharp M (2001) Spatial patterns of glacier motion during a high-velocity event: Haut glacier d'Arolla, Switzerland. *Journal of Glaciology*, **47**(156), 9–20

Maksymiuk O, Mayer C and Stilla U (2016) Velocity estimation of glaciers with physically-based spatial regularization Experiments using satellite SAR intensity images. *Remote Sensing of Environment*, **172**, 190–204

Marsh O and Rack W (2012) A method of calculating ice-shelf surface velocity using ICESat altimetry. *Polar Record*, **48**(1), 25–30

Mayer C, Fowler AC, Lambrecht A and Scharrer K (2011) A surge of north Gasherbrum glacier, Karakoram, China. *Journal of Glaciology*, **57**(205), 904–916

McDonald R (1995) CORONA-success for space reconnaissance, a look into the cold war, and a revolution for intelligence. *Photogrammetric Engineering & Remote Sensing*, **61**(6), 689–720

McNabb R, Hock R, ONeel S, Rasmussen LA, Ahn Y, Braun M, Conway H, Herreid S, Joughin I, Pfeffer W et al. (2012) Using surface velocities to calculate ice thickness and bed topography: a case study at Columbia Glacier, Alaska, USA. *Journal of Glaciology*, **58**(212), 1151–1164

Meier M and Post A (1987) Fast tidewater glaciers. *Journal of Geophysical Research: Solid Earth*, **92**(B9), 9051–9058

Meier MF, Rasmussen LA, Krimmel RM, Olsen R and Frank D (1985) Photogrammetric determination of surface altitude, terminus position, and ice velocity of Columbia glacier, Alaska. U.S. geological survey professional papers 1258-F, U.S. geological survey

Meinhart CD, Wereley ST and Santiago JG (1999) PIV measurements of a microchannel flow. *Experiments in fluids*, **27**(5), 414–419

Melkonian AK, Willis MJ and Pritchard ME (2014) Satellite-derived volume loss rates and glacier speeds for the Juneau icefield, Alaska. *Journal of Glaciology*, **60**(222), 743–760

Messerli A and Grinsted A (2015) Image georectification and feature tracking toolbox: ImGRAFT. *Geoscientific Instrumentation, Methods and Data Systems*, **4**(1), 23

Michel R and Rignot E (1999) Flow of glaciar Moreno, Argentina, from repeat-pass Shuttle imaging Radar images: comparison of the phase correlation method with radar interferometry. *Journal of Glaciology*, **45**(149), 93–100

Miles ES, Steiner J, Willis I, Buri P, Immerzeel WW, Chesnokova A and Pellicciotti F (2017) Pond dynamics and supraglacial-englacial connectivity on debris-covered Lirung glacier, Nepal. *Frontiers in Earth Science*, **5**, 69

Millan R, Mouginot J and Rignot E (2017) Mass budget of the glaciers and ice caps of the Queen Elizabeth islands, Canada, from 1991 to 2015. *Environmental Research Letters*, **12**(2), 024016

Minchew B, Simons M, Riel B and Milillo P (2017) Tidally induced variations in vertical and horizontal motion on Rutford ice stream, west Antarctica, inferred from remotely sensed observations. *Journal of Geophysical Research: Earth Surface*, **122**(1), 167–190

Moisan L (2011) Periodic plus smooth image decomposition. *Journal of Mathematical Imaging and Vision*, **39**(2), 161–179

Moon T, Joughin I, Smith B, Broeke MR, Berg WJ, Noël B and Usher M (2014) Distinct patterns of seasonal Greenland glacier velocity. *Geophysical research letters*, **41**(20), 7209–7216

Moons T, Van Gool L and Vergauwen M (2009) 3D reconstruction from multiple images, part 1: Principles. *Foundations and Trends in Computer Graphics and Vision*, **4**(4), 287–404

Morlighem M, Rignot E, Seroussi H, Larour E, Ben Dhia H and Aubry D (2011) A mass conservation approach for mapping glacier ice thickness. *Geophysical Research Letters*, **38**(19)

Mosbeux C, Gillet-Chaulet F and Gagliardini O (2016) Comparison of adjoint and nudging methods to initialise ice sheet model basal conditions. *Geoscientific Model Development*, **9**(7), 2549–2562

Mouginot J and Rignot E (2015) Ice motion of the patagonian icefields of South America: 1984–2014. *Geophysical Research Letters*, **42**(5), 1441–1449

Mousivand A, Verhoef W, Menenti M and Gorte B (2015) Modeling top of atmosphere radiance over heterogeneous non-lambertian rugged terrain. *Remote Sensing*, **7**(6), 8019–8044

Müller F and Iken A (1973) Velocity fluctuations and water regime of Arctic valley glaciers. *International Association of Scientific Hydrology Publication*, **95**, 165–182

Nagler T, Rott H, Hetzenecker M, Wuite J and Potin P (2015) The Sentinel-1 mission: New opportunities for ice sheet observations. *Remote Sensing*, **7**(7), 9371–9389

Narama C, Duishonakunov M, Kääb A, Daiyrov M and Abdrakhmatov K (2010) The 24 july 2008 outburst flood at the western Zyndan glacier lake and recent regional changes in glacier lakes of the Teskey Ala-Too range, Tien Shan, Kyrgyzstan. *Natural Hazards and Earth System Sciences*, **10**(4), 647–659

Naruse R, Fukami H and Aniya M (1992) Short-term variations in flow velocity of Glaciar Soler, Patagonia, Chile. *Journal of Glaciology*, **38**(128), 152–156

Ng FS (2015) Spatial complexity of ice flow across the antarctic ice sheet. *Nature Geoscience*, **8**(11), 847

Nguyen T, Méger N, Rigotti C, Pothier C, Trouvé E and Gourmelen N (2017) Handling coherence measures of displacement field time series: Application to greenland ice sheet glaciers. In *9th International Workshop on the Analysis of Multitemporal Remote Sensing Images (MultiTemp)*, 1–4, IEEE

Ninomiya Y, Fu B and Cudahy TJ (2005) Detecting lithology with advanced spaceborne thermal emission and reflection radiometer (ASTER) multispectral thermal infrared 'radiance-at-sensor' data. *Remote Sensing of Environment*, **99**(1), 127–139

References

Nobach H and Honkanen M (2005) Two-dimensional Gaussian regression for sub-pixel displacement estimation in particle image velocimetry or particle position estimation in particle tracking velocimetry. *Experiments in fluids*, **38**(4), 511–515

Nolan M (2003) The galloping glacier trots: Decadal-scale speed oscillations within the quiescent phase. *Annals of Glaciology*, **36**, 7–13

Nuth C, Kohler J, König M, Von Deschwanden A, Hagen J, Kääb A, Moholdt G and Pettersson R (2013) Decadal changes from a multi-temporal glacier inventory of Svalbard. *The Cryosphere*, **7**(5), 1603

Nye J (1958) A theory of wave formation in glaciers. *Physics of the movement of ice. Publications of the International Association of Hydrological Sciences (IAHS)*, **47**, 139–154

Nye J (1965) The flow of a glacier in a channel of rectangular, elliptic or parabolic cross-section. *Journal of Glaciology*, **5**(41), 661–690

Oerlemans J (1997) Climate sensitivity of Franz Josef glacier, New Zealand, as revealed by numerical modeling. *Arctic and Alpine Research*, 233–239

Oerlemans J (2007) Estimating response times of vadret da Morteratsch, vadret da Palü, Briksdalsbreen and Nigardsbreen from their length records. *Journal of Glaciology*, **53**(182), 357–362

Oerlemans J (2013) A note on the water budget of temperate glaciers. *The Cryosphere*, **7**(5), 1557

Oerlemans J and Reichert B (2000) Relating glacier mass balance to meteorological data by using a seasonal sensitivity characteristic. *Journal of Glaciology*, **46**(152), 1–6

Oh J (2011) *Novel approach to epipolar resampling of HRSI and satellite stereo imagery-based georeferencing of aerial images*. Ph.D. thesis, Ohio State University

O'Neel S, Pfeffer WT, Krimmel R and Meier M (2005) Evolving force balance at Columbia Glacier, Alaska, during its rapid retreat. *Journal of Geophysical Research: Earth Surface*, **110**(F3)

Oppenheim AV and Lim JS (1981) The importance of phase in signals. *Proceedings of the IEEE*, **69**(5), 529–541

Østrem G (1975) ERTS data in glaciologyan effort to monitor glacier mass balance from satellite imagery. *Journal of Glaciology*, **15**(73), 403–415

Padfield D (2012) Masked object registration in the Fourier domain. *IEEE Transactions on Image Processing*, **21**(5), 2706–2718

Palubinskas G, Reinartz P and Bamler R (2010) Image acquisition geometry analysis for the fusion of optical and radar remote sensing data. *International Journal of Image and Data Fusion*, **1**(3), 271–282

Papasodoro C, Royer A, Langlois A and Berthier E (2016) Potential of Radarsat-2 stereo radargrammetry for the generation of glacier DEMs. *Journal of Glaciology*, **62**(233), 486–496

Parrot JF, Lyberis N, Lefauconnier B and Manby G (1993) SPOT multispectral data and digital terrain model for the analysis of ice-snow fields on arctic glaciers. *International Journal of Remote Sensing*, **14**(3), 425–440

Paterson W (1994) *The physics of glaciers*. Elsevier, ISBN 0750647426

Patterson T and Jenny B (2011) The development and rationale of cross-blended hypsometric tints. *Cartographic Perspectives*, (69), 31–46

Paul F (2000) Evaluation of different methods for glacier mapping using Landsat TM. In *Proceedings of EARSeL-SIG workshop land ice and snow*

Paul F, Bolch T, Kääb A, Nagler T, Nuth C, Scharrer K, Shepherd A, Strozzi T, Ticconi F, Bhambri R et al. (2015) The glaciers climate change initiative: Methods for creating glacier area, elevation change and velocity products. *Remote Sensing of Environment*, **162**, 408–426

Peel M, Finlayson B and McMahon T (2007) Updated world map of the Köppen-Geiger climate classification. *Hydrology and Earth system sciences discussions*, **4**(2), 439–473

Pfeffer W (2007) A simple mechanism for irreversible tidewater glacier retreat. *Journal of Geophysical Research: Earth Surface*, **112**(F3)

Pfeffer WT, Meier M and Illangasekare T (1991) Retention of Greenland runoff by refreezing: implications for projected future sea level change. *Journal of Geophysical Research*, **96**(C12), 22117–22124 (doi: 10.1029/91JC02502)

Pfeffer WT, Arendt AA, Bliss A, Bolch T, Cogley JG, Gardner AS, Hagen JO, Hock R, Kaser G, Kienholz C et al. (2014) The Randolph glacier inventory: a globally complete inventory of glaciers. *Journal of Glaciology*, **60**(221), 537–552

Phillips T, Rajaram H and Steffen K (2010) Cryo-hydrologic warming: A potential mechanism for rapid thermal response of ice sheets. *Geophysical Research Letters*, **37**(20)

Phillips T, Rajaram H, Colgan W, Steffen K and Abdalati W (2013) Evaluation of cryo-hydrologic warming as an explanation for increased ice velocities in the wet snow zone, Sermeq Avannarleq, West Greenland. *Journal of Geophysical Research: Earth Surface*, **118**(3), 1241–1256

Pillewizer W and Voigt U (1968) Block movement of glaciers. *Geodätische und Geophysikalische Veröffentlichungen*, **3**(9)

Poghosyan A and Golkar A (2017) Cubesat evolution: Analyzing cubesat capabilities for conducting science missions. *Progress in Aerospace Sciences*, **88**, 59–83

Posamentier H (1978) Thoughts on ogive formation. *Journal of Glaciology*, **20**, 218–220

Praks J, Kestilä A, Hallikainen M, Saari H, Antila J, Janhunen P and Vainio R (2011) Aalto-1-an experimental nanosatellite for hyperspectral remote sensing. In *IEEE International Geoscience and Remote Sensing Symposium*, 4367–4370, IEEE

Prantl H, Nicholson L, Sailer R, Hanzer F, Juen IF and Rastner P (2017) Glacier snowline determination from terrestrial laser scanning intensity data. *Geosciences*, **7**(3), 60

Price KE (1985) Relaxation matching techniques - a comparison. *IEEE Transactions on Pattern Analysis and Machine Intelligence*, (5), 617–623

Price S, Payne A, Catania G and Neumann T (2008) Seasonal acceleration of inland ice via longitudinal coupling to marginal ice. *Journal of Glaciology*, **54**(185), 213–219

Pritchard HD (2017) Asias glaciers are a regionally important buffer against drought. *Nature*, **545**(7653), 169–174

Quincey D and Luckman A (2009) Progress in satellite remote sensing of ice sheets. *Progress in Physical Geography*, **33**(4), 547–567

Quincey DJ, Glasser NF, Cook SJ and Luckman A (2015) Heterogeneity in Karakoram glacier surges. *Journal of Geophysical Research: Earth Surface*, **120**(7), 1288–1300

References

Rabatel A, Sirguey P, Drolon V, Maisongrande P, Arnaud Y, Berthier E, Davaze L, Dedieu JP and Dumont M (2017) Annual and seasonal glacier-wide surface mass balance quantified from changes in glacier surface state: A review on existing methods using optical satellite imagery. *Remote Sensing*, **9**(5), 507

Rabault J, Kolaas J and Jensen A (2017) Performing particle image velocimetry using artificial neural networks: a proof-of-concept. *Measurement Science and Technology*, **28**(12), 125301

Raffel M, Willert C, Wereley S and Kompenhans J (2013) *Particle image velocimetry: a practical guide*. Springer, 2 edition (doi: 10.1007/978-3-540-72308-0)

Raup B, Kieffer H, Hare T and Kargel J (2000) Generation of data acquisition requests for the ASTER satellite instrument for monitoring a globally distributed target: glaciers. *IEEE transactions on Geosciences and Remote Sensing*, **38**(2), 1–10

Raup B, Scambos T and Haran T (2005) Topography of streaklines on an Antarctic ice shelf from photoclinometry applied to a single advanced land imager (ALI) image. *Geoscience and Remote Sensing, IEEE Transactions on*, **43**(4), 736–742, ISSN 0196-2892

Redpath T, Sirguey P, Fitzsimons S and Kääb A (2013) Accuracy assessment for mapping glacier flow velocity and detecting flow dynamics from aster satellite imagery: Tasman glacier, new zealand. *Remote sensing of environment*, **133**, 90–101

Rees W (2006) *Remote sensing of snow and ice*. CRC, ISBN 0415298318

Rees WG and Arnold NS (2007) Mass balance and dynamics of a valley glacier measured by high-resolution LiDAR. *Polar Record*, **43**(4), 311–319

Reiner M (1964) The deborah number. *Physics today*, **17**(1), 62

Rentsch H (1997) Terrestrial photogrammetry on the Juneau icefield. *Schriftenreihe Studiengang Vermessungswesen, Universität der Bundeswehr München*, (50), 167–170

Rentsch H, Welsch W, Heipke C and Miller MM (1990) Digital terrain models as a tool for glacier studies. *Journal of Glaciology*, **36**(124), 273–278

Revaud J, Weinzaepfel P, Harchaoui Z and Schmid C (2016) Deepmatching: Hierarchical deformable dense matching. *International Journal of Computer Vision*, **120**(3), 300–323

Rius A, Nogués-Correig O, Ribó S, Cardellach E, Oliveras S, Valencia E, Park H, Tarongí JM, Camps A, van der Marel H, vanBree R and Altena B (2012) Altimetry with GNSS-R interferometry: First proof of concept experiment. *GPS solutions*, **16**(2), 231–241

Rolstad C, Amlien J, Hagen JO and Lundén B (1997) Visible and near-infrared digital images for determination of ice velocities and surface elevation during a surge on Osbornebreen, a tidewater glacier in Svalbard. *Annals of Glaciology*, **24**, 255–261

Rommelaere V and MacAyeal DR (1997) Large-scale rheology of the Ross ice shelf, Antarctica, computed by a control method. *Annals of Glaciology*, **24**, 43–48

Rosenau R, Scheinert M and Dietrich R (2015) A processing system to monitor Greenland outlet glacier velocity variations at decadal and seasonal time scales utilizing the Landsat imagery. *Remote sensing of environment*, **169**, 1–19 (doi: 10.1016/j.rse.2015.07.012)

Rösgen T (2003) Optimal subpixel interpolation in particle image velocimetry. *Experiments in Fluids*, **35**(3), 252–256

Rothlisberger H (1981) Eislawinen und ausbrüche von gletscherseen. *Jahrbuch der Schweizerischell Naturforschellden Gesellschaft. wissenschaftlicher Teil*, **1978**, 170–212

Rott H, Scheuchl B, Siegel A and Grasemann B (1999) Monitoring very slow slope movements by means of SAR interferometry: a case study from a mass waste above a reservoir in the ötztal alps, Austria. *Geophysical Research Letters*, **26**(11), 1629–1632

Rousseeuw PJ, Ruts I and Tukey JW (1999) The bagplot: a bivariate boxplot. *The American Statistician*, **53**(4), 382–387

Sá C and Grieco J (2016) Open data for science, policy, and the public good. *Review of Policy Research*, **33**(5), 526–543

Sandau R (2010) Status and trends of small satellite missions for Earth observation. *Acta Astronautica*, **66**(1), 1–12

Saunier S, Northrop A, Lavender S, Galli L, Ferrara R, Mica S, Biasutti R, Goryl P, Gascon F and Meloni M (2017) Bulk processing of the Landsat MSS/TM/ETM+ archive of the European Space Agency: an insight into the level 1 MSS processing. In *Image and Signal Processing for Remote Sensing XXIII*, volume 10427, 1042702, International Society for Optics and Photonics

Scambos T and Fahnestock M (1998) Improving digital elevation models over ice sheets using AVHRR-based photoclinometry. *Journal of glaciology*, **44**(146), 97–103

Scambos T, Dutkiewicz M, Wilson J and Bindschadler R (1992) Application of image cross-correlation to the measurement of glacier velocity using satellite image data. *Remote sensing of environment*, **42**(3), 177–186

Scambos T, Fahnestock M, Moon T, Gardner A and Klinger M (2016) Global land ice velocity extraction from Landsat 8 (GoLIVE), version 1. NSIDC: National Snow and Ice Data Center, Boulder, Colorado USA (doi: 10.7265/N5ZP442B)

Scambos TA, Bohlander J, Shuman Cu and Skvarca P (2004) Glacier acceleration and thinning after ice shelf collapse in the Larsen B embayment, Antarctica. *Geophysical Research Letters*, **31**(18)

Scaramuzza P, Micijevic E and Chander G (2004) SLC gap-filled products phase one methodology. *Landsat Technical Notes*, 5

Scarano F (2001) Iterative image deformation methods in PIV. *Measurement science and technology*, **13**(1), R1

Scharr H (2007) Optimal filters for extended optical flow. *Lecture Notes in Computer Science*, **3417**, 14–29

Scherler D and Strecker MR (2012) Large surface velocity fluctuations of Biafo glacier, central Karakoram, at high spatial and temporal resolution from optical satellite images. *Journal of Glaciology*, **58**(209), 569–580

Schuler DL, Ainsworth T, Lee J and De Grandi G (1998) Topographic mapping using polarimetric SAR data. *International Journal of Remote Sensing*, **19**(1), 141–160

Schuler TV, Loe E, Taurisano A, Eiken T, Hagen JO and Kohler J (2007) Calibrating a surface mass-balance model for Austfonna ice cap, Svalbard. *Annals of Glaciology*, **46**, 241–248

Schwalbe E, Maas H, Dietrich R and Ewert H (2008) Glacier velocity determination from multi temporal terrestrial long range laser scanner point clouds. *The International Archives of the Photogrammetry, Remote Sensensing and Spatial Information Sciences*, **37**, 457–462

Schwalbe E, Koschitzki R and Maas HG (2016) Recognition of drainage tunnels during glacier lake outburst events from terrestrial image sequences. *ISPRS International Archives of Photogrammetry Remote Sensing and Spatial Information Sciences*, **XLI-B8**, 537–543 (doi: 10.5194/isprsarchives-XLI-B8-537-20)

References

Selva D and Krejci D (2012) A survey and assessment of the capabilities of cubesats for Earth observation. *Acta Astronautica*, **74**, 50–68

Serreze M, Walsh J, Chapin FS, Osterkamp T, Dyurgerov M, Romanovsky V, Oechel W, Morison J, Zhang T and Barry R (2000) Observational evidence of recent change in the northern high-latitude environment. *Climatic change*, **46**(1-2), 159–207

Sevestre H, Benn DI, Hulton NR and Bælum K (2015) Thermal structure of Svalbard glaciers and implications for thermal switch models of glacier surging. *Journal of Geophysical Research: Earth Surface*, **120**(10), 2220–2236

Shrestha DP and Zinck JA (2001) Land use classification in mountainous areas: integration of image processing, digital elevation data and field knowledge (application to Nepal). *International Journal of Applied Earth Observation and Geoinformation*, **3**(1), 78–85

Sidjak R and Wheate R (1999) Glacier mapping of the Illecillewaet icefield, British Columbia, Canada, using Landsat TM and digital elevation data. *International Journal of Remote Sensing*, **20**(2), 273–284

Sjögren B, Brandt O, Nuth C, Isaksson E, Pohjola V, Kohler J and Van De Wal RS (2007) Determination of firn density in ice cores using image analysis. *Journal of Glaciology*, **53**(182), 413–419

Skvarca P, Raup B and De Angelis H (2003) Recent behaviour of glaciar Upsala, a fast-flowing calving glacier in Lago Argentino, southern Patagonia. *Annals of Glaciology*, **36**(1), 184–188

Socolinsky DA and Wolff LB (2002) Multispectral image visualization through first-order fusion. *IEEE Transactions on Image Processing*, **11**(8), 923–931

Sohn HG, Kim GH and Yom JH (2004) Mathematical modelling of historical reconnaissance CORONA KH-4B imagery. *The Photogrammetric Record*, **19**(105), 51–66

Stearns L and Hamilton G (2005) A new velocity map for Byrd glacier, east Antarctica, from sequential ASTER satellite imagery. *Annals of glaciology*, **41**(1), 71–76

Steinemann S (1954) Results of preliminary experiments on the plasticity of ice crystals. *Journal of Glaciology*, **2**(16), 404–416

Stoffel M and Huggel C (2012) Effects of climate change on mass movements in mountain environments. *Progress in physical geography*, **36**(3), 421–439

Stroeven AP, Hättestrand C, Kleman J, Heyman J, Fabel D, Fredin O, Goodfellow BW, Harbor JM, Jansen JD, Olsen L et al. (2016) Deglaciation of Fennoscandia. *Quaternary Science Reviews*, **147**, 91–121

Strozzi T, Kääb A and Frauenfelder R (2004) Detecting and quantifying mountain permafrost creep from in situ inventory, space-borne radar interferometry and airborne digital photogrammetry. *International Journal of Remote Sensing*, **25**(15), 2919–2931

Strozzi T, Werner C, Wiesmann A and Wegmuller U (2012) Topography mapping with a portable real-aperture radar interferometer. *IEEE Geoscience and Remote Sensing Letters*, **9**(2), 277–281

Strozzi T, Kääb A and Schellenberger T (2017) Frontal destabilization of Stonebreen, Edgeøya, Svalbard. *The Cryosphere*, **11**(1), 553

Stumpf A, Malet JP, Kerle N, Niethammer U and Rothmund S (2013) Image-based mapping of surface fissures for the investigation of landslide dynamics. *Geomorphology*, **186**, 12–27

Stumpf A, Michéa D and Malet JP (2018) Improved co-registration of Sentinel-2 and Landsat-8 imagery for Earth surface motion measurements. *Remote Sensing*, **10**(2), 160

Sugiyama S and Gudmundsson H (2004) Short-term variations in glacier flow controlled by subglacial water pressure at Lauteraargletscher, Bernese Alps, Switzerland. *Journal of Glaciology*, **50**(170), 353–362

Tebaldini S, Nagler T, Rott H and Heilig A (2016) Imaging the internal structure of an alpine glacier via L-band airborne SAR tomography. *IEEE Transactions on Geoscience and Remote Sensing*, **54**(12), 7197–7209

Telling JW, Glennie C, Fountain AG and Finnegan DC (2017) Analyzing glacier surface motion using lidar data. *Remote Sensing*, **9**(3), 283

Tennant C, Menounos B, Wheate R and Clague J (2012) Area change of glaciers in the Canadian rocky mountains, 1919 to 2006. *The Cryosphere*, **6**(6), 1541

Teunissen P (2000) *Testing theory*. Series on Mathematical Geodesy and Positioning, Delft Academic Press, ISBN 9040719756

Thomson LI and Copland L (2017) Multi-decadal reduction in glacier velocities and mechanisms driving deceleration at polythermal White glacier, Arctic Canada. *Journal of Glaciology*, **63**(239), 450–463

Thorsteinsson T, Raymond CF, Gudmundsson GH, Bindschadler RA, Vornberger P and Joughin I (2003) Bed topography and lubrication inferred from surface measurements on fast-flowing ice streams. *Journal of Glaciology*, **49**(167), 481–490

Tian L, Yao T, Gao Y, Thompson L, Mosley-Thompson E, Muhammad S, Zong J, Wang C, Jin S and Li Z (2017) Two glaciers collapse in western Tibet. *Journal of Glaciology*, **63**(237), 194–197

Toth C and Jóźków G (2016) Remote sensing platforms and sensors: A survey. *ISPRS Journal of Photogrammetry and Remote Sensing*, **115**, 22–36

Toutin T and Gray L (2000) State-of-the-art of elevation extraction from satellite SAR data. *ISPRS Journal of Photogrammetry and Remote Sensing*, **55**(1), 13–33

Toutin T, Blondel E, Clavet D and Schmitt C (2013) Stereo radargrammetry with Radarsat-2 in the Canadian Arctic. *IEEE Transactions on Geoscience and Remote Sensing*, **51**(5), 2601–2609

Treichler D and Kääb A (2017) Snow depth from ICESat laser altimetrya test study in southern Norway. *Remote Sensing of Environment*, **191**, 389–401

Truffer M and Echelmeyer KA (2003) Of isbræ and ice streams. *Annals of Glaciology*, **36**(1), 66–72

Truffer M, Harrison WD and Echelmeyer KA (2000) Glacier motion dominated by processes deep in underlying till. *Journal of Glaciology*, **46**(153), 213–221

Tsushima A, Matoba S, Shiraiwa T, Okamoto S, Sasaki H, Solie D and Yoshikawa K (2015) Reconstruction of recent climate change in Alaska from the Aurora peak ice core, central Alaska. *Climate of the Past*, **11**(2), 217–226

Uras S, Girosi F, Verri A and Torre V (1988) A computational approach to motion perception. *Biological Cybernetics*, **60**(2), 79–87

Usset J, Maity A, Staicu AM and Schwartzman A (2015) Glacier terminus estimation from Landsat image intensity profiles. *Journal of Agricultural, Biological, and Environmental Statistics*, **20**(2), 279–298

van de Wal R, Boot W, van den Broeke M, Smeets C, Reijmer C, Donker J and Oerlemans J (2008) Large and rapid melt-induced velocity changes in the ablation zone of the Greenland ice sheet. *science*, **321**(5885), 111–113

van der Veen CJ (2013) *Fundamentals of glacier dynamics*. CRC Press

References

van der Veen CJ and Whillans I (1989) Force budget: I. theory and numerical methods. *Journal of Glaciology*, **35**(119), 53–60

van Pelt W and Kohler J (2015) Modelling the long-term mass balance and firn evolution of glaciers around Kongsfjorden, Svalbard. *Journal of Glaciology*, **61**(228), 731–744

Vaughan DG (1993) Relating the occurrence of crevasses to surface strain rates. *Journal of Glaciology*, **39**(132), 255–266

Vincent C and Moreau L (2016) Sliding velocity fluctuations and subglacial hydrology over the last two decades on Argentière glacier, Mont Blanc area. *Journal of Glaciology*, **62**(235), 805–815

Vosselman G (1992) *Relational matching*, volume 628 of *Lecture Notes in Computer Science*. Springer Science & Business Media

Voytenko D, Dixon T, Holland D, Cassotto R, Howat I, Fahnestock M, Truffer M and De La Peña S (2017) Acquisition of a 3 min, two-dimensional glacier velocity field with terrestrial radar interferometry. *Journal of Glaciology*, 1–8

Waddington E (1986) Wave ogives. *Journal of Glaciology*, **32**(112), 325–334

Warner RC and Roberts JL (2013) Pine island glacier (Antarctica) velocities from Landsat7 images between 2001 and 2011: FFT-based image correlation for images with data gaps. *Journal of Glaciology*, **59**(215), 571–582

Warren SG (1982) Optical properties of snow. *Reviews of Geophysics*, **20**(1), 67–89

Watson C and Quincey D (2012) Glacier movement. In S Cook, L Clarke and J Nield (eds.), *Geomorphological Techniques (Online Edition)*, British Society for Geomorphology, London

Welsch W (2000) Juneau icefield, Alaska: Glacio-geodetic measurements. Geodesy and Geomatics Engineering Technical Report 205, Festschrift in Honour of Adam Chrzanowski. University of New Brunswick.

Westerweel J (1997) Fundamentals of digital particle image velocimetry. *Measurement science and technology*, **8**(12), 1379

Westerweel J, Geelhoed P and Lindken R (2004) Single-pixel resolution ensemble correlation for micro-PIV applications. *Experiments in Fluids*, **37**(3), 375–384

Weydahl DJ (2001) Analysis of ERS tandem SAR coherence from glaciers, valleys, and fjord ice on Svalbard. *IEEE Transactions on Geoscience and Remote Sensing*, **39**(9), 2029–2039

Whillans IM and Tseng YH (1995) Automatic tracking of crevasses on satellite images. *Cold Regions Science and Technology*, **23**(2), 201–214

Winsvold S (2017) *Mapping glaciers using time-series of remote sensing data*. Ph.D. thesis, University of Oslo

Winsvold SH, Kääb A, Nuth C, Andreassen LM, van Pelt WJ and Schellenberger T (2018) Using SAR satellite data time series for regional glacier mapping. *The Cryosphere*, **12**(3), 867

Wiscombe W and Warren S (1980) A model for the spectral albedo of snow. i: Pure snow. *Journal of the Atmospheric Sciences*, **37**(12), 2712–2733

Wouters B, Bonin J, Chambers D, Riva R, Sasgen I and Wahr J (2014) GRACE, time-varying gravity, Earth system dynamics and climate change. *Reports on Progress in Physics*, **77**(11), 116801

Wu QX (1995) A correlation-relaxation-labeling framework for computing optical flow-template matching from a new perspective. *IEEE Transactions on Pattern Analysis and Machine Intelligence*, **17**(9), 843–853

Wulder MA, Masek JG, Cohen WB, Loveland TR and Woodcock CE (2012) Opening the archive: How free data has enabled the science and monitoring promise of Landsat. *Remote Sensing of Environment*, **122**, 2–10

Wulder MA, White JC, Loveland TR, Woodcock CE, Belward AS, Cohen WB, Fosnight EA, Shaw J, Masek JG and Roy DP (2016) The global Landsat archive: Status, consolidation, and direction. *Remote Sensing of Environment*, **185**, 271–283

Zeisl B, Georgel PF, Schweiger F, Steinbach EG, Navab N and Munich G (2009) Estimation of location uncertainty for scale invariant features points. In *British Machine Vision Conference*, 1–12

Zhu Z and Woodcock CE (2012) Object-based cloud and cloud shadow detection in Landsat imagery. *Remote sensing of environment*, **118**, 83–94

Zwally HJ (1977) Microwave emissivity and accumulation rate of polar firn. *Journal of Glaciology*, **18**(79), 195–215

Zwinger T, Schäfer M, Martín C and Moore JC (2014) Influence of anisotropy on velocity and age distribution at Scharffenbergbotnen blue ice area. *The Cryosphere*, **8**(2), 607–621

Part II

Journal Publications

Paper I: Elevation change and improved velocity retrieval using orthorectified optical satellite data from different orbits

remote sensing

MDPI

Article

Elevation Change and Improved Velocity Retrieval Using Orthorectified Optical Satellite Data from Different Orbits

Bas Altena * and **Andreas Kääb**

Department of Geosciences, University of Oslo, P.O. Box 1047, 0316 Oslo, Norway; kaeaeb@geo.uio.no
* Correspondence: bas.altena@geo.uio.no; Tel.: +47-22-850-113

Academic Editors: Frank Paul, Kate Briggs, Robert McNabb, Christopher Nuth, Jan Wuite, Xiaofeng Li and Prasad S. Thenkabail
Received: 21 January 2017; Accepted: 17 March 2017; Published: 22 March 2017

Abstract: Optical satellite products are available at different processing levels. Of these products, terrain corrected (i.e., orthorectified) products are the ones mostly used for glacier displacement estimation. For terrain correction, a digital elevation model (DEM) is used that typically stems from various data sources with variable qualities, from dispersed time instances, or with different spatial resolutions. Consequently, terrain representation used for orthorectifying satellite images is often in disagreement with reality at image acquisition. Normally, the lateral orthoprojection offsets resulting from vertical DEM errors are taken into account in the geolocation error budget of the corrected images, or may even be neglected. The largest offsets of this type are often found over glaciers, as these may show strong elevation changes over time and thus large elevation errors in the reference DEM with respect to image acquisition. The detection and correction of such orthorectification offsets is further complicated by ice flow which adds a second offset component to the displacement vectors between orthorectified data. Vice versa, measurement of glacier flow is complicated by the inherent superposition of ice movement vectors and orthorectification offset vectors. In this study, we try to estimate these orthorectification offsets in the presence of terrain movement and translate them to elevation biases in the reference surface. We demonstrate our method using three different sites which include very dynamic glaciers. For the Oriental Glacier, an outlet of the Southern Patagonian icefield, Landsat 7 and 8 data from different orbits enabled the identification of trends related to elevation change. For the Aletsch Glacier, Swiss Alps, we assess the terrain offsets of both Landsat 8 and Sentinel-2A: a superior DEM appears to be used for Landsat in comparison to Sentinel-2, however a systematic bias is observed in the snow covered areas. Lastly, we demonstrate our methodology in a pipeline structure; displacement estimates for the Helheim-glacier, in Greenland, are mapped and corrected for orthorectification offsets between data from different orbits, which enables a twice as dense a temporal resolution of velocity data, as compared to the standard method of measuring velocities from repeat-orbit data only. In addition, we introduce and implement a novel matching method which uses image triplets. By formulating the three image displacements as a convolution, a geometric constraint can be exploited. Such a constraint enhances the reliability of the displacement estimations. Furthermore the implementation is simple and computationally swift.

Keywords: glacier motion; image matching; cross-track offset; ortho-rectification error; triplet-matching

---

1. Introduction

Repeat satellite observation is a powerful way of estimating planetary surface displacements [1], for geophysical phenomena such as glaciers especially. Monitoring glacier velocities is important because observable flow instabilities are a direct result of changes in basal stress [2] or frontal dynamics [3] and thus important to understand glacier dynamics and its impacts, such as on sea level changes or glacier-related hazards. These processes of interest often occur in either inaccessible or dangerous locations (e.g., due to icefall) which favors remote sensing methods. In particular the Landsat-archive is a popular resource for worldwide glacier velocity estimation [4], due to its long history and free availability [5,6]. Nonetheless, for many applications, the matching of whiskbroom (up to Landsat 7) and pushbroom sensors (Landsat 8) is limited to acquisitions from the same relative orbit. As such, the repeat data are acquired with similar looking angles, and differential displacements from orthorectification offsets in the different images are minimized due to vertical DEM errors. Alternatively, the orthoprojection discrepancy can be adjusted by remapping, for instance with the help of elevation data [6]. However, in many cases there will be a difference between the DEM used for orthorectification and the true elevation at acquisition time as glaciers are dynamic topographic features that may exhibit vertical changes of many meters per year. Other methodologies to treat orthorectification offsets have been proposed, but these focused on improving the miss-alignment, assuming stable terrain [7–10]. In the complicated case of a changing topography, an independent, self-reliant method is preferred, to limit the introduction of varying bias through the additional elevation data sources used for terrain corrections.

The availability of suitable optical image pairs for displacement estimation is further hampered by the presence of clouds which obstruct the visibility of the Earth surface. Hence, a method capable of handling orthorectified products from different sensors and orbits can increase the potential availability of suitable image pairs. Such cross-platform harmonization with the Landsat archive can fill the gaps in time (e.g., using SPOT-legacy or CBERS-program), or for recent studies, increase the spatial and temporal coverage (e.g., combining Landsat 8 with Sentinel-2 or Ziyuan-3A). This is feasible when exploiting the fact that such instruments are on satellites following similar sun-synchronous orbits. It is thus of interest to explore the possibilities of tracking terrain displacements from repeat images that are contaminated by differential orthorectification offsets, originating from the projection of DEM errors along different viewing angles, i.e., from different orbits. Hitherto, no integrated methodology is available for this purpose.

A second, unrelated challenge posed by optical displacement estimation that we try to tackle in this work as a side-result, lies in the reliability of a match. Conventionally, two images from different times are compared, providing no redundancy and thus limiting the ability to check whether the displacement measured is correct. Common practice is to look for supporting evidence in the geographical vicinity of a displacement or within a temporal stack of displacements, both at a later stage in the post-processing. However if an additional, third image is available, this can be included in the matching process to increase redundancy and enhance the reliability of the estimation. Consequently, geometric or temporal constraints can be imposed, as explored in [11–13]. We follow up on this work and formulate an approach which is more robust and computationally efficient.

In this contribution, we first provide the necessary background on sensor geometry, orthorectification, the mathematical formulation of imaging projection and related offsets, and the matching of such offsets. A description of the method developed here follows. After introducing the study sites and data employed, we present and discuss our results for three different application scenarios and wrap up with our conclusions.

2. Image Processing Background

2.1. Sensor Geometry

The acquisition geometry of a pushbroom sensor, such as the Landsat 8 or Sentinel-2, and of a whiskbroom sensor, such as the Landsat series up to 7, is illustrated in Figure 1. For simplicity, the world coordinate frame (with coordinates in X,Y,Z) is aligned with the orientation of the flight path ($\mathbf{e}$, with normal $\mathbf{n}$). The mapping of a pixel on the ground (P) onto the (line) sensor (p with coordinates in i,j) can be written in matrix form as [14]:

$$\underbrace{\begin{bmatrix} j \\ i \\ 1 \end{bmatrix}}_{p} = \underbrace{\begin{bmatrix} \alpha_x & 0 & \tau_j \\ 0 & \alpha_y & \tau_i \\ 0 & 0 & 1 \end{bmatrix} \begin{bmatrix} e_x & e_x^{\perp} & n_x \\ e_y & e_y^{\perp} & n_y \\ e_z & e_z^{\perp} & n_z \end{bmatrix}}_{\mathbf{KR}} \underbrace{\begin{bmatrix} X - X_P \\ Y - Y_P \\ Z - Z_P \end{bmatrix}}_{P} \tag{1}$$

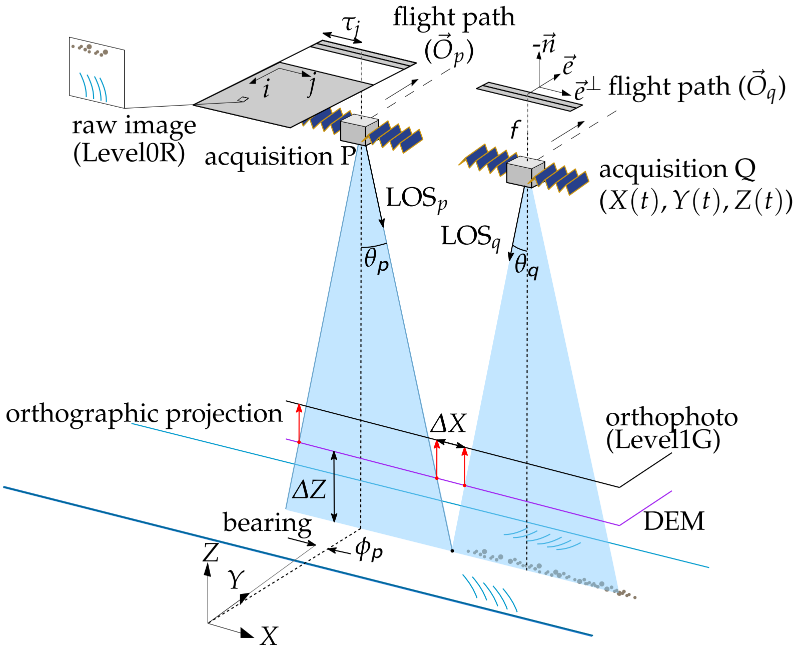

Figure 1. Schematic drawing of orthorectification offsets due to DEM errors in respect to different viewing acquisitions.

In this case, the axis directions of the coordinate system and the sensor are similar, thus the rotation matrix ($\mathbf{R}$) reduces to an identity matrix ($\mathbf{I}$). The camera matrix ($\mathbf{K}$) is composed of a translation (τ) to move from pixel origin to the edge of the sensor array. On the diagonal, the focal length (α) is given in pixel units. It is composed of the focal length and the size of a photosensitive cell ($\alpha_x = f \cdot m_j$). For this example, a line scanner is used, thus the principal point given by the translation ($\vec{\tau}$) is zero for the j-component. A point in space is seen when, after transformation, the pixel coordinates fall within the size of the sensor array. The formation of a two-dimensional image is due to the movement, scanning the area as though it where cleaning with a whiskbroom. When the pushbroom case is taken, then the dependency in the Y-direction drops and one obtains:

$$j = (\alpha_x \cdot X)/Z = \alpha_x \cdot \tan\theta_p. \tag{2}$$

Here $1/Z$ emerges in Equation (2) because of the translation from a homogenous coordinate formulation in Equation (1) to a Cartesian system. This formulation has focal length and pixel size, but can be reformulated to be written as a function of zenith distance (θ_p). By doing so, the focal length cancels out;

$$\tan\theta_p = X/Z = (X + \Delta X_p)/(Z + \Delta Z). \tag{3}$$

Here, we introduce the vertical bias (ΔZ) between the elevation between acquisition and the elevation of the DEM used for orthorectification. Due to Thales' theorem, the across-track offset (ΔX_p) appears. Now, terms can be rearranged so that the terms of each axis are on either side of the equals sign:

$$\tan\theta_p \cdot (Z + \Delta Z) = X + \Delta X_p, \tag{4}$$

or written out fully,

$$(\tan\theta_p \cdot Z) + (\tan(\theta_p) \cdot \Delta Z) = X + \Delta X_p. \tag{5}$$

If Equations (3) and (5) are now combined, one ends up with the simple formulation for dependency of elevation bias to lateral displacement within an image:

$$\tan\theta_p \cdot \Delta Z = \Delta X_p. \tag{6}$$

From this equation it is clear that the displacement artifacts become more pronounced as one migrates along the across-track direction. This is less the case in the along-track direction, as it is only one pixel wide. Furthermore, the offset can have a negative sign, which is dependent on the observation angle and on whether the elevation bias is positive or negative.

2.2. Orthorectification

The orthorectification process adjusts the satellite acquisition to meet the properties of a map with orthogonal projection. The perspective distortions and terrain variations are compensated through knowledge of the instrument's flight path, projection geometry, and the local terrain geometry. Position, orientation and acceleration readings are recorded during the flight, resulting in an orbital estimation. This estimate is sometimes improved further through searching for known ground control points in the imagery. For the Landsat legacy, known ground points are taken from a master orthophoto mosaic with worldwide coverage, which is a composite of multiple acquisitions that are triangulated. A similar process is foreseen for Sentinel-2. Imagery with as little clouds or haze as possible were selected (≈8500) and triangulated and orthorectified by the Earth Satellite Corporation [15]. For whiskbroom acquisitions, the line-of-sight (LOS) vector is calculated and then a synthetic image is produced based on the projection of the LOS intersection with the ellipsoid. The LOS can be given in Cartesian components (l_x, l_y, l_z), or in zenith and zenith distance angels (ϕ, θ). This results in an irregular sampling pattern which is then transformed to an image with equal pixel spacing through cubic interpolation, filling any voids [16].

The synthetic image projected on the ellipsoid is then terrain-corrected. Due to sampling geometry, the correction is only applied in the across track direction (l_x or $\mathbf{e}^{\perp}$). The displacement correction for every pixel can be calculated through a simple ray-tracing method, as in [17]. The elevation model used in case of Landsat is the Digital Terrain Elevation Data (DTED-1); a 3-as (90 m at the equator) topographic raster database. When the denser United States Geological Survey (USGS) elevation model was used, the vertical accuracy was better than 15 m RMSE [16]. Access to DTED-1 is only authorized for Defense Department contractors and the United States government, however for middle latitudes most elevation data are presumably based on the Shuttle Radar Topography Mission (SRTM) mission from February 2000. The accuracy of SRTM is an improvement over the former DTED-1 and, for flat areas, it remains within a specification of 16 m (90%) or better [18]. However, for high mountain terrain the distribution of deviations still has heavy tails, the SRTM DEM contains voids [19] and the spatial resolution is still too sparse to describe the terrain accurately. In addition, glaciers have ever-changing geometry and thus the terrain model rarely coincides with the actual topography during image acquisition. The study presented here attempts to invert the process, and to deduce the real terrain from observed co-registration artifacts. Due to the displacement being written as a function of a bearing angle in Equation (6), the difference describes an intersection. Hence, in this form, a linear relation can be formulated between relative across-track displacement and elevation bias, which is given by:

$$\Delta X = \Delta X_p - \Delta X_q. \tag{7}$$

Using the trigonometry as in Equation (3), the lateral difference can be formulated as a function of depth variation,

$$\Delta X = \Delta Z \cdot \tan\theta_p - \Delta Z \cdot \tan\theta_q. \tag{8}$$

After simple reformulation this equation simplifies to,

$$\Delta X = (\tan\theta_p - \tan\theta_q)\Delta Z. \tag{9}$$

This relation is the backbone of the present study. For within-orbit (also known as repeat-orbit) acquisitions, the relation diminishes. On the other end of the spectrum are the wide-looking instruments, such as Sentinel-2, where this factor can be up to 1/5.4 [20].

2.3. Projective Geometry

In this study we are interested in the source of the orthorectification offset, which is the vertical DEM error. However, the latter might not be of explicit interest for applications such as displacement measurements. If only the speed variation is of interest, then a simpler formulation of Equation (12), Section 2.4 can be used. It helps to see the acquisition configuration in epipolar geometry. In the direction of flight, the pushbroom sensor records as an affine camera model, while perpendicular to the flightpath, a projective camera model is used. Hence, offsets only occur along this second direction. When matching between images from different orbits is done, the resulting vector field will be ill-posed in cross-track direction as the solution lies then on the epipolar line, $\mathbf{e}^{\perp}$. If the glacier flow direction is known a priori $(\tilde{d}_x, \tilde{d}_y)$ and the orientation of this flow has not changed, the offset vector can else simply be mapped onto this glacier flow direction:

$$\begin{bmatrix} \hat{d}_x \\ \hat{d}_y \end{bmatrix} = \frac{d_x \cdot e_x^{\perp} - d_y \cdot e_y^{\perp}}{\tilde{d}_y \cdot e_x^{\perp} - \tilde{d}_x \cdot e_y^{\perp}} \cdot \begin{bmatrix} d_x \\ d_y \end{bmatrix}. \tag{10}$$

This resembles an intersection calculation. For clarity its configuration is illustrated in Figure 2. The satellite metadata normally gives the flight direction (bearing e_x, e_y). For this formulation no estimation of the elevation offset is needed. Thus it can directly be implemented in normal image matching pipelines. However, one needs to assume that the glacier flow, or other terrain movement did not change direction over time with respect to the a priori direction estimate.

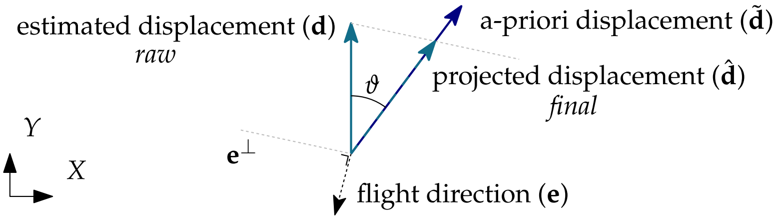

Figure 2. Planar view of components for the displacement projection. The estimated displacement (**d**) is the raw image displacement estimation from an image pair from different viewing angles. The initial displacement ($\tilde{\mathbf{d}}$) is an assumed correct terrain movement that can be derived from a repeat-orbit pair (i.e., with minimal orthorectification offsets), or auxiliary data. The key condition of this initial displacement is that its direction sufficiently approximates the real terrain movement, not necessarily its correct magnitude. This assumption takes into account that for instance glaciers will typically change their flow magnitude much faster and stronger than their flow direction. The projected displacement ($\hat{\mathbf{d}}$) is then the final estimation of terrain movement, with orthorectification offsets removed.

2.4. Parameter Estimation

Over time, a point on the Earth's surface can be sensed by multiple sensors and/or from different orbits. When the resulting images are matched with each other, a relative displacement $(\vec{d}_{\cdot\cdot})$ is estimated. In an Eulerian framework such displacements can be concatenated into a measurement vector (**y**). This is connected to the velocities (**v**) at this point through the design matrix (**A**). The matrix is filled with certain time intervals ($\delta t_{..}$). In the case of stable flow, or when a first order estimate is sufficient, this results in a direct linear relationship,

$$\mathbf{y} = \mathbf{A}\mathbf{x}, \quad \text{where,} \quad \mathbf{y} = \begin{bmatrix} \vec{d}_{pq} \\ \vec{d}_{qr} \\ \vec{d}_{pr} \\ \vdots \end{bmatrix}, \quad \mathbf{A} = \begin{bmatrix} \delta t_{pq} & 0 \\ 0 & \delta t_{qr} \\ \delta t_{pq} & \delta t_{qr} \\ \vdots & \vdots \end{bmatrix}, \quad \mathbf{x} = \begin{bmatrix} \vec{v}_{pq} \\ \vec{v}_{qr} \end{bmatrix}. \tag{11}$$

This system of equations holds when images are acquired from the same observation angle, as exemplified in Equation (9). For acquisitions that are matched from different orbits, an additional configuration matrix needs to be constructed to formulate the orthorectification offset based on Equation (9);

$$\mathbf{C}^{\top} = \begin{bmatrix} \tan\theta_p \cdot \cos\phi_p - \tan\theta_q \cdot \cos\phi_q & \cdots \\ \tan\theta_p \cdot \sin\phi_p - \tan\theta_q \cdot \cos\phi_q & \cdots \end{bmatrix}. \tag{12}$$

In this matrix an orbital angle (ϕ) is introduced, denoting the azimuthal direction of flight (bearing e_x, e_y). This needs to be incorporated, as the axis in our former formulation of equations was for simplicity aligned with the flight direction. Combining Equations (11) and (12) makes it possible to have an integrated linear estimation of real movement ($\mathbf{x}$) and terrain offset correction (∇), through the extended matrix formulation:

$$E\{\,\mathbf{y}\} = \begin{bmatrix} \mathbf{A} & \mathbf{C} \end{bmatrix} \begin{bmatrix} \mathbf{x} \\ \nabla \end{bmatrix}. \tag{13}$$

The accuracy of the raw displacement estimation is mostly dependent on the matching algorithm, image pattern, and radiometry. If an estimate of the dispersion of a displacement measurement is present, these can be formulated in a dispersion matrix ($\mathbf{Q}_y$). More importantly, the propagation of dispersion can now be estimated, for example one can estimate the dependence of a measurement onto the estimated parameters (p. 47 [21]);

$$\mathbf{Q}_{xy} = (\mathbf{A}^{\top}\mathbf{Q}_y^{-1}\mathbf{A})^{-1}\mathbf{A}^{\top}. \tag{14}$$

And the parameters can be estimated through ordinary least squares (i.e., $\underline{\hat{\mathbf{x}}} = \mathbf{Q}_{xy}\mathbf{Q}_y^{-1}\underline{\mathbf{y}}$). Such a formulation gives an integrated and direct solution, with additional insight into the error propagation.

2.5. Image Matching

Estimating displacements from one image to another can be done through different strategies or formulations. Optical flow is a method which can estimate the displacement up to individual pixel level [22,23], attempts of exploiting this novel approach have been made over glaciers, but yet without satisfying results [24]. The lack of successful attempts stems from the condition within the optical flow formulation that the illumination and albedo should not change over time, otherwise artificial movement is introduced. However, the combination of glacial surfaces on the one hand, which change continuously through melt, snow accumulation, flow and related strain, etc., and considerable sun elevation change on the other hand due to the separation time of several days and weeks for Landsat make optical flow implementations unstable. Robust implementations start to become available [25], however up to now this is only demonstrated on satellite imagery with particularly high revisit rates. In conclusion, optical flow techniques are not very useful for Landsat archive imagery, and in particular not over ever-changing glaciers.

Another approach for displacements estimation between different images is the matching of feature descriptors. This strategy formulates a brief description of a surrounding. Such approaches where first used for a selection of corners or interest points [26] within an image, but nowadays they are also available in dense form [27,28], making it possible to use them for glacial studies, such as in [29]. Nevertheless, when such methods are employed onto the Landsat archive, success is limited, because features on a glacier are typically smaller than the pixel resolution, while feature descriptors use neighborhood operators, i.e., require features composed of many pixels. Furthermore, the feature descriptors try to reduce the size of the descriptor by attempting to extract only the significant information within an image window. However, for glacier surfaces the information content can have a very low amplitude such as diffuse dust or snow variations, thus any reduction of information lowers the support of the similarity measure. Consequently, the naive method of matching image windows is the robust and well-established standard approach in glaciology and no other superior method has been found so far [30–33].

In image matching, one estimates the displacement that is needed to transform the pattern of one image onto the other. The image can be pre-processed to enhance features, for example using filter banks [34], or high-pass filtering [31]. Enhancing is mostly done in the high-frequencies and their intensities are normalized to account for albedo and sun elevation change. The similarity measure between the two image windows can be assessed through different metrics [35]. Direct measures like Sum of Absolute Differences are fast, but sensitive to noise, which is very common on medium-resolution imagery of real surfaces, in contrast to laboratory environments where for example Particle Image Velocimetry is applied. Therefore, Normalized Cross-Correlation and its variations are a more popular metric in glacial studies. Other metrics such as Mutual Information [36], or Median of Absolute Difference are less exploited, but such robust measures certainly have potential.

Finding the displacement translation can be done in the spatial domain, by moving a small image window over a larger search window and calculating the similarity for each translation step. This results in a two-dimensional surface of potential translation candidates. Normally, the translation with the highest similarity score is picked. The same calculation can be implemented in the frequency domain by first transforming the image with a Fourier transform ($\mathcal{F}(\cdot)$) [37]. In such case similar formulations of the metrics can be implemented, for a specific evaluation on glacier velocity estimation see [33]. Worth mentioning is the Orientation Correlation, which is used in this study, which normalizes the gradients of a image subset. This is similar to high pass filtering in the spatial domain, and therefore, less sensitive to high intensity changes such as changing shadows. Another advantage of this approach is its computational simplicity, as convolution simplifies to multiplication in the frequency domain, and the displacement ($\mathbf{D}$) estimation becomes

$$\mathbf{D}_{pq} = \mathcal{F}^{-1}\left(\mathcal{F}(\mathbf{I}_p) \cdot \mathcal{F}(\mathbf{I}_q)^*\right). \tag{15}$$

In this equation $*$ denotes the complex conjugate and $\mathbf{I}_p$ is an image window around a neighbourhood of a point. The resulting matrix ($\mathbf{D}_{pq}$) includes scores for potential displacements, and is typically filled with low values and one or some particularly high spikes. As more images are included into the matching process, the amount of pair combinations increases. If, for example, a third image ($\mathbf{I}_r$) is included, the displacement is the vector sum of the two individual displacements, or the operation of Equation (15) is done twice,

$$\mathbf{D}_{pqr} = \mathcal{F}^{-1}\left(\mathcal{F}(\mathbf{D}_{pq}) \cdot \mathcal{F}(\mathbf{D}_{qr})^*\right). \tag{16}$$

Written out fully, this vector addition becomes more pronounced,

$$\mathbf{D}_{pqr} = \mathcal{F}^{-1}\left(\left[\mathcal{F}(\mathbf{I}_p) \cdot \mathcal{F}(\mathbf{I}_q)^*\right] \cdot \left[\mathcal{F}(\mathbf{I}_q) \cdot \mathcal{F}(\mathbf{I}_r)^*\right]^*\right). \tag{17}$$

For the longest temporal baseline ($p \rightarrow r$) two paths can be chosen: a direct match between first and the last image or as a two step convolution calculation. In a case when coherent features are followed, one can assume:

$$\mathbf{D}_{pqr} \approx \mathbf{D}_{pr}. \tag{18}$$

Because this triangle closure holds, this path-independence property can be used to assess the consistency of all three matches. Hence, the quality of a match is now not only assessed through its similarity, but has a geometric constraint as well. This geometric constraint has not been exploited, except for a pair-wise relation known as reverse correlation [31], where ($\mathbf{D}_{pq} = \text{Rot}(\pi)\mathbf{D}_{qp}$) or for error detection [20]. Now, we can enhance the correlation function, in a similar fashion as in [38], but instead of spatial support the backing comes from the temporal neighbourhood,

$$\hat{\mathbf{D}}_{pr} = \mathbf{D}_{pqr} \cdot \mathbf{D}_{pr}. \tag{19}$$

Matching can be seen as estimating a vector displacement, that can take the form of a convolution matrix. Using these convolution matrices in the network configuration now makes it possible to constrain the matches trigonometricaly. The advantage of the frequency domain method is the high signal-to-noise ratio of the displacement matrix. If multiplication is applied and a correct triangulation is present, the score is significantly exaggerated. It is this property that enhances the correct match within three or more images and makes our implementation particularly robust.

3. Implementation

Our method is built upon a probabilistic model, hence the covariance model used has a strong influence on the decision making. In this study we set a conservative estimate of 0.5 pixel to the accuracy with which we can estimate a displacement. With this error budget we describe both the co-registration errors, as well as, the matching accuracy.

The matching of all imagery was done through orientation correlation in the frequency domain [33]. The 15 m panchromatic bands for Landsat 7 and 8, and the 10 m band 8 for Sentinel-2 was used. The spacing between matching windows was done at every pixel. The image matching window itself had a width of 30 × 30 pixels. Only matches with a signal-to-noise ratio (SNR) higher than 6 were used. For the estimation of velocity, as in Equation (11), a constant flow direction was assumed throughout the year and the image matching window sizes were 80 × 80 pixels.

3.1. Speed Regime

The design matrix consists of a fixed part depending on the geometry (**C**, Equation (12)) and a part dependent on the displacement regime (**A**, Equation (11)). The content of this matrix can be formulated differently. In the simple case the velocity is assumed to be constant and the matrix is a simple column. Its entries within the matrix are the amount of days between the two acquisitions, divided by the amount of days in a year. However, glaciers can change their speed regime over time. This is already reflected in Equation (11), where different columns in the design matrix describe different time periods. The advantage of such a framework is the ability to build a network, creating the possibility to do testing and data-snooping.

3.2. Velocity Projection

When a glacier flow is stable over time, its direction will not change much. For the case of a least squares formulation as in Equation (11) with just one column, this assumption is made. Velocity change of a glacier is usually only a change in magnitude, as valley walls, bedrock troughs or neighbour glaciers channelize its flow, although a number of exceptions exist such as surges or icestream slowdown/speed-up. However, these exceptions should be seen in a temporal perspective. The constraint of no change in flow direction still holds when the timescale of the displacement estimation is significantly shorter than the one of change. For example, the slowdown of icestreams is in the order of decades. Hence we expect that estimating monthly speed changes over such streams through projection on a yearly average will still provide a good approximation. Thus, mainly only the rapid onset of surges might in reality cause problems to our method and require careful selection of matching images and their timing.

A second point of consideration is the detectability of a displacement because of two criteria that need to be met in order for the projection method to be ignorant of outliers. First, a displacement can have a bearing in the same direction as the epipolar line ($\mathbf{e}^{\perp}$). In that case the new vector will be mapped to infinity, as is illustrated in Figure 3; Second, if the displacement is not significant ($\mathbf{d}/\sigma_d$), thus within the measurement error (circle in Figure 3), the same effect can happen. Hence, a cut-off can be used for velocity magnitude and orientation, in order to filter the vectors which will be misguided. If the displacement field is estimated, this threshold can be used prior to the mapping because the satellite geometry and the a priori displacements are known.

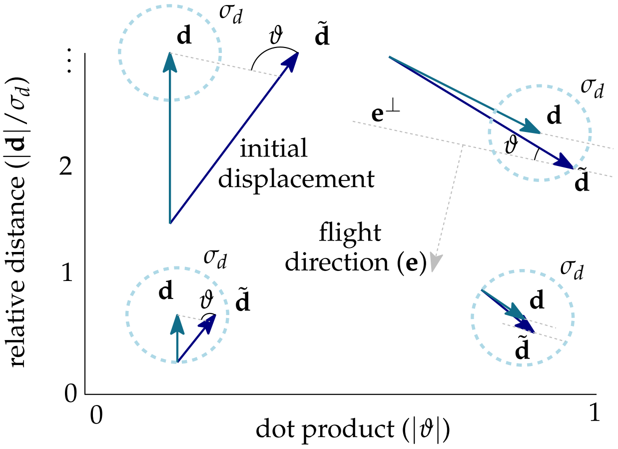

Figure 3. Illustration of the sensitivity of the projection method. In dashed light blue the accuracy of matching is illustrated (σ_d) on the displacement vector ($\mathbf{d}$). The dark blue vector is the a priori displacement ($\tilde{\mathbf{d}}$) from a pair with the same viewing angle or from auxiliary data. Finally, the dashed gray line illustrates the across-track looking direction, or epipolar line ($\mathbf{e}^{\perp}$) and relative angle (ϑ). In this case only the upper left situation is a valid projection example.

4. Data and Study Areas

The methodology given above can be used for several application scenarios. Within the present study we highlight three different case studies. All studies have varying objectives in order to show the wide range of possibilities of applying our methodology, but they also show the diversity of challenges that occur for mountain glaciers in relation to fast-flowing and big outlet glaciers.

4.1. Aletsch, Switzerland

At 83 km^2 the Grosser Aletsch Glacier is the largest glacier in the European Alps (Figure 4a). Since 1881 the net balance of this glacier has been negative. This resulted in a retreat of the front and a reduction of elevation at its snout, which can be up to four meters per year [39].

In this study, we use data from Landsat 8 and Sentinel-2 (see Figure A1 in the Appendix for a baseline plot and a list of individual scenes). Data from both satellites are freely available and are therefore popular. Landsat 8 has a same-orbit revisit time of 16 days, while Sentinel-2 will consist of two satellites forming a constellation with a revisit time of 5 days. When imagery from different looking angles is used, the chance of acquiring cloud-free imagery increases, especially for Sentinel-2 where the wide looking angle results in overlap between orbits, and greatly increases as orbits converge to the poles, see Figure 2 in [20]. However, the wide looking angle results in more cross-track offset. In addition, the Aletsch Glacier is surrounded by steep topography and has an icefall, making it a representative case for studying high mountain glaciers. For the assessment of our estimated vertical DEM offsets we use a no-voids filled version of SRTM.

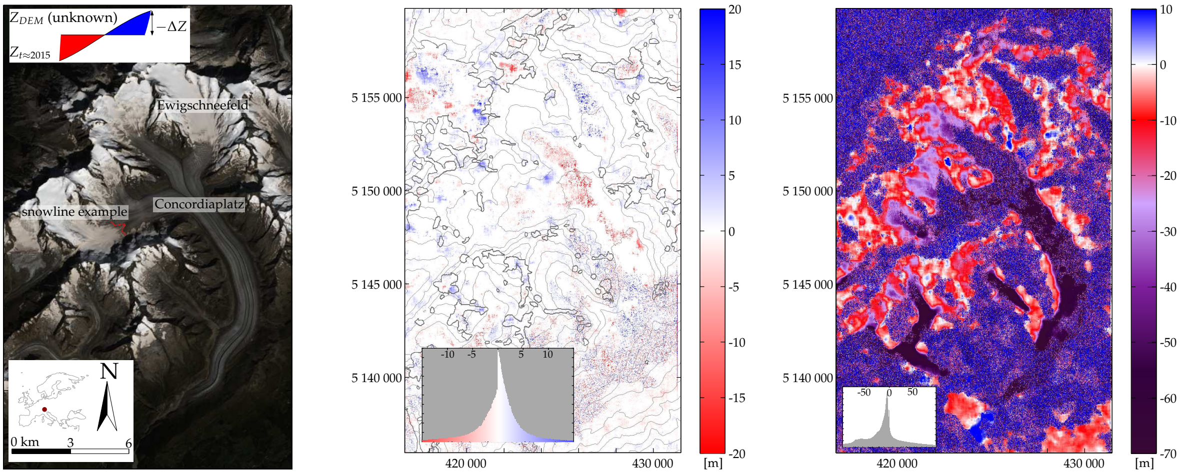

(**a**) Aletsch Glacier (**b**) Landsat 8 (**c**) Sentinel-2

Figure 4. Estimation of terrain bias between surface elevation (Z_t) during acquisition and DEM (Z_{DEM}) used for orthorectification ($-\Delta Z$ in Figure 1) for different sensors. When the estimation is negative the reference DEM used for orthorectification is higher than the real surface at image acquisition. The histograms in the lower left corners illustrate the distributions of the estimated terrain bias.

4.2. Oriental, Patagonia

Oriental Glacier (Figure 5) is situated at the northeastern side of the southern Patagonian icefield. Most outlet glaciers on the western side of the icefield drain into fjords, while eastern glaciers often terminate in freshwater lakes. Oriental Glacier is physically, but not hydrologically connected to the icefield. The glacier has a wide accumulation area and below an icefall it flows northwards where it funnels and elongates until it terminates into a lake. Another glacier branch, called Mellizos Sur, flows southwards and is also lake-terminating. The frontal positions of both snouts have been retreating slowly over the last decades. Its areal extent has decreased by 1% per decade for the last three decades [40]. In 1986 the area of the glacier was 73.68 km^2. Generally, most glaciers within this area are retreating [41], and the Oriental is no exception [42], though minor in a regional perspective [40]. Together with the ancillary retreat, an elevation loss is observed over large parts of the icefield since 2000 [43]. In the three decades prior to 2000, significant lowering is observed at most snouts of the icefield [44]. For the Oriental glacier, the ice loss over 1975–2000 is estimated to be 0.03 km^3.

For this case study we want to investigate if it is possible to detect elevation differences over a time span of a decade through a temporal variation in orthoprojection offsets. Therefore we use data from the beginning of the Landsat 7 and 8 missions, as illustrated in Figure A2 and listed in the Appendix. Archive imagery was selected that was cloud free, or with only a limited amount of obstruction by clouds. The elevation models used to assess our estimated DEM offsets are a SRTM DEM from 2000 and a TandDEM-X DEM from 2012.

4.3. Helheim, Greenland

Helheim Glacier (66.5°N, 38°W) is the third largest of the many outlets of the Greenland ice sheet. The Helheim Glacier drains into the Sermilik fjord, together with Fenris and Midgård glaciers.

In the previous decade, an increase in velocity was observed for Helheim between 2000 and 2005 [45]. This was accompanied by a drawdown of the surface. Because surface melt is not able to account for all measured elevation loss, ice dynamics must have played a prominent role [46]. Within the period of 2000–2005, the ice front seemed to be at or near floatation. In this unstable situation the front could advance and retreat several kilometres within a season [47]. The other glacier within this study site is Fenris Glacier, which is also a marine terminating glacier. It transports ice from the

Greenland ice sheet through a narrow fjord and has less seasonal front variations compared to the Helheim Glacier. Between 1972–2011 the front of Fenris Glacier has retreated 2.6 km [48].

These two glaciers appear to represent two different types of outlets. Helheim Glacier is an unstable case, which is heavily effected by frontal ablation and is close to floatation, while Fenris Glacier might be less sensitive due to its narrow outlet. Assessing the weekly velocity change might reveal patterns which occur at these time scales. Up to now, it was not possible to assess the contribution of melt-water triggered speed-up [45]. However, by increasing the number of satellite images included into the image matching, as is the aim of this study, it might be possible to gain more insight into such processes.

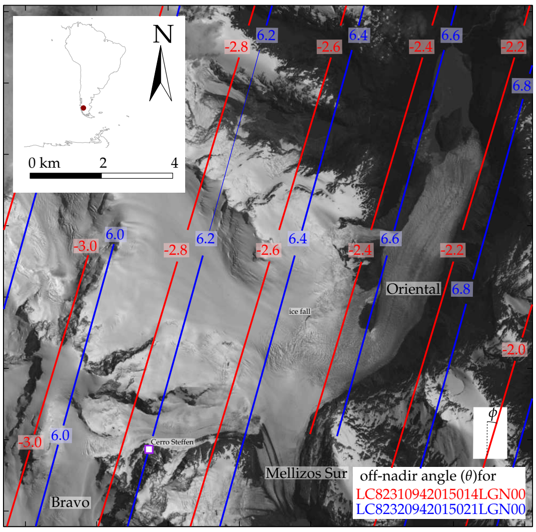

Figure 5. Landsat acquisition over Oriental Glacier, iso-lines indicate the off-nadir looking angle in degrees of two different orbits (path 231 & 232) of Landsat.

5. Results

The methodology as described above is applied to the three different case studies, each highlighting a different application of information retrieval. In the first case, the Aletsch Glacier, the orthorectification error is estimated for two different satellites, Landsat 8 and Sentinel-2. This is of technical interest towards homogenization of data from both missions, highlighting the processing pipeline abilities and can be seen as a quality indicator of the underlying topographic data sources. In the second case, the Oriental Glacier, the orthorectification offsets are assessed over time in order to evaluate if elevation changes over glaciers can be extracted. This is to show the capabilities of our methodology and can also be seen as an assessment of the relative georeferencing abilities of the processing pipeline. In the last case, Helheim Glacier, the temporal sampling of velocity measurements over an outlet is increased. Here the processing is without complicated estimations of the orthorectification offsets. This last case study mimics the use for more general geophysical purposes, where one is interested in the temporal flow dynamics of glaciers. Due to its simplicity this last case study is the most relevant methodology for operational use and bulk processing.

5.1. DEM Bias (Aletsch Glacier)

Over Aletsch Glacier (see Figure 4a) the estimation of single-time DEM bias, reconstructed from lateral orthorectification offsets between neighboring orbits following Equations (11) and (12) from Landsat 8 and Sentinel-2A imagery is illustrated in Figure 4b,c. In total, 7 and 10 image triplets were used for the Landsat 8 and Sentinel-2 case, respectively. For Landsat 8, as shown in Figure 4b, the SRTM DEM dataset is also included. The SRTM contours (with 250 m interval) are shown, and the thicker lines indicate void areas. Within the void areas, patches of significant vertical bias are located at mountain tops. However, patches of strong bias also occur on other non-glacial terrain. The DEM bias pattern shows a consistent signal of positive values on the lower tongue and upper north-eastern part (the Ewigschneefeld, see Figure 4a) (i.e., the DEM used for orthorectification is lower than the terrain at image acquisition). A clear transition is present at the ice-fall where the snowline is situated. The elevation bias in the middle glacier part (around Concordiaplatz and below) might be due to the negative net mass balance and according elevation loss. However, the signal in the upper part (Ewigschneefeld) does not correspond with the expected spatial distribution of the mass balance, as in [39]. Presumably, an elevation model rooted from the SRTM mission is used for Landsat 8 orthorectification. SRTM radar waves penetrate into the snow pack and the resulting backscatter phase center might be situated several meters within the snowpack [49–51]. This effect would have led to a too low reference DEM, not (yet) compensated by actual surface elevation loss. In the lower part of the glacier, the estimates are scattered and fluctuate. This is rooted in the unfortunate timing for this case, as in spring the snowline is in close proximity, hence visual surface features are not stable. For the other imagery which was acquired in summer and autumn, the scenes have partial cloud cover over the lower glacier snout. Consequently, only a limited sample size produces these estimates and should therefore be interpreted with caution. In theory, also a massive paraglacial landslide ongoing directly adjacent to the orographic left side of the glacier tongue [52] could have influenced glacier elevation and/or flow regime.

The estimated terrain bias for the Sentinel-2A data is illustrated in Figure 4c. Rough speckle surrounds the glacier and corresponds to clouds, present within the imagery. In addition, speckle is present on the accumulation areas, as a migrating snowline corrupts the stability of visual appearance in these areas. A negative bias seems to be present over the full dataset (note the different colour scale in Figure 4c displaying almost exclusively negative values compared to Figure 4b), and overall the magnitude of the bias is larger by one order of magnitude compared to the Landsat 8 data. Within the histogram a second peak is observable at around −60 m, largely corresponding to the lower part of the glaciers. For the icefall above the central part of the glacier, called Concordiaplatz, an opposite signal can be observed. This reversal of the bias might be due to the use of a lower resolution elevation model. This covers the lower frequencies of the terrain, but is not able to represent finer transitions [53]. The suspicion of a low resolution elevation model is also detected for Sentinel-2 in a Norwegian case study [20]. Unfortunately, these artifacts are of serious concern for the optimal exploitation of Sentinel-2 data for high mountain glacier studies.

5.2. Elevation Change over Time (Oriental Glacier)

In this second application, we test whether orthorectification offsets from different times could be used to roughly identify actual elevation changes over time. Here, we compare orthorectification offsets from Landsat 7 data from the early 2000s to those in Landsat 8 data from the mid 2010s. The estimation of orthorectification errors and velocity is based on matches from a collection of different images. Finding an optimal combination of imagery to match is challenging, firstly, because glacier displacement estimation relies on visual similarity. However, within an imagewindow different features contribute to the pattern. Such features have different life spans, and can be short lived or obstructed. Secondly, the movements need to be statistically significant in order to be above the noise level of the displacement estimation. Consequently, all combinations between imagery are used in this study, as individual triplets contain no-data values or outliers, but these might be populated by other combinations. For example, the elevation difference estimation for a single triplet is illustrated in Figure 6.

Because of the long timespan of a year for the specific image pairs matched, many features are de-correlated in the middle part of the glacier. In the upper part of the glacier the saturation of the bands results in voids (black) or in very small displacements. Nonetheless, the snout seems to exhibit a consistent velocity estimate. Because the relative intersection angle is small (≈9° see Figure 5), the elevation estimation fluctuates heavily. Patches are observable, which might show co-registration and ortho-rectification errors, but these errors are within the same order as the noise due to the bad viewing geometry.

In order to exceed the noise level, the elevation bias and velocity field is estimated for multiple image triplets; 286 combinations for Landsat 7 and 120 for Landsat 8. Because every scene can be hampered by clouds, and because of co-registration errors and different temporal feature degradations, the single estimates are very noisy. However, the co-registration errors can be assumed to be random, as well as the cloud cover to some extent. As the sampling has different temporal baselines, different features within the image windows are used to estimate the displacements. Consequently, when the median of all estimates is taken the outliers and noise are diminished, revealing a more accurate and reliable elevation bias than if only single triplets are used as in Figure 6. For both sensors, Landsat 7 and 8, the median of the elevation estimations is illustrated in Figure 7a,b. For Landsat 7 the most extreme outliers correspond to the mountain tops, such as Cerro Steffen (the purple square in Figure 5), and at icefalls. This might be due to the coarse resolution of the elevation model used for orthorectifying the Landsat data [53]. A clear pattern at the snout is observable as well, with a bias of several meters. For the Landsat 8 elevation bias estimation the pattern is more clearly observable. The height of glaciated terrain is larger by our method compared to the orthorectification DEM, while rock outcrops and terrain features are lower. However, the clear difference pattern of outliers on mountain tops found for the Landsat 7 data is not present in our Landsat 8-based reconstruction. Furthermore, the accumulation area of the glacier exhibits better estimates, which is due to the superior radiometric range of the Landsat 8 instrument.

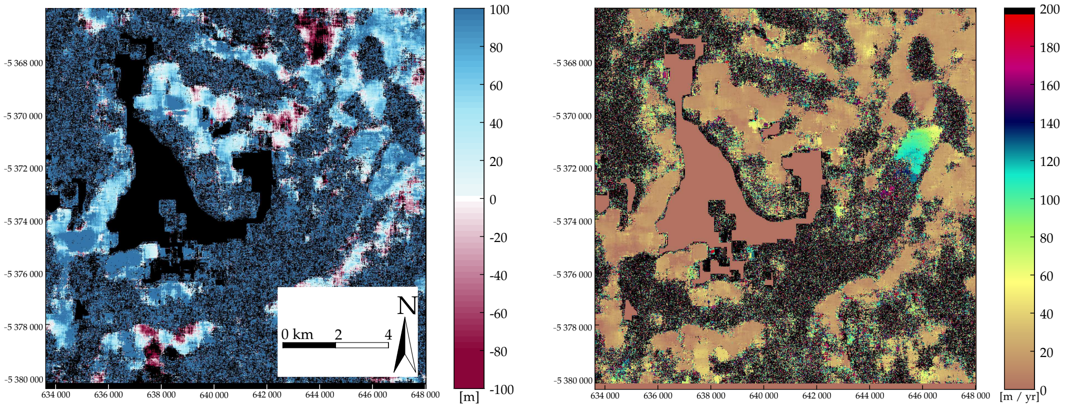

(**a**) Elevation bias (ΔZ) for Landsat 7 (**b**) Velocity estimation ($\mathbf{v}$) from Landsat 7

Figure 6. Elevation bias reconstructed from inter-orbit orthoimage offsets (**a**) and simultaneous estimation of velocity (**b**) over Oriental Glacier, constructed from three scenes.

When the elevation bias estimates from both the Landsat 7 and 8 data (i.e., Figure 7a,b) are differenced, topographic change should become observable. This is illustrated in Figure 8. Apart from the speckle, due to noise, some coherent elevation change patterns are observable, firstly on the mountain tops, but also the snout of the Oriental Glacier has clearly changed in elevation. Because the inaccuracy of the matching is strongly exaggerated through error propagation in combination with the small intersection angle, one should focus more on the trend pattern than its absolute numbers. Hence, only the sign of the change can be seen as significant.

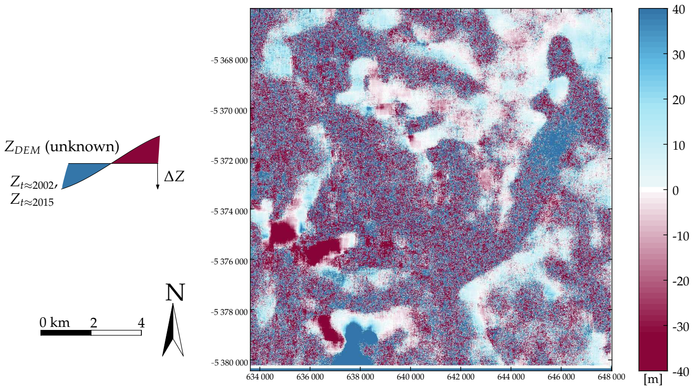

(**a**) Median of elevation bias (ΔZ) for Landsat 7

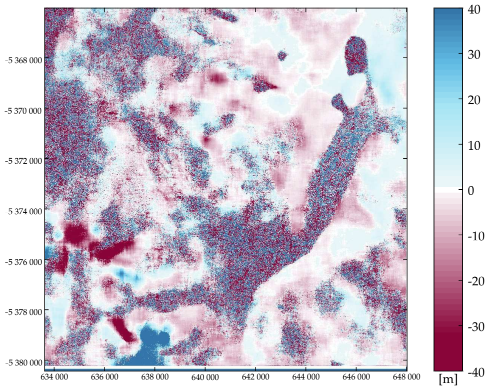

(**b**) Median ΔZ for Landsat 8

Figure 7. Estimation of terrain bias from around 2002 estimated through 286 triplets (**a**). A similar estimated terrain bias from around 2015, from 120 triplets is shown in (**b**). The estimated offsets are with respect to the DEM used for orthorectification (Z_{DEM}), the sign of the offset and its corresponding colours are illustrated at the left side of the figure.

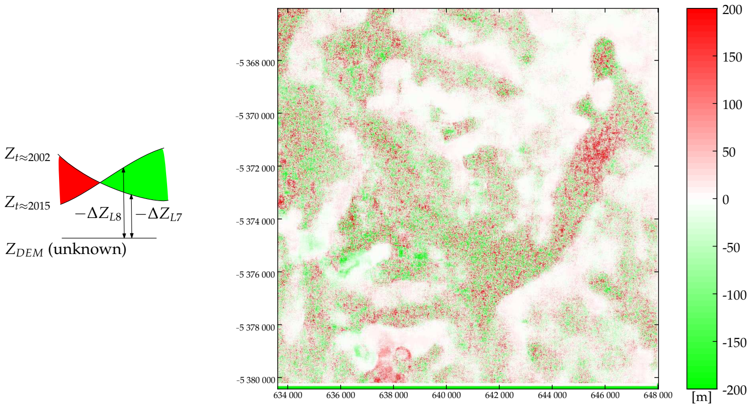

Figure 8. Difference between the Landsat 7 and Landsat 8 derived elevation bias (ΔZ), as shown in Figure 7. The inset on the left illustrates the interpretation of the colour scheme, as red colours indicate elevation decreases from around 2002 to 2015, while green colours express an increase.

5.3. Increased Temporal Resolution (Helheim Glacier)

In this third and final test we eliminate orthorectification offsets between satellite images from different orbits in order to arrive at a bias-free velocity time-series with higher temporal resolution than is achievable from repeat orbits only.

An Landsat 8 acquisition over Sermilik fjord, and its extracted base-line velocity are illustrated in Figure 9a,b. The time-series of Helheim and Fenris glaciers are illustrated in Figure 10. The median velocity is calculated from matches which have a signal-to-noise ratio (SNR) higher than 10. Furthermore, only displacements which where higher than 2.5 times the relative distance ($|\mathbf{d}|/\sigma_d$, see Figure 3) where taken into consideration for projecting the raw estimated displacement onto the assumed constant flow direction. For both glaciers in early spring and late autumn, a steady background velocity seems to be present before a speed-up occurs in July. For Fenris Glacier this speed-up is even observed far inland, but seems short lived. At the Helheim outlet a more complicated signal is present. Here, the speed-up is of a factor of four times accelerated from the lowest speeds in late/early winter, but its effect is less visible further upstream. In addition, later in the season an increase of speed near the terminus is observed, which relates to a longitudinal extension of the ice, creating more fractures/crevasses, connected to a less stable snout.

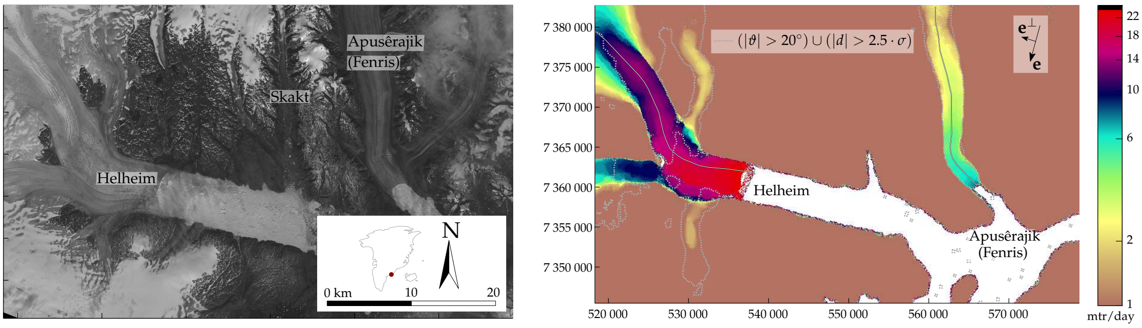

(**a**) Landsat acquisition over Sermilik fjord (**b**) Median speed of Helheim and Fenris glacier

Figure 9. Sermilik fjord, Greenland, in the summer of 2015. Colourbar of the speed is in logarithmic scale. The black and white line indicate the flowlines used for the speed estimation of Figure 10. The dashed gray lines indicate the filtering which can be applied, as shown in Figure 3.

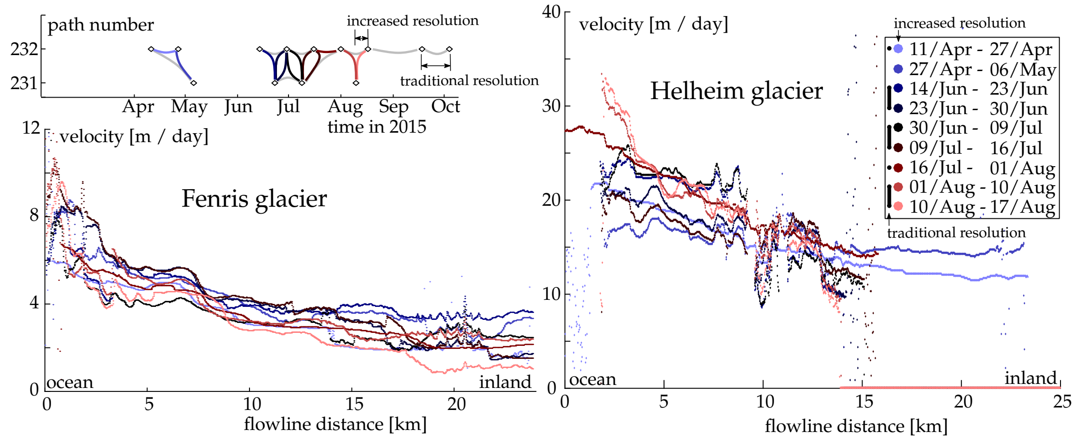

Figure 10. Up to weekly glacier speed evolution along the flow line of Helheim and Fenris, as illustrated in Figure 9b. In the upperleft, the baseline plot of the matchable imagery is shown, where the colour coding is in accordance with the other panels. Using the traditional same-orbit approach would span only 5 intervals over the plotted period (see also black markers in the legend), however, by including 4 cross-track images the coverage of the time series becomes more complete (9 periods) and increases in temporal resolution as well (see upper left corner).

In both speed plots all projections are illustrated, and the filter as illustrated in Figure 3 is not applied for the relative flow angle (ϑ). As can be seen in the speed plots, outliers occur at specific places. For Helheim Glacier the scatter occurs where the outlet makes a turn and the displacement is in the same direction as the across-track direction ($\mathbf{e}^{\perp}$), which leads to strong amplification of matching inaccuracy in our projection process. Scatter occurs on Fenris Glacier as well, but this is due to the flowline sampling displacement estimates within the fjord water and not on the glacial ice.

6. Discussion

As demonstrated, our methodology is capable of assessing the geometric quality of orthorectified Earth observation images. However, the implementation has also its limitations. The bearing of glacier flow is the most confining parameter. If the glacier flow is in the across-track direction of the observing platform, the system of equations is ill-posed. Because most Earth observation systems follow the same near-polar orbit, specific parts of a glacier will give poor estimates for all available data. For example, velocities over the sharp bend within the Helheim Glacier can only be estimated using the traditional repeat-orbit method, as well as over the icefall behind the tongue of the Oriental Glacier. In future work, it might be possible to constrain the estimates by including the property of ice to be incompressible into the system of equations. However, this complicates the estimation structure, from a straight forward individual scheme to an iterative locally dependent structure. Furthermore, it will neglect the possibility for ice to extend in the vertical direction. Optical satellites/instruments in an International Space Station (ISS) orbit might be able to constrain the geometry, however are not able to cover polar glaciers.

Furthermore, the geometry of the acquisition matters. Most affected by orthorectification bias are acquisitions with a wide off-nadir angle, through its wide viewing (e.g., Sentinel-2) or its steering capabilities (e.g., ASTER, SPOT). With such systems the combination of intersection angle and resolution is sufficient to estimate a significant displacement. For the Landsat case, the results are more noisy. This is partly due to the narrow intersection angle between acquisitions from different orbits, but also the assumption of perfect georeferencing does play a role. Stable and flat terrain are needed to find such overall lateral displacements. However, if such scene specific parameters are included, the system of equations becomes ill-conditioned.

A second subject of concern is the warping applied to the Landsat imagery [7]. This causes local distortions, and might be the reason why not every part of the bias pattern can be explained. However, the difference between Landsat 7 and 8 on Oriental Glacier is not solely dependent on the warping. It is a combination of warping and absolute orientation error, as the absolute orientation does produce a terrain-dependent signal [54]. Untangling these effects is challenging as both errors are directly related to topography. Fortunately, for the case of the Oriental Glacier we do have elevation data of SRTM, which were acquired in austral summer. In February 2000, it was exceptionally warm, thus radar penetration was minimal. Furthermore, an elevation model from the recent Deutsches Zentrum für Luft- und Raumfahrt (DLR) TanDEM-X mission gives us an opportunity to assess our estimate of glacier thickness change. By replicating the DLR TanDEM-X DEM and applying a planar shift to its copy, a georeferencing error can be simulated. Both components; the one in the direction of the flight line and the one perpendicular to it, are illustrated in Figure 11a,b, respectively. The patterns of these components do not seem to be observable in our estimates. This implies that the distribution of geo-referencing errors could be stochastic. The elevation difference between both the 2000 SRTM and 2012 TanDEM-X elevation models is illustrated in Figure 11c. Here a clear signal of an elevation loss on the snout can be seen, which does relate to our estimates (Figure 8) in both spatial distribution and magnitude of bias/elevation change. Unfortunately, the elevation models have no elevation information on the mountain tops because of interferometric phase unwrapping problems.

Our estimation model used in the Aletsch and Oriental case studies relies on constant speed. However, some dynamics might be present in the flow regime, which are not formulated in the model. Consequently, any deviation will propagate into the elevation bias estimate, which is already sensitive due to its slim intersection angle. Hence in this study we used short time ranges within a year or up to three years. Furthermore, a variable speed model can cause overfitting of the data, resulting in velocities estimations with different flow directions. This is especially the case when the base-line is close to perpendicular in space-time. On the other hand, because of these potential variations in speed the simple model of constant speed over the study period was not executed on the far more dynamic tide water Helheim Glacier.

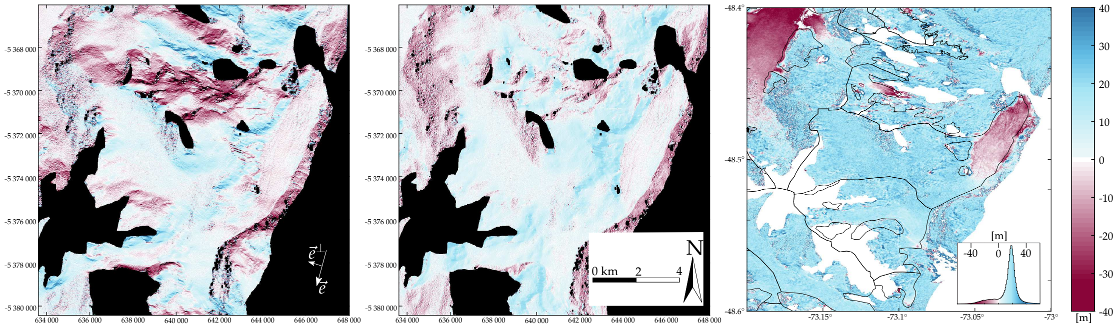

(**a**) Mis-registration ($\sigma_{\vec{e}\parallel}$) (**b**) Miss-registration ($\sigma_{\vec{e}\perp}$) (**c**) Elevation difference 2000–2012

Figure 11. Synthetic miss-alignment based on TanDEM-X elevation model. These miss-alignments are related to the lateral offsets expected for Landsat, decomposed in the direction parallel to the flight line and perpendicular to the flight line (**a**,**b**). (**c**) illustrates the elevation difference between the SRTM and TanDEM-X elevation models, the black lines indicate the glacier outline. In the right corner the corresponding distribution is illustrated.

7. Conclusions

This study introduces a sensor-independent method to analyse DEM-induced errors in repeat orthorectified optical data, even when terrain might be moving. The framework is built around simple ordinary least squares, hence the estimation is extendable to various sensors and terrain movement types. In addition, an efficient and robust manner of triplet matching, instead of traditional pairwise matching, is introduced. Because the full spectrum of candidate displacements is used in triplet matching, the triangle closure constraint is able to identify secondary correlation peaks as valid, which would otherwise be disregarded in traditional pairwise matching, where the highest correlation value is considered the valid match. The implementation of the triangle closure constraint is built upon simple convolution. It can be implemented both in the spatial and the frequency domain. The robustness of the triplet matching method is enhanced through the multiplication of the displacement scores. A benefit is achieved when implementing the method in the frequency domain, as such displacement estimates produce only a limited amount of peaks that stand out sharp and clearly, hence displacement estimates should be aligned otherwise the signal will be damped. In the spatial domain, such peaks are mostly smoother, and have lower signal to noise ratios, hence the geometric constraint through multiplication will stand out less.

Our methodology of exploiting orthorectification offsets is demonstrated using three different case studies. We were able to identify artifacts in the orthorectification processes, and show elevation changes over time related to glacier change. Furthermore, we were able to compare Landsat 8 and Sentinel-2 products, and find an order of magnitude larger orthorectification errors for Sentinel-2. However, these differences can solely be attributed to the reference model, hence when a better DEM is used for Sentinel-2 the quality might enhance accordingly. Lastly, we introduced a mapping routine, which bypasses the elevation bias estimate and directly produces velocity estimates using imagery from different orbits, eventually leading to elevation bias-free velocity measurements with higher temporal resolution than can be achieved using repeat-pass data only.

The ordinary least squares framework given in this study is a diverse structure to build upon, and can be exploited in various other ways. For example, if more acquisitions are taken into the system of equations, a network can be built. This opens up the possibility to apply statistical tests and data-snooping, due to an increase in redundancy. Furthermore, our framework has the ability to propagate errors, when normally distributed, and thus estimate the deviation of estimated parameters. Such procedures become more and more valuable with the increasing availability of optical satellite data, such as from the recently successful launched Sentinel-2B. In principle, our method is also applicable to SAR data, but inter-orbit image matching might be complicated by the oblique viewing angle and active acquisition nature of SAR that make the appearance of ground features likely more variable.

This study underlines that the orthorectification procedure is an essential aspect of data quality of remote sensing image products. When the underlying elevation model is of sufficient quality, across-track analyses are possible and have the potential to increase information retrieval considerably and enhance homogenization between data from different missions such as Landsat and Sentinel-2.

Acknowledgments: We thank three anonymous reviewers for their valuable comments which helped to improve the manuscript. We also thank Kim Menage for improving the English language of an early version of this contribution. This study is funded by the European Research Council under the European Union's Seventh Framework Programme grant agreement No. 320816, the ESA project Glaciers_cci (4000109873/14/I-NB) and the Norwegian Space Centre under contract NIT.06.15.5. We are very grateful to USGS, ESA and the EU Copernicus program for free provision of the Landsat and Sentinel-2 imagery. We also thank Wael Abdel Jaber of DLR for providing the TanDEM-X DEM.

Author Contributions: Bas Altena and Andreas Kääb initiated the study. Bas Altena designed the structure, developed and implemented the methodology. Both authors interpreted the results and wrote the article.

Conflicts of Interest: The authors declare no conflict of interest. The funding sponsors had no role in the design of the study; in the collection, analyses, or interpretation of data; in the writing of the manuscript, and in the decision to publish the results.

Abbreviations

The following abbreviations are used in this manuscript:

ASTER	Advanced Spaceborne Thermal Emission and Reflection Radiometer
CBERS	China–Brazil Earth Resources Satellite
DEM	Digital Elevation Model
DLR	Deutsches zentrum für Luft- und Raumfahrt
DTED	Digital Terrain Elevation Data
ESA	European Space Agency
GDEM	Global Digital Elevation Model
ISS	International Space Station
LOS	line of sight
RADAR	RAdio Detection And Ranging
RMSE	Root Mean Square Error
SAR	Synthetic Aperture Radar
SNR	signal-to-noise ratio
SPOT	Satellite Pour l'Observation de la Terre
SRTM	Shuttle Radar Topography Mission
USGS	United States Geological Survey
ZY3	Ziyuan-3, Resources-3

The following symbols are used to describe operators or denotation of properties:

$\mathcal{F}(\cdot)$	Fourier transform
$\tilde{\cdot}$	Initial parameter
$\hat{\cdot}$	Estimated parameter
$*$	Complex conjugate
$\cdot^{-1}$	Matrix inverse
$\cdot^{\top}$	Matrix transpose
$E\{\cdot\}$	Expectation operator
$\mathrm{Rot}(\cdot)$	Rotation

The following list are symbols used in this manuscript, where bold upper case letters denote matrices, and bold lower case letters symbolize vectors:

i	Image coordinate in along-track direction
j	Image coordinate in cross-track direction
$\vec{\tau}$	Image coordinate translation from center of scene to the corner of the sensor
α	Normalized focal length
$\mathbf{e}$	Flight direction of satellite
$\mathbf{n}$	Normal of satellite
X	Metric coordinate in along-track direction
Y	Metric coordinate in cross-track direction
Z	Metric coordinate in zenit direction
$\mathbf{K}$	Camera matrix
$\mathbf{R}$	Rotation matrix
p	Point in an image
P	Point on the earth surface
f	Focal length
m	Size of photosensative cell
ΔZ	Vertical bias between real surface and elevation model
ΔX	Lateral displacement due to orthorectification error
θ	Zenit distance in cross-track direction
ϕ	Bearing of satellite flight path
$\mathbf{l}$	Line of sight vector in cross-track direction
$\mathbf{d}$	Relative displacement of a feature between images
$\mathbf{A}$	Design matrix
$\mathbf{y}$	Measurement vector
$\mathbf{x}$	Vector with unknown parameter
u	Velocity along the X-axis
v	Velocity along the Y-axis
δt	Time separation between two acquisitions
$\mathbf{C}$	Configuration matrix
∇	Terrain correction
$\mathbf{Q}$	Dispersion matrix
σ	Dispersion
ϑ	Relative angle between initial displacement and epipolar line
$\mathbf{I}$	Image (subset)
$\mathbf{D}$	Displacement matrix

Appendix A

Used imagery for Aletsch Glacier,
LC81940282015155LGN00, LC81940282015267LGN00, LC81950282015130LGN00,
LC81940282015203LGN00, LC81940282015283LGN00, LC81950282015242LGN00,
LC81940282015219LGN00, LC81950282015098LGN00, LC81940282015251LGN00,
LC81950282015114LGN00
S2A_R065_06_08_2015_T32TMS, S2A_R108_29_08_2015_T32TMS,
S2A_R065_25_09_2015_T32TMS, S2A_R108_30_07_2015_T32TMS,
S2A_R108_08_09_2015_T32TMS

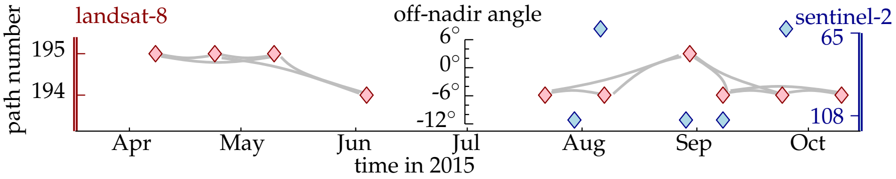

Figure A1. Baseline plot of the acquisitions over Aletsch Glacier.

Used imagery for Oriental Glacier,
LC82310942013344LGN00, LC82320942016040LGN00, LC82310942015334LGN00,
LC82310942016033LGN00, LC82320942015021LGN00, LC82310942015014LGN00,
LC82320942016072LGN00, LC82310942016065LGN00, LC82310942016081LGN00,
LC82320942016008LGN00.
LE72320942001070EDC00, LE72320942000260EDC00, LE72310941999282COA00 †,
LE72320942002041EDC00, LE72310942000013COA00†, LE72320942002345PFS00,
LE72310942000093COA00, LE72320942003012EDC00, LE72310942001287EDC00 †,
LE72320942003092EDC00, LE72310942003069EDC00, LE72320942003140ASN00,
LE72310942003133EDC00.

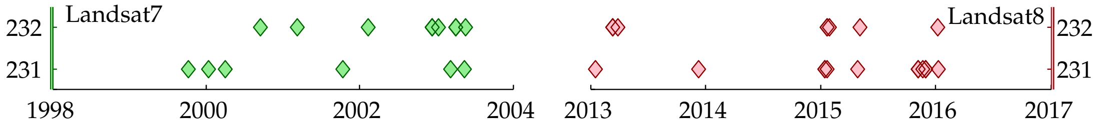

Figure A2. Baseline plot of the acquisitions over Oriental Glacier.

(†) used for construction of Figure 6.

Used imagery for Helheim glacier,
LC82310142015126LGN00, LC82320132015117LGN00, LC82320132015229LGN00,
LC82310142015174LGN00, LC82320132015165LGN00, LC82320132015261LGN00,
LC82310142015190LGN00, LC82320132015181LGN00, LC82320132015277LGN00,
LC82310142015222LGN00, LC82320132015197LGN00, LC82320132015101LGN00,
LC82320132015213LGN00

References

1. Kääb, A.; Leprince, S. Motion detection using near-simultaneous satellite acquisitions. *Remote Sens. Environ.* **2014**, *154*, 164–179.
2. Van der Veen, C. *Fundamentals of Glacier Dynamics*; CRC Press: Boca Raton, FL, USA, 2013.
3. Nick, F.; Van der Veen, C.; Vieli, A.; Benn, D. A physically based calving model applied to marine outlet glaciers and implications for the glacier dynamics. *J. Glaciol.* **2010**, *56*, 781–794.
4. Fahnestock, M.; Scambos, T.; Moon, T.; Gardner, A.; Haran, T.; Klinger, M. Rapid large-area mapping of ice flow using Landsat 8. *Remote Sens. Environ.* **2016**, *185*, 84–94.
5. Dehecq, A.; Gourmelen, N.; Trouve, E. Deriving large-scale glacier velocities from a complete satellite archive: Application to the Pamir–Karakoram–Himalaya. *Remote Sens. Environ.* **2015**, *162*, 55–66.
6. Rosenau, R.; Scheinert, M.; Dietrich, R. A processing system to monitor Greenland outlet glacier velocity variations at decadal and seasonal time scales utilizing the Landsat imagery. *Remote Sens. Environ.* **2015**, *169*, 1–19.
7. Gao, F.; Masek, J.; Wolfe, R. Automated registration and orthorectification package for Landsat and Landsat-like data processing. *J. Appl. Remote Sens.* **2009**, *3*, 033515.
8. Bian, J.H.; Li, A.N.; Jin, H.A.; Lei, G.B.; Huang, C.Q.; Li, M.X. Auto-registration and orthorecification algorithm for the time series HJ-1A/B CCD images. *J. Mt. Sci.* **2013**, *10*, 754–767.

9. Devaraj, C.; Shah, C. Automated geometric correction of Landsat MSS L1G imagery. *IEEE Geosci. Remote Sens. Lett.* **2014**, *11*, 347–351.
10. Devaraj, C.; Shah, C. Automated geometric correction of multispectral images from High Resolution CCD Camera (HRCC) on-board CBERS-2 and CBERS-2B. *ISPRS J. Photogramm. Remote Sens.* **2014**, *89*, 13–24.
11. Altena, B.; Kääb, A.; Nuth, C. Robust glacier displacements using knowledge-based image matching. In Proceedings of the 2015 8th International Workshop on the Analysis of Multitemporal Remote Sensing Images (Multi-Temp), Annecy, France, 22–24 July 2015; pp. 1–4.
12. Stumpf, A.; Malet, J.P.; Delacourt, C. Correlation of satellite image time-series for the detection and monitoring of slow-moving landslides. *Remote Sens. Environ.* **2017**, *189*, 40–55.
13. Jeong, S.; Howat, I.M.; Ahn, Y. Improved multiple matching method for observing glacier motion with repeat image feature tracking. *IEEE Trans. Geosci. Remote Sens.* **2017**, *55*, 2431–2441.
14. Moons, T.; Van Gool, L.; Vergauwen, M. *3D Reconstruction from Multiple Images, Part 1: Principles*; Foundations and Trends® in Computer Graphics and Vision; Now Publishers Inc.: Breda, The Netherlands, 2009.
15. Tucker, C.; Grant, D.; Dykstra, J. NASAs global orthorectified Landsat data set. *Photogramm. Eng. Remote Sens.* **2004**, *70*, 313–322.
16. Storey, J.; Strande, D.; Hayes, R.; Meyerink, A.; Labahn, S.; Lacasse, J. *Landsat 7 Image Assessment System (IAS) Geometric Algorithm Theoretical Basis Document*; Technical Report; USGS: Reston, VA, USA, 2006.
17. Chen, L.C.; Lee, L.H. Rigorous generation of digital orthophotos from SPOT images. *Photogramm. Eng. Remote Sens.* **1993**, *59*, 655–661.
18. Sun, G.; Ranson, K.; Kharuk, V.; Kovacs, K. Validation of surface height from shuttle radar topography mission using shuttle laser altimeter. *Remote Sens. Environ.* **2003**, *88*, 401–411.
19. Kääb, A. *Remote Sensing of Mountain Glaciers and Permafrost Creep*; Geographisches Institut der Universität Zürich: Zürich, Switzerland, 2005.
20. Kääb, A.; Winsvold, S.; Altena, B.; Nuth, C.; Nagler, T.; Wuite, J. Glacier Remote Sensing using Sentinel-2. Part I: Radiometric and Geometric Performance, Application to Ice Velocity, and Comparison to Landsat 8. *Remote Sens.* **2016**, *8*, 598.
21. Teunissen, P. *Adjustment Theory. An Introduction, Series on Mathematical Geodesy and Positioning*; VSSD: Delft, The Netherlands, 2003.
22. Barron, J.; Fleet, D.; Beauchemin, S. Performance of optical flow techniques. *Int. J. Comput. Vis.* **1994**, *12*, 43–77.
23. Baker, S.; Scharstein, D.; Lewis, J.; Roth, S.; Black, M.; Szeliski, R. A database and evaluation methodology for optical flow. *Int. J. Comput. Vis.* **2011**, *92*, 1–31.
24. Vogel, C.; Bauder, A.; Schindler, K. Optical Flow for Glacier Motion Estimation. In Proceedings of the 22nd ISPRS Congress, Melbourne, Australia, 25 August–1 September 2012.
25. Altena, B.; Kääb, A. Weekly glacier flow estimation from dense satellite time series using adapted optical flow technology. *Front. Earth Sci.* **2017**, in review.
26. Tuytelaars, T.; Mikolajczyk, K. Local invariant feature detectors: A survey. *Found. Trends Comput. Gr. Visi.* **2008**, *3*, 177–280.
27. Tola, E.; Lepetit, V.; Fua, P. Daisy: An efficient dense descriptor applied to wide-baseline stereo. *IEEE Trans. Pattern Anal. Mach. Intell.* **2010**, *32*, 815–830.
28. Kokkinos, I.; Bronstein, M.; Yuille, A. *Dense Scale Invariant Descriptors for Images and Surfaces*; INRIA: Paris, France, 2012.
29. Muye, N.; Chunxia, Z.; Tingting, L. Derivation of ice-flow of Polar Record Glacier using an improved NCC algorithm. *Chin. J. Polar Res.* **2016**, *28*, 243–249.
30. Bindschadler, R.; Scambos, T. Satellite-image-derived velocity field of an Antarctic ice stream. *Science* **1991**, *252*, 242.
31. Scambos, T.; Dutkiewicz, M.; Wilson, J.; Bindschadler, R. Application of image cross-correlation to the measurement of glacier velocity using satellite image data. *Remote Sens. Environ.* **1992**, *42*, 177–186.
32. Kääb, A.; Vollmer, M. Surface geometry, thickness changes and flow fields on creeping mountain permafrost: Automatic extraction by digital image analysis. *Permafr. Periglac. Process.* **2000**, *11*, 315–326.
33. Heid, T.; Kääb, A. Evaluation of existing image matching methods for deriving glacier surface displacements globally from optical satellite imagery. *Remote Sens. Environ.* **2012**, *118*, 339–355.

34. Ahn, Y.; Howat, I. Efficient automated glacier surface velocity measurement from repeat images using multi-image/multichip and null exclusion feature tracking. *IEEE Trans. Geosci. Remote Sens.* **2011**, *49*, 2838–2846.
35. Goshtasby, A. *Image Registration: Principles, Tools and Methods*; Advances in Computer Vision and Pattern Recognition; Springer: Berlin, Germany, 2012.
36. Erten, E. Glacier velocity estimation by means of a polarimetric similarity measure. *IEEE Trans. Geosci. Remote Sens.* **2013**, *51*, 3319–3327.
37. Rolstad, C.; Amlien, J.; Hagen, J.O.; Lundén, B. Visible and near-infrared digital images for determination of ice velocities and surface elevation during a surge on Osbornebreen, a tidewater glacier in Svalbard. *Ann. Glaciol.* **1997**, *24*, 255–261.
38. Hart, D. PIV error correction. *Exp. Fluids* **2000**, *29*, 13–22.
39. Bauder, A.; Funk, M.; Huss, M. Ice-volume changes of selected glaciers in the Swiss Alps since the end of the 19th century. *Ann. Glaciol.* **2007**, *46*, 145–149.
40. White, A.; Copland, L. Decadal-scale variations in glacier area changes across the Southern Patagonian Icefield since the 1970s. *Arct. Antarct. Alp. Res.* **2015**, *47*, 147–167.
41. Lopez, P.; Chevallier, P.; Favier, V.; Pouyaud, B.; Ordenes, F.; Oerlemans, J. A regional view of fluctuations in glacier length in southern South America. *Glob. Planet. Chang.* **2010**, *71*, 85–108.
42. Davies, B.; Glasser, N. Accelerating shrinkage of Patagonian glaciers from the Little Ice Age (AD 1870) to 2011. *J. Glaciol.* **2012**, *58*, 1063–1084.
43. Willis, M.; Melkonian, A.; Pritchard, M.; Rivera, A. Ice loss from the Southern Patagonian Ice Field, South America, between 2000 and 2012. *Geophys. Res. Lett.* **2012**, *39*, L17501.
44. Rignot, E.; Rivera, A.; Casassa, G. Contribution of the Patagonia Icefields of South America to sea level rise. *Science* **2003**, *302*, 434–437.
45. Howat, I.; Joughin, I.; Tulaczyk, S.; Gogineni, S. Rapid retreat and acceleration of Helheim Glacier, east Greenland. *Geophys. Res. Lett.* **2005**, doi:10.1029/2005GL024737.
46. Stearns, L.; Hamilton, G. Rapid volume loss from two East Greenland outlet glaciers quantified using repeat stereo satellite imagery. *Geophys. Res. Lett.* **2007**, doi:10.1029/2006GL028982.
47. Joughin, I.; Howat, I.; Alley, R.; Ekström, G.; Fahnestock, M.; Moon, T.; Nettles, M.; Truffer, M.; Tsai, V. Ice-front variation and tidewater behavior on Helheim and Kangerdlugssuaq Glaciers, Greenland. *J. Geophys. Res. Earth Surf.* **2008**, doi:10.1029/2007JF000837.
48. Mernild, S.; Malmros, J.; Yde, J.; Knudsen, N. Multi-decadal marine-and land-terminating glacier recession in the Ammassalik region, southeast Greenland. *Cryosphere* **2012**, *6*, 625–639.
49. Rignot, E.; Echelmeyer, K.; Krabill, W. Penetration depth of interferometric synthetic-aperture radar signals in snow and ice. *Geophys. Res. Lett.* **2001**, *28*, 3501–3504.
50. Berthier, E.; Arnaud, Y.; Vincent, C.; Remy, F. Biases of SRTM in high-mountain areas: Implications for the monitoring of glacier volume changes. *Geophys. Res. Lett.* **2006**, doi:10.1029/2006GL025862.
51. Kääb, A.; Berthier, E.; Nuth, C.; Gardelle, J.; Arnaud, Y. Contrasting patterns of early twenty-first-century glacier mass change in the Himalayas. *Nature* **2012**, *488*, 495–498.
52. Strozzi, T.; Delaloye, R.; Kääb, A.; Ambrosi, C.; Perruchoud, E.; Wegmüller, U. Combined observations of rock mass movements using satellite SAR interferometry, differential GPS, airborne digital photogrammetry, and airborne photography interpretation. *J. Geophys. Res. Earth Surf.* **2010**, doi:10.1029/2009JF001311.
53. Paul, F. Calculation of glacier elevation changes with SRTM: Is there an elevation-dependent bias? *J. Glaciol.* **2008**, *54*, 945–946.
54. Nuth, C.; Kääb, A. Co-registration and bias corrections of satellite elevation data sets for quantifying glacier thickness change. *Cryosphere* **2011**, *5*, 271–290.

Paper II:

Weekly glacier flow estimation from dense satellite time series using adapted optical flow technology

frontiers
in Earth Science

ORIGINAL RESEARCH
published: 30 June 2017
doi: 10.3389/feart.2017.00053

Weekly Glacier Flow Estimation from Dense Satellite Time Series Using Adapted Optical Flow Technology

*Bas Altena * and Andreas Kääb*

Department of Geosciences, University of Oslo, Oslo, Norway

Contemporary optical remote sensing satellites or constellations of satellites can acquire imagery at sub-weekly or even daily timescales. These systems have the potential to facilitate intra-seasonal, short-term surface velocity variations across a range of ice masses. Current techniques for displacement estimation are based on matching image pairs with sufficient displacement and/or preservation of the surface over time and consequently, do not benefit from an increase in satellite revisit times. Here, we explore an approach that is fundamentally different from image correlation or similar approaches and engages the concept of optical flow. Our goal is to assess whether this technique could overcome the limitations of image matching and yield new insights in glacier flow dynamics. We implement two different methods of optical flow, and test these implementations utilizing the SPOT5 Take5 dataset at two glaciers: Kronebreen, Svalbard and Kaskawulsh Glacier, Yukon. At Kaskawulsh Glacier, we extract intra-seasonal velocity variations that are synchronous with episodes of increased air temperature. Moreover, even for the cloudy dataset of Kronebreen, we can extract spatio-temporal trajectories that correlate well with measured GPS flow paths. Since the underlying concept is simple and computationally efficient due to data-reduction, our optical flow methodology can be rapidly adapted for a range of studies from the investigation of large scale ice sheet dynamics down to the estimation of displacements over small and slow flowing glaciers.

Keywords: temporal glacier flow, multi-sensor tracking, optical flow, particle tracking velocimetry, space-time imaging

Edited by:
Alun Hubbard,
University of Tromsø, Norway

Reviewed by:
Martin Rückamp,
Alfred-Wegener-Institut für Polar- und Meeresforschung, Germany
Ninglian Wang,
Cold and Arid Regions Environmental and Engineering Research Institute (CAS), China
Jonathan Ryan,
Aberystwyth University, United Kingdom

Correspondence:
Bas Altena
bas.altena@geo.uio.no

Specialty section:
This article was submitted to Cryospheric Sciences, a section of the journal Frontiers in Earth Science

Received: *12 January 2017*
Accepted: *09 June 2017*
Published: *30 June 2017*

Citation:
Altena B and Kääb A (2017) Weekly Glacier Flow Estimation from Dense Satellite Time Series Using Adapted Optical Flow Technology. Front. Earth Sci. 5:53. doi: 10.3389/feart.2017.00053

1. INTRODUCTION

In recent years, the focus in optical remote sensing has shifted from the use of a few scenes from individual satellites toward exploitation of full constellations. Twin satellites or flocks of satellites have been launched, sensing the globe with ever shorter revisit times. The advantages of short temporal sampling rates for glaciology are now being investigated (Fahnestock et al., 2015). One of these opportunities has been the exploration of short term changes in glacier flow, on the scale of an individual season (Berthier et al., 2005; Armstrong et al., 2016). These demonstrations focus on specific glaciers through targeted acquisitions. However, newly launched earth observation constellations are designed to sense almost continuously in a non-discriminate fashion. This process is facilitated through commercial constellations of satellites, as some sense the globe daily with high resolution (Planet Team, 2017). Continuous sensing is also facilitated through multiple public constellations (e.g., Landsat 8 and Sentinels-2A and -2B) when combined, reduce revisit times from weekly to daily timescales, particularly toward the poles. With the technique proposed here, it may be possible to detect local, short-lived events, such as speed-up events, glacier outbursts (*jökulhlaup*), calving, surging, or galloping on any glacier.

The advancement of satellite technology has pushed the typical bottleneck of (glacier) remote sensing from data availability to the exploration and processing of large data volumes. Glacier displacement estimation from optical remote sensing has traditionally been done by matching patterns from two subsequent image subsets. The displacement is rooted from a voting over candidate displacements where the similarity is maximized, or its difference in appearance minimized. This pair-based processing is computationally intensive and inefficient, because of its two-dimensional search space, and its simple "winner takes all" approach. This could partially be overcome by including a third image (Altena and Kääb, 2017), but that approach would only enhance the reliability not the processing load. Furthermore, because of the vast amount of imagery within the archives, selection of the best pair might be troublesome, as cloud cover hampers the visibility and adequate cloud detection methods are not yet available for every constellation. Bulk processing of the Landsat 8 archive has recently become operational (Scambos et al., 2016). The vast collection of velocity fields has a wealth of information within, and makes it possible to assess glacier velocity on regional or global scale. Yet this still has not solved the data volume problem, as the velocity data needs to be converted into information or filtered through advanced post-processing procedures, which have not operated at an adequate level. Consequently, alternative approaches have come into sight. One possible strategy includes the implementation of exploratory and quantitative tools, which enable the rapid and reliable extraction of information from remote sensing data. This is the aim of our study; the ability to identify the temporal flow behavior of a glacier within a large collection of remote sensing images without having to match a large number of image pair combinations.

A second concern is the concept behind standard image matching. Standard image matching is a useful tool for measuring larger displacements, but is not optimal for small displacements or noisy time-series. The common framework of image matching finds the displacement of two sub-windows from orthorectified images (Scambos et al., 1992; Kääb and Vollmer, 2000; Heid and Kääb, 2012). Typically, the estimated precision of image matching ranges between 1/2 (Prasad et al., 1992) down to 1/16 (Debella-Gilo and Kääb, 2011) of a pixel. Several requirements must be met in order to establish a successful match. First, the displacement must be statistically significant in order to be observable. However, before any sufficient displacement has occurred on a glacier, the appearance of observable surface features might have degraded. Appearance of an image can change over time (due to snow cover changes and ice melt, for instance) or space (surface deformation instead of simple translation). These surface processes greatly modify the configuration of the surface pattern, and thus the matching quality. Because of these requirements, which can contradict each other, most studies focus on large valley glaciers, or converging glacial outlets which have considerable speed. However, the majority of glaciers move slow and extracted displacements with optical satellite-based remote sensing from these are still a challenge, which we aim to tackle here.

The glaciological community lacks sufficient processing approaches for large volume data exploration. It is therefore useful to investigate how other scientific fields handle the processing of displacements from dense image time-series. Ideally, glaciologists need a method which is robust, sensor independent, and able to process vast amounts of data. Here, we introduce one such methodology, based on a combination of optical flow technology (from computer vision) and particle tracking velocimetry (which is an established technique in experimental fluid mechanics). The advantage of such an approach is its simplicity in formulation and implementation. The achievable localization occurs at the resolution of an individual pixel. The applicability of this methodology is highlighted on a continental mountain glacier in Yukon, Canada, and a maritime glacier on Svalbard: Kronebreen. We first introduce the data, then provide background for our hybrid methodology. We then describe our actual implementation, present and discuss our case study results, and finally draw perspectives and conclusions.

2. BACKGROUND

Acquiring images with a high repetition-rate with respect to the movement rate of the object is a new possibility in remote sensing and glaciology. However, such a setup is common practice in computer vision and experimental fluid mechanics where imaging is often done under controlled laboratory conditions with almost free choice of acquisition frequency. Both latter fields of science have thus well-developed methods to extract displacement fields under such conditions, not least optical flow and particle tracking velocimetry.

2.1. Strategies of Glacier Flow Estimation

Prior to our discussion of technical content, we wish to clarify our nomenclature, as a wide range of names exist for image-matching. Names are mostly a combination of a starting term such as, *speckle, offset, feature, pattern, chip*, and *image*, followed by, *matching, sampling*, or *tracking*.

In image matching, a subset of an image is taken and searched for in the second image. A brute force or *ad-hoc* strategy is applied and image subsets on a regular grid with overlap are processed. Commonly the imagery is pre-processed by applying a band-pass filter (Scambos et al., 1992) or a filter-bank (Ahn and Howat, 2011), in order to enhance the pattern within the image. The size of the subset is dependent on the amount of information within the pattern, which is used to establish a unique similarity. The resulting displacement or offset estimate is therefore a group velocity of the contributing pattern within this subset (Debella-Gilo and Kääb, 2012).

Another strategy includes a search for pronounced features (Tuytelaars and Mikolajczyk, 2008) (*intensity corners* or *blobs*) and the process of finding these features in other acquisitions. The mating of features is done by finding correspondences through descriptors and solving an assignment problem. The field glaciology has not engaged this technique, but it may be a promising approach because the strategy is efficient and as there is an increase of volume from available remote sensing data. This strategy also changes the mathematical framework of the information extracted. Image matching is mostly operating in an Eulerian framework, while feature (or particle) tracking is a Lagrangian framework. Transforming from one to the other is done through the material derivative,

$$\frac{d\vec{\mathbf{u}}}{dt} = \frac{\partial \vec{\mathbf{u}}}{\partial t} + (\nabla \cdot \vec{\mathbf{u}})\vec{\mathbf{u}}. \tag{1}$$

The difference between both systems is not very distinct when an image pair is used. However, the nomenclature becomes important when more than two instances in time are taken into account. The use of *tracking* implies to follow a specific feature within the fluid, thus is in a Lagrangian framework. While *sampling* might imply a site specific sensing strategy with fixed positions, corresponding to a Eulerian framework.

2.2. Optical Flow

There is a rich body of literature on optical flow (Barron et al., 1994; Baker et al., 2011). The field has continued to evolve since its introduction in the 1980's (Horn and Schunck, 1981). The optical flow problem can be formulated as,

$$\frac{\partial \mathbf{I}}{\partial t} = \frac{\partial \mathbf{I}}{\partial x}\frac{\partial x}{\partial t} + \frac{\partial \mathbf{I}}{\partial y}\frac{\partial y}{\partial t}. \tag{2}$$

Here, $\mathbf{I}$ denotes the intensity of a pixel within the image, and the derivatives are in space (x, y) and time (t). The right side of the equation is a common entity for many studies in glaciology. The gradient operators are used to enhance edges, and off course the velocity field $(\frac{dx}{dt}, \frac{dy}{dt})$ is the component searched for through optical pattern matching. The left-hand-side of the equation is, to our best knowledge, only highlighted in Bindschadler et al. (2010). In that study, visually stable icesheet imagery was differenced, and directly related to changes in the slope of the terrain. A connection to movement was not made, though this was done by Kääb (2005), see their Figures 4–7, but only in a qualitative manner of change/no-change.

The advantage of this formulation is its ability to work at the level of individual pixels, while image matching needs a support region of several pixels. Consequently, derivative products, such as strain rates, can have a higher spatial resolution. But the system of equations in Equation (2) is ill-posed, and can only be solved in a global approach through regularization, where in general a constraint on the curvature of the velocity field is given. Alternatively, a local approach can be taken, where Equation (2) is formulated as linear system of equations. In this approach, the neighborhood is taken into the least squares estimation in order to make the design matrix full-rank. An assessment of optical flow methodologies for glacier flow has been done by Vogel et al. (2012), however the results were not encouraging. One reason might have been the temporal baseline of the images, which were taken a year apart, and which resulted in considerable change of surface features.

In order for optical flow to work reliably, the constraint of consistency of brightness should hold, because illumination changes (left-hand-side of Equation 2) always resolve in movement (right-hand-side). However, two effects interfere with this constraint. First, glaciers are partially covered by snow, which has a certain reflection curve. As snow "ages," the grain size increases and the reflection intensity decreases (Warren, 1982). Second, a considerable portion of glaciers is situated at high latitudes. Consequently, irradiance varies as the sun elevation changes rapidly in autumn and spring. These two processes are highly influential, such that finding acquisitions which do satisfy the brightness consistency constraint is difficult. Hence, direct use of typical past and current satellite image time series for optical flow is not useful in general.

2.3. Particle Tracking Velocimetry

In experimental fluid mechanics, the flow of fluids is examined through recording a fluid seeded with particles or grains using high frame-rate cameras. Again, the literature is very rich (Maas et al., 1993; Guezennec et al., 1994) and references given here are therefore limited. Within particle tracking velocimetry also cross-breeding is found where optical flow is solved within a stream function (Heitz et al., 2010; Luttman et al., 2013). When the rate of displacement is more than several pixels, the main methods used are based on matching windows according to similarity. This pattern matching technique is known as Particle Image Velocimetry (PIV) (Sveen and Cowen, 2004; Raffel et al., 2013). These experiments are done in a laboratory setting, where influencing parameters are highly controlled. For in-plain flow the particles are lighted with a lightsheet and the camera is aligned perpendicular to this plain. The resulting imagery is transformed to a binary image by a threshold and converted to features. Features in consecutive images are then connected through a nearest neighbor search. This is robust, because the movement is within the pixel. When longer displacements occur or the seeding of particles increases this methodology needs regularization and transforms into a correspondence problem.

Again, if this methodology is directly related to glacier flow some complications appear. First, the observed features on a glacier are dynamic in appearance. On a glacier, features have different time scales, and may exist for decades (*ogive*), years (*looped morain*), months (*crevasse*), weeks (*meltwater channel*), or days (*snow patch*). Snow cover can cause features to appear and reappear, which forces the thresholding to be adaptive. Furthermore, it is difficult to specify what a traceable feature is, as the feature can be a dust pattern of several meters or a slim melting channel, for instance. But particle tracking velocimetry has methodological elements that are potentially useful for glacier movement estimation.

2.4. Space-Time

A third view-angle tries to look at repeat images through the transformation to space-time imaging. If displacement is reduced to motion (dx/dt) in a known direction, a scatterer has a certain position (X) and reflected intensity,

$$X_{t=i+1} = \frac{dx}{dt} \cdot t + X_{t=i}. \tag{3}$$

This is a first-order Taylor extension and grasps the concept that velocity is orientation in the space-time domain (Adelson and Bergen, 1985; Bruce et al., 2003). A conceptual drawing might illustrate this concept better, as is done in **Figure 1**. Thus, if repeat images are stacked, forming a cube of voxels, any slice through the cube in the third dimension (vertical dimension in **Figure 1**) will give a space-time image (i.e., horizontal axes: space; vertical axis: time). When the sampling is regular over time, it is possible to estimate speed directly within such space-time image through the use of directional filters (Freeman and Adelson, 1991). When transforming the space-axis to the direction of motion, Equation (2) is much simplified, and velocity can directly be estimated:

$$\frac{\partial \mathbf{I}}{\partial t} / \frac{\partial \mathbf{I}}{\partial x} = \frac{\partial x}{\partial t}. \tag{4}$$

These relationships have been exploited within the computer vision community, recently it has evolved into a branch known as video magnification (Wadhwa et al., 2013). Even when outdoor scenes are used in video magnification, the sampling interval is sufficiently high, so that the data complies with the above brightness consistency constraint. Similar advances have been implemented in the field of ocean sciences, see for an extensive account (Jähne, 1993). Again the data have mostly been collected in laboratory settings or had strong coherence in appearance. More complicated flow has been analyzed such as blood flow (Chen et al., 2011), but again this is done in a situation where illumination and features are stable. These approaches might be of particular use for repeat Synthetic Aperture Radar (SAR) imagery, as glacial features are more visually coherent in this type of data over short time scales due to active illumination.

3. DATA AND SITES

Landsat 8 acquires imagery every 16 days from the same orbital track. The Sentinel-2 constellation is planned to provide coverage every 5 days and thus has an improved capability to monitor glacier flow (Kääb et al., 2016). At the time of writing only the first satellite of the Sentinel-2 constellation, 2A, is operational, thus the potential revisit time is 10 days from the same orbital track. Sentinel-2B is successfully launched, though. In the summer season of 2015, before Sentinel-2A was launched, the SPOT5 satellite was set into a different orbit before it was finally de-orbited. This maneuver, called SPOT5 Take5, was commissioned to mimic the fully operational Sentinel-2 constellation, that is a 5 day revisit time. Because of its low orbit the spatial resolution of the acquired multispectral imagery is 10 m, creating a time-series which was up to then not met in terms of resolution and revisit times by any other satellite mission. The maneuver was a presage for the current situation we are in now, where the Earth is sensed on a daily or sub-weekly basis with high resolution.

The SPOT5 Take5 mission had 150 selected sites, including three glaciers. Two of these glaciers are examined in this study. Kronebreen is a typical case for a maritime terminating glacier setting, where much of the collected imagery has clouds. A second site is the Kaskawulsh Glacier (**Figure 2**), which is in a continental setting and is an example of a more "clean" dataset

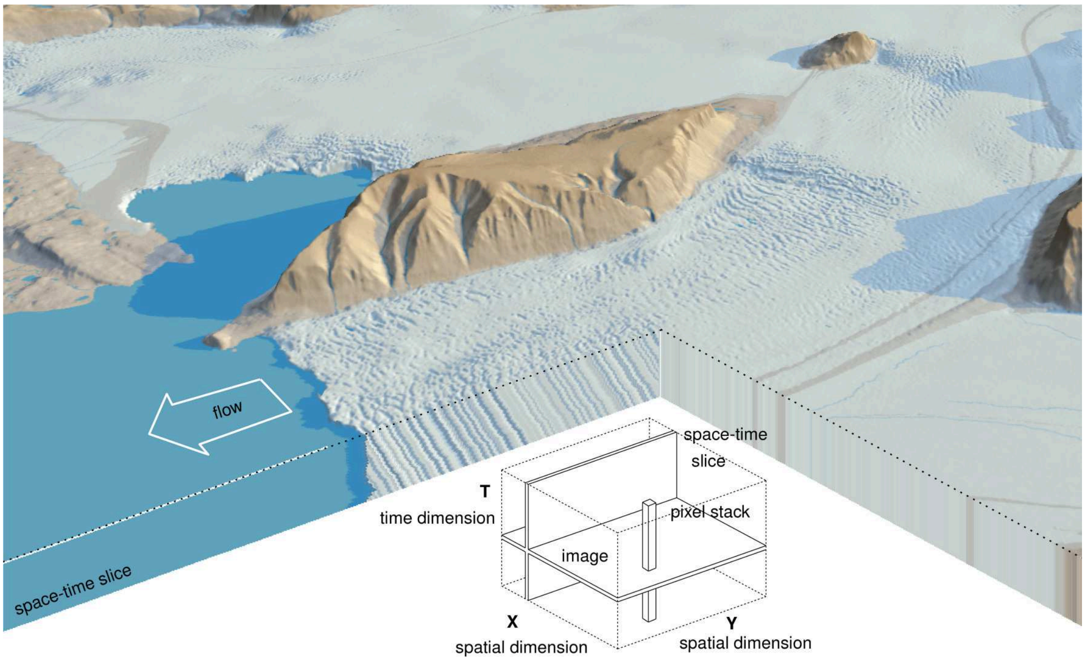

FIGURE 1 | Schematic illustration of an image stack. In the background is the interpretation of such a slice. Movement in the spatial domain results in orientation in the space-time domain. The 3D background image shows Kronebreen, image courtesy of mapping division at Norwegian Polar Institute.

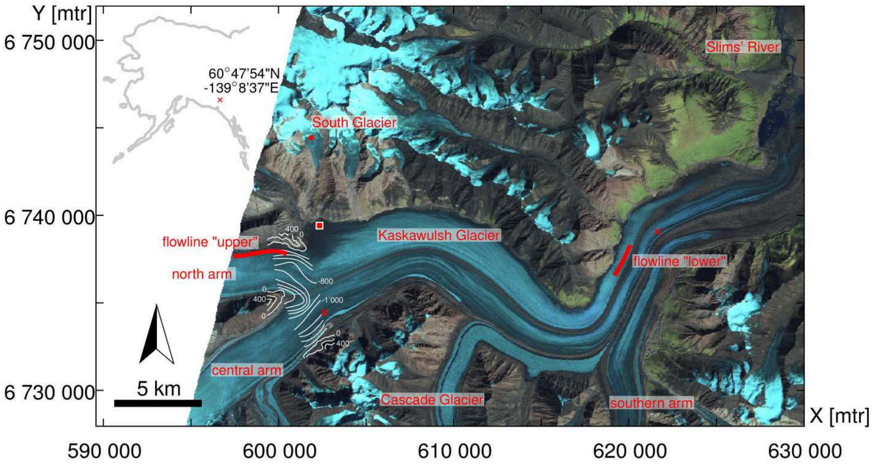

FIGURE 2 | False color composite of a SPOT5 acquisition taken on the 4th of August 2015 of the lower part of Kaskawulsh Glacier, together with the flowlines used in this study. The square indicates the location of a glacier-dammed lake, the circle indicates the position of the automatic weather station, and the two crosses indicate dismantled dGPS stations. The flow direction is from left to right. In the confluence of Northern and Central Arm the local (bedrock) topography is illustrated with white isohypses, they have an interval of 200 m and are redrawn from Dewart (1968).

due to reduced cloud cover. The latter site was selected for other purposes than glaciology, hence, only the lower half of this glacier is acquired. The third glacier site within the SPOT5 Take5 campaign is Glacier de la Plaine Morte, Switzerland. During the ablation season most melt water is supraglacial, hence water input to the bed is minimal due to minimal glacier dynamics (Huss et al., 2013). Hence, much of the velocity variation is absent, so data from this site was neglected. All campaign imagery is freely available through https://spot-take5.org, hosted by the THEIA land data center.

The acquisitions of the SPOT5 Take5 campaigns where taken from the 11th of July 2015 till the 8th of September 2015. Imagery was collected with an interval of 5 days, with an exception for the 31st of May and the 24th of August. The imagery is multispectral (green, red, NIR, and SWIR), the pixel resolution is 10 m and the imagery has an extent of roughly 62 km.

4. METHOD

In this section, the implementation of our approach based on the above methodological background is laid out. Our implementation comprises of two approaches and thrives on data reduction, through the simplification of the spatial domain to a glacier flowline. By doing so, we assume the flowline does not change, i.e., the flow direction stays constant over time. Hence motion out of the vertical plane through the flowline will result in a reduced estimation of speed. This might be the case when tributaries surge, or competing flows interfere. Normally, the dominant change in velocity is due to sliding, hence mainly the magnitude of velocity changes, not or much less its direction.

4.1. Trajectory

In order to obtain the flowline that is used to slice through the data-cube, we rely on traditional image matching. Alternatively, it is possible to estimate a centerline through GIS routines based on a DEM (Kienholz et al., 2014; Machguth and Huss, 2014; Le Moine and Gsell, 2015) or glacier outlines, but for instance on flat glaciers such an estimated line may not align well with the flow. Therefore, in our implementation, out of a collection of imagery, good pairs are selected that have a minimum of cloud cover and strong visual contrast to do image matching and extract a velocity field. Specifically, we used two image pairs, one from spring and one from autumn, and after local median filtering the two velocity fields are combined by taking the mean. The resulting vector field is then used to estimate a trajectory, given a seed point (see **Figure 3**).

4.2. Space-Time

This estimated trajectory is the reference line for the image data sampling and tracking. Two different strategies can now be exploited, one based on the pattern given by the imagery and one based on features within the imagery.

The construction of the image stack, i.e., of the temporal axis, is done by sampling the Red, Green, and NIR image bands at 10 m spacings along the flowline (i.e., above trajectory). As we are interested in local features, and less so in the absolute values, a high-pass filter is applied onto this image, prior to the sampling. The flowline is not aligned with the pixel array, thus bi-linear interpolation is used for the sampling. Then for every time instance, which has a fixed time interval of 5 days in our case, a line of high-frequency interpolated intensities is added to the stack, forming a space-time slice. Manual delineation is applied onto the space-time image to estimate the temporal velocity change. Features are tracked by clicking several polylines within the space-time slice. The slope of a line segment from such a polyline is a direct estimate of the velocity, see Equation (4). From this it becomes clear that the longer the time interval (i.e., the

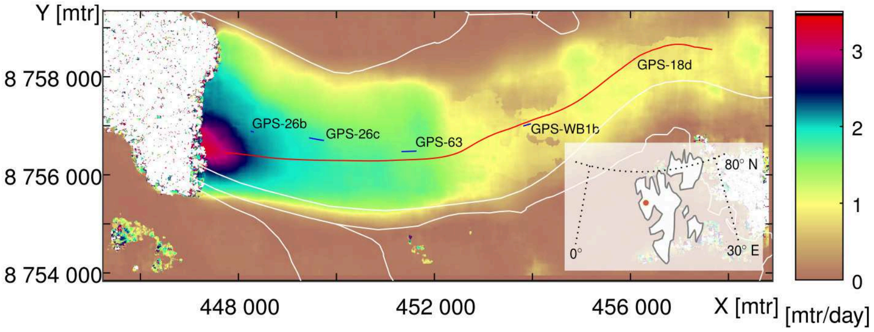

FIGURE 3 | Flow magnitude of Kronebreen, derived from SPOT5 Take5 imagery (merge between spring and autumn speed, see text). In red the flowline, used for this study is highlighted. The blue lines indicate the travel path of the GPS stakes, its data is kindly provided by J. Kohler, Norwegian Polar Institute.

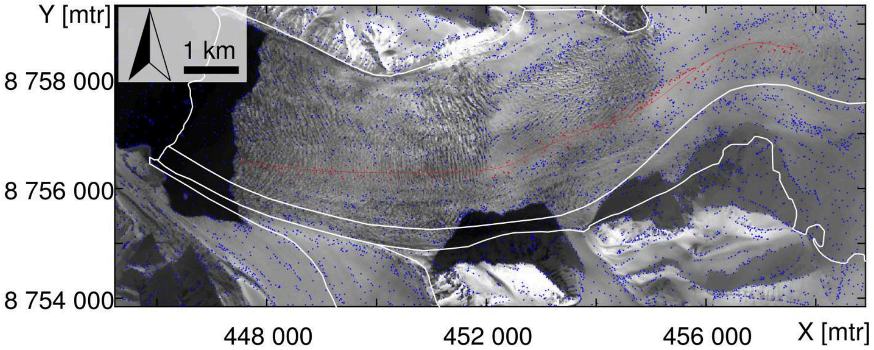

FIGURE 4 | SPOT5 imagery taken over Kronebreen at the 29th of April 2015. The blue dots highlight the Harris corner detections, the red dots indicate Harris interest points within the buffer of the flowline, which are used for the tracking. The white lines are glacier outlines from Nuth et al. (2013).

length of the time-domain segment), the more accurate the slope (i.e., velocity estimation) is.

A second strategy is based on image features. First, the Harris feature detector (Harris and Stephens, 1988), creates an energy field which is thresholded in absolute sense, resulting however in clustering (Brown et al., 2005). Therefore, a moving window is used, including the local maximum, consequently, features are more spread out over the scene, see **Figure 4**. For robustness, the sub-pixel localization is done through a center-of-gravity estimation (van Assen et al., 2002), and not a parabolic fitting of some sort. The resulting features are not necessarily strictly on the flowline, thus a buffer is created to select features close to the flowline. This procedure is applied to every image. From this collection of features within the image collection, connections need to be made. Every feature recorded at one time instance can be connected with another feature. Many combinations are possible, therefore a rule needs to be implemented, to do so. This assignment problem is solved by a simple implementation. The search space in time is set to a certain upper limit at three times the mean speed at that point to account for speed changes, plus an additional 7.5 m to account for potential co-registration errors. Thus, per unit of time one is limited to look up to a certain distance away from the feature, beginning with a master image and a collection of features in it, and a slave image where features are searched for. Then, for each feature in the slave image, the position is reversed with a tracer to get to the position at the time of the master image. Thereby, the same velocity field as used for extraction of the flowline is utilized. The tracer estimates the position of the feature in the master-image. When this estimated position is at close proximity to a master-image feature, it is considered a candidate connection. The specification of close proximity is depended on the quality of the velocity field and the magnitude of variability in speed. Nonetheless, multiple candidate connections can be established, therefore a descriptor, a local binary pattern (Heikkilä et al., 2009), is used to assess the amount of similarity and validity of a connection. Thus, our assignment is implemented by several levels. The use of a moving window ensures that features are more evenly distributed. Then the potential feature-set is reduced through back-tracking, and the local binary pattern serves as a final hard classification rule.

5. RESULTS

5.1. Kaskawulsh, St. Elias, Yukon

Kaskawulsh Glacier lies within the St. Elias mountain range, Yukon. It is a 70 km long temperate glacier which originates

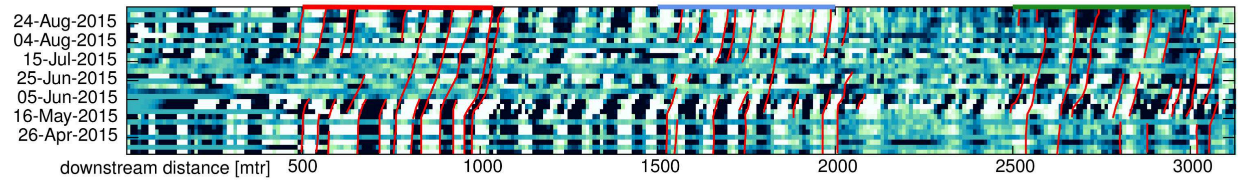

FIGURE 5 | Space-time image from SPOT5 Take5 imagery of flowline "upper" of Kaskawulsh Glacier, as in **Figure 2**. The white-green-black patterns are the high frequency intensities on the drawn flowline. Because many features are discontinuous, tracking is done on different section of the flowline. The horizontal colored bars on top of the figure indicate these sections of displacement estimates, which colors correspond to the velocity estimates in **Figure 7**.

from the Kluane icefield. The annual variability of flow speed can at some places be in the order of 25% (Waechter et al., 2015). The overall annual cumulative speed, or displacement per year, has not changed considerably throughout the last decades. From all 29 SPOT5 Take5 acquisitions, only seven are to a large extent cloud-covered, the rest are cloudless or have minor clouds scattered over the scene. This dataset is therefore ideal to implement the pattern-method, as described in Section 4.2, where imagery is stacked and a vertical slice is analyzed.

A continuous measurement campaign of several dGPS stations has been deployed for 7 years on Kaskawulsh Glacier. However, the campaign ended a year prior to the 2015 Take5 mission. Dependent on the season, different velocity patterns occurred. At the start of the melt season, velocities increase and this increase propagates up-glacier as time progresses. In winter season the velocities decrease again, but this velocity change propagates down-glacier over time (Herdes, 2014, Luke Copland, pers. comm.). Therefore, it is of interest to not only investigate one point at high precision, but to also study the spatial pattern of the seasonal flow evolution. Another network of GPS-stations is installed in the vicinity of a glacier dammed lake (see the square in **Figure 2**). These instruments are set out to look at short-term drainage processes. At the lake border the glacier flow is very limited. In addition, on this glacier section, or on the neighboring South Glacier almost no visually coherent features can be found that can be tracked over time. Therefore, no direct verification data is available over the Kaskawulsh site. However the cloud cover is very much limited, and this case study is thus meant to demonstrate our pattern method for upcoming dense time-series of optical data.

Two flowlines were sampled on the Kaskawulsh Glacier. The first flowline (named "upper") leads over a crevasse field that, due to its shading and shadowing, is visible over the full time period. Furthermore, it is in proximity of the location where formerly an installation of a dGPS has been recording. Its space-time image is illustrated in **Figure 5**. In our space-time visualization speed-ups appear as inclinations tilting into flow direction (here: right), and slow-downs as tiltings against flow direction, i.e., toward the vertical. A change in displacement is clearly visible starting in mid-May, then velocity slowly declines throughout the summer.

Over the full 3 km extracted, the glacier seems to move as a bulk. This is more clearly observable when features are tracked manually and not interpreted. These are the red lines superimposed onto the image, following features along the space-time slice. Every segment of these polylines has a coordinate in space and time, consequently, its slope gives the velocity over this period. Estimates over such time intervals are plotted in **Figure 5** as horizontal lines. The lines following features are subdivided in three different segments, and color coded, to assess the reliability and spread of the velocity estimates. Their timing and magnitude seem to be in accordance with each other. A multiple annual mean seasonal velocity estimate from a dGPS station from the nearby Central arm is also plotted in this figure, as a thicker gray line. The magnitude of the late-winter velocities seems to be higher for this station, than the sampled flow line. This can be due to the difference in depth, as the sampled line is in a shallower part then the dGPS station, see **Figure 2**. The factor between different magnitudes in glacier speed is due to the position of the flowline, which is in a shearing zone with high differential motion, see Figure 3B in Waechter et al. (2015). The mean velocity in the spring season covers both slow and high speeds, and is therefore difficult to assess. The fall season seems again to be in accordance with our estimate, however the estimates are noisy.

The second flowline is named "lower" like the dGPS station which has been recording for several years, but was dismantled a year before the Take5 campaign. The flowline is situated over a crevasse field, in the middle of the glacier branch that is also connected to the "upper" flowline. The space-time slice over this flow line is illustrated in **Figure 6**. Its conversion to velocities is illustrated in **Figure 7**. In the background is the temperature record from an automatic weather station for South Glacier, which is at 2,280 masl. The "upper" profile is closer to South Glacier and at an approximate elevation of 1,750 masl, while the "lower" flowline is situated at around 1,150 masl. Nevertheless, over a short period of time the temperature increases in late winter/early spring. This warming results in more meltwater input into the hydrological network. Due to the meteorological lapse rate, melt occurs later at higher elevations. This effect is observable when the timing of speed-up at the "upper" and "lower" locations are compared to each other, see the vertical lines in **Figure 7**. The "lower" flowline experiences an earlier speed-up, roughly 10 days earlier. Such an effect has been observed in the dGPS campaign in the years prior to the Take5 campaign (Darling, 2012; Herdes, 2014), and our

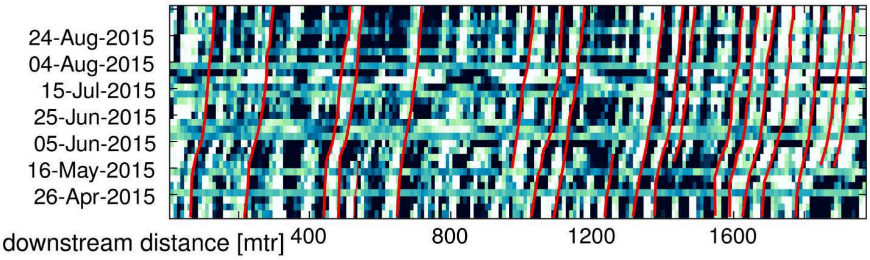

FIGURE 6 | Space-time image from SPOT5 Take5 imagery of flowline "lower" of Kaskawulsh Glacier, as illustrated in **Figure 2**. In the background the white-green-black color scheme corresponds to high-pass filtered intensities of the image at the position of the flowline. The red lines try to follow features within the slice and are used in the velocity estimates in **Figure 7**.

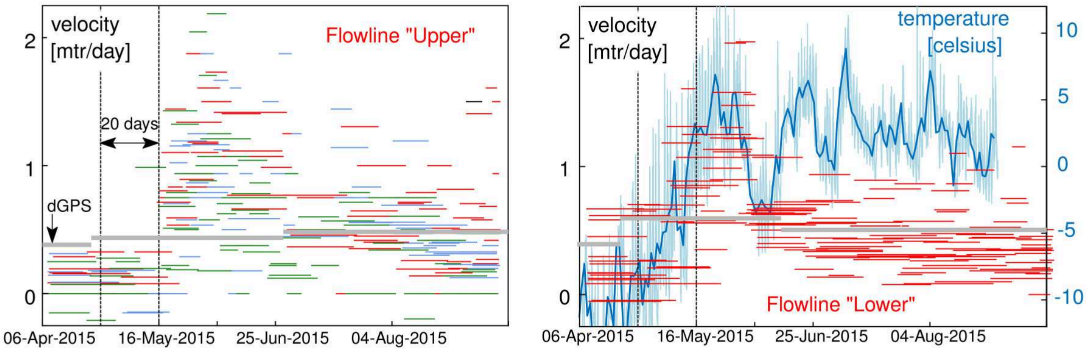

FIGURE 7 | Velocity estimation at different positions on the flowline of Kaskawulsh Glacier. These curves are integrated from the lines drawn in **Figure 5**. Colors correspond to the segments shown on top of **Figures 5**, **6**. The 5 min interval temperature data is in light blue and its daily mean in darker blue. The automatic weather station data is kindly provided by G. Flowers, Simon Fraser University. The dark gray horizontal lines are the multi-year seasonal average of nearby GPS stations, data from L. Copland, University of Ottawa.

estimates seem to be able to observe the timing of such dynamics. Furthermore, in the beginning of July the glacier dammed lake drained (Gwenn Flowers, pers. comm.), however no speed change is observable for this period in our estimates at point "lower".

5.2. Kronebreen, Svalbard

Kronebreen is a tidewater glacier near Ny-Ålesund on Svalbard, it is an outlet glacier that transports ice from the 300km^2 Holtedahlfonna and the 70km^2 Infantfonna icefield into the ocean. Its lower part is constrained by a narrow valley of roughly 5 km wide, see **Figures 3**, **4**. The flow is all-year round at a high speed of a couple of meters per day (Kääb et al., 2005; Schellenberger et al., 2016). From the 30 SPOT5 Take5 acquisitions taken over Kronebreen, only five where cloud free. Especially July 2015 was unusually cloudy. Hence, in order to have a more useful dense image stack, cloud-free Landsat 8 imagery was included to form a time series together with the SPOT5 Take5 data. Due to Landsat 8 s continuous sampling strategy and the high latitude of Svalbard, images were collected from different orbit paths and different times of the day, ranging from 04:47 to 23:52 local time. The varying sun angles changed the visual appearance of the images heavily. Since 2009, several stand-alone single-frequency GPS receivers have been installed on Kronebreen. In our case, the positional estimates used are daily averages of four GPS stakes.

A total of 50 Landsat 8 and SPOT5 images were used for the extraction of velocity over the Kronebreen glacier. For this case study the feature method, as described in Section 4.2, is used. This is done because the pattern method, using the intensities directly is not sufficient. Such a pattern stack is illustrated in **Figure 8**, to illustrate the complications. Within the space-time image slice of **Figure 8**, the features are clearly observable; however this is also a weakness. For example, when over a period clouds were present and movement has been significant, it is difficult to follow the correctly corresponding crevasse feature, as they all have a self-similar alternating pattern. This is the case in July, which was a cloudy month, resulting in gray noise without coherent texture. In addition, co-registration errors, because of different acquisition angles (Altena and Kääb, 2017), can potentially cause bending/tilting. Therefore, in this section we use the feature based method.

The Harris corner detector had a moving window with an extent of 300 m, intensity corners were selected with a regular threshold setting (sensitivity factor, $\alpha = 0.04$). First, the correspondence problem was solved only with a neighborhood

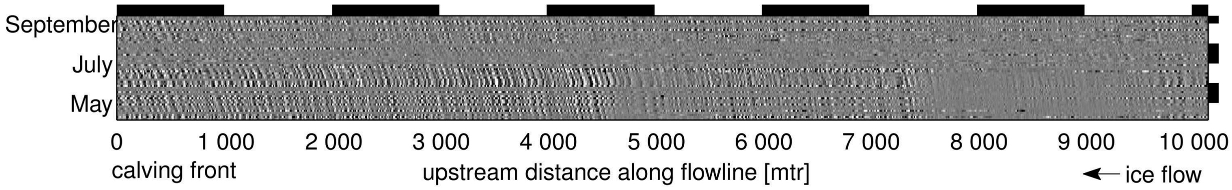

FIGURE 8 | Space-time image slice pattern from SPOT5 Take5 imagery of Kronebreen. The black and white patterns are high-pass filtered intensities. The flowline used to slice the data-cube is illustrated in **Figure 3**. Flow direction is from right to left of the slice.

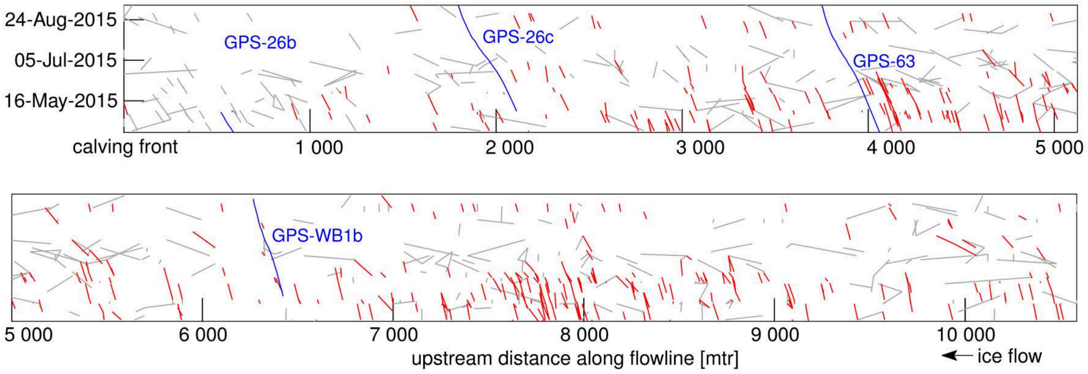

FIGURE 9 | Space-time image of the Kronebreen flowline illustrated in **Figure 2** in red. The filtered correspondences are in gray. Trajectories of the GPS stakes are shown in blue.

constraint, i.e., if a feature was close by (within 7.5 m), a connection was made. This resulted in a well-populated space-time slice, as illustrated in dark gray within **Figure 9**. Though coherent tilts in the spatial and temporal domain are observable, outliers existed. A descriptor was therefore included into the selection program and multiple candidates could be tested. This resulted in a harder selection, though more reliable, and the resulting trajectories are illustrated in red within **Figure 9**. In addition to the estimated trajectories, the GPS measurements (position see **Figure 3**) are illustrated as well. Though the spatio-temporal trajectories from the optical dataset are sparse, there is general agreement with the GPS trajectories (**Figure 10**). In July a speed-up occurred, and was recorded by the GPS, is not apparent in our velocity estimates due to cloud cover. The spread of the estimates is also observable, but when multiple estimates are present, when sufficient estimates are present they do align with the measured GPS speed. Nonetheless, outliers exist. In order to be of use for analysis, the samples need to be of considerable size and trend estimators need to be robust against heavy tails.

6. DISCUSSION

In both case studies, our approach reveals reasonable and validated seasonal and spatial variations in glacier speed. We simplify the space-time domain along flow-lines which results in a reduction of the spatial coverage in comparison to classical image matching approaches. However, the temporal resolution becomes maximum in our approach (i.e., all available images are included) such that short events become visible in ways that would be difficult or computationally intensive to identify using traditional image matching.

The SPOT5 Take5 dataset, as well as the Landsat imagery will have geo-referencing errors and orthorectification errors. The absolute localization was refined through co-registering all images to a Landsat scene, while relatively the SPOT5 data where registered on sub-pixel level (Hagolle et al., 2015). This will have an effect on the absolute geolocation, but this is not of interest in this study. Relative to each other, the images will have some remaining co-registration inaccuracies. In this study, we are using tens of images, hence the co-registration inaccuracies will appear as small roughness of the time-domain features, leaving them displayed as a whole. When the temporal baseline increases the patterns start to emerge above the co-registration noise, i.e., roughness of the space-time features.

In the "upper" section of the Kaskawulsh Glacier velocity estimates have been subdivided into three sections. Although some spread occurs in the velocity estimates, the timing of the increase in speed is clear and in accordance with each other. The velocity estimates have different spans of time, hence fusion of such estimates into a coherent time-series can be complicated. Furthermore, the pattern extraction is manual and thrives on

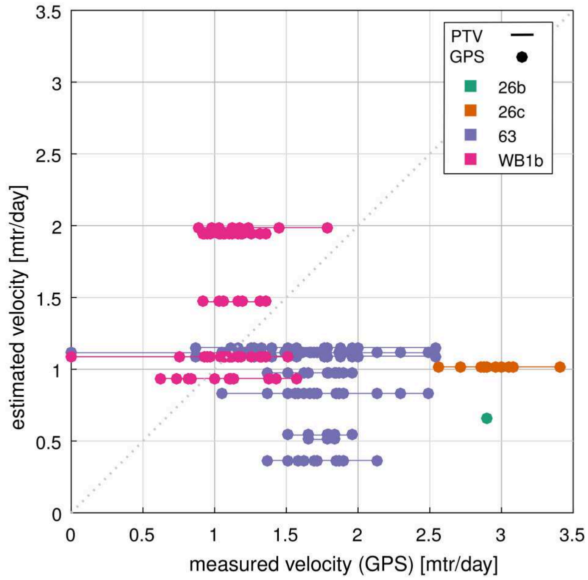

FIGURE 10 | Velocity measurements of the GPS on Kronebreen are plotted in different colors and are indicated by the dots. These measurements are set against th the estimated velocities of features, as in **Figure 3**. These estimates cover a certain time span and are therefore illustrated as a line. Only estimates within a spatio-temporal neighborhood of 200 m of the GPS's are included and shown.

visual interpretation. Attempts for automatic procedures for such data did not work out. Consequently, our method is clearly an exploratory tool and no replacement for image matching. Nevertheless, it can be of help in selection the appropriate set of images in a large image collection or for identifying special dynamic events.

The combination of a Harris-corner detection and center-of-mass sub-pixel estimation is a computationally fast detector. However, due to this choice, a compromise is made with the localization of the corner. For example, the Plessy-detector (Noble, 1988) might be more precise in its estimate for "cornerness" at every pixel. The Föstner-detector (Förstner and Gülch, 1987) directly estimates corners at sub-pixel level through ordinary least squares adjustment, but is computationally more intensive. A similar sub-pixel Harris detector, also using least squares adjustment (Zhu et al., 2007), was implemented, but seemed sensitive to noise and outliers. It is this repeatability of a detector which is of more importance for our application, and for blur (*thin clouds*) and noise (*loss of visual coherence*) these properties seem to be relatively good for the Harris-detector (Montero et al., 2010).

In the summer period, when the speed up of Kronebreen occurred, almost no cloudless images are available for the year studied. The additional Landsat imagery was thus only helpful to a limited extent. This can be due to the simple feature descriptor used in this study. The sun angle heavily changed the appearance of the crevasse field of Kronebreen. More advanced feature descriptors, such as for example SIFT (Lowe, 2004) or LIOP (Wang et al., 2011), might be able to better describe the feature in such instances. In such implementation, the difference with traditional image matching will reduce, and similar limitations will start to occur. Nevertheless, illumination-invariant image descriptors reduce miss-assignments of correspondences and with the help of robust neighborhood statistics, one might be able to produce a detailed time-series. For the Kronebreen case, such an approach might still not be able to extract the speed-up occurring in summer as cloud cover stays a problem, which cannot be tackled with optical remote sensing data. Eventually thus, the optical flow methods demonstrated here could be applied to merged optical and SAR data.

One extension to enhance robustness is by incorporating image matching. Annual displacements can be estimated from two selected scenes, which relates to two end-nodes on a space-time representation. These end-nodes can be used to constrain the path-finding within the space-time imagery.

7. PROSPECT

The key strength of this method is the ability to explore the timing of glacier speed variations from massive image stacks without the need of matching image pairs. Image matching is computationally costly when applied to large data sets and prone to specific problems, for instance related to image selection or assignment of corresponding patterns. In contrast, image stacks and space-time slices can be extracted and visualized fast and efficient. We therefore envisage a range of three potential application scenarios for the approaches introduced here:

First, our methods offer a simple alternative technique for visualizing glacier speed variations over time from massive stacks of repeat images. In view of the wealth of current and in particular upcoming satellite data, it might not be sufficient to use only classical visualization approaches, such as vector fields or image animations (Paul, 2015).

Second, our methods can be used to visualize the space-time content of a massive series of repeat images in order to select a subset of the most suitable (cloud-free) image pairs to apply image matching to, manually or automatically. For instance, suitable matching scenes become well-visible in our space-time slices. Or, a higher density of matching pairs can be selected around variations in speed as visible in the deviations of space-time features from straight lines in the time domain, leading to some kind of adaptive selection of matching pairs.

Third, our methods can be used to directly derive glacier speed and its variation over time by extracting and analyzing space-time features, as demonstrated for both case studies. Again, (near-)future amounts of satellite data suitable to monitor glacier flow might simply be too large to apply classical image matching methods.

8. CONCLUSION

This case study explores the potential of increased satellite revisit time in combination with tracking approaches from other scientific fields, optical flow, and particle tracking velocimetry, for the monitoring of glacier speed. Our methods explored the simplification of current approaches through data reduction by means of flowlines. This approach is new, though it has been applied to other glaciological applications, such as glacier snout extent (Usset et al., 2015).

Two technical approaches were highlighted, including pattern-based and feature-based, and were applied to two glaciers. In both studies, the seasonal pattern and timing of the summer acceleration could be identified. The strategies for connecting features or finding orientation within the space-time data were primitive in the context of this study. However, there is potential knowledge within the research field of computer vision or fluid mechanics available to automate robust procedures to mate features or estimate orientation.

This study also shows the potential of our approaches for multi-sensor integration. The velocity of Kronebreen was extracted from acquisitions of different satellites. In addition, the feature based methodology seemed to be less hindered by cloud cover, then traditional image matching. This promise opens the possibility for high resolution imagery with daily revisit time. Hence, our methodology is relevant for Sentinel-2, when the companion-satellite constellation is in full operation. However, upcoming constellations of small satellites (e.g., Planet, UrtheCast, Blacksky, ...) might even enhance the opportunity to monitor the inter-seasonal dynamics of glaciers using the approaches evaluated and demonstrated here.

AUTHOR CONTRIBUTIONS

BA and AK initiated the study. BA designed the structure, developed, and implemented the methodology. Both authors interpreted the results and wrote the article.

ACKNOWLEDGMENTS

We would like to thank Jack Kohler for providing us the GPS data over Kronebreen and Gwenn Flowers for the AWS data over South Glacier. Furthermore, we thank Luke Copland for discussions about the flow dynamics of Kaskawulsh Glacier. We are also grateful to three referees and the editor Alun Hubbard for their constructive comments that certainly helped to improve the paper. We also thank Shae Frydenlund for improving the English language of an early version of this contribution. This study is funded by the European Research Council under the European Union's Seventh Framework Programme grant agreement no. 320816 and the ESA project Glaciers_cci (4000109873/14/I-NB). We are very grateful to ESA and the EU Copernicus program for free provision of the SPOT5 imagery.

REFERENCES

Adelson, E., and Bergen, J. (1985). Spatiotemporal energy models for the perception of motion. *J. Opt. Soc. Am. A* 2, 284–299.

Ahn, Y., and Howat, I. (2011). Efficient automated glacier surface velocity measurement from repeat images using multi-image/multichip and null exclusion feature tracking. *IEEE Trans. Geosci. Remote Sens.* 49, 2838–2846. doi: 10.1109/TGRS.2011.2114891

Altena, B., and Kääb, A. (2017). Elevation change and improved velocity retrieval using orthorectified optical satellite data from different orbits. *Remote Sens.* 9:300. doi: 10.3390/rs9030300

Armstrong, W. H., Anderson, R. S., Allen, J., and Rajaram, H. (2016). Modeling the WorldView-derived seasonal velocity evolution of Kennicott glacier, Alaska. *J. Glaciol.* 62, 763–777. doi: 10.1017/jog.2016.66

Baker, S., Scharstein, D., Lewis, J., Roth, S., Black, M., and Szeliski, R. (2011). A database and evaluation methodology for optical flow. *Int. J. Comp. Vis.* 92, 1–31. doi: 10.1007/s11263-010-0390-2

Barron, J., Fleet, D., and Beauchemin, S. (1994). Performance of optical flow techniques. *Int. J. Comp. Vis.* 12, 43–77.

Berthier, E., Vadon, H., Baratoux, D., Arnaud, Y., Vincent, C., Feigl, K., et al. (2005). Surface motion of mountain glaciers derived from satellite optical imagery. *Remote Sens. Environ.* 95, 14–28. doi: 10.1016/j.rse.2004.11.005

Bindschadler, R., Scambos, T., Choi, H., and Haran, T. (2010). Ice sheet change detection by satellite image differencing. *Remote Sens. Environ.* 114, 1353–1362. doi: 10.1016/j.rse.2010.01.014

Brown, M., Szeliski, R., and Winder, S. (2005). "Multi-image matching using multi-scale oriented patches," in *IEEE Conference on Computer Vision and Pattern Recognition, Vol. 1* (San Diego, CA), 510–517.

Bruce, V., Green, P., and Georgeson, M. (2003). *Visual Perception: Physiology, Psychology, & Ecology*. New York, NY: Psychology Press.

Chen, Y., Zhao, Z., Liu, L., and Li, H. (2011). Automatic tracking and measurement of the motion of blood cells in microvessels based on analysis of multiple spatiotemporal images. *Meas. Sci. Technol.* 22:045803. doi: 10.1088/0957-0233/22/4/045803

Darling, S. (2012). *Velocity Variations of the Kaskawulsh Glacier, Yukon Territory, 2009-2011.* Master's thesis, University of Ottawa.

Debella-Gilo, M., and Kääb, A. (2011). Sub-pixel precision image matching for measuring surface displacements on mass movements using normalized cross-correlation. *Remote Sens. Environ.* 115, 130–142. doi: 10.1016/j.rse.2010.08.012

Debella-Gilo, M., and Kääb, A. (2012). Measurement of surface displacement and deformation of mass movements using least squares matching of repeat high resolution satellite and aerial images. *Remote Sens.* 4, 43–67. doi: 10.3390/rs4010043

Dewart, G. (1968). *Seismic Investigation of Ice Properties and Bedrock Topography at the Confluence of Two Glaciers, Kaskawulsh Glacier, Yukon Territory, Canada.* Technical Report 27, Institute of Polar Studies, The Ohio State University.

Fahnestock, M., Scambos, T., Moon, T., Gardner, A., Haran, T., and Klinger, M. (2015). Rapid large-area mapping of ice flow using Landsat 8. *Remote Sens. Environ.* 185, 84–94. doi: 10.1016/j.rse.2015.11.023

Förstner, W., and Gülch, E. (1987). "A fast operator for detection and precise location of distinct points, corners and centres of circular features," in *Proc. ISPRS Intercommission Conference on Fast Processing of Photogrammetric Data* (Interlaken), 281–305.

Freeman, W. T., and Adelson, E. H. (1991). The design and use of steerable filters. *IEEE Trans. Pattern Anal. Mach. Intell.* 13, 891–906.

Guezennec, Y., Brodkey, R., Trigui, N., and Kent, J. (1994). Algorithms for fully automated three-dimensional particle tracking velocimetry. *Exp. Fluids* 17, 209–219.

Hagolle, O., Sylvander, S., Huc, M., Claverie, M., Clesse, D., Dechoz, C., et al. (2015). SPOT-4 (take 5): simulation of Sentinel-2 time series on 45 large sites. *Remote Sens.* 7, 12242–12264. doi: 10.3390/rs70912242

Harris, C., and Stephens, M. (1988). "A combined corner and edge detector," in *Alvey Vision Conference*, *Vol. 15* (Manchester), 147–151.

Heid, T., and Kääb, A. (2012). Evaluation of existing image matching methods for deriving glacier surface displacements globally from optical satellite imagery. *Remote Sens. Environ.* 118, 339–355. doi: 10.1016/j.rse.2011.11.024

Heikkilä, M., Pietikäinen, M., and Schmid, C. (2009). Description of interest regions with local binary patterns. *Pattern Recognit.* 42, 425–436. doi: 10.1016/j.patcog.2008.08.014

Heitz, D., Mémin, E., and Schnörr, C. (2010). Variational fluid flow measurements from image sequences: synopsis and perspectives. *Exp. Fluids* 48, 369–393. doi: 10.1007/s00348-009-0778-3

Herdes, É. (2014). *Evolution of Seasonal Variations in Motion of the Kaskawulsh Glacier, Yukon Territory*. Master's thesis, University of Ottawa.

Horn, B., and Schunck, B. (1981). "Determining optical flow," in *1981 Technical Symposium East* (Washington, DC: International Society for Optics and Photonics), 319–331.

Huss, M., Voinesco, A., and Hoelzle, M. (2013). Implications of climate change on Glacier de la Plaine Morte, Switzerland. *Geogr. Helv.* 68, 227–237. doi: 10.5194/gh-68-227-2013

Jähne, B. (1993). *Spatio-Temporal Image Processing: Theory and Scientific Applications*. Heidelberg: Springer. doi: 10.1007/3-540-57418-2

Kääb, A. (2005). *Remote Sensing of Mountain Glaciers and Permafrost Creep, Vol. 48*. Zürich: Schriftenreihe Physische Geographie.

Kääb, A., Lefauconnier, B., and Melvold, K. (2005). Flow field of Kronebreen, Svalbard, using repeated Landsat 7 and ASTER data. *Ann. Glaciol.* 42, 7–13. doi: 10.3189/172756405781812916

Kääb, A., and Vollmer, M. (2000). Surface geometry, thickness changes and flow fields on creeping mountain permafrost: automatic extraction by digital image analysis. *Permafrost Periglacial Process.* 11, 315–326. doi: 10.1002/1099-1530(200012)11:4<315::AID-PPP365>3.0.CO;2-J

Kääb, A., Winsvold, S., Altena, B., Nuth, C., Nagler, T., and Wuite, J. (2016). Glacier remote sensing using Sentinel-2. part I: Radiometric and geometric performance, and application to ice velocity. *Remote Sens.* 8, 598. doi: 10.3390/rs8070598

Kienholz, C., Rich, J., Arendt, A., and Hock, R. (2014). A new method for deriving glacier centerlines applied to glaciers in Alaska and northwest Canada. *Cryosphere* 8, 503–519. doi: 10.5194/tc-8-503-2014

Le Moine, N., and Gsell, P.-S. (2015). A graph-based approach to glacier flowline extraction: an application to glaciers in Switzerland. *Comp. Geosci.* 85, 91–101. doi: 10.1016/j.cageo.2015.09.010

Lowe, D. (2004). Distinctive image features from scale-invariant keypoints. *Int. J. Comp. Vis.* 60, 91–110. doi: 10.1023/B:VISI.0000029664.99615.94

Luttman, A., Bollt, E., Basnayake, R., Kramer, S., and Tufillaro, N. (2013). A framework for estimating potential fluid flow from digital imagery. *Chaos* 23:033134. doi: 10.1063/1.4821188

Maas, H., Gruen, A., and Papantoniou, D. (1993). Particle tracking velocimetry in three-dimensional flows. *Exp. Fluids* 15, 133–146.

Machguth, H., and Huss, M. (2014). The length of the world's glaciers–a new approach for the global calculation of center lines. *Cryosphere* 8, 1741–1755. doi: 10.5194/tc-8-1741-2014

Montero, A., Stojmenovic, M., and Nayak, A. (2010). "Robust detection of corners and corner-line links in images," in *IEEE 10th International Conference on Computer and Information Technology* (Bradford), 495–502.

Noble, J. (1988). Finding corners. *Image Vis. Comput.* 6, 121–128.

Nuth, C., Kohler, J., König, M., Deschwanden, A. V., Hagen, J., Kääb, A., et al. (2013). Decadal changes from a multi-temporal glacier inventory of Svalbard. *Cryosphere* 7, 1603–1621. doi: 10.5194/tc-7-1603-2013

Paul, F. (2015). Revealing glacier flow and surge dynamics from animated satellite image sequences: examples from the Karakoram. *Cryosphere* 9, 2201–2214. doi: 10.5194/tc-9-2201-2015

Planet Team (2017). *Planet Application Program Interface: In Space for Life on Earth*. San Francisco, CA.

Prasad, A., Adrian, R., Landreth, C., and Offutt, P. (1992). Effect of resolution on the speed and accuracy of particle image velocimetry interrogation. *Exp. Fluids* 13, 105–116.

Raffel, M., Willert, C., Wereley, S., and Kompenhans, J. (2013). *Particle Image Velocimetry: A Practical Guide*. Heidelberg: Springer.

Scambos, T., Dutkiewicz, M., Wilson, J., and Bindschadler, R. (1992). Application of image cross-correlation to the measurement of glacier velocity using satellite image data. *Remote Sens. Environ.* 42, 177–186.

Scambos, T., Fahnestock, M., Moon, T., Gardner, A., and Klinger, M. (2016). *Global Land Ice Velocity Extraction from Landsat 8 (GoLIVE), Version 1*. Boulder, CO: NSIDC: National Snow and Ice Data Center.

Schellenberger, T., Van Wychen, W., Copland, L., Kääb, A., and Gray, L. (2016). An inter-comparison of techniques for determining velocities of maritime arctic glaciers, Svalbard, using Radarsat-2 wide fine mode data. *Remote Sens.* 8:785. doi: 10.3390/rs8090785

Sveen, J., and Cowen, E. (2004). "Chapter 1: quantitative imaging techniques and their application to wavy flows," in *PIV and Water Waves, Vol. 9*, eds J. Grue, P. L.-F. Liu, and G. K. Pedersen (World Scientific Publishing), 1–49.

Tuytelaars, T., and Mikolajczyk, K. (2008). Local invariant feature detectors: a survey. *Found. Trends. Comp. Graph. Vis.* 3, 177–280. doi: 10.1561/0600000017

Usset, J., Maity, A., Staicu, A.-M., and Schwartzman, A. (2015). Glacier terminus estimation from Landsat image intensity profiles. *J. Agric. Biol. Environ. Stat.* 20, 279–298. doi: 10.1007/s13253-015-0207-4

van Assen, H., Egmont-Petersen, M., and Reiber, J. (2002). Accurate object localization in gray level images using the center of gravity measure: accuracy versus precision. *IEEE Trans. Image Process.* 11, 1379–1384. doi: 10.1109/TIP.2002.806250

Vogel, C., Bauder, A., and Schindler, K. (2012). "Optical flow for glacier motion estimation," in *Proceedings of the 22nd ISPRS Congress*, *Vol. 25* (Melbourne, VIC).

Wadhwa, N., Rubinstein, M., Durand, F., and Freeman, W. (2013). Phase-based video motion processing. *ACM Trans. Graph.* 32:80. doi: 10.1145/2461912.2461966

Waechter, A., Copland, L., and Herdes, E. (2015). Modern glacier velocities across the Icefield Ranges, St Elias Mountains, and variability at selected glaciers from 1959 to 2012. *J. Glaciol.* 61, 624–634. doi: 10.3189/2015JoG14J147

Wang, Z., Fan, B., and Wu, F. (2011). "Local intensity order pattern for feature description," in *IEEE International Conference on Computer Vision* (Barcelona), 603–610.

Warren, S. (1982). Optical properties of snow. *Rev. Geophys. Space Phys.* 20, 67–89.

Zhu, Q., Wu, B., and Wan, N. (2007). A sub-pixel location method for interest points by means of the Harris interest strength. *Photogrammetric Rec.* 22, 321–335. doi: 10.1111/j.1477-9730.2007.00450.x

Conflict of Interest Statement: The authors declare that the research was conducted in the absence of any commercial or financial relationships that could be construed as a potential conflict of interest.

Paper III: Extracting recent short-term glacier velocity evolution over Southern Alaska from a large collection of Landsat data

Extracting recent short-term glacier velocity evolution over Southern Alaska from a large collection of Landsat data

Bas Altena[1], Ted Scambos[2], Mark Fahnestock[3], and Andreas Kääb[1]

[1]Department of Geosciences, University of Oslo, Blindern, 0316 Oslo, Norway
[2]National Snow and Ice Data Center (NSIDC), University of Colorado, Boulder, CO 80303, USA
[3]Geophysical Institute, University of Alaska Fairbanks, Fairbanks, AK 99775, USA

Correspondence to: Bas Altena (bas.altena@geo.uio.no)

Abstract. The measurement of glacier velocity fields using repeat satellite imagery has become a standard method of cryospheric research. However, the reliable discovery of important glacier velocity variations on a large scale from noisy time-series of such data is still problematic. In this study we propose a new post-processing procedure for assembling a set of velocity fields in time-series that generates a better visualization of glacier speed changes when the velocity fields are sparse or noisy. We demonstrate this automatic method on a large glacier area in Alaska/Canada. The visualization tool provides an overview of where and when interesting glacier dynamics are occurring. The goal is not to improve accuracy or precision, but the timing and location of ice flow events such as glacier surges. Building upon existing glacier velocity products from the GoLIVE data set (https://nsidc.org/data/golive), we compile a multi-temporal stack of velocity data over the Saint Elias Mountain range and vicinity. Each layer has a time separation of 32 days, making it possible to observe details such as within-season velocity change over an area of roughly 600 000 km^2. Our methodology is robust as it is based upon a fuzzy voting scheme to filter multiple outliers. The multi-temporal data stack is then smoothed to facilitate interpretation. This results in a spatio-temporal dataset where one can identify short-term glacier dynamics on a regional scale. Our implementation is fully automatic and the approach is independent of geographical area or satellite system used. Within the Saint Elias and Kluane mountain ranges, several surges and their propagation characteristics are identified and tracked through time, as well as more complicated dynamics in the Wrangell's mountains.

1 Introduction

Alaskan glaciers have a high mass turn-over rate (Arendt, 2011) and they can contribute considerably to sea level rise (Gardner et al., 2013; Arendt et al., 2013). Many of the glaciers have been identified as surge-type, from direct observations or from their looped moraines (Post, 1969; Herreid and Truffer, 2016). Furthermore, topographic glacier change in this region is heterogeneous (Muskett et al., 2003; Berthier et al., 2010; Melkonian et al., 2014) which is another indication of complicated responses.

Gaining better understanding of the drivers that cause glacier mass re-distribution is therefore of great importance.

Glacier velocity monitoring through satellite remote sensing has proven to be a useful tool to observe velocity change on a basin scale. Several studies have focused on dynamics of individual glaciers in Alaska, at an annual or seasonal resolution (Fatland and Lingle, 2002; Burgess et al., 2012; Turrin et al., 2013; Abe and Furuya, 2015; Abe et al., 2016). Such studies can give a better understanding of the specific characteristics of a glacier, and which circumstances are of importance for this behaviour and response. Region-wide annual or "snapshot" velocities also have been estimated over the Saint Elias Mountain range in previous studies (Burgess et al., 2013; Waechter et al., 2015). Their results give a first-order estimate of the dynamics at hand. With frequent satellite data coverage, it is possible to detect the time of glacier speed-ups to within a week (Altena and Kääb, 2017b), although the study did not include an automated approach. In the most recent work, regional analyses have been conducted with over sub-seasonal (Moon et al., 2014; Armstrong et al., 2017) and multi-decadal (Heid and Kääb, 2012; Dehecq et al., 2015) periods. With such data one is able to observe the behaviour of groups of glaciers that experience similar climatic settings. Consequently, surges and other glacier-dynamical events can be put into a wider spatio-temporal perspective. In this contribution we want to develop the methodological possibilities further and try to extract glacier velocities at a monthly resolution over a large region. The presented method retains spatial detail present in the data and does not simplify the flow structure. Consequently, we want to improve knowledge about the influence and timing of tributary and neighbouring ice flow variations.

Since the launch of Landsat 8 in 2013 a wealth of high-quality medium-resolution imagery is being acquired over the cryosphere on a global scale. Onboard data storage and rapid ground-system processing have made it possible to almost continuously acquire imagery. The archived data has enormous potential to advance our knowledge in glacier flow. Extraction of glacier velocity is one of the stated mission objectives (Roy et al., 2014). However, the data rate far exceeds the possibilities for manual interpretation. Fortunately, automatically generated velocity products are now available (Scambos et al., 2016; Rosenau et al., 2016), though at this point sophisticated quality control and post processing methods are still being developed.

Up to now, most studies of glacial velocity have had an emphasis on either spatial or temporal detail. When temporal detail is present, studies focus on a single or a handful of glaciers (Scherler et al., 2008; Quincey et al., 2011; Paul et al., 2017). On the other hand, when regional assessments are the focus, the temporal resolution ranges from a single time stamp up to annual resolution (Copland et al., 2009; Dehecq et al., 2015; Rosenau et al., 2015). Furthermore, most studies rely on filtering in the post-processing of vector data by using the correlation (Scambos et al., 1992; Kääb and Vollmer, 2000) or through median filtering within a zonal neighborhood (Skvarca, 1994; Paul et al., 2015). Some sophisticated post-processing procedures are available (Maksymiuk et al., 2016), but rely on the coupling with models based upon the Navier-Stokes equations. Also geometric properties can be taken into account during the matching to improve robustness and reduce post-processing efforts, such as reverse-correlation (Scambos et al., 1992; Jeong et al., 2017) or triangle closure (Altena and Kääb, 2017a).

Thus glacier velocity data is increasingly available, but in general post-processing is not at a sufficient level to directly exploit the full information content within these products. In this study we aim at the construction of a post-processing chain that is capable of extracting temporal information from stacks of noisy velocity data. Our emphasis is on discovering patterns over a mountain-range scale. Analysis of the individual details of the glacier-dynamical patterns identified by the processing will be considered in later work. For a single glacier, a manual selection of low-noise, good-coverage velocity data sets is possible. However, such a strategy will not be efficient when multiple glaciers or mountain ranges are of interest. Therefor, our implementation focuses on automatic post-processing, without the help of expert knowledge or human interaction.

In this study, we discuss the data used and provide background on the area under study. We then introduce the spatio-temporal structure of the data, followed by an explaination of our process for vector "voting" and vector field smoothing. The next section highlights our results and our validation and assessment of the performance of our method.

2 Data and study region

2.1 GoLIVE velocity fields

The velocity fields used in this study are based upon repeat optical remote sensing imagery and are distributed through the National Snow and Ice Data Center (NSIDC) (Scambos et al., 2016). These velocity fields are derived from finding displacements between pairs of Landsat 8 imagery, using the panchromatic band with 15 meter resolution. A high-pass filter of one kilometer spatial scale is applied before processing. Normalized cross-correlation is applied between the image pairs on a sampling grid with 300 meters spacing (Fahnestock et al., 2016; Scambos et al., 1992) and a template size of 20 pixels (or 300 m). The resulting products are grids with lateral displacements, the absolute correlation value, signal-to-noise ratio and ratio between the two best matches. For a detailed description of the processing chain see Fahnestock et al. (2016).

The Landsat 8 satellite has a same-orbit revisit time of 16 days and a swath width of 185 km. Only scenes which are at least 50% cloud-free are used (as determined by the provided estimate in the metadata for the scenes). Consequently, not every theoretical pair combination is matched, and also pairs across tracks are neglected (cf. (Altena and Kääb, 2017a)) to avoid more complicated viewing geometry adjustments. Georeference errors are compensated by the estimation of a polynomial bias surface through areas outside glaciers (i.e., assumed stable). The glacier mask used for that purpose is from the Randolp Glacier Inventory (RGI) (Pfeffer et al., 2014). The resulting grids come in Universal Transverse Mercator (UTM) projection and if orthorectification errors are minimal, displacements for precise georeferencing require only horizontal movement of a few meters (generally <10 m). In total we use twelve Landsat path/row tiles to cover our study area (Figure 1).

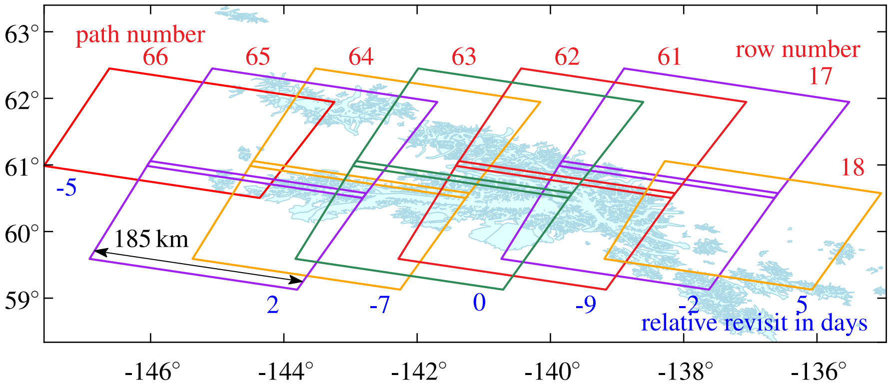

Figure 1. Nominal Landsat 8 footprints used over the studied region; colors are used to distinguish between different paths. Blue polygons are glacier outlines over the area of interest, stemming from the Randolph glacier inventory (Pfeffer et al., 2014).

2.2 Study region

The region of interest covers the Saint Elias, Wrangell and Kluane Mountain ranges, as well as some parts of the Chugach range. These ranges host roughly 42 000 000 km^2 glacier area, whereby roughly 22% of the glacier area is connected to marine terminating fronts draining into the Gulf of Alaska. The glaciological distribution of glacier types is diverse (Clarke and Holdsworth, 2002) and there is a large precipitation gradient over the mountain range. The highest amount of precipitation falls in summer or autumn. The study area covers mountain ranges that have two different clusters of climate. Along the coast one finds a maritime climate with a small annual temperature range. These mountains function as a barrier, and the mountain ranges behind, in the interior, have therefore a more continental climate (Bieniek et al., 2012).

3 Methodology

GoLIVE and other velocity products are composed products from at least two acquisitions. Such velocity fields with different time spans need to be combined, in order to be of use for time-serie analysis. To reduce the noise, the temporal configuration of these products can be used to synthesize a multi-temporal velocity field.

3.1 Temporal network configuration

At the high latitude of the Southern Alaska scenes from adjacent tracks have an overlap of 60%. Looking at only one track (or satellite path), multiple combinations of images over time periods of integer multitudes of 16 days can be matched against each other. For example, over a 96-days period (Δt), seven images are acquired in one track and their potential pairing combinations can be illustrated as a network (Figure 2). In this network every acquisition (I) is a node, and these nodes are connected through

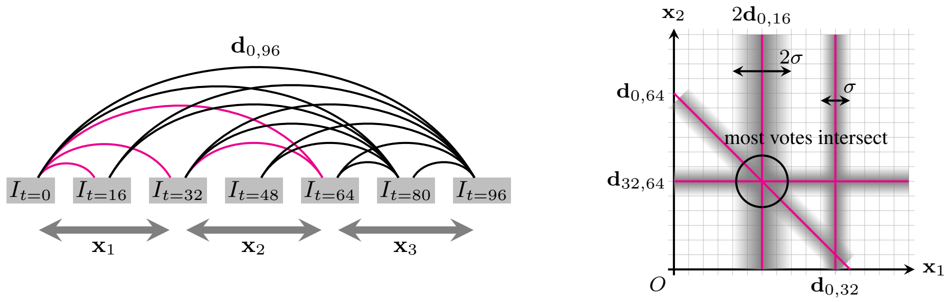

Figure 2. On the left is a graphical representation of Landsat 8 acquisitions (I) at different times (t) illustrated as nodes and matching solutions with displacements ($\mathbf{d}$) are shown as edges, within a network. The subscript for the displacement denotes the time interval. The velocities ($\mathbf{x}$) are estimated through the collection of all these displacements. At the right the mathematical representation or its parameter (Hough) space for voting of displacements over two time instances is shown, in this case the parameter space of only $\mathbf{x}_1$ & $\mathbf{x}_2$ are shown. The displacements ($\mathbf{d}$) translate in a solid line and the fading illustrates the different weighting to take measurement precision (σ) into account. Note the wider spread of the displacement noise for the image pair with a small interval ($\mathbf{d}_{0,16}$).

an edge that represents a matched pair leading to a collection of displacements (d) with an associated similarity measures (ρ).

When individual time steps need to be estimated, this network has in theory a great amount of redundancy. However in practice this is complicated, as combinations of images are not processed when there is too much obstruction by clouds. Furthermore, individual matches can be gross outliers due to surface change or lack of contrast and thus loss of similarity (displacement $\mathbf{d}_{0,32}$ in Figure 2). Consequently, when data from such a network is combined to synthesize one consistent velocity time series the estimation procedure needs to be able to resist multiple outliers or be able to identify whether displacement estimates could be extracted at a reliable level at all.

The network shown in figure 2 can be seen as a graph; nodes correspond to timestamps and edges to matched image pairs. Such a graph can be transformed into an adjacency matrix (A_G, see Figure 3). In this matrix the columns and rows represent different timestamps. The edges can be directed, meaning it can assign which acquisition is the master (reference) or the slave (search) image during the matching procedure. For the GoLIVE data, the oldest acquisition is always the reference image, hence within the matrix only the upper triangular part has filled entities. The spacing of the timesteps is 16 days and the amount of days is set into the corresponding entries when a time step is covered by an edge. Individual days are specified instead of a binary entity, to be able to merge adjacency matrices from different tracks which have different acquiring dates. If partial overlap of an edge occurs, then the time steps are proportionally distributed. For example, for a small network of three

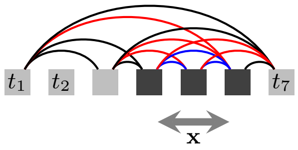

image timestamps $\longrightarrow$

$$A_G = \begin{array}{c|ccccccc} & t_1 & t_2 & t_3 & t_4 & t_5 & t_6 & t_7 \\ \hline t_1 & 0 & 0 & 1 & 1 & \color{red}{0} & \color{red}{1} & 1 \\ t_2 & 0 & 0 & 0 & 0 & \color{red}{0} & \color{red}{0} & 0 \\ t_3 & 0 & 0 & 0 & 1 & \color{red}{1} & \color{red}{1} & 1 \\ t_4 & 0 & 0 & 0 & 0 & \color{blue}{1} & \color{blue}{1} & \color{red}{1} \\ t_5 & 0 & 0 & 0 & 0 & 0 & \color{blue}{1} & \color{red}{1} \\ t_6 & 0 & 0 & 0 & 0 & 0 & 0 & 1 \\ t_7 & 0 & 0 & 0 & 0 & 0 & 0 & 0 \end{array}$$

timestamps $\downarrow$

Figure 3. Graphical and matrix representation of a network. Here acquisition pairs within a network are illustrated and written down in an adjacency matrix (A_G). The dark gray squares indicate acquisitions within a period to be estimated. The connecting colors symbolize an open (red) or closed (blue) selection of displacements to be used for the velocity estimation over this period ($\mathbf{x}$).

nodes, velocity (x) can be estimated through least-square adjustment through the following systems of equations (Altena and Kääb, 2017a),

$$\mathbf{y} = \mathbf{A}\mathbf{x}, \text{ where} \qquad \mathbf{y} = \begin{bmatrix} d_{12} \\ d_{23} \\ d_{13} \end{bmatrix}, \quad \mathbf{A} = \begin{bmatrix} \Delta t_{12} & 0 \\ 0 & \Delta t_{23} \\ \Delta t_{12} & \Delta t_{23} \end{bmatrix}, \quad \mathbf{x} = \begin{bmatrix} x_{12} \\ x_{23} \end{bmatrix}, \qquad (1)$$

The construction of the temporal network makes it possible to estimate the unknown parameters, i.e. the temporal components of the velocity time series, through different formulations. This is illustrated in Figure 3, where a selection of two velocities is estimated. Displacements between the three images within this time frame can be estimated (here blue), which we here call a "closed" network. But as can be seen in the figure as red connections, other displacements from outside the time frame are over-arching and stretching further than the initial time interval. Such measurements can be of interest as they can fill in gaps, but the glacier dynamics obtained will be smeared compared to the real ones. Consequently, we call such a network configuration an "open" network (here red).

3.2 Voting

The velocity dataset we use (like any) contains a large amount of incorrect or noisy displacements. Moreover, a least-square adjustment is very sensitive to outliers contained in the data to be fitted. Therefore, direct estimation of velocity through the above network is not easily possible and some selection procedure is needed to exclude gross errors. Outlier detection within a network such as in equation 1 can be done through statistical testing (Baarda, 1968; Teunissen, 2000), assuming measurements (d) are normally distributed. However, such procedures are less effective when several gross errors are present within the set of observations. Extracting information from highly contaminated data is therefore an active field of research. For example, robust estimators change the normal distribution to a heavy tailed distribution. Nevertheless, such estimations typically still start with normal least-squares adjustment based on the full initial set of observations, and only in the next step the weights are iteratively adjusted according to the amount of misfit. Hence, such methods are still restricted to robust a-priori knowledge or a data-set with relatively small amounts of contamination by gross errors.

Another common approach to cope with the adjustment of error-rich observations is through sampling strategies such as least-median of squares (Rousseeuw and Leroy, 2005), or random sampling and consensus (RANSAC) (Fischler and Bolles, 1981). A minimum amount of observations are picked randomly to solve the model. The estimated parameters are then used to assess how the initial model fits in respect to all observations. Then the procedure is repeated with a new set of observations. The sampling procedure is stopped when a solution is within predefined bounds, or executed a defined amount of times after which the best set is taken. Such methods are very popular as they can handle high contamination of data (up to 50%) and still resolve in a correct estimate. Put differently, the break-down point is .5 (Rousseeuw and Leroy, 2005). However, we use a different approach as these methods implement polynomial models. Our data set benefits from including conditional equations as well.

Exploration into possibility theory, through the use of fuzzy-logic, is another approach towards a solution (Sun, 1994). In this study we follow this latter direction and discretize the displacement-matching search-space after which we exploit a voting strategy. In that way, a fuzzy Hough transform (Han et al., 1994) is implemented. Our matching search space is simply the linear system of equations of the network described above. To illustrate the system, an example of a network with three image pairs (similar to equation 1) is shown in Figure 2. Every observation will fill the parameter space with a discretized weighting function. In one dimension this is a simple histogram, but in higher dimensions this will translate into a line which radially decreases in weight.

The advantage of a Hough search space is the resistance to multiple outliers. It builds support and is not reliant on the whole group of observations. Especially, when a second or third dimensional space is used, the chances of random (line)crossing decrease significantly. Hence, such events will stand out when multiple measurements do align. Furthermore, random measurement errors can be incorporated through introducing a distribution function. In our implementation this is a Gaussian, but other functions are possible as well. The disadvantage of the fuzzy Hough transform is its limitation to implement a large and detailed search space, as the dimension and resolution depend on the available computing resources.

The fuzzy Hough transform functions as a selection process to find observations which are to a certain extent in agreement. With this selection of inliers the velocity can finally be estimated through ordinary least-squares estimation. The model is the same as used to construct the network. However, the observations without consensus (i.e. outliers) are not used. The remaining observations can, nevertheless, still be misfits, such as from shadow casting, as no ice flow behavior is prescribed in the design

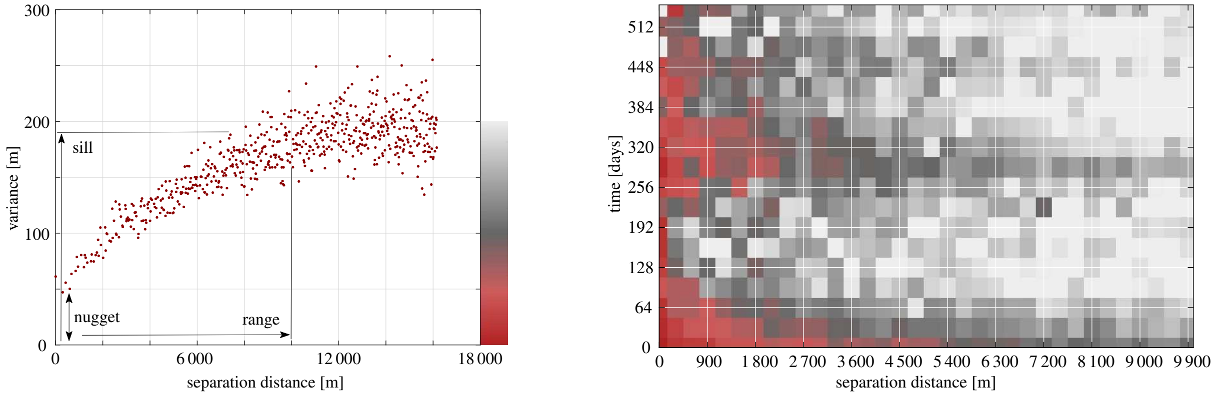

(a) Experimental variogram in the spatial domain

(b) Spatio-temporal experimental variogram

Figure 4. Experimental variograms over a slice of the stack and over a subset of the spatio-temporal stack.The colorbar along the axis of figure 4a, is used for the coloring of figure 4b

matrix of equation 1.

3.3 Smoothing

Because the voting and least-squares adjustment in our implementation has no neighborhood constraints but is rather strictly per matching grid point, the velocity estimates contain systematic, gross and random errors, though reduced with respect to the initial data set. Resulting in a spatio-temporal stack of velocity displacements, constructed with a regular temporal spacing that can thus be better analyzed. However, due to undersampling as a result of cloud cover, the stack might have holes. We apply a spatial-temporal smoothing taking both spatial and temporal information into account using the Whitacker approach that tries to minimize the following function,

$$S = \sum_i w_i(\hat{x}_i - x_i)^2 + \lambda \sum_i (\Delta^2 x_i)^2. \tag{2}$$

Here Δ denotes the difference operator, thus $\Delta x_i = x_{i+1} - x_i$. Similarly, Δ^2 is the double difference, describing the curvature of a signal ($\Delta^2 x_i = x_{+1} - 2x_i - x_{i-1}$). For the implementation of this method we use the procedure presented by Garcia (2010). This routine has an automatic procedure to estimate the smoothing parameter (λ) and has robust adaptive weighting (w). Its implementation is conducted through a discrete cosine transform (DCT), which eases the computational load. Furthermore, a discrete cosine transform operates both globally and locally, and in multiple dimensions. Lastly, in order to include all data at once, the vector field is configured as a complex number field.

The smoothing parameter is operating over both the space and time dimensions, but it is a single scalar. Hence in this form it would be dependent on the choice of grid resolutions in time and space. Therefore, in order to get rid of this dependency and fulfil the isotropy property, the spatial and temporal dimensions are scaled. For this scaling estimation we construct an experimental variogram and look at its distribution (Wackernagel, 2013). Along the spatial axis, the variogram in Figure 4a shows spatial correlation up to about 10 kilometers. This sampling interval is then used to look at the spatio-temporal dependencies, as illustrated in Figure 4b. Around a year temporal distance, one can see a clear correlation, which corresponds to the seasonal cycle of glacier velocity. From this variogram a rough scaling was estimated, and the anistropy was set towards a factor of four. In our case the pixel spacing is 300 meters and the time separation is 32 days.

4 Results

4.1 Method performance

Two different temporal networks (combinations of time intervals) can be formulated in order to calculate a velocity estimate, as is described in section 3.1. The "open" configuration includes a greater number of velocity estimates from image pairs, but this has consequences. It results in a more complete dataset, with coherent velocity fields, but when short-term glacier dynamics occur, temporal resolution of the event may be smeared. As an example, velocity estimates from two different network configurations are shown in Figure 5 with circles highlighting selected effects. For example, a longer stretch of the speeding-up section can be seen (A) on Fisher Glacier. In the "closed" configuration, this section is slimmer and has more details. However, by including more imagery as with an open configuration, the velocity estimates are more complete (B) and are better over stable ground (C). With more displacement vectors in the configuration, smaller-scale details, such as tributaries (D), become more apparent. Hence, depending on the application, the configuration can estimate a more complete velocity field or alternatively a temporally more precise product.

The spatio-temporal least-square estimates are still noisy or have outliers within. Therefore spatial-temporal smoothing is applied, in order to extract a better overview from the data, as is described in section 3.3. The results for one time interval are shown in Figure 6 and again some specific details are highlighted and discussed below.

Because the surroundings of glaciers are stable or slow moving terrain is included in the smoothing, high speed-ups such as on the surge bulge on the Steele glacier (E) are dampened. They do not disappear, as the signal is strong and persistent over time, but damping does occur. Furthermore, because the smoothing makes use of the temporal domain as well, small features emerge out of the noise such as flow tranches in the snow-covered upper parts of Kaskawulsh glacier (F). Also small areas of stable consistent fast flow like the icefall of Gates glacier, and the neighbouring staircase icefall of Root glacier (G), or the icefall between Dusty and Lowell glacier (H) get better pronounced in the smoothed data. Steps in along-track direction (I) are reduced because stable ground is motionless over time. In the along-track direction, these steps are filtered as for most of

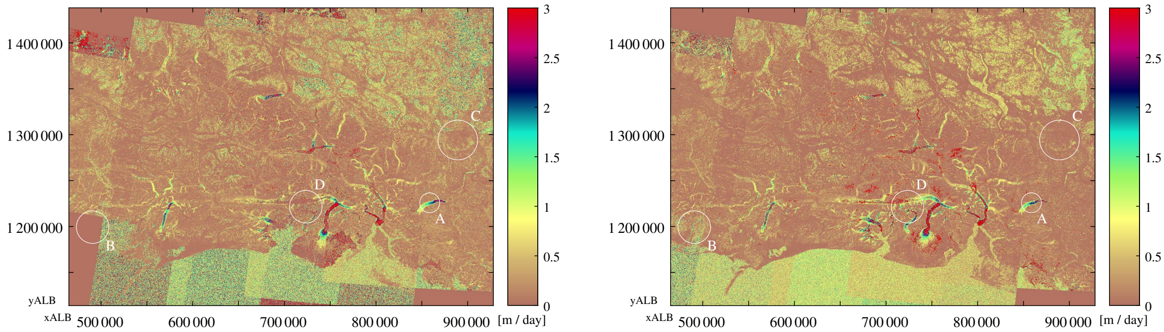

(a) Closed network selection

(b) Open network selection

Figure 5. Least square estimates of velocities with different network configurations, see Figure 2 for a toy example of the terminology. The study region spread over several UTM zones, hence the dataset is in Albers equal-area projection (ALB) with North American Datum 83.

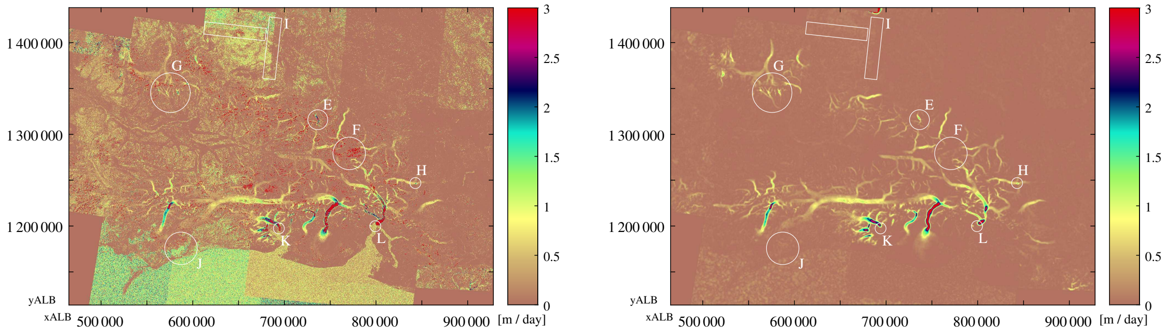

(a) Least squares estimation

(b) Spatio-temporal smoothing

Figure 6. Raw velocity estimates and smoothed estimates (taking space and time into account, see equation 2 and Figure 4).

the data the overlap is from the same path and thus acquired at the same time. Also random measurements over Vitus lake (J) are smoothed, as most of the estimates have a random velocity magnitude and orientation. An aspect of concern is the velocity bulge retreat of Guyot glacier (K); its front with large velocities seems to retreat in the smoothed version, while this is not the case for the original least-squares estimate. This is an effect caused by surrounding zero-valued water bodies. However, this effect is not at play at every glacier, as can be seen for example at Hubbard glacier (L). In general, this small damping effect of water bodies seem to be overweighed by the advantages from a clear image.

Because the stable terrain, which has no movement, impacts the smoothed velocity estimates in particular for surge and calving fronts (i.e. for strong spatial velocity gradients), the smoothing can be supported by a glacier mask. In our case, this mask is a rasterization of the Randolph Glacier Inventory (Pfeffer et al., 2014), with an additional dilation operation, to take potential advance or errors in the inventory into account. The difference in result for this masking procedure is shown in Figure 7, with

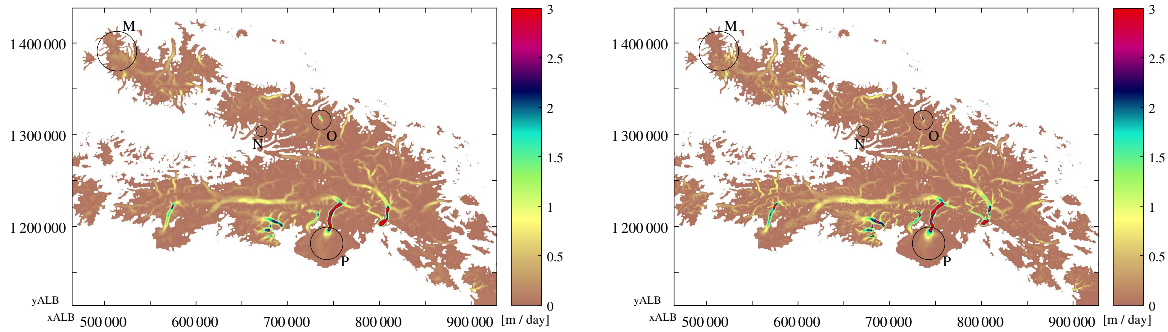

(a) Spatio-temporal smoothing without mask

(b) Spatio-temporal smoothing with mask

Figure 7. Smoothed grid of velocities, with masking of non-glaciated terrain (a) and with no masking (b).

some highlights. Unfortunately, speckles emerge in the estimates (M), though these only occur in the slower glacier areas. On the other hand, the masking makes it possible that individual flow branches become apparent, as can be seen for the tributaries of Barnard glacier (N). Also the surge bulges of Steele glacier (O), for example, become more pronounced. Still, the front of fast velocities of Malaspina Glacier that is reaching into the piedmont lobe (P) are taken a bit back into the Seward Threat presumably because higher frequencies are given a higher weight when a mask is used. All these steps were taken to arrive at the resulting velocity sequence which reveals glaciological dynamic changes.

4.2 Glaciological observations

When looking at the spatio-temporal dataset some patterns that are observed by others also appear in our dataset. For example, the full extent of Bering glacier slows down, as highlighted by Burgess et al. (2012), however our time series cover a period where the full deceleration towards a quiescent state can be seen. This observation of a slow down can also be made for Donjek Glacier (Abe et al., 2016) and Loogan Glacier (Abe and Furuya, 2015), see also Figure B2a for the velocity evolution at a point. In the time period covered by our study some surges appear to initiate. For example, our dataset comprises a surge traveling along the main trunk of Klutlan Glacier, see Figure B2b,B3a&B3b.

When looking at the surge occurring at Klutlan Glacier, the dataset does capture the evolution of its dynamics, as can be seen in Figure 9. The surge ignition seems to happen in the central trunk of the glacier, as the surge front progresses (with steady bulk velocities around four meters per day). The surge also propagates upwards mainly into the most westwards basin. The eastward basin does also increase in speed, but to a lesser extent, while the middle basin of this glacier system does not seem to be affected significantly. Though, its extent is mostly pronounced in the lower part of the glacier, as the upward creep of velocity increase is limited and does not reach the headwalls of any basin. In Landsat imagery of late 2017, there is no indication of

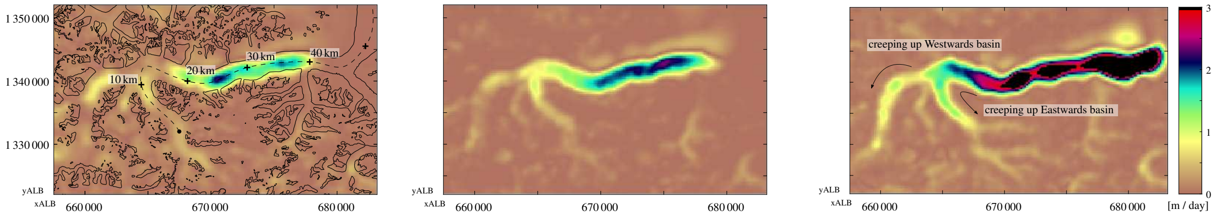

(a) 20 Jul 2014 - 21 Aug 2014 (b) 1 Mar 2015 - 2 Apr 2015 (c) 23 Jun 2016 - 25 Jul 2016

Figure 8. Snapshots of ice speeds at different time instances from a data compilation for the summer 2016 surge occurring on Klutlan Glacier.

any heavily crevassed terrain in the upper parts of these basins, which supports the hypothesis of a partially developed surge.

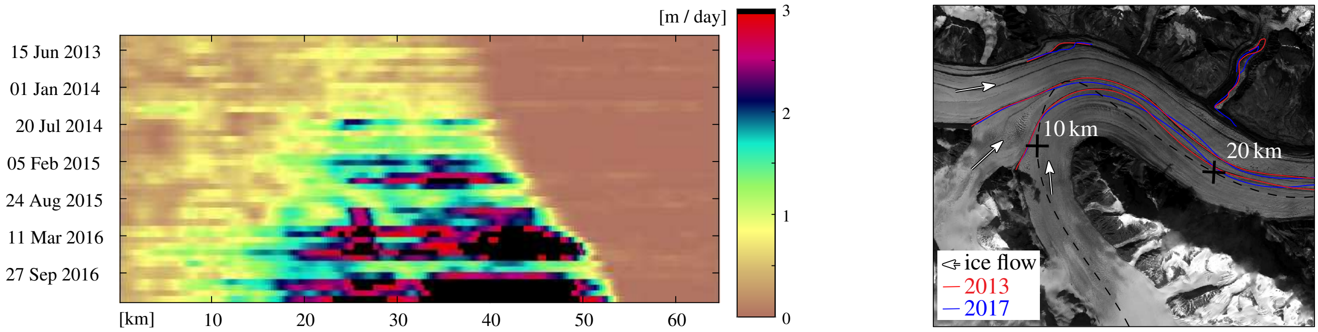

(a) Speed along flowline of Klutlan Glacier, line given in Figure 8a. (b) Moraine positions

Figure 9. The speed over the central flowline of Klutlan Glacier. The markings of this flowline are shown in figure 8a. In Figure 9b the convergence of different basins of the Klutlan glacier is shown, data is from a RapidEye acquisition on the 5th of September 2013 and at the 23rd of September 2017. For comparison the 2013 image is overlain with the two morraine positions.

When looking at the velocities over the flowline of the glacier, as in Figure 9a, both the extension downstream as well as the upstream progression of the surge can be seen. Most clearly, the surge front seems to propagate downwards with a steady velocity, but seems to slow down around the 50 km mark. Here, the glacier widens but the surge does continue. This suggests glacier depth is homogeneous here or glacier depth does not seem to play an important role in surge propagation.

At the end of the summer of 2016 the tributary just north of the 20 kilometer mark seems to increase in speed. This can be confirmed by tracing the extent of the looped moraines, as in Figure 9b. In the same imagery the medial moraines of the meeting point of all basins are mapped as well. Here, the moraine bands before and after the event align well in the junction, indicating a steady or similar contribution over the full period. Or an insignificant effect, as the surge has not been developing into very fast flow. In contrast, the lower part of this glacial trunk has moraine bands that do not align.

The surge behavior we observe for Klutlan Glacier is not unique and can be observed at other glaciers within the mountain ranges. For Fisher Glacier, a similar increase in speed is observed within the main trunk that later propagates downstream as well as upstream. Similarly, this seems to be the case for Walsh Glacier, where a speed increase at the eastern trunk triggers a surge on the northern trunk leading to glacier-wide acceleration. On its way the fast flowing ice initiates surges in tributaries downflow, but the surge extent also creeps upslope and tributaries that were more up-glacier from the initial surge start to speed up. This is also true for Steele Glacier, that develops into a surge and Hodgson Glacier is entrained into this fast flow as well.

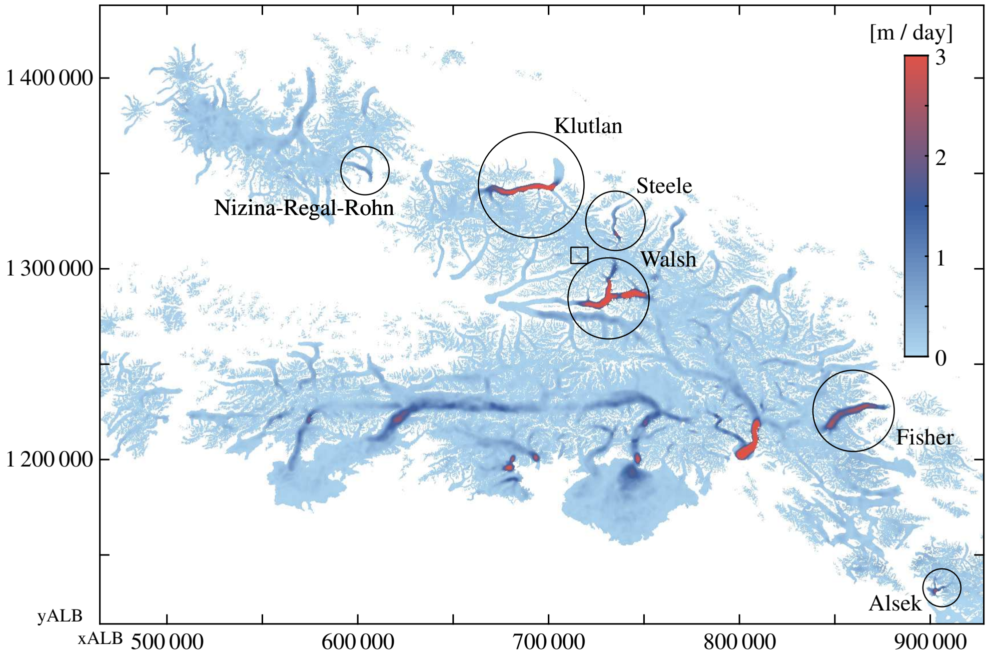

Figure 10. Spread of variation in flow speed over the observed period (using the difference between the 20th and 80th percentile). Different dynamic glaciers are encircled, and the square indicates the tributary glacier shown in Figure C1.

These analysis were best observed with the help of an animation (see supplement) but the identification was done through a simple visualization of the spread of flow speed, see Figure 10. Here the surging glaciers stand out, but also most of the tide-water glaciers, which have a highly dynamic nature at their fronts. Not only large glaciers can be identified also the dynamics in smaller tributaries. For example, a tributary of the Chitina Glacier seems to have pushed itself into the main trunk within a two-year time-period, see figure C1.

Apart from these already known dynamics at these glaciers, additional patterns are observed. At the Nizina-Regal-Rohn glacier system in the eastern Wrangell Mountains (Figure 10), formerly negative mass balance glaciers (Das et al., 2014) appear to have generally increased in speed, but are decelerating as our data record begins. A brief period of speed-up in 2014 is followed by an extended period of low variability. These two glaciers then seem to alternate in their summer speed magnitude, see animation and Figure B4.

5 Validation

5.1 Validation of post-processing procedures

The voting used in our procedure is assessed through validation with an independent velocity estimate. Terrestrial measurements are limited in the study area, hence we use satellite imagery from RapidEye satellites over a similar timespan. Data from this constellation has a resolution of 5 meters and through processing in a pyramid fashion, a detailed flow field can be extracted. This functions as a baseline dataset to compare the GoLIVE and the synthesized data. Here we will look at a section of Klutlan Glacier, which flows from west to east, thus aligned with one of the map axis. The velocity of this glacier, is due to its surge of significant magnitude, and therefor will have a wide spread in the voting space.

The two RapidEye images used over Klutlan Glacier were taken on 7th of September, and on 7th of October 2016. To retrieve the most complete displacement field of the glacier, we used a coarse-to-fine image matching scheme. The search window decreased stepwise (Kolaas, 2016) and the matching itself was done through Orientation Correlation (Heid and Kääb, 2012). At every step a local post-processing step (Westerweel and Scarano, 2005) was implemented, to filter outliers. The resulting displacement field over one axis (that is x, the general direction of flow) for this period is illustrated in the top inset of Figure 11.

For the voting of the Landsat 8-based GoLIVE data, an overlapping time period was chosen, from the 11th of September up to the 13th of October 2016, nearly but not exactly overlapping with the RapidEye pair. An open configuration was used for the voting, meaning all GoLIVE displacement fields covering this time period were used, resulting in a total of 36 velocity fields involved in the voting. The voted estimates and scores are illustrated in the third and fourth panel of Figure 11. The voted estimates have gray patches within, as these are estimates which had not enough displacement data to get a reliable estimate of equation 1, or are on stable terrain. Voting scores are high over the stable terrain, but low over the glacier trunk. To some extent this can be attributed to the surge event. The median over the stack and the median of absolute differences (MAD) are shown in the lower two panels of figure 11. These two measures are frequently used to analyze multi-temporal datasets (Dehecq et al., 2015).

When looking at this time period for the GoLIVE data, a clear displacement field is shown, as both images (11th Sept., 13th Oct.) from Landsat 8 were cloud free. The pattern is in close agreement with the RapidEye version. When looking at the voted

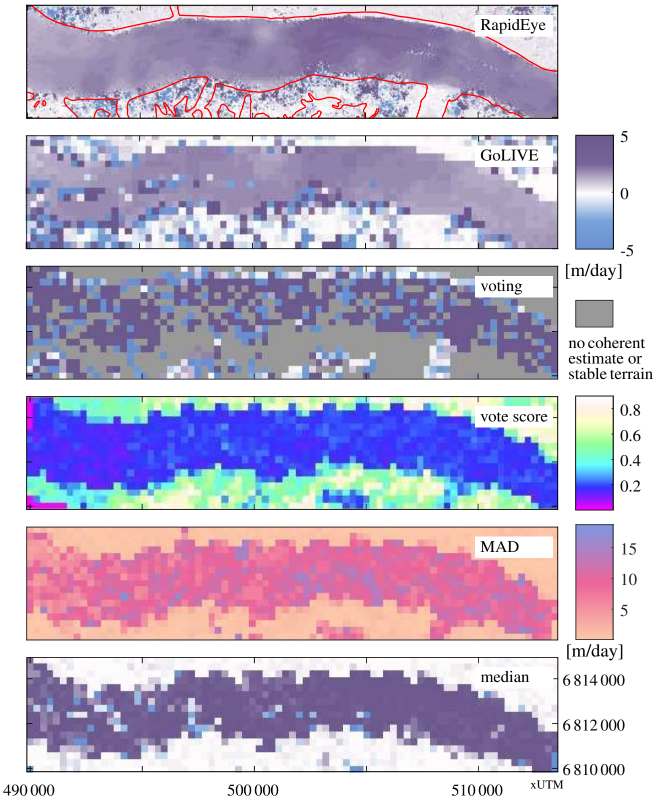

Figure 11. Monthly displacement in x-direction over the Klutlan Glacier using several data sources and velocity assessment schemes. The top panel shows velocities derived from two RapidEye images. Glacier borders are outlined in red. The second figure shows displacement estimates from a GoLIVE dataset (input), and the resulting voted estimate of a combination of 36 GoLIVE datasets (output). Its corresponding voting score of these estimates is shown in the fourth figure. The last two figures show the median over the full dataset, and the median of absolute deviation (MAD). These last two results would typically be used for data exploration.

estimate a similar pattern is observable but more corrupted and some data is not available. In some respect the median estimate appears to produce a better mapping. However the spread, as shown by the MAD, is considerable and will not help to justify which displacement is correct. Furthermore, the voted estimate is an estimate over a short interval, while the median estimate is calculated over the full stack.

To better assess these results, the distribution of both displacement fields are illustrated in Figure 12a and 12b. Two groups of displacement states are clearly visible, showing little movement, or a dominant movement eastwards. The voted distribution has more spread, and more outliers are present, but in general the mapping has the correct direction and magnitude. When the x-component of these displacements are compared against the RapidEye displacements a similar trend can be seen. These comparisons are shown in Figure 12c and 12d, where again a similar pattern is visible. The illustrated validation do show the

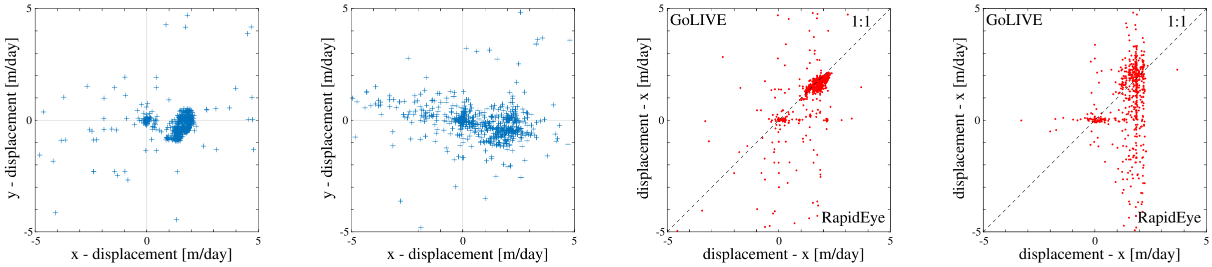

(a) distribution GoLIVE (b) distribution vote (c) RapidEye vs GoLIVE (d) RapidEye vs voting

Figure 12. Figure 12a & 12b show the distribution of velocities for a section of Klutlan glacier, their map view are shown in figure 11. In figure 12c & 12d the same data, but now only for the x-component is set against the validation displacement.

voting scheme is able to grasp the general trend of the short term glacier flow through a large stack of corrupted velocity fields. The pair shown by for the GoLIVE dataset is one clean example, while a large extent of these velocity fields are corrupted with clouds. Hence it is a step towards efficient information extraction, though the implemented voting has many potential aspects of improvements.

5.2 Validation over stable terrain

A second component for validation is an analysis of the stable ground, and the effect of the smoothing of the voted estimates. The non-glaciated terrain are the locations stemming from a mask. A similar mask, also based on the Randolpg glacier inventory, is used within the GoLIVE pipeline. Here, displacements over land and non-glaciated terrain are used to co-align the imagery, as geo-location errors might be present in the individual Landsat imagery. The fitting is done through a polynomial fit, still, in general these should be random, and its mean should be zero.

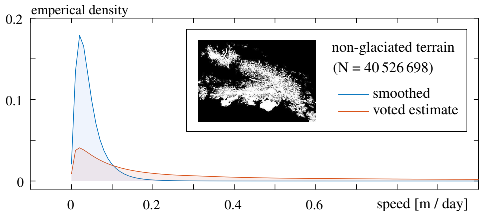

Figure 13. Distribution of the speed over stable terrain, for displacements extracted from the voting process, or after spatial temporal smoothing. The mask used is within the inset.

The distribution of these stable terrain measurements, more than 40 million in total, are illustrated in figure 13. Similar to the visual inspection already illustrated in Figure 6b, the distributions also show a clear improvement. This is a welcome property as the voted estimates still seem to be noisy with significant outliers.

6 Discussions

Synthesized velocity estimates from our post-processing chain of GoLIVE image-pair velocity determinations are dependent on the number and distribution of measured displacements (see Appendix A). Furthermore, the adjustment model assigns equal weighting to individual displacements if no other information is available. Hence some velocity changes might be missed or blurred in time. Such a drawback might be overcome with spatial constraints, such as an advection pattern imposed on the data, although this would increase the amount of post-processing.

Another limitation of our method concerns the glacier dynamics that are constrained by our model. In the current implementation the deviation (σ) is dependent on the time interval. From a measurement perspective this makes sense, but the model does thus not inherently account for speed change. Hence, for long time intervals the fuzzy function forces the deviation to become slim. This reduces the ability to get a correct match, especially when glacier-dynamical changes are occurring. It might therefore be worthwhile to explore the improvements occurring when a fixed deviation is set instead. In addition, the low score over glaciated terrain, might indicate the deviation of the displacement is set to tight. When this deviation is given higher bounds, the score increases and such parameter can then be used as a meaningful measure.

The smoothing parameter used is a single global parameter that assumes isotropy. In order to fulfill this property the spatio-temporal data has been scaled accordingly. However, when severe data gaps are present, the velocity dataset still seems to jump. This will improve when more data is available, for example by including Sentinel-2 data or incorporate across-track matching (Altena and Kääb, 2017a). An increase in votes will result in a better population of the vote space. In addition, the voting score, that is the consensus score in the Hough space, can be used for the initial weighting for the smoothing procedure (w in equation 2). This might reduce the amount of iterations used by the robust smoother.

In the Wrangell mountain range, Armstrong et al. (2017) found a significant speed-up in summer for the lower part for most large glaciers. We use the same data, and also see these speed-ups, but not every year. This might indicate that for these glaciers an efficient subglacial system is not developed each year, hence storage should occur. Such storage would be in line with the other glaciers in this region that are of surge-type. Also with our post processing it seems that signals from smaller or slimmer glaciers such as Copper Glacier can be picked up. And this glacier can be clearly identified as a speedup glacier type.

7 Conclusions

In the last couple of years the increase of high quality optical satellite systems have made it possible to extract detailed velocity fields over glaciers, ice caps and ice sheets. The GoLIVE dataset is a repository of such velocity fields available for analysis by the community. Discovery and exploration of this resource can be complicated due to its vast, unstructured and growing volume. Hence, in this study we introduce an efficient post-processing scheme to combine such displacement fields from different, but overlapping time-spans. The methodology is resistant to multiple outliers, as voting is used instead of testing. Though as spatial flow relations are not incorporated, the resulting synthesized timeseries still have outliers. Therefore, we use a data-driven spatio-temporal smoother to enhance the glacier flow changes.

Our synthesized time-series has a semi-monthly (32 days) temporal interval and a 300 meter spatial resolution. The time-series spans from 2013 till 2017 and covers the Saint Elias Mountain range and its neighbours. Within these ranges, we could identify several surges, among different glaciers at different times. Such details can even be extracted for small tributary glaciers. Velocities for the snow-covered upper glacier areas are in general estimated correctly.

This study is a demonstration of the capabilities of newly available remote sensing products. In this case we developed an effective tool to explore and discover glacier dynamics spanning a large region. Several glacier surges are identified and their development over time can be observed. The synthesized dataset has a semi-monthly resolution and is thus able to capture the seasonal evolution of glacier speed-ups and slow-downs. We demonstrate that it can be implemented with ease for a large region, covering several mountain ranges. Some velocity time series are highlighted as examples, but the dataset has much more information within. Furthermore, this dataset can be combined with digital elevation model (DEM) time-series (Wang and Kääb, 2015), and in this way ice fluxes can be estimated.

The demonstration of this study has a high temporal dimension, especially in respect to the sensor specific 16-days same-orbit repeat cycle. Our procedure uses produced velocity fields exploiting geometric properties, and is thus not dependent on matching scores or other auxiliary data. Consequently, harmonization with other velocity datasets from optical or SAR sensors can be easily implemented. This makes it possible to compose the patchwork of remote sensing products into a consistent time-series. Opening the opportunity to exploit the strengths of both SAR and optical satellite systems for glacier velocity monitoring. Especially when Sentinel-2 imagery and matching across orbits (Altena and Kääb, 2017a) is implemented. Then the temporal resolution might be reduced even further and a weekly resolution might be achievable for fast flowing glaciers.

Data availability. The Global Land Ice Velocity Extraction from Landsat 8 (GoLIVE) data is available at nsidc.org/data/golive (dx.doi.org/10.7265/N5ZP442B)

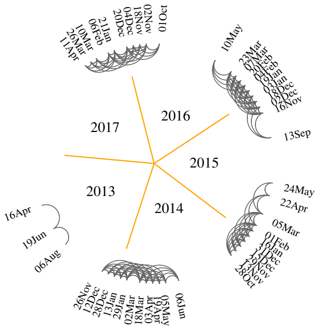

Figure A1. Node network of the velocity fields used in this study, for a specific path and row, 060 and 018, respectively.

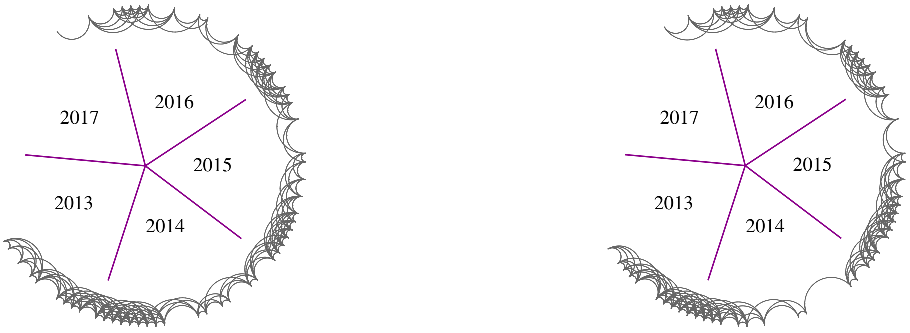

(a) path 061 row 017

(b) path 061 row 018

Appendix A: Used velocity pairs

The GoLIVE velocity fields used in this study are of a considerable amount. In order to get an overview of the data used, the velocity pairs are plotted in data graphs. In the example of Figure A1 the graph is annotated with dates, in order to better understand the other graphs corresponding to other path and rows which are given afterwards. Within the graph each gray arch represent a displacement field used in this study. The nodes of these arches come down to certain dates, where time is oriented counter clockwise. The colored lines represent year marks and are in correspondence with the colored footprints used in Figure 1. For sake of simplicity, dates are removed from all other graphs.

Appendix B: Corrections done by smoothing

In the following section plots are given of speed variations over selected areas of interest, the locations are denoted in Figure B1 by red crosses. Every plot has a bloxplot with the least squares estimate of a selection of observations. This selection was done

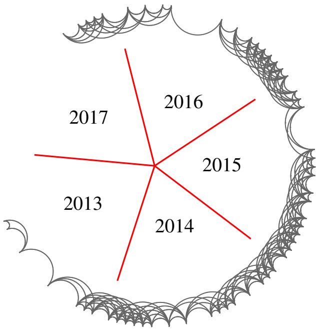

(a) path 062 row 017

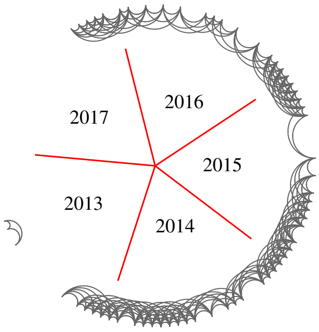

(b) path 062 row 018

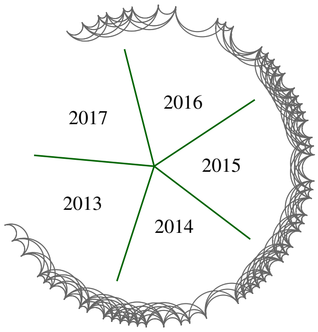

(a) path 063 row 017

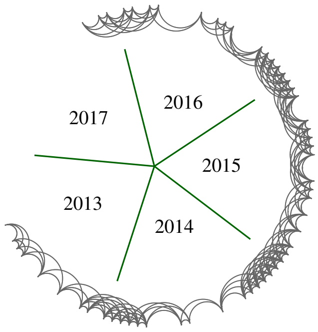

(b) path 063 row 018

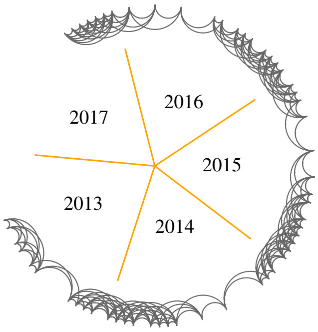

(a) path 064 row 017

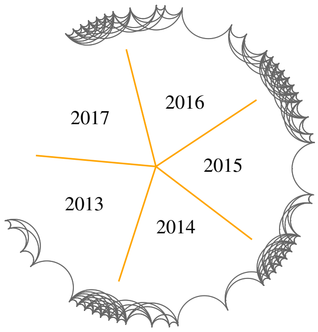

(b) path 064 row 018

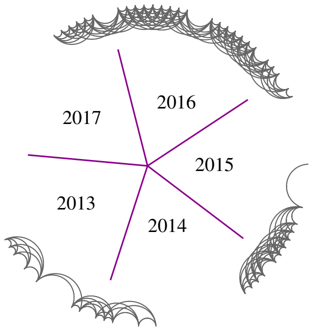

(a) path 065 row 017

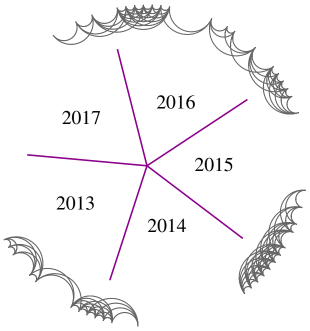

(b) path 065 row 018

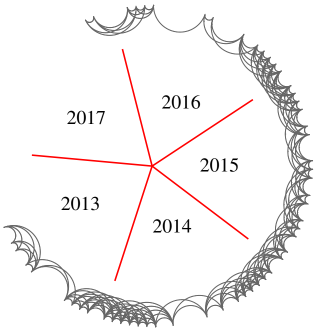

(a) path 066 row 017

through consensus, by voting as described in the paper. The gray lines indicate the smoothed spatio-temporal velocity. These are multiple lines, as not one estimate is taken, but a surrounding area of 5x5 pixels wide neighborhood is taken. This is done in order to have sufficient data points and see the spread of the observations and the influence of the smoother. A comparison between both estimated and smoothed version is shown in the right graph of each figure, where the white line indicates the 1:1.

Appendix C: Tributary dynamics

From the constructed multi-temporal time-series the variance of a low and high quantile can be estimated. This gives an overview of ice masses with a highly dynamic nature. Through this simple analysis, an unknown tributary surge was identified. The push of this tributary into the medial moraine and its velocity record over time can be seen in Figure C1.

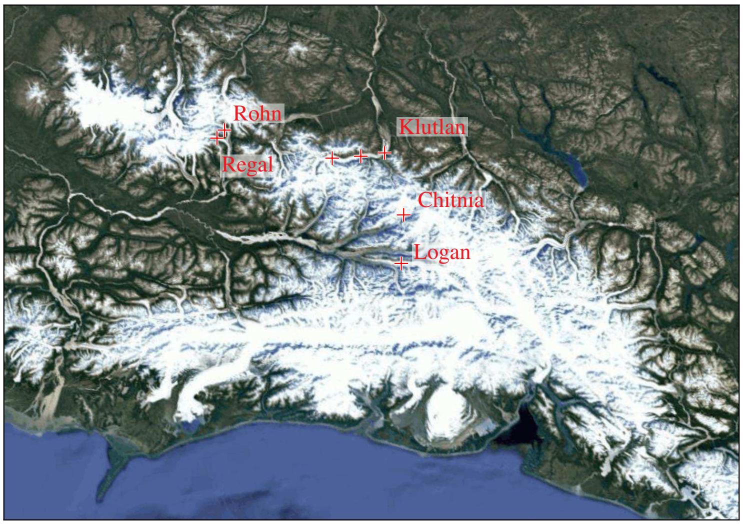

Figure B1. Location of the sampled points given in this section of the appendix. The background image is a Google Maps composite.

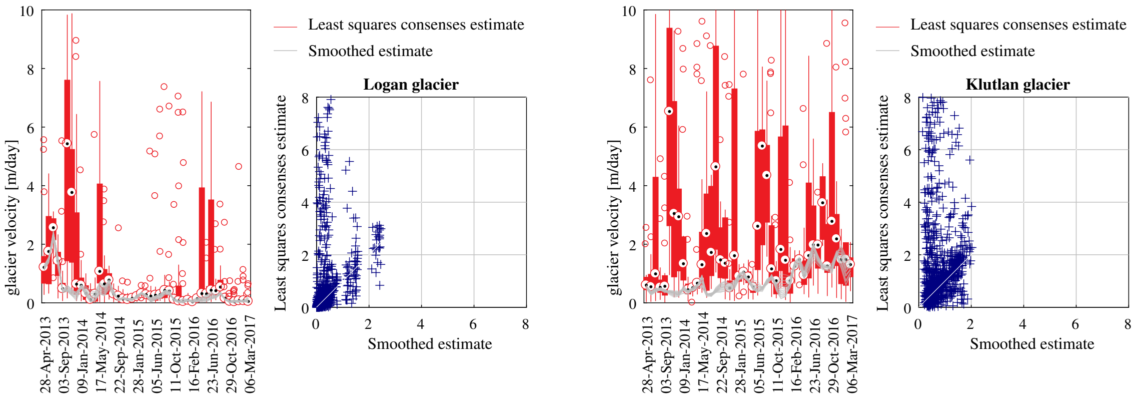

(a) middle part of Logan Glacier

(b) upper part of Klutlan Glacier.

Figure B2. The velocity of Logan glacier slows down and goes into quiescence, but it still seems to have some velocity increase in summertime. For the upperpart of Klutlan the summer velocities seem to increase as the surge develops over the years.

Author contributions. Bas Altena led the development of this study. All authors discussed the results and commented on the manuscript at all stages.

Competing interests. All authors declare no competing interests.

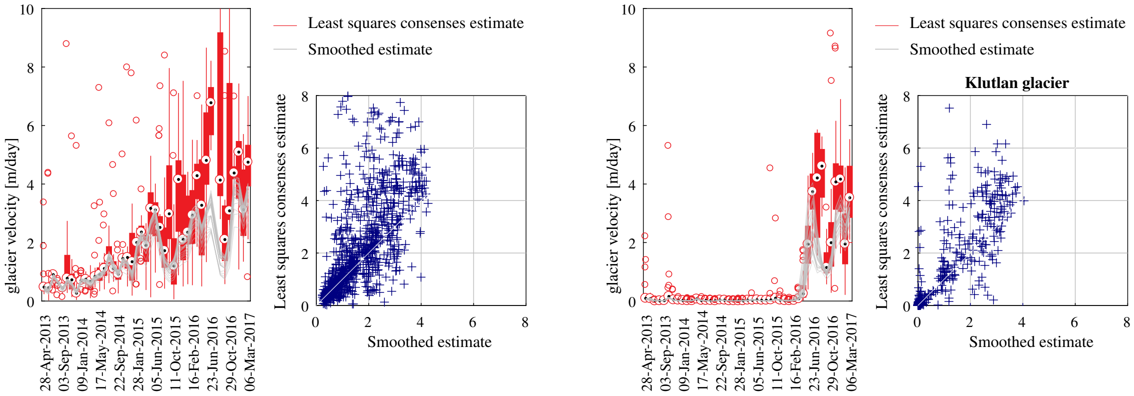

(a) middle part of Klutlan Glacier

(b) lower part of Klutlan Glacier

Figure B3. From our dataset the middle part of Klutlan seems to get in a surge, with heavy fluctuations, as several pulses come through. Two of these pulses seem to be visible as wel in the lower part of Klutlan glacier, which had been moving slow prior to the surge.

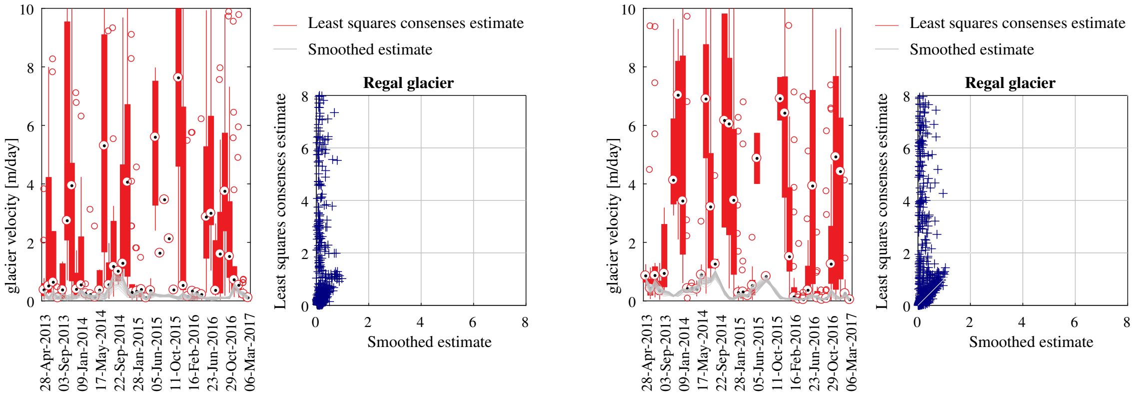

(a) middle part of Rohn Glacier

(b) middle part of Regal Glacier

Figure B4. Velocity evolution of the Rohn and Regal glacier that together make the Nizina glacier system. Both glaciers have every summer a small increase, however 2014 seems to stick out significantly for both. While, seems to have had another speed-up prior to 2013.

Acknowledgements. The research of B.A. and A.K. has been conducted through support from the European Union FP7 ERC project ICE-MASS (320816) and the ESA project Glaciers_cci (4000109873 14 I-NB). This work was supported by USGS award G12PC00066. The GoLIVE data processing and distribution system is supported by NASA Cryosphere award NNX16AJ88G. The authors are grateful to Planet Labs Inc for providing RapidEye satellite data for this study via Planet's Ambassadors Program.

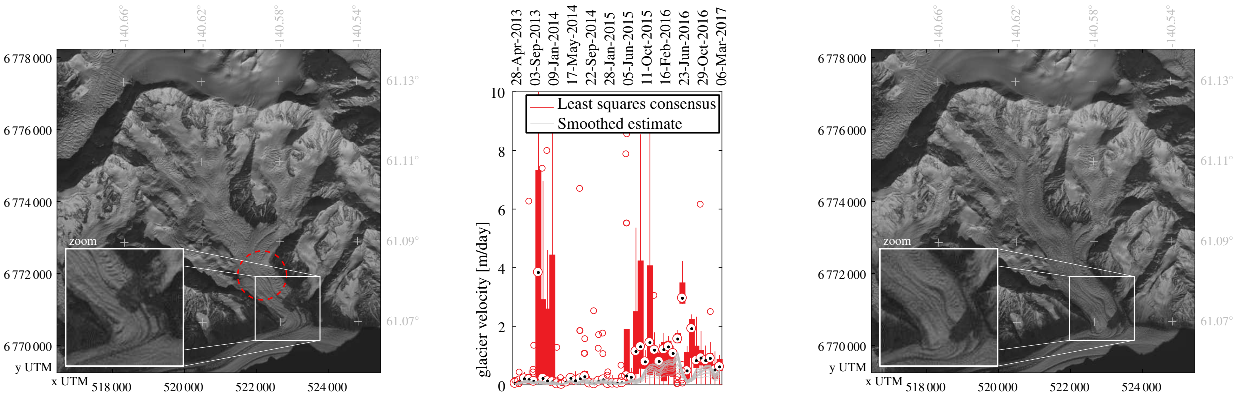

(a) 24 Sep 2014

(b) estimated velocities

(c) 23 Sep 2017

Figure C1. A tributary of Chitina Glacier surged in the period 2015-2016. Images are both acquired by Landsat 8, its location is indicated by a square in figure 10. The location of the time-series in figure C1b, is indicated by a red dashed circle in figure C1a.

References

Abe, T. and Furuya, M.: Winter speed-up of quiescent surge-type glaciers in Yukon, Canada, The Cryosphere, 9, 1183–1190, https://doi.org/10.5194/tc-9-1183-2015, 2015.

Abe, T., Furuya, M., and Sakakibara, D.: Brief Communication: Twelve-year cyclic surging episodes at Donjek Glacier in Yukon, Canada, The Cryosphere, 10, 1427–1432, https://doi.org/10.5194/tc-10-1427-2016, 2016.

Altena, B. and Kääb, A.: Elevation change and improved velocity retrieval using orthorectified optical satellite data from different orbits, Remote Sensing, 9, 300, https://doi.org/10.3390/rs9030300, 2017a.

Altena, B. and Kääb, A.: Weekly glacier flow estimation from dense satellite time series using adapted optical flow technology, Frontiers in Earth Science, 5, 53, https://doi.org/10.3389/feart.2017.00053, 2017b.

Arendt, A., Luthcke, S., Gardner, A., O'neel, S., Hill, D., Moholdt, G., and Abdalati, W.: Analysis of a GRACE global mascon solution for Gulf of Alaska glaciers, Journal of Glaciology, 59, 913–924, https://doi.org/10.3189/2013JoG12J197, 2013.

Arendt, A. A.: Assessing the status of Alaska's glaciers, Science, 332, 1044–1045, 2011.

Armstrong, W. H., Anderson, R. S., and Fahnestock, M. A.: Spatial patterns of summer speedup on South central Alaska glaciers, Geophysical Research Letters, 44, 1–10, https://doi.org/10.1002/2017GL074370, 2017.

Baarda, W.: A testing procedure for use in geodetic networks, Rijkscommissie voor Geodesie, 1968.

Berthier, E., Schiefer, E., Clarke, G. K., Menounos, B., and Rémy, F.: Contribution of Alaskan glaciers to sea-level rise derived from satellite imagery, Nature Geoscience, 3, 92, https://doi.org/10.1038/ngeo737, 2010.

Bieniek, P. A., Bhatt, U. S., Thoman, R. L., Angeloff, H., Partain, J., Papineau, J., Fritsch, F., Holloway, E., Walsh, J. E., Daly, C., et al.: Climate divisions for Alaska based on objective methods, Journal of Applied Meteorology and Climatology, 51, 1276–1289, 2012.

Burgess, E., Forster, R., Larsen, C., and Braun, M.: Surge dynamics on Bering Glacier, Alaska, in 2008-2011, The Cryosphere, 6, 1251, https://doi.org/10.5194/tc-6-1251-2012, 2012.

Burgess, E. W., Forster, R. R., and Larsen, C. F.: Flow velocities of Alaskan glaciers, Nature communications, 4, 2146, https://doi.org/10.1038/ncomms3146, 2013.

Clarke, G. K. and Holdsworth, G.: Glaciers of the St. Elias mountains, US Geological Survey professional paper, 2002.

Copland, L., Pope, S., Bishop, M. P., Shroder, J. F., Clendon, P., Bush, A., Kamp, U., Seong, Y. B., and Owen, L. A.: Glacier velocities across the central Karakoram, Annals of Glaciology, 50, 41–49, 2009.

Das, I., Hock, R., Berthier, E., and Lingle, C. S.: 21st-century increase in glacier mass loss in the Wrangell Mountains, Alaska, USA, from airborne laser altimetry and satellite stereo imagery, Journal of Glaciology, 60, 283–293, https://doi.org/10.3189/2014JoG13J119, 2014.

Dehecq, A., Gourmelen, N., and Trouvé, E.: Deriving large-scale glacier velocities from a complete satellite archive: Application to the Pamir–Karakoram–Himalaya, Remote Sensing of Environment, 162, 55–66, https://doi.org/10.1016/j.rse.2015.01.031, 2015.

Fahnestock, M., Scambos, T., Moon, T., Gardner, A., Haran, T., and Klinger, M.: Rapid large-area mapping of ice flow using Landsat 8, Remote Sensing of Environment, 185, 84–94, https://doi.org/10.1016/j.rse.2015.11.023, 2016.

Fatland, D. R. and Lingle, C. S.: InSAR observations of the 1993-95 Bering Glacier (Alaska, USA) surge and a surge hypothesis, Journal of Glaciology, 48, 439–451, https://doi.org/10.3189/172756502781831296, 2002.

Fischler, M. A. and Bolles, R. C.: Random sample consensus: a paradigm for model fitting with applications to image analysis and automated cartography, Communications of the ACM, 24, 381–395, https://doi.org/10.1145/358669.358692, 1981.

Garcia, D.: Robust smoothing of gridded data in one and higher dimensions with missing values, Computational statistics & data analysis, 54, 1167–1178, https://doi.org/10.1016/j.csda.2009.09.020, 2010.

Gardner, A. S., Moholdt, G., Cogley, J. G., Wouters, B., Arendt, A. A., Wahr, J., Berthier, E., Hock, R., Pfeffer, W. T., Kaser, G., et al.: A reconciled estimate of glacier contributions to sea level rise: 2003 to 2009, science, 340, 852–857, https://doi.org/10.1126/science.1234532, 2013.

Han, J., Kóczy, L., and Poston, T.: Fuzzy Hough transform, Pattern recognition letters, 15, 649–658, https://doi.org/10.1016/0167-8655(94)90068-X, 1994.

Heid, T. and Kääb, A.: Evaluation of existing image matching methods for deriving glacier surface displacements globally from optical satellite imagery, Remote Sensing of Environment, 118, 339–355, https://doi.org/10.1016/j.rse.2011.11.024, 2012.

Herreid, S. and Truffer, M.: Automated detection of unstable glacier flow and a spectrum of speedup behavior in the Alaska Range, Journal of Geophysical Research: Earth Surface, 121, 64–81, https://doi.org/10.1002/2015JF003502, 2016.

Jeong, S., Howat, I. M., and Ahn, Y.: Improved multiple matching method for observing glacier motion with repeat image feature tracking, IEEE Transactions on Geoscience and Remote Sensing, 55, 2431–2441, https://doi.org/10.1109/TGRS.2016.2643699, 2017.

Kääb, A. and Vollmer, M.: Surface geometry, thickness changes and flow fields on creeping mountain permafrost: automatic extraction by digital image analysis, Permafrost and Periglacial Processes, 11, 315–326, https://doi.org/10.1002/1099-1530(200012)11:4<315::AID-PPP365>3.0.CO;2-J, 2000.

Kolaas, J.: Getting started with HydrolabPIV v1.0, Research report in mechanics 2016:01, University of Oslo, urn.nb.no/URN:NBN:no-53997, 2016.

Maksymiuk, O., Mayer, C., and Stilla, U.: Velocity estimation of glaciers with physically-based spatial regularization. Experiments using satellite SAR intensity images, Remote Sensing of Environment, 172, 190–204, https://doi.org/10.1016/j.rse.2015.11.007, 2016.

Melkonian, A. K., Willis, M. J., and Pritchard, M. E.: Satellite-derived volume loss rates and glacier speeds for the Juneau Icefield, Alaska, Journal of Glaciology, 60, 743–760, https://doi.org/10.3189/2014JoG13J181, 2014.

Moon, T., Joughin, I., Smith, B., Broeke, M. R., Berg, W. J., Noël, B., and Usher, M.: Distinct patterns of seasonal Greenland glacier velocity, Geophysical research letters, 41, 7209–7216, https://doi.org/10.1002/2014GL061836, 2014.

Muskett, R. R., Lingle, C. S., Tangborn, W. V., and Rabus, B. T.: Multi-decadal elevation changes on Bagley ice valley and Malaspina glacier, Alaska, Geophysical Research Letters, 30, https://doi.org/10.1029/2003GL017707, 2003.

Paul, F., Bolch, T., Kääb, A., Nagler, T., Nuth, C., Scharrer, K., Shepherd, A., Strozzi, T., Ticconi, F., Bhambri, R., et al.: The glaciers climate change initiative: Methods for creating glacier area, elevation change and velocity products, Remote Sensing of Environment, 162, 408–426, 2015.

Paul, F., Strozzi, T., Schellenberger, T., and Kääb, A.: The 2015 Surge of Hispar glacier in the Karakoram, Remote Sensing, 9, 888, https://doi.org/10.3390/rs9090888, 2017.

Pfeffer, W. T., Arendt, A. A., Bliss, A., Bolch, T., Cogley, J. G., Gardner, A. S., Hagen, J.-O., Hock, R., Kaser, G., Kienholz, C., et al.: The Randolph Glacier Inventory: a globally complete inventory of glaciers, Journal of Glaciology, 60, 537–552, 2014.

Post, A.: Distribution of surging glaciers in western North America, Journal of Glaciology, 8, 229–240, 1969.

Quincey, D., Braun, M., Glasser, N., Bishop, M., Hewitt, K., and Luckman, A.: Karakoram glacier surge dynamics, Geophysical Research Letters, 38, https://doi.org/10.1029/2011GL049004, 2011.

Rosenau, R., Scheinert, M., and Dietrich, R.: A processing system to monitor Greenland outlet glacier velocity variations at decadal and seasonal time scales utilizing the Landsat imagery, Remote sensing of environment, 169, 1–19, https://doi.org/10.1016/j.rse.2015.07.012, 2015.

Rosenau, R., Scheinert, M., and Ebermann, B.: Velocity fields of Greenland outlet glaciers, Technische Universität Dresden, Germany, data1.geo.tu-dresden.de/flow_velocity/, 2016.

Rousseeuw, P. and Leroy, A.: Robust regression and outlier detection, vol. 589, John wiley & sons, https://doi.org/10.1002/0471725382, 2005.

Roy, D., Wulder, M., Loveland, T., Woodcock, C., Allen, R., Anderson, M., Helder, D., Irons, J., Johnson, D., Kennedy, R., Scambos, T., Schaaf, C., Schott, J., Sheng, Y., Vermote, E., Belward, A., Bindschadler, R., Cohen, W., Gao, F., Hipple, J., Hostert, P., Huntington, J., Justice, C., Kilic, A., Kovalskyy, V., Lee, Z., Lymburner, L., Masek, J., McCorkel, J., Shuai, Y., Trezza, R., Vogelmann, J., Wynne, R., and Zhu, Z.: Landsat-8: Science and product vision for terrestrial global change research, Remote Sensing of Environment, 145, 154–172, https://doi.org/10.1016/j.rse.2014.02.001, 2014.

Scambos, T., Dutkiewicz, M., Wilson, J., and Bindschadler, R.: Application of image cross-correlation to the measurement of glacier velocity using satellite image data, Remote Sensing of Environment, 42, 177–186, https://doi.org/10.1016/0034-4257(92)90101-O, 1992.

Scambos, T., Fahnestock, M., Moon, T., Gardner, A., and Klinger, M.: Global Land Ice Velocity Extraction from Landsat 8 (GoLIVE), Version 1, NSIDC: National Snow and Ice Data Center, Boulder, Colorado USA, https://doi.org/10.7265/N5ZP442B, nsidc.org/data/golive, 2016.

Scherler, D., Leprince, S., and Strecker, M. R.: Glacier-surface velocities in alpine terrain from optical satellite imagery - Accuracy improvement and quality assessment, Remote Sensing of Environment, 112, 3806–3819, https://doi.org/10.1016/j.rse.2008.05.018, 2008.

Skvarca, P.: Changes and surface features of the Larsen Ice Shelf, Antarctica, derived from Landsat and Kosmos mosaics, Annals of Glaciology, 20, 6–12, https://doi.org/10.3189/172756494794587140, 1994.

Sun, W.: A new method for localisation of gross errors, Survey review, 252, 344–358, https://doi.org/10.1179/sre.1994.32.252.344, 1994.

Teunissen, P.: Testing theory, Delft Academic Press, 2000.

Turrin, J., Forster, R. R., Larsen, C., and Sauber, J.: The propagation of a surge front on Bering glacier, Alaska, 2001–2011, Annals of Glaciology, 54, 221–228, https://doi.org/10.3189/2013AoG63A341, 2013.

Wackernagel, H.: Multivariate geostatistics: An introduction with applications, Springer Science & Business Media, https://doi.org/10.1007/978-3-662-05294-5, 2013.

Waechter, A., Copland, L., and Herdes, E.: Modern glacier velocities across the Icefield Ranges, St Elias Mountains, and variability at selected glaciers from 1959 to 2012, Journal of Glaciology, 61, 624–634, https://doi.org/10.3189/2015JoG14J14, 2015.

Wang, D. and Kääb, A.: Modeling glacier elevation change from DEM time series, Remote Sensing, 7, 10 117–10 142, https://doi.org/10.3390/rs70810117, 2015.

Westerweel, J. and Scarano, F.: Universal outlier detection for PIV data, Experiments in fluids, 39, 1096–1100, 2005.

Part III

Appendix

A Research Summary

A.1 Publications

A. Kääb, S.H. Windsvold, **B. Altena**, C. Nuth, T. Nagler, J. Wuite. 2016. *Glacier remote sensing using Sentinel-2. Part I: Radiometric and geometric performance, and application to ice velocity*, Remote Sensing.

A. Kääb, **B. Altena** & J. Mascaro. 2017. *Coseismic displacements of the 14 November 2016 Mw7.8 Kaikoura, New Zealand, earthquake using an optical cubesat constellation*, Natural Hazards and Earth Systems Sciences.

B. Altena & A. Kääb. 2017. *Elevation change and improved velocity retrieval using orthorectified optical satellite data from different orbits*, Remote Sensing.

B. Altena & A. Kääb. 2017. *Weekly glacier flow estimation from dense satellite time series using adapted optical flow technology*, Frontiers of Earth Sciences - Cryspheric sciece.

Y. Gong, T. Zwinger, J. ström, **B. Altena**, T. Schellenberger, R. Gladstone & J. Moore. 2017. *Basal friction evolution and crevasse distribution during the surge of Basin-3, Austfonna ice-cap*, The Crysphere Discussions.

B. Altena, T. Scambos, M. Fahnestock & A. kääb. 2017. *Recent short-term glacier velocity evolution over Southern Alaska from a large collection of Landsat data*, The Crysphere Discussions.

A.2 Conference proceedings

B. Altena, A. Kääb & C. Nuth. 2015. *Robust glacier displacements using knowledge-based image matching*, IEEE international workshop on the analysis of multitemporal Remote Sensing images.

B. Altena & A. Kääb. 2017. *Glacier ice loss monitored through the Planet cubesat constellation*, IEEE international workshop on the analysis of multitemporal Remote Sensing images.

S. Saunier, A. Northrop, S. Lavender, L. Galli, R. Ferrara, S. Mica, R. Biasutti, P. Goryl,

F. Gascon, M. Meloni, B. Desclee, **B. Altena**. 2017. *European Space Agency (ESA) Landsat MSS/TM/ETM+/OLI Archive: 42 years of our history Landsat MSS dataset improvements and multi temporal analysis*, IEEE international workshop on the analysis of multitemporal Remote Sensing images.
B. Altena, A. Mousivand, J. Mascaro & A. Kääb. 2017. *Potential and limitations of photometric reconstruction through a flock of Dove cubesats*, ISPRS Frontiers in Spectral imaging and 3D Technologies for Geospatial Solutions.

A.3 Popular science

Observing change in glacier flow from space, Frontiers for young minds.
Vele beekjes maken een groot water, Geografie.
Watching from space if the ferry is on time, Medium.
Bewegende reuzen - Onderzoek naar alpiene permafrost in Noorse rotswanden, Hoogtelijn.
Små supersatellitter revolusjonerer forskningen, Titan.

A.4 Attended courses

Pattern recognition and image interpretation, 2013. Leuven, Belgium.
Cryospheric modeling, 2015. Oslo, Norway.
Science, ethics & society, 2015. Oslo, Norway.
Experimental methods in fluid mechanics, 2016. Oslo, Norway.

A.5 Workshops

Ice sheets and glaciers in the climate system, 2015. Karthaus, Italy.
International glaciological summer school, 2016. McCarthy, AK, USA.
Writing successful research proposals, 2016. Bergen, Norway.
Polar Hackaton, 2017. Stony Brook, NY, USA.

A.6 Research visits

national snow and ice data center (NSIDC), spring 2017. Boulder, CO, USA.
subject: Getting usefull information out of GoLIVE data.
visiting: Ted Scambos.

A.7 Scientific involvement

Ambasador program, Planet Labs.
Reviewed for the following journals: Climate Dynamics, Journal of Selected Topics in Applied Earth Observation and Remote Sensing (JSTARS), Remote Sensing, & Water.